College I

University College London

The Properties of Molecular Ions

Caroline Sophie Scott O'Connor

Thesis submitted for Degree of Doctor of Philosophy

1999

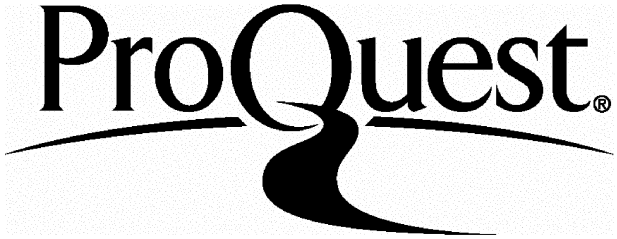

Abstract

This thesis presents the results of a series of experimental investigations of the single and double ionization of atmospheric molecules. In particular, the formation and dissociation of singly and doubly charged molecular ions are studied using electron-impact time-of-flight mass spectrometry and ion-ion coincidence techniques. The target atmospheric molecules under investigation are dinitrogen pentoxide (N_2O_5), nitric acid (HNO_3), chlorine dioxide (OClO) and chlorine monoxide (Cl_2O). These molecules are thought to play significant roles in the atmospheric ozone cycle as the sources of ozone-destroying radicals. However, despite the potential atmospheric importance of these reactive molecules and the interest in their photodissociation and spectroscopic properties, there have been relatively few investigations of their ionization.

In the single ionization studies, electron-impact time-of-flight mass spectrometry is used to determine the relative partial single ionization cross sections of the ions produced upon single ionization of the target molecules from near threshold to 500 eV. In the case of N_2O_5 and HNO_3, the appearance energies of previously unobserved fragment ions are also reported.

The first investigations of the double ionization of the target species are also reported in this thesis. In order to study the formation and fragmentation of the doubly charged molecular ions (dications), ion-ion coincidence techniques coupled with time-of-flight mass spectrometry have been developed. One and two-dimensional coincidence experiments have been performed, where the distinction between these experiments arises from the dimensionality of the data set recorded. In the one-dimensional experiments, comparisons of the experimentally determined appearance energies for the dication dissociation reactions with the energetics derived from the kinetic energy release involved in these dissociation processes give (i) an indication of the mechanisms by which the doubly-charged molecules dissociate and (ii) the energy of the dication electronic states which are the source of the fragment ions. From the 2D coincidence spectra, analysis of the ion pair intensities and peak slopes can also be interpreted to yield information concerning dication dissociation mechanisms. These investigations have led to the first evaluation of the ratio of double-to-single ionization cross sections for Cl_2O, OClO and HNO_3. In addition, first estimates of the double ionization energy of N_2O_5, HNO_3, OClO and Cl_2O and the development of the first models of their decay dynamics have also been made.

Contents

Abstract 2
Contents 3
Acknowledgements 5
Publications 6

Chapter 1 Introduction 7
1.1 Properties of Singly Charged Ions 8
1.2 Properties of Doubly Charged Ions 9
1.3 Ionization 12
1.4 Dissociation 15
1.5 Experimental Studies of Singly and Doubly Charged Ions 16
1.6 Conclusions 20
References 21

Chapter 2 Experimental Details 25
2.1 Introduction 25
2.2 Mass Spectrometry of Reactive Species 25
2.3 One-Dimensional Studies 26
2.4 Two-Dimensional Studies 40
2.5 Overall Conclusions 48
References 49

Chapter 3 Data Analysis 50
3.1 Introduction 50
3.2 One-Dimensional Studies 50
3.3 Two-Dimensional Studies 65
3.4 Overall Conclusions 79
References 80

Chapter 4 Single and Double Ionization of N_2O_5 82
4.1 Introduction 82
4.2 Experimental Details 82
4.3 One-Dimensional Studies 84
4.4 Overall Conclusions 97
References 98

Chapter 5 Single and Double Ionization of Cl_2O 100
5.1 Introduction 100
5.2 Experimental Details 101
5.3 One-Dimensional Studies 102
5.4 Two-Dimensional Studies 115
5.5 Overall Conclusions 127
References 129

Chapter 6 Single and Double Ionization of OClO 131
6.1 Introduction 131
6.2 Experimental Details 132
6.3 One-Dimensional Studies 133

6.4 Two-Dimensional Studies 144
6.5 Overall Conclusions 156
References 158

Chapter 7 Single and Double Ionization of HNO_3 160
7.1 Introduction 160
7.2 Experimental Details 161
7.3 One-Dimensional Studies 161
7.4 Two-Dimensional Studies 178
7.5 Overall Conclusions 196
References 198

Chapter 8 Further Work 199
Further Work 199
References 201

Appendix 1 202

Acknowledgements

I would like to thank my supervisor, Stephen Price, for all the help and support he has given me throughout both my undergraduate and postgraduate years at UCL. He has always been there to help with any major technical disasters in the lab or grammatical disasters when proof-reading my thesis. I am very grateful to him for being an excellent supervisor and friend over the years I have spent in the Ion Chemistry lab.

I would like to acknowledge the undergraduates who have worked in the lab either for their final year projects or vacation research placements; Kathy O'Neale, Nykola Jones, Fiona Cowen, Nurun Tafadar, Gurprit Lidder and Pietro Calandra. Their experimental and analytical work was invaluable during this research project and it is greatly appreciated. Thanks also to all the technical staff in the Chemistry Department at UCL and to the EPSRC for funding my research grant.

Finally I would like to thank my family and friends, in particular my parents and George, for all their support, both emotional and financial, over the past few years. Although they have yet to read the final product, I hope they will think, as I do, that all the hard work and endless re-writing of chapters was worth it.

Publications

The following publications are based on the work discussed in this thesis:

"Electron-impact ionization of dinitrogen pentoxide", Caroline S.S. O'Connor, Nykola C. Jones, Kathy O'Neale and Stephen D. Price, *International Journal of Mass Spectrometry and Ion Processes*, **154** (1996) 203-211.

"The formation and dissociation of the dinitrogen pentoxide dication", Caroline S.S. O'Connor, Nykola C. Jones and Stephen D. Price, *Chemical Physics*, **214** (1997) 131-141.

"Electron-impact ionization of nitric acid", Caroline S.S. O'Connor, Nykola C. Jones and Stephen D. Price, *International Journal of Mass Spectrometry and Ion Processes*, **163** (1997) 131-139.

"Formation and dissociation of the nitric acid dication", Caroline S.S. O'Connor and Stephen D. Price, *International Journal of Mass Spectrometry and Ion Processes*, **177** (1998) 119-129.

"Single and double electron-impact ionization of chlorine dioxide", Caroline S.S. O'Connor, Nurun Tafadar and Stephen D. Price, *Journal of the Chemical Society – Faraday Transactions*, **94** (1998) 1797-1803.

"Single and double electron-impact ionization of dichlorine monoxide (Cl_2O)", Caroline S.S. O'Connor and Stephen D. Price, *International Journal of Mass Spectrometry and Ion Processes*, **184** (1999) 11-23.

1. Introduction

This thesis discusses the single and double ionization of atmospheric molecules. In particular, the experimental investigation of the formation and dissociation of singly and doubly charged molecular ions.

Experimental developments over the years have made it possible to perform detailed studies of the structure, spectroscopy and dynamics of singly charged positive ions, monocations.[1] As a result, there now exists a substantial amount of information on these species.[2] However, despite the mass spectrometric observation of the first atomic doubly charged ion (dication) over 70 years ago,[3] followed closely by the observation of doubly charged carbon monoxide molecules,[4] the amount of information available concerning the properties of molecular dications is limited. This is the result of relatively high energies required for their formation and their inherent instability, which complicate experiments.[5]

Over recent years, the properties of molecular dications have, however, been the subject of a steadily increasing number of experimental investigations. This increase has occurred in part because several new experimental techniques have been developed to probe these short-lived species.[6-8] As a result of these experimental efforts, a clearer picture is now emerging of the energetics and fates of the low-lying electronic states of several diatomic and a small handful of triatomic dications. Indeed, in some cases information is now available concerning the energies and dynamics of the vibrational levels supported in dication metastable electronic states.[9-12] The majority of these experimental studies have probed the properties of isolated molecular dications but recently the reactivity of molecular dications in collisions with neutral atomic or molecular species has been investigated, both experimentally and theoretically.[8,13-17]

Quantitative studies of molecular ionization, both single and double, have inherent utility as they provide experimental data for comparison with the theoretical models of molecular dications[18-20] and electron/molecule scattering[21-23]. In addition, an understanding of the properties of ions provided by these experiments allows the modelling of their role in energised media such as plasmas, planetary ionospheres and the interstellar environment.[24-27]

This thesis presents the results of investigations into the single and double ionization of reactive species present in the stratosphere. The atmospheric molecules studied are dinitrogen pentoxide (N_2O_5), chlorine monoxide (Cl_2O), chlorine dioxide (OClO) and nitric acid (HNO_3). These molecules are thought to play significant roles in the atmospheric ozone cycle as sources of ozone-destroying radicals.[28] Despite the possible atmospheric importance of these reactive molecules, there have been relatively few investigations of their ionization.[29-39]

One and two-dimensional studies of the single and double ionization of these molecules have been performed using a conventional time-of-flight mass spectrometer. The distinction between the one and two-dimensional studies is given in Chapter 2, together with a description of the experimental apparatus and methodology. The procedures used to analysis the experimental data obtained from the single and double ionization studies are discussed in detail in Chapter 3. The remainder of the thesis involves the presentation of the results of the experimental work and a discussion of the results for each target molecule in turn.

This thesis presents results of the single ionization of N_2O_5, Cl_2O, OClO and HNO_3 and the first investigations of the double ionization of these target molecules using time-of-flight mass spectrometry and ion-ion coincidence techniques. However, in order to place the results and conclusions discussed in this thesis into context, it is first necessary to begin with an introduction to the properties of singly and doubly charged ions, together with a brief overview of ionization, dissociation and relevant experimental techniques used to investigate these charged species.

1.1 Properties of Singly Charged Ions

Single ionization of a neutral molecule involves a transition between two well-defined electronic states of the molecule and the molecular ion, resulting in the removal of an electron from the neutral species to form a singly charged ion. According to the Franck-Condon principle, there is no change in the molecular geometry or the velocity of relative nuclear motion during ionization, due to the large nuclear to electronic mass ratio and short interaction times. Therefore, a vertical transition from the ground electronic state to the ionic electronic state occurs.

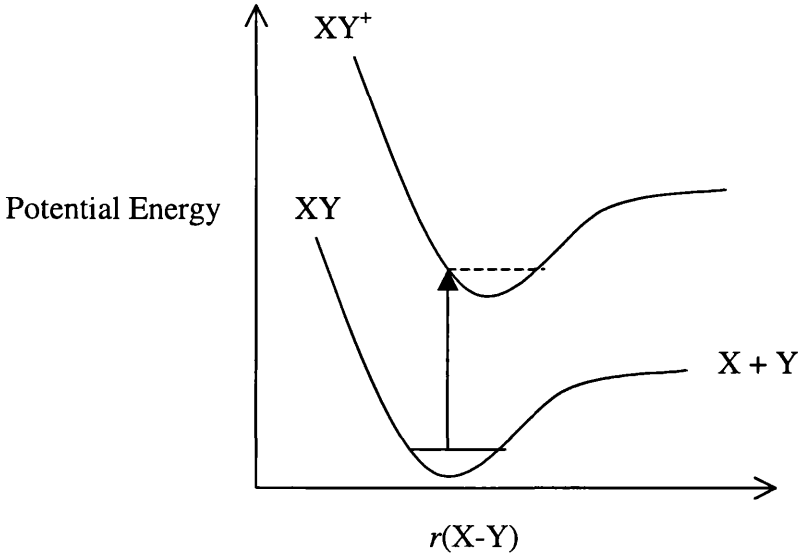

Fig. 1.1 Schematic potential energy curves for a diatomic molecule XY illustrating the formation of the monocation on a bound surface forming XY^+.

Vibrational and rotational excitation also occurs but the energy transferred into these excitations is significantly less than the energy of the electronic transition.

Upon ionization, different reaction channels, such as dissociative ionization or stable parent monocation formation, may be accessed depending on the relative shape of the potential energy curves in a specific system. For example, the cation could be formed on either a bound surface, resulting in a stable species XY^+ (Fig. 1.1) or a repulsive surface, resulting in an unstable entity which subsequently dissociates (Fig. 1.2). In fact, due to the inherent electrostatic attraction between a charged ion and a neutral, all monocations must possess at least one bound electronic state. However, in some cases the relative shape of the neutral and cationic potential energy curves means that the bound region of the excited electronic state cannot be accessed *via* a vertical transition from the ground state neutral molecule (Fig. 1.2). As a result, the parent monocation will rapidly fragment forming a daughter monocation and a neutral product,

$$XY^+ \rightarrow X^+ + Y \qquad (1.I)$$

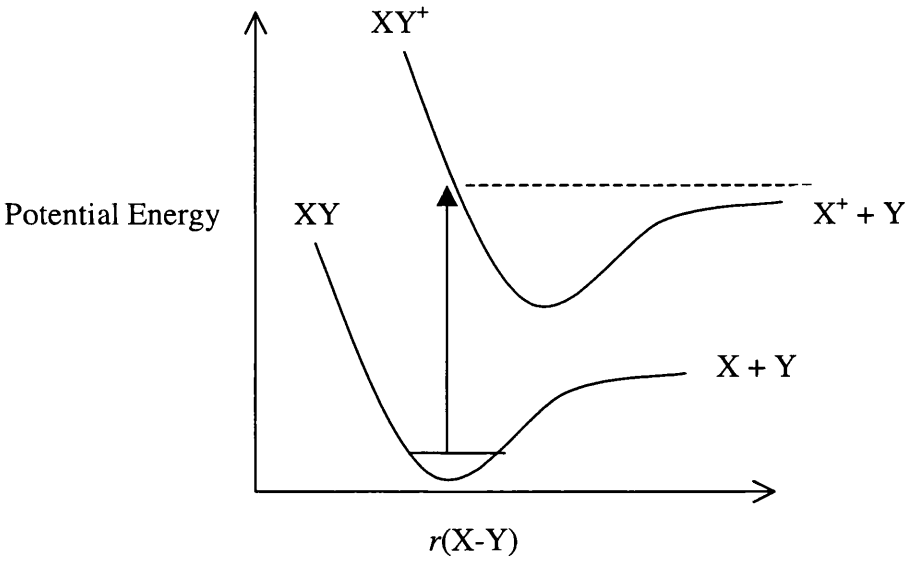

Fig. 1.2 Schematic potential energy curves for a diatomic monocation illustrating the formation of the monocation on the repulsive surface of a bound state leading to dissociation to form $X^+ + Y$.

1.2 Properties of Doubly Charged Ions

In contrast to monocations, the majority of dication electronic states are thermodynamically unstable with respect to dissociation, lying at energies above the asymptote for charge separation (Fig. 1.3).[5] As a result, upon formation most molecular dications undergo immediate fragmentation to give a pair of singly charged ions and, in some cases, additional neutral products.

$$XY^{2+} \rightarrow X^+ + Y^+ \qquad (1.II)$$

$$XY_2^{2+} \rightarrow X^+ + Y^+ + Y \qquad (1.III)$$

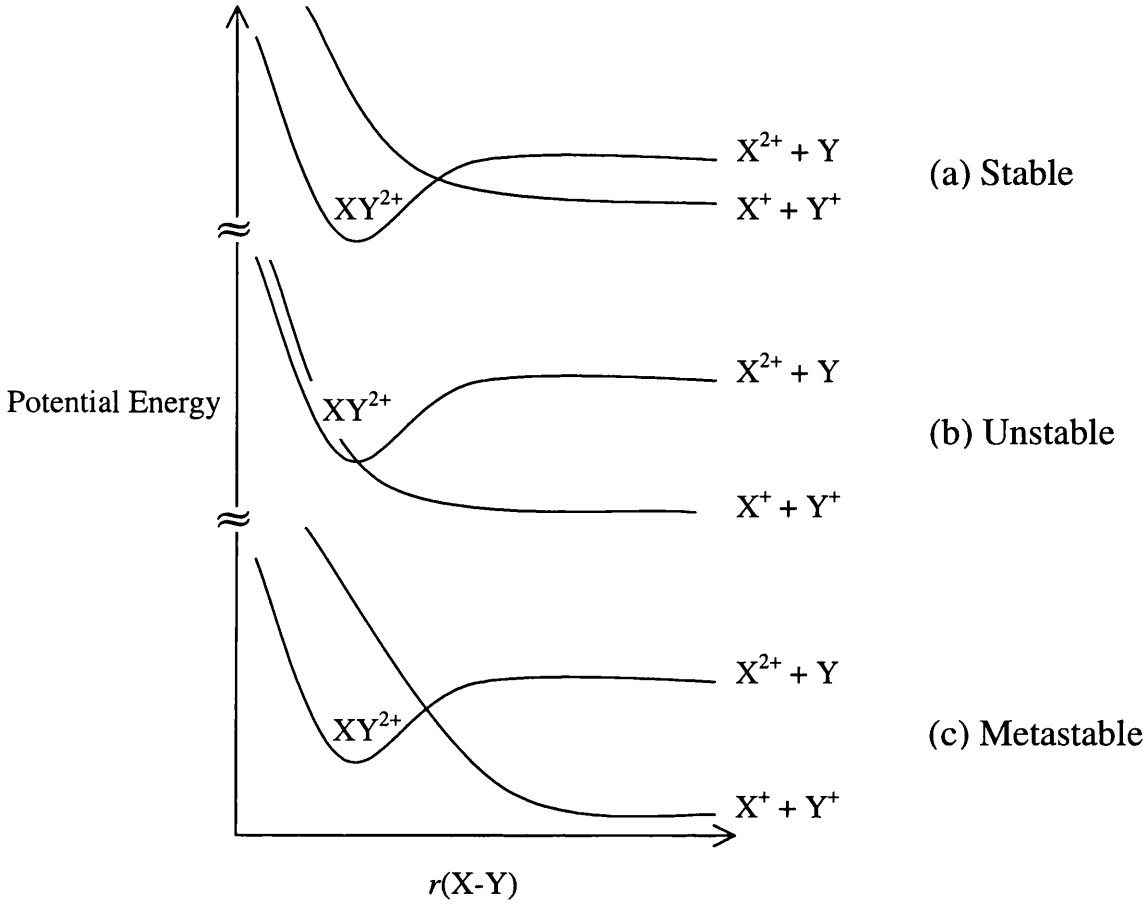

Fig. 1.3 Schematic potential energy curves for diatomic dications XY^{2+}: (a) thermodynamically stable dication, (b) thermodynamically unstable dication and (c) metastable dication.

The dication potential energy surface leading to the charge separating dissociation asymptote is often repulsive at small r(X-Y) due to the large Coulombic repulsion between the positive ions. As a result, molecular dications are generally unstable with lifetimes in the sub-nanosecond range and they exhibit a large kinetic energy release (~5 eV) upon dissociation (Fig. 1.4).[5]

Although, as mentioned above, most dication electronic states lie above the charge separation asymptote, thermodynamically stable dications, for which the bound XY^{2+} state is lower in energy than the lowest asymptote, do exist (Fig. 1.3).[40-42] Recent interest[41] in small thermodynamically stable dications such as $XeHe^{2+}$, AlF^{2+} and $FeNH^{2+}$ has arisen because they may provide insight into the nature of chemical bonding in the presence of multiple charges.

The dissociation of some molecular dications may occur *via* deferred charge separation [Reaction (1.IV)], although such behaviour occurs predominantly in larger molecules, such as napthalene.[43]

$$XY_2^{2+} \rightarrow XY^{2+} + Y \qquad (1.IV)$$

Following deferred charge separation, the daughter dication XY^{2+} may undergo further fragmentation to form a pair of singly charged ions [Reaction (1.V)], or undergo further neutral loss [Reaction (1.VI)].

$$XY^{2+} \rightarrow X^{+} + Y^{+} \quad (1.V)$$

$$XY^{2+} \rightarrow X^{2+} + Y \quad (1.VI)$$

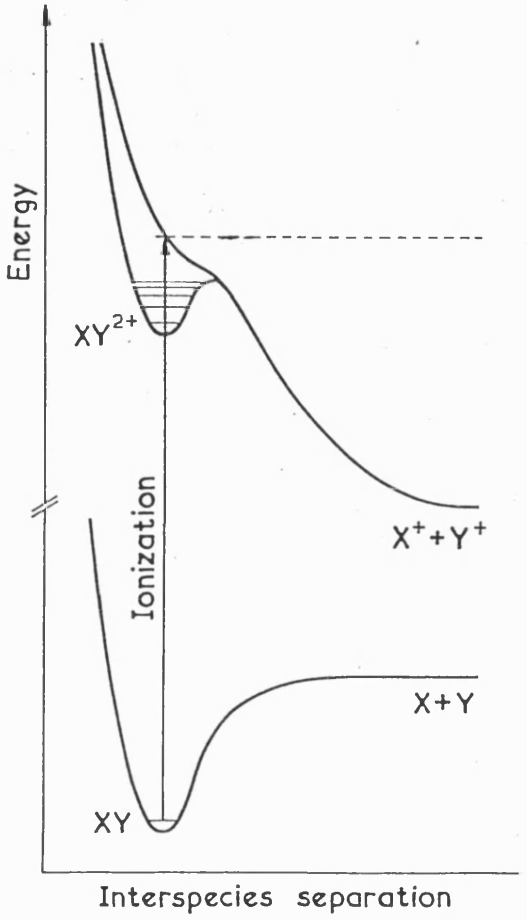

Fig. 1.4 Schematic potential energy curves for a diatomic dication.

For many dications at least one long-lived electronic state exists as a result of a barrier in the potential energy surface correlating with the charge separation asymptote. This state is termed "metastable" as it usually lies at an energy above the charge separation asymptote (Fig. 1.3 & Fig. 1.4). Commonly, one or more of the vibrational levels supported in such a metastable state have a lifetime of the order of the mass spectrometric (microsecond) timescale.[44-46]

Currently, there are two interpretations proposed as to the origin of the barrier in the potential energy surface which gives rise to dication metastable states. The first explanation considers that the avoided crossing between the attractive energy curve corresponding to $X^{2+} + Y$ and the predominantly repulsive curve corresponding to the charge separation $X^{+} + Y^{+}$ gives rise to the potential barrier (Fig. 1.5). Such an avoided crossing can give rise to a potential well whose depth and width are sufficient to permit the existence of metastable molecular dications XY^{2+}.[7]

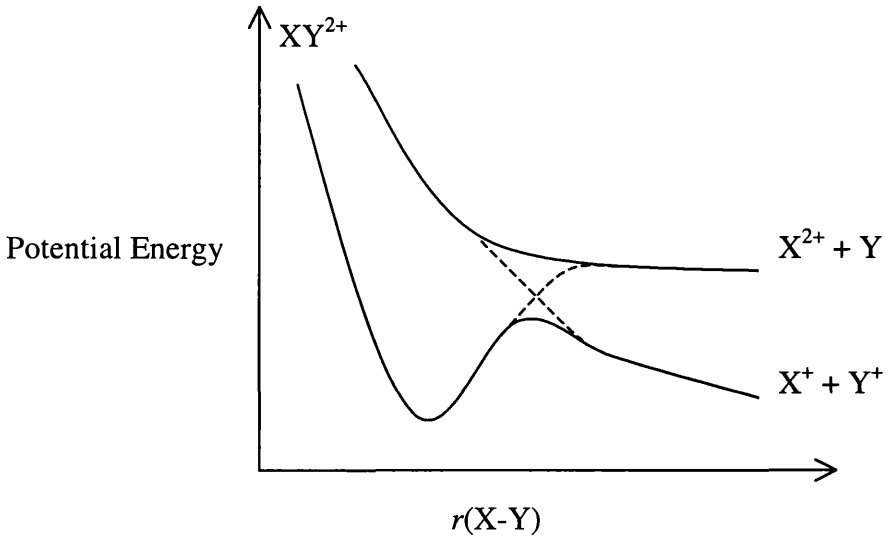

Fig. 1.5 Avoided crossing of the potential energy curves of XY^{2+} leading to the $X^{2+} + Y$ and $X^{+} + Y^{+}$ dissociation limits.

The second interpretation of the existence of metastable dications was proposed following the theoretical investigation of the electronic structure of F_2^{2+}. This study of F_2^{2+} found that the potential energy curves of this dication could be reproduced by adding a Coulomb repulsion potential to the potential energy curves of O_2, the isoelectronic neutral.[47] Therefore, it is proposed that dication states can be thought of as arising from the combination of the chemical binding potential of the isoelectronic neutral molecule and the Coulomb repulsion of the constituent ion pair. Thus, metastable states of the dication will exist when the strength of the chemical bond is sufficient to overcome the repulsion between the two positive charges. However, in some heteronuclear diatomic dications, such as HCl^{2+}, this additive model is unsuitable since, at small internuclear distances, both positive charges reside on the same atom.[48]

1.3 Ionization

In order to achieve the single and double ionization of neutral molecules, there are three methods that are commonly used: electron-impact ionization, photoionization and collisional ionization. In the work discussed in this thesis, electron-impact ionization alone is used in the single and double ionization experiments. However, a brief description of each ionization process is given below.

Electron-Impact Ionization

Electron-impact ionization generally involves the formation of ions following collisions between electrons, usually produced from the thermionic emission of a filament, and neutral species. Electron-impact ionization is a well-established method of ion generation and is still widely used in experiments investigating the formation and fragmentation of ions.[49-55]

If the energy of an electron beam colliding with a gas-phase molecule is greater than a critical value (ionization energy or appearance energy), and depending on the cross section, some target species will be ionized.

$$XY + e^- \rightarrow XY^+ + 2e^- \qquad (1.VII)$$

The majority of ions formed by electron-impact ionization are singly charged parent and fragment ions formed from dissociative single ionization. In electron-impact ionization experiments, single ionization is predominant since, in general, the multiple ionization cross section is significantly smaller (1-5%) than the single ionization cross section.[2]

The cross section for the electron-impact single ionization process σ_{ion} depends on the amount E by which the energy of the system exceeds the ionization energy of the species. The relationship between σ_{ion} and E is described by the Wannier Law,[56] where

$$\sigma_{ion} \propto E^{1.127} \qquad \text{Eq. 1.1}$$

The Wannier Law is a threshold law since it only applies when E is small.[56] As the ionizing electron energy is increased above the threshold value, the variety and abundance of the ions produced will increase initially because the electron-impact ionization process may proceed *via* different channels, such as multiple or dissociative ionization. For electron-impact double ionization, the cross section of the double ionization process is approximately proportional to E^2, in the absence of long-range interactions.[57]

The electron-impact single ionization processes for atoms and molecules have been widely investigated and as a result, a great deal of information is known about single ionization mechanisms such as direct ionization and autoionization.[2,58] Conversely, there have been far fewer studies of double ionization processes, due in part to the small multiple ionization cross sections. However, investigations of the electron-impact double ionization of the rare gases studied by (e, 3e) experiments,[59] where the three outgoing electrons from the double ionization process are simultaneously analysed both in direction and energy and are detected in coincidence, are consistent with a two-step model for the double ionization mechanism. In this two-step mechanism, the incident electron collides with two target electrons, resulting in the sequential ejection of them both.

Photoionization

With the increasing availability of synchrotron radiation sources and improved laser technology, photoionization is now a frequently used method of ionization. This process involves the interaction of a photon of known energy emitted by a discharge lamp, synchrotron radiation source or laser with a neutral target, thus resulting in ionization.

$$XY + h\nu \rightarrow XY^+ + e^- \qquad (1.VIII)$$

As with electron-impact, there are a variety of possible reaction channels that may be accessed upon photoionization such as single/multiple ionization, fragmentation and ion pair formation. However, the advantage of using photoionization is that the energy of the incident photon is known and therefore, in contrast to electron-impact ionization, the energy deposition in the target molecule upon ionization is also known.[1]

Collisional Ionization

Collisional ionization involves the formation of ions following collisions between neutrals and high-energy ions. Following the collision, ionization of either the projectile or the target molecule is produced.[60] Ionization of the projectile A^+, which has an energy of several keV, occurs *via* charge stripping in which the projectile loses an electron,[61]

$$A^+ + X \rightarrow A^{2+} + X + e^- \qquad (1.IX)$$

From the measurement of the velocity of the product dication A^{2+}, the double ionization energy of the projectile, representing a vertical transition at the geometry of the singly charged ion, can be determined.[62] Ionization of the target can occur by charge transfer,[63]

$$A^+ + X \rightarrow A^- + X^{2+} \qquad (1.X)$$

The probability of this type of reaction is small but such experiments are useful in measuring spectra of highly unstable doubly charged ions, since if the product A^- ions are detected within a small angle of the original projectile direction, the double ionization energy of X can be deduced from the observed change in velocity of A.[64,65]

1.3.1 Partial Ionization Cross Sections

As described above, ionization involves the collision of an ionizing agent with a target gas and results in the subsequent formation of dissociation products, such as ions, neutrals and ejected electrons. An indication of the probability of such a reaction is the total ionization cross section. The total ionization cross section is the cross section for producing a positive charge in the exit channel of the ionization reaction regardless of the detail of the reaction products, such as mass-to-charge ratio, electronic states and the production of neutrals.[2] The total ionization cross section is therefore the sum of the various single and multiple cross sections.

$$\sigma_{total} = \sigma^+ + \sigma^{2+} + \sigma^{3+} + ... \qquad \text{Eq. 1.2}$$

For most molecules, the single ionization cross section will be significantly larger than the multiple ionization cross sections.[2] For a polyatomic ion, there are a number of possible dissociation pathways and the intrinsic probability of the ion following a particular dissociation pathway is expressed as a number called the partial ionization cross section. The partial ionization cross section is a more detailed measurement than the total ionization cross section as it describes the probability

for an individual ionization process, including dissociative ionization, multiple ionization and ionization to a particular final electronic state of the ion produced. Any partial ionization cross section, in fact any cross section, is defined by an equation analogous to the Beer-Lambert Law,

$$D_e = D_0 e^{-nl\sigma} \qquad \text{Eq. 1.3}$$

where D_e is the electron flux after passing through a target gas, D_0 is the initial electron flux, n is the number density of the target gas, l is the electron pathlength and σ is the cross section. The number of ionization events of the appropriate type is $I = D_0 - D_e$ and if $nl\sigma$ is small then

$$I = D_0 nl\sigma \qquad \text{Eq. 1.4}$$

and if n and l are small, the cross section is directly related to the intrinsic probability of a given dissociation pathway.

The number of ionization events, and therefore the intensity of peaks in a time-of-flight mass spectrum, is directly linked to the absolute partial ionization cross section. However, it is difficult to measure the absolute partial ionization cross section for the formation of a given fragment ion experimentally, as this would require the accurate determination of the electron pathlength, the number density of the target gas in the interaction region of the mass spectrometer and the electron flux. Therefore relative partial ionization cross sections are more often determined, where the ratio of the intensity of each fragment ion against the intensity of a specific ion, usually the most abundant, is calculated.

1.4 Dissociation

The number and identity of fragment ions produced upon dissociation of a given parent ion, and the form of their relative ionization cross sections, are characteristic of the corresponding parent molecule. In the case of diatomic parent molecules (*e.g.* H_2),[66] ionic fragmentation can be treated quantitatively in terms of the Franck-Condon principle.[2] This implies that if the vertical transition from the initial to the ionic state of the diatomic is to a repulsive region of the potential energy curve then dissociation occurs and the final products can be identified. In the case of polyatomics (with the exception of small polyatomics of high symmetry), the multi-dimensional potential energy surfaces are complex as the resulting polyatomic ion can undergo further internal transitions leading to subsequent unimolecular decomposition. Therefore, a different approach using statistical methods is required to determine the dissociation pathways followed by large polyatomic ions. The statistical approach to the theory of unimolecular reactions used to investigate dissociation pathways is the RRKM (Rice, Ramsperger, Kassel and Marcus)[67] and the quasi-equilibrium theory (QET).[68] The RRKM/QET equation,[69,70] which yields the rate constant $k(E)$ for a molecule at a given energy E and with an activation energy for fragmentation of E_0, is given by

$$k(E) = \frac{\sigma N^{\ddagger}(E - E_0)}{h\rho(E)} \qquad \text{Eq. 1.5}$$

where σ is the reaction path degeneracy, $N^{\ddagger}(E\text{-}E_0)$ is the transition state sum of states from 0 to $(E - E_0)$, h is Planck's constant and $\rho(E)$ is the parent ion density of states at an energy E.

In general, the relative abundance of any fragment ion is related to its rate of formation and its rate of dissociation by unimolecular decomposition. Therefore, a mass spectrum is a record in time of the position of this 'quasi-equilibrium' of those rates and the respective partial ionization cross sections of the fragment ions will depend on the time after formation of the parent ion. The RRKM/QET statistical theories can therefore be used to calculate a mass spectrum by determining the rate coefficients of formation and dissociation of the fragment ions.[71] In addition, dissociation rates of ions derived from photoionization mass spectrometry (PIMS) and photoelectron-photoion coincidence (PEPICO) experiments can be compared with calculated RRKM/QET rate constants to derive information about fragmentation mechanisms.[72]

1.5 Experimental Studies of Singly and Doubly Charged Ions

1.5.1 Singly Charged Ions

A wide variety of experimental techniques have been used to investigate the properties of singly charged ions with the vast majority of these experiments probing the electronic spectroscopy of these ions.[1] The spectroscopic techniques, including photoelectron spectroscopy, ion emission and absorption spectroscopy and electron energy-loss spectroscopy, used to study singly charged ions generally probe the electronic structure of the parent monocation.[1] However, as discussed above, it is the dissociation of the singly charged ions that is being investigated in this thesis and therefore to study monocation fragmentation it is necessary to employ techniques which can monitor the production of fragment ions.

The stable nature of the majority of monocations means that the species are typically long-lived with lifetimes on the mass spectrometric timescale. Hence, using mass spectrometry, ionic fragmentation, and therefore dissociation processes, can be studied in addition to parent ion formation. The most commonly used mass spectrometric technique is *photoionization mass spectrometry (PIMS).*[1,33-35,37,73] In these experiments, the yields of parent and fragment ions sorted according to charge and mass are measured as a function of the ionizing photon energy. From these experiments, information about branching ratios and appearance energies of fragment ions can be deduced. The equivalent technique using electrons as the ionizing agent is known as *electron-impact mass spectrometry (EIMS).*[29-32,36,38,39]

One of the main classes of more modern experimental techniques devised to investigate dissociative ionization are coincidence techniques.[60] In principle, a coincidence experiment involves the simultaneous detection of two or more species, such as singly charged fragment ions and electrons [Reaction (1.XI)], formed in the same dissociation event using a time-of-flight mass spectrometer. See below for more details of coincidence techniques.

$$XY^+ \rightarrow X^+ + Y + e^- \qquad (1.XI)$$

In single ionization studies, the most commonly used techniques employed to investigate the dissociation of monocations are *photoelectron-photoion coincidence (PEPICO)*[1,74] and *threshold photoelectron-photoion coincidence (TPEPICO)*[1,70,75], where electrons and ions produced together in single ionization events are detected. In PEPICO experiments, the target molecules are photoionized by a monochromatic light source and the detected electrons and ions are energy and mass analysed respectively. Analysis of the resulting spectra provides information of the initial state of the parent monocation prior to fragmentation and the dissociation products of this state-selected ion. The ionizing photon energy can be varied to access different initial states of the parent ion thus making PEPICO a useful tool in the study of state-selected single ionization. In TPEPICO, a variable photon energy is used and zero energy (threshold) electrons are detected in coincidence with singly charged fragment ions. The production of a threshold photoelectron occurs whenever the scanned photon energy passes through the threshold of a parent ion state. The advantage of using TPEPICO is higher energy resolution, allowing singly charged ion processes to be probed within a few meV of their thresholds. This enables the vibrational structure of the ion to be observed and accurate values of the ionization potential to be determined.

In the work discussed in this thesis, the formation and fragmentation of singly charged ions are investigated using EIMS techniques in order to characterise the fragmentation products from near threshold to high ionizing electron energies.

1.5.2 Doubly Charged Ions

The first molecular dication observed experimentally was CO^{2+}, identified in mass spectrometric studies of CO when ionized by electron impact.[4,76] However, as discussed in Section 1.2, the majority of dications are very short-lived and therefore mass spectrometric studies of dications are limited to the study of metastable states, as only these ions have lifetimes of the order of the mass spectrometric timescale. But, when studying doubly charged diatomics such as N_2^{2+} mass spectrometrically,[77] problems arise as the peak corresponding to the parent dication is in the same position in the mass spectrum as the N^+ fragment ion peak. Therefore, in order to study short-lived doubly charged ions, alternative techniques have been developed.[9,10,12,78]

The dissociation of molecular dications is generally investigated using coincidence techniques.[60] In the case of doubly charged ions, the experimental procedure usually involves measuring the difference between the flight times of selected dissociation products formed upon dissociative double ionization in a time-of-flight mass spectrometer.

$$XY^{2+} \rightarrow X^+ + Y^+ + 2e^- \qquad (1.XII)$$

In the earliest molecular double ionization experiments, electrons were used as the ionizing agent but with improved photon sources, the same methods have more recently been extended to photoionization.

There are several types of coincidence experiments that detect different dissociation products in coincidence with each other. These experiments can yield information on the dynamics of the double ionization process and the electronic spectroscopy of the dications. They can also yield information on dissociation processes such as fragmentation pathways and appearance energies of fragment ions. A brief description of the coincidence techniques relevant to the work discussed in this thesis is given below.

The *ion-ion coincidence* technique uses an electron-impact time-of-flight mass spectrometer to investigate the following dissociation process,[50,79,80]

$$e^- + XY \rightarrow [XY^{2+} + 3e^-] \rightarrow X^+ + Y^+ + 3e^- \qquad (1.XIII)$$

recording the coincidences between the pair of fragment ions by measuring the difference in their flight times in the time-of-flight mass spectrometer. These experiments measure the kinetic energy release upon dissociation and can also yield information on branching ratios for various dissociation channels as well as the mechanisms of the dissociation reaction. The equivalent techniques using photoionization, where the advantage is that the energy of the incident photon is known, involves recording *photoion-photoion coincidences (PIPICO).*[5,81-83]

As mentioned above, ion-ion coincidence and PIPICO experiments measure the time-of-flight difference between pairs of fragment ions formed upon dissociative double ionization. If these two-particle coincidence techniques are applied to polyatomic dications, ion pairs of equal mass are centred on zero time-of-flight difference and therefore the identity of these equal mass ion pairs cannot be determined. In addition, for complex polyatomic dications, these two-particle techniques do not unambiguously identify the ions responsible for the coincidence signals, as there are a large number of available fragmentation channels which yield ion pairs with the same time-of-flight difference.

These problems associated with two-particle coincidence techniques were resolved by the development of triple coincidence techniques, in which the time of ion formation is recorded by detection of one or more of the ejected electrons. This three-particle coincidence technique involves recording *photoelectron-photoion-photoion coincidences (PEPIPICO).*[84,85] PEPIPICO is a

coincidence technique that detects a single photoelectron and a pair of photoions in coincidence. Measurements of the intensity of the ion pair and the ions' flight times with respect to the photoelectron allow a two-dimensional mass spectrum to be produced. The measurement of the actual ion flight times allows the identification of all the fragment ion pairs formed upon dicationic dissociation. The PEPIPICO spectrum gives information analogous to that obtained from ion-ion coincidence and PIPICO spectra, but PEPIPICO also enables the distinction to be made between different dissociation mechanisms, such as a Coulomb explosion or a sequential mechanism, by considering the intensity distributions as functions of the initial momenta of the detected ions.[60,63,86-90]

A similar technique to PEPIPICO is *covariance mapping mass spectroscopy*,[7,91-93] where the fragmentation of highly charged molecular ions formed in a single laser pulse is investigated. If XY_2^{2+} formed in the laser pulse dissociates to form $XY^+ + Y^+$ and an XY^+ fragment is detected in a TOFMS, then the probability of detecting a Y^+ fragment in the same pulse is enhanced. Calculation of the covariance between the two ion flight times over a large number of laser pulses results in a positive value and the result is a two-dimensional map which can be analysed in a similar manner to the PEPIPICO spectra to identify the fragmentation products and dication dissociation mechanisms.[7,91-93]

The techniques described above can be used to determine the energy of the dication states responsible for the observed dissociation reactions. However, they cannot provide detailed information on the electronic or vibrational structure of dications. A recently developed technique *Doppler free kinetic energy release spectroscopy (DFKER)*[10] enables detailed investigations of the electronic structure, as well as the dissociation dynamics of molecular dications, to be made. The simultaneous measurement of the energies of the fragment ions produced upon the dissociation of a diatomic dication results in the elimination of Doppler broadening caused by the thermal motion of the parent molecules. This Doppler broadening limits the energy resolution in conventional kinetic energy release spectra, which precludes the observation of electronic and vibrational states. This technique therefore allows detailed investigations of the electronic structure, as well as the dissociation dynamics, of doubly charged diatomics, such as N_2^{2+}, O_2^{2+} and NO^{2+}.[94-96]

In the work discussed in this thesis, ion-ion coincidence techniques have been used to investigate the formation and fragmentation of doubly charged molecular ions. In addition, a novel technique, similar to PEPIPICO but using electron-impact ionization, has been developed to record two-dimensional ion-ion coincidence spectra.

1.6 Conclusions

As has been discussed in this chapter, although singly charged molecular ions have been extensively investigated, the study of doubly charged molecules is a relatively recent field. The continued improvements in experimental techniques and accuracy of theoretical data derived from computational studies of ions means that more complex ionic systems are being investigated and the understanding of monocation and dication dissociation processes is continually improving. In this thesis, the formation and fragmentation of molecular ions are investigated using electron-impact mass spectrometry to study the dissociation of monocations and ion-ion coincidence techniques to study dissociative double ionization.

References

1 J.H.D. Eland, *Photoelectron Spectroscopy*, Butterworths, London, 1984

2 T.D. Märk, in T.D Märk, G.H. Dunn (Eds.), *Electron Impact Ionization*, Springer-Verlag, New York, 1985

3 J.J. Thomson, *Philos. Mag.*, **24** (1912) 668

4 R. Conrad, *Physik. Z.*, **31** (1930) 888

5 D.M. Curtis and J.H.D. Eland, *Int. J. Mass Spectrom. Ion Proc.*, **63** (1985) 241

6 M. Larsson, *Com. At. Mol. Phys.*, **29** (1993) 39

7 D. Mathur, *Phys. Rep.*, **225** (1993) 193

8 S.D. Price, *J. Chem. Soc., Faraday Trans.*, **93** (1997) 2451

9 G. Dawber, A.G. McConkey, L. Avaldi, M.A. Macdonald, G.C. King and R.I. Hall, *J. Phys. B*, **27** (1994) 2191

10 M. Lundqvist, P. Baltzer, D. Edvardsson, L. Karlsson and B. Wannberg, *Phys. Rev. Lett.*, **75** (1995) 1058

11 P. Lablanquie, M. Lavollee, J.H.D. Eland, F. Penent and R.I. Hall, *Meas. Sci. Tech.*, **6** (1995) 939

12 D.M. Szaflarski, A.S. Mullin, K. Yokoyama, M.N.R. Ashfold and W.C. Lineberger, *J. Phys. Chem.*, **95** (1991) 2122

13 K.A. Newson and S.D. Price, *Chem. Phys. Lett.*, **269** (1997) 93

14 K.A. Newson, N. Tafadar and S.D. Price, *J. Chem. Soc., Faraday Trans.*, **94** (1998) 2735

15 K.A. Newson and S.D. Price, *Chem. Phys. Lett.*, **294** (1998) 223

16 P. Champkin, N. Kaltsoyannis and S.D. Price, *Int. J. Mass Spectrom. Ion Proc.*, **172** (1998) 57

17 Y. Lee, S.R. Leone, P. Champkin, N. Kaltsoyannis and S.D. Price, *J. Chem. Phys.*, **106** (1997) 7981

18 P. Champkin, N. Kaltsoyannis and S.D. Price, *J. Electron Spectrosc. Relat. Phenom.*, in press (1999)

19 H. Hogreve, *J. Chem. Phys.*, **102** (1994) 3281

20 D. Duflot, J.-M. Robbe and J.-P. Flament, *J. Chem. Phys.*, **103** (1995) 10571

21 Y. Okamoto and Y. Itikawa, *Chem. Phys. Lett.*, **203** (1993) 61

22 K.N. Joshipura, *Ind. J. Pure and App. Phys.*, **23** (1985) 525

23 K.N. Joshipura, *Pramana*, **32** (1989) 139

24 D. Smith and P. Spanel, *Mass Spectrom. Rev.*, **14** (1995) 225

25 D. Smith and N.G. Adams, *J. Chem. Soc., Faraday Trans.*, **85** (1989) 1613

26 D. Smith, *Chem. Rev.*, **92** (1992) 1473

27 G. Winnewisser and E. Herbst, *Rep. Prog. Phys.*, **56** (1993) 1209

28 B.A. Thrush, *Rep. Prog. Phys.*, **51** (1988) 1341

29 I.P. Fisher, *Trans. Faraday Soc.*, **63** (1967) 684

30 I.P. Fisher, *Trans. Faraday Soc.*, **64** (1968) 1852

31 C.G. Freeman and L.F. Phillips, *J. Phys. Chem.*, **72** (1968) 3025

32 H.F. Cordes and S.R. Smith, *J. Chem. Eng. Data,* **15** (1970) 158

33 R.P. Thorn, L.J. Stief, S.-C. Kuo and R.B. Klemm, *J. Phys. Chem.*, **100** (1996) 14178

34 U. Rockland, H. Baumgärtel, E. Rühl, O. Lösking, H.S.P. Müller and H. Willner, *Ber. Bunsenges. Phys. Chem.*, **99** (1995) 969

35 R. Flesch, E. Rühl, K. Hottmann and H. Baumgärtel, *J. Phys. Chem.*, **97** (1993) 837

36 A.V. Baluev, Z.K. Nikitina, L.I. Fedorova and V.Y. Rosolovskii, *Izv. Akad. Nauk SSSR, Ser. Khim.*, **9** (1980) 1963

37 H.-W. Jochims, W. Denzer, H. Baumgärtel, O. Lösking and H. Willner, *Ber. Bunsenges. Phys. Chem.*, **96** (1992) 573

38 G. Liuti, S. Dondes and P. Harteck, *J. Phys. Chem.*, **72** (1968) 1081

39 R.A. Friedel, J.L. Shultz and A.G. Sharkey, *Anal. Chem.*, **31** (1959) 1128

40 M. Kolbuszewski and J.S. Wright, *J. Phys. Chem.*, **99** (1995) 3455

41 D. Schröder and H. Schwarz, *J. Phys. Chem. A,* in press (1999)

42 J.S. Wright, D.J. Carpenter, A.B. Alekseyev, H.-P. Liebermann, R. Lingott and R.J. Buenker, *Chem. Phys. Lett.*, **266** (1997) 391

43 S. Leach, J.H.D. Eland and S.D. Price, *J. Phys. Chem.*, **93** (1989) 7575

44 J. Senekowitsch, S. O'Neil, P. Knowles and H.J. Werner, *J. Phys. Chem.*, **95** (1991) 2125

45 L.H. Andersen, J.H. Posthumus, O. Vahtras, H. Agren, N. Elander, A. Nunez, A. Scrinzi, M. Natiello and M. Larsson, *Phys. Rev. Lett.*, **71** (1993) 1812

46 D. Mathur, L.H. Andersen, P. Hvelplund, D. Kella and C.P. Safvan, *J. Phys. B,* **28** (1995) 3415

47 J. Senekowitsch and S. O'Neil, *J. Chem. Phys.*, **95** (1991) 1847

48 F.R. Bennett and I.R. McNab, *Chem. Phys. Lett.*, **251** (1996) 405

49 K.A. Newson, S.M. Luc, S.D. Price and N.J. Mason, *Int. J. Mass Spectrom. Ion Proc.*, **148** (1995) 203

50 K.A. Newson and S.D. Price, *Int. J. Mass Spectrom. Ion Proc.*, **153** (1996) 151

51 C. Tian and C.R. Vidal, *J. Phys. B,* **31** (1998) 895

52 C. Tian and C.R. Vidal, *Chem. Phys.*, **222** (1997) 105

53 S.-H. Zheng and S.K. Srivastava, *J. Phys. B,* **29** (1996) 3235

54 R. Basner, M. Schmidt, V. Tarnovsky, K. Becker and H. Deutsch, *Int. J. Mass Spectrom. Ion Proc.*, **171** (1997) 83

55 M.R. Bruce, C. Ma and R.A. Bonham, *Chem. Phys. Lett.*, **190** (1992) 285

56 G.H. Wannier, *Phys. Rev.*, **90** (1953) 817

57 F.H. Read, in T.D. Märk, G.H. Dunn (Eds.), *Electron Impact Ionization*, Springer-Verlag, New York, 1985

58 E.W. McDaniel, *Atomic Collisions: Electron and Photon Projectiles*, John Wiley & Sons, New York, 1989

59 A. Lahmam-Bennani, C. Dupré and A. Duguet, *Phys. Rev. Lett.*, **63** (1989) 1582

60 J.H.D. Eland, in C.Y. Ng (Ed.), *Vacuum Ultraviolet Photoionization and Photodissociation of Molecules and Clusters*, World Scientific, Singapore, 1991

61 J.L. Holmes, *Org. Mass Spectrom.*, **20** (1985) 169

62 C.J. Procter, C.J. Porter, T. Ast, P.D. Bolton and J.H. Beynon, *Org. Mass Spectrom.*, **16** (1981) 454

63 M. Lange, O. Pfaff, U. Müller and R. Brenn, *Chem. Phys.*, **230** (1998) 117

64 P.G. Fournier, F. Fournier, F. Salama, D. Stark, S.D. Peyerimhoff and J.H.D. Eland, *Phys. Rev. A*, **34** (1986) 1657

65 J. Appell, J. Durup, F.C. Fehsenfeld and P.G. Fournier, *J. Phys. B*, **6** (1973) 197

66 A. Crowe and J.W. McConkey, *J. Phys. B*, **6** (1973) 2088

67 R.A. Marcus and O.K. Rice, *J. Phys. Colloid Chem.*, **55** (1951) 894

68 H.M. Rosenstock, M.B. Wallenstein, A.L. Wahrhaftig and H. Eyring, *Proc. Nat. Acad. Sci. U.S.A*, **38** (1952) 667

69 T. Baer and P.M. Mayer, *J. Am. Soc., Mass Spectrom.*, **8** (1997) 103

70 T. Baer and W.L. Hase, *Unimolecular Reaction Dynamics: Theory and Experiments*, Oxford University Press, Oxford, 1996

71 A. Maccoll, *Org. Mass Spec.*, **26** (1991) 235

72 P.M. Mayer, J.W. Keister, T. Baer, M. Evans, C.Y. Ng and C.-W. Hsu, *J. Phys. Chem. A*, **101** (1997) 1270

73 B.P. Tsai and J.H.D. Eland, *Int. J. Mass Spectrom. Ion Proc.*, **36** (1980) 143

74 T. Baer, *Adv. Chem. Phys.*, **64** (1986) 111

75 J.C. Creasey, D.M. Smith, R.P. Tuckett, K.R. Yokall, K. Codling and P.A. Hatherly, *J. Phys. Chem.*, **100** (1996) 4350

76 A.L. Vaughan, *Phys. Rev.*, **38** (1931) 1687

77 T.D. Märk, *J. Chem. Phys.*, **63** (1975) 3731

78 R.I. Hall, G. Dawber, A. McConkey, M.A. Macdonald and G.C. King, *Phys. Rev. Lett.*, **68** (1992) 2751

79 B. Brehm and G. de Frênes, *Int. J. Mass Spectrom. Ion Proc.*, **26** (1978) 251

80 K.E. McCulloh, T.E. Sharp and H.M. Rosenstock, *J. Chem. Phys.*, **42** (1965) 3501

81 G. Dujardin, S. Leach, O. Dutuit, P.M. Guyon and M. Richardviard, *Chem. Phys.*, **88** (1984) 339

82 T. Masuoka, *Phys. Rev. A*, **48** (1993) 1955

83 P. Lablanquie, I. Nenner, P. Millie, P. Morin, J.H.D. Eland, M.J. Hubin-Franskin and J. Delwiche, *J. Chem. Phys.*, **82** (1985) 2951

84 L.J. Frasinski, M. Stankiewicz, K.J. Randall, P.A. Hatherly and K. Codling, *J. Phys. B*, **19** (1986) L819

85 J.H.D. Eland, F.S. Wort and R.N. Royds, *J. Electron Spectrosc. Relat. Phenom.*, **41** (1986) 297

86 J.H.D. Eland, *Mol. Phys.*, **61** (1987) 725

87 J.H.D. Eland, *Chem. Phys. Lett.*, **203** (1993) 353

88 S. Hsieh and J.H.D. Eland, *J. Chem. Phys.*, **103** (1995) 1006

89 S. Hsieh and J.H.D. Eland, *Int. J. Mass Spectrom. Ion Proc.*, **167/168** (1997) 415

90 I. Nenner and J.H.D. Eland, *Z. Phys. D*, **25** (1992) 47

91 M.R. Bruce, L. Mi, C.R. Sporleder and R.A. Bonham, *J. Phys. B*, **27** (1994) 5773

92 D.A. Card, D.E. Folmer, S. Sato, S.A. Buzza and A.W. Castleman Jr., *J. Phys. Chem.*, **101** (1997) 3417

93 L.J. Frasinski, K. Codling and P.A. Hatherly, *Science*, **246** (1989) 973

94 M. Lundqvist, D. Edvardsson, P. Baltzer, M. Larsson and B. Wannberg, *J. Phys. B*, **29** (1996) 499

95 M. Lundqvist, D. Edvardsson, P. Baltzer and B. Wannberg, *J. Phys. B*, **29** (1996) 1489

96 D. Edvardsson, M. Lundqvist, P. Baltzer, B. Wannberg and S. Lunell, *Chem. Phys. Lett.*, **256** (1996) 341

2. Experimental Details

2.1 Introduction

As mentioned in Chapter 1, there are a large number of techniques available to investigate the formation and fragmentation of both singly and doubly charged molecular ions. In the investigations of the ionization of reactive molecules described in this thesis, only two of these techniques have been employed. Electron-impact time-of-flight mass spectrometry is used to study the fragmentation of singly charged molecular ions and ion-ion coincidence experiments are used to study the dissociation of molecular dications. In this chapter the basis and implementation of these techniques are described in detail and the experimental arrangements employed in the one-dimensional and two-dimensional studies are discussed.

2.2 Mass Spectrometry of Reactive Species

The experiments discussed in this thesis involve the ionization of reactive species and there are many problems that need to be overcome in order to record reproducible mass spectra of such unstable molecules. There are inherent difficulties associated with the preparation of pure samples of many reactive species and so careful synthesis of each sample is required *via* unbranched, mechanistic pathways. The details of the synthetic procedures followed for the preparation of each target molecule will be discussed in the relevant chapter.

The problem of preparing a pure sample of reactive molecules is exacerbated by the tendency of these species to decompose on contact with many metallic and non-metallic surfaces,[1] such as are commonly found in the inlet systems of conventional mass spectrometers. Preliminary work indicated that degradation of the samples occurred if the gaseous molecules spent an appreciable time in the inlet system before reaching the ionization region of the time-of-flight mass spectrometer (TOFMS) used in these experiments. To overcome this problem, a wide bore, high conductance inlet system (Teflon/glass) was constructed so that any molecules would be rapidly drawn into the TOFMS. The pressure in the inlet system is kept low to ensure that any gaseous sample molecules spend a minimal amount of time in the inlet system and quickly enter the ionization region. In order to maintain these low pressures in the inlet system, the gaseous samples (Cl_2O and OClO) are synthesised as required *in situ* and the solid and liquid samples (N_2O_5 and HNO_3 respectively) are kept in cold traps during the experiments so that the vaporisation of gaseous molecules from the sample can be carefully controlled. The details of the experimental procedures for each molecule will be given in the relevant chapter.

As mentioned in the following chapters, there are large discrepancies in the data derived from studies of the ionization of reactive molecules reported in the literature, highlighting the problems outlined above involved in investigating the ionization of reactive molecules. Therefore, the efforts made to prepare pure samples and avoid decomposition prior to entering the TOFMS are initially necessary in order to obtain reliable data.

2.3 One-Dimensional Studies

This section is entitled one-dimensional studies since, using the apparatus set-up described below, the data collected in the ion-ion coincidence experiments involves the coincidence signal intensities as a function of time-of-flight difference, a one-dimensional data set.

2.3.1 Single Ionization

2.3.1.1 Time-of-Flight Mass Spectrometry

Investigations of the single ionization of reactive molecules are performed using time-of-flight mass spectrometry to detect and identify the ionic products formed. Time-of-flight mass spectrometry, a widely-used experimental technique,[2] relies on the principle that ions of differing mass when accelerated to equal kinetic energies by a set of electric fields, have different velocities. Therefore the time-of-flight of ions of differing mass over a set distance will be different. The flight time of an ion in a TOFMS can be derived using a combination of Newtonian mechanics and electrostatics (Appendix 1) and it is found that the time-of-flight of an ion t_{tof} is proportional to the square root of its mass m,

$$t_{tof} = k\sqrt{m} \qquad \text{Eq. 2.1}$$

where k is a constant for a given set of electric fields and apparatus geometry.

Time-of-flight mass spectrometry has a number of advantages over conventional mass spectrometry.[2] These include the ability to detect ions of all masses simultaneously and high scanning speeds, which enables the collection of a complete spectrum in a few microseconds. As a result the entire mass spectrum can be recorded for each ionizing event. These properties enable accurate measurements of relative intensities to be made despite fluctuating source conditions, making time-of-flight mass spectrometry a highly reliable experimental technique that is ideal for analysing pulsed or spatially limited ionization events. Another important consideration is the relative simplicity of the design of the TOFMS, which does not require expensive and heavy magnets, components which are crucial in conventional mass spectrometry.

2.3.1.2 Time-of-Flight Mass Spectrometer

The TOFMS used in these experiments is an implementation of the commonly used two-field device constructed to the standard Wiley-McLaren design,[3] with a first-order space focus (see below for details). A schematic diagram of this apparatus is shown in Fig. 2.1.[1] This design of TOFMS contains a source region, a second acceleration region and a drift region, which is free of electric fields. These regions of the TOFMS are traditionally assigned lengths of $2S$, d and D respectively. The ions are formed by electron impact and are then accelerated out of the source region by a pulsed positive voltage V_0 applied to the repeller plate. The ions then enter the second acceleration region where they undergo further acceleration before entering the field-free drift region and eventually impinge on the channeltron detector. So, to record a time-of-flight mass spectrum the flight time of an ion between the source region and the detector must be measured.

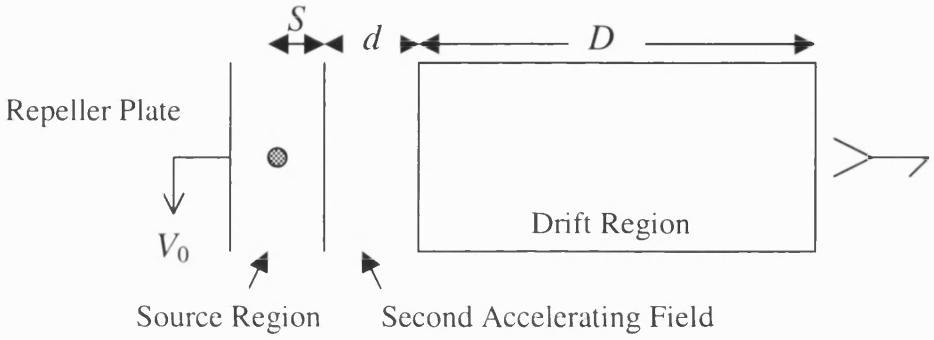

Fig. 2.1 Schematic diagram of a two-field TOFMS.

With such an experimental arrangement, it is expected that all ions of the same mass will have equal flight times in the TOFMS. However, when the electric field is applied to the source region, the ions present have some spatial distribution. Therefore, the final energy of the ions after acceleration will not be single-valued since the ions will have an initial potential energy dependent on their position. As a result, ions of the same mass will have different flight times depending on their initial position in the source. The 'space focus' condition is achieved when all the ions of the same mass arrive at the detector at the same instant regardless of their initial position in the source, leading to a narrow peak in the time-of-flight mass spectrum, which results in higher mass resolution. To find the necessary conditions for a first-order space focus, there should be no variation in the flight time t_{tof} of an ion with the initial position S of the ion in source,

$$\frac{dt_{tof}}{dS} = 0 \qquad \text{Eq. 2.2}$$

If this mathematical condition is applied to the equation for the total flight time of an ion in a two-field TOFMS, given in Appendix 1, the following expression is obtained

$$D = 2Sk^{\frac{3}{2}}\left[1 - \frac{1}{k + k^{\frac{1}{2}}}\frac{d}{S}\right] \qquad \text{Eq. 2.3}$$

$$k = \left[\frac{SE_S + dE_d}{SE_S}\right] \qquad \text{Eq. 2.4}$$

where E_S and E_d are the strength of the electric fields in the source and accelerating regions respectively. Therefore, for a two-field TOFMS, this differential tells us that space focusing can be achieved by simply adjusting the ratio of E_d/E_S.[3] Thus, a first-order space focus can be achieved for a two-field device with a wide variety of S, d and D parameters, in contrast to a single-field TOFMS which has a purely geometric space focus.

Improved space focusing in a two-field TOFMS can be achieved using second-order focus conditions,[4] which calls for lengthening of the acceleration region for a given total length of flight path. The use of a TOFMS with second-order focusing is advantageous when diffuse ion sources are employed and also in the study of energetic and heavy ions. However, for the experiments discussed here, first-order focusing of the TOFMS is sufficient.

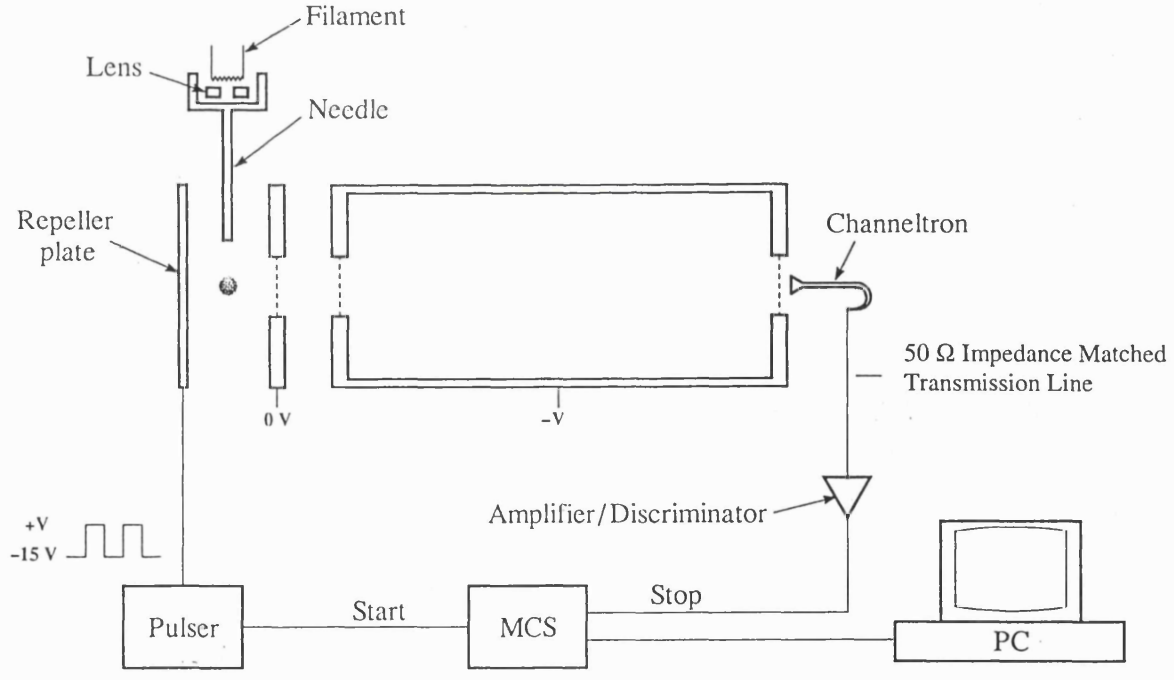

Fig. 2.2 Schematic diagram of the electron-impact TOFMS. The gas inlet is perpendicular to the plane of the figure and is not shown.

Experimental Arrangement

The TOFMS constructed to perform the experiments discussed in this thesis is mounted in a single stainless steel chamber evacuated by a diffusion pump. The values of the parameters S, d and D for the TOFMS are 0.5, 1.8 and 23.1 cm respectively. Ionization of the target molecules occurs at the centre of the source region, defined by 6 cm diameter plates supporting 90 % transmission grids,

at the intersection of an effusive jet of the target gas with an electron beam generated from a modified VG electron gun. The current emitted from the electron gun filament is monitored at a lens element situated before a needle which transports the electron beam into the ion source. The intensity of the electron beam is stabilised so that an electron current of no more than 0.5 nA passes down the needle (Fig. 2.2) and crosses the interaction region. The energy of the electron beam was calibrated by the determination of the ionization thresholds of argon[5] and in these experiments a conservative estimate of the error in the energy resolution was found to ± 2 eV.

The target gas and electron beam are transported into the centre of the source region of the TOFMS *via* hypodermic needles (Fig. 2.2) held at the appropriate voltage for their position in the 1 cm long source electric field. The two hypodermic needles are orientated orthogonal to each other and the axis of the TOFMS and the ends of both needles are situated ~2 mm from the axis of the TOFMS.

Ions formed following the interaction of the electron beam with the target gas are accelerated into the drift region of the TOFMS by the extraction pulse applied to the repeller plate. To record a time-of-flight mass spectrum, the repeller plate is pulsed to +200 V and the subsequent arrival times of positive ions at the channeltron detector are recorded using a multichannel scalar MCS (EG&G Turbo-MCS). The MCS records the counting rate of events as a function of time. When a scan is started, the MCS begins counting input events in the first channel of its digital memory. At the end of the preselected dwell time (5 ns), the MCS advances to the next channel of memory to count the events. This process is repeated until all the channels in the memory have been scanned. A display of the contents of the memory shows the counting rate of the input event versus time.

To begin recording a time-of-flight mass spectrum, a pulse generator sends a signal simultaneously to the pulser to trigger the extraction pulse, with a width of 20 μs and a period of 50 μs, and to the MCS to start its scan. As described before, the ions are accelerated from the ionization region by the application of the extraction pulse and as they finally impinge on the detector, the 'stop' pulses generated in the channeltron are counted as input events by the MCS. Thus t_{tof} of an ion between the source and the detector is recorded and a spectrum of the number of ions versus t_{tof} is recorded in the MCS memory.

Operation of the Channeltron Detector

The channeltron detector is a single electron multiplier which detects the arrival of an ion. It is a small, curved, glass tube with an entrance aperture of 6 mm which has a high surface resistance on the inside walls. When a potential is applied between the two ends of the tube, the resistive surface becomes a dynode. As an ion enters the channeltron it strikes the wall of the tube and this collision results in the production of secondary electrons, as depicted in Fig. 2.3. These secondary

electrons are accelerated along the tube until they, in turn, strike the wall and produce further electrons. This process continues along the length of the tube so a large number of electrons reach the positive end of the tube. So, an input of one ion may result in an output pulse of up to 10^8 electrons and the width of this output pulse (at FWHM) is ~ 10 ns.[6]

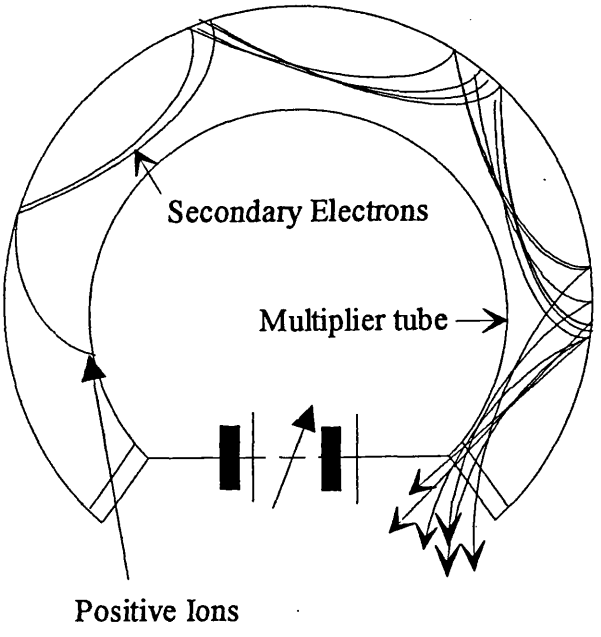

Fig. 2.3 Electron multiplication in a single channel electron multiplier.

Due to the differing paths of incoming ions and secondary electrons along the walls of the channeltron, it takes a finite time to fully recharge the dynode before the next ion can be detected. The reduced detection efficiency when the channeltron has not fully recharged results in a dead time, a period of time after the detection of one ion when any further ions reaching the channeltron will be detected with reduced efficiency.[6]

The output pulse from the channeltron passes onto the preamplifier (Fig. 2.2) where it is multiplied by 200 times, and onto the discriminator. The discriminator is set at such a level that any unwanted background noise can be filtered out before the 'stop' pulse reaches the MCS where it is 'binned' according to its arrival time.

This procedure is repeated and a histogram of ion flight times is produced. The histogram consists of a series of time channels each corresponding to points on a mass scale. Therefore, the number of ions in each channel is a measure of the intensity of ions of that particular mass and a complete histogram represents the mass spectrum. The data is transferred to a PC where it can be displayed and analysed as required. As described in the Chapter 3, from this raw data information about the branching ratios and the appearance energies of fragment ions can be deduced.

Discrimination Effects in the TOFMS

Problems can be encountered in a prototypical one-dimensional experimental set-up due to the trapping of ions with low translational energy within the space-charge of the electron beam. Such trapping would lead to discrimination effects in the mass spectra,[5] with the signal intensities of any translationally energetic species being markedly reduced with respect to those of ions with low translational energies, the latter being more efficiently trapped in the potential well of the electron beam.

To overcome the electrostatic attraction of the electron beam, which could otherwise lead to trapping, a negative voltage (-15 V) is applied to the repeller plate in between the extraction pulses. As a result of this bias voltage, any ions formed during the inter-pulse period are not trapped but are accelerated out of the interaction region and towards the repeller plate. If the pulse width is long enough to allow all the ions formed to exit the source region and the inter-pulse period is long enough for the electron beam to re-establish its central position, the intensities of the ion signals in the mass spectrum are seen to be insensitive to variations of the extraction pulse width and its duty cycle. This observation indicates that the trapping has been eliminated since, if trapping were still occurring the relative intensities of low kinetic energy ions would increase with the interpulse period. Another indication that the trapping has been eliminated is that the relative intensities of the ion signals are seen to be insensitive to variations in the electron beam currents, as a significant change would be observed if the trapping effects were still present.

Operating Parameters

Typical operating parameters for the TOFMS are listed in Table 2.1.

Table 2.1 Typical operating parameters for the TOFMS for recording time-of-flight mass spectra at 150 eV.

Parameter	Typical Value
Filament emission current	0.5-50 μA
Lens potential	100 V
Electron needle potential	100 V
Gas needle potential	100 V
Pulsed repeller plate voltage	200 V
Bias voltage	-15 V
Width of repeller plate pulse	20 μs
Period of repeller plate pulse	50 μs
Drift tube voltage	-777 V
Channeltron potential	-2200 V
Discriminator threshold	50 mV

Typical operating pressures in the TOFMS during the mass spectrometric experiments, as recorded by an ion gauge, were of the order of 6×10^{-5} Pa. Low pressures are employed when recording time-

of-flight mass spectra to ensure that far less than one ion per extraction pulse reaches the detector. If the number of ions per pulse reaching the channeltron is greater than or close to unity, a reduced detection efficiency of a second ion arrival may be observed due to channeltron saturation.[6] Low operating pressures are therefore used, in conjunction with the optimal emission current, to give an average count rate of the order of 0.1 ions per pulse. At these low pressures the saturation effects described above were eliminated, as was shown by the invariance of the fragment ion intensity ratios to changes in target gas pressure in the ionization region.

2.3.1.3 Calibration of the Time-of-Flight Mass Spectrum

Fig. 2.4 shows a typical time-of-flight mass spectrum of argon, used to calibrate the apparatus, recorded at an electron energy of 150 eV. As can be seen from the figure, Ar^+ and Ar^{2+} are detected and from the flight times of Ar^+ and Ar^{2+} the time-of-flight mass spectrum can be calibrated by simultaneously solving the following equation,

$$t_{tof} = k\sqrt{m} + c \qquad \text{Eq. 2.5}$$

where c is a constant required due to the intrinsic delays in the electronics. Hence, once the values of k and c have been derived, the identification of any ion signals giving rise to peaks in the time-of-flight mass spectrum can be made using Eq. 2.5.

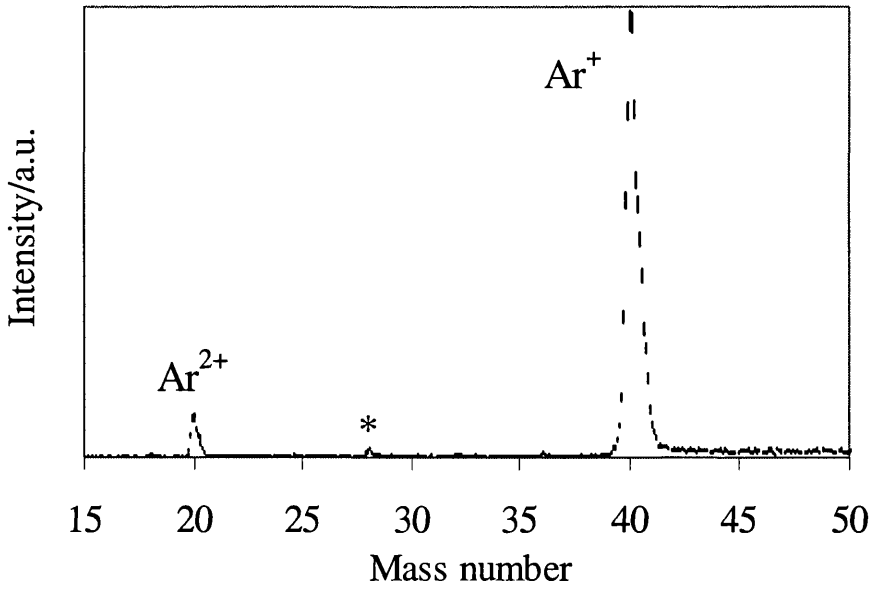

Fig. 2.4 Typical time-of-flight mass spectrum of Ar recorded at an electron energy of 150 eV. The error bars are derived from the counting statistics and represent two standard deviations. The peak marked with an asterisk corresponds to N_2^+, a signal arising from traces of air in the Ar sample.

Note that the spectrum (Fig. 2.4) has a characteristic 'stepped' background, that is the background level rises after each ion signal. When the extraction pulse is applied to the repeller plate, ions present in the region of space focused onto the detector are accelerated out of the

ionization region and into the drift region. These ions are then detected and give rise to the sharp mass peaks whose intensities are related to the partial ionization cross sections as described in the next chapter. However, the application of the extraction voltage also deflects the electron beam so that ionization no longer occurs in the focused volume. Therefore, some background ions will still reach the detector. But these ions have longer flight times than ions of the same mass that were in the focused volume, due to their formation after the onset of the extraction pulse and their initial position in the source, and so a stepped background results.

2.3.2 Double Ionization

2.3.2.1 Ion-Ion Coincidence Techniques

In conventional time-of-flight mass spectrometric experiments such as those described above, it is difficult to distinguish between the monocation fragments generated by the dissociation of a singly charged ion XY_2^+ and those resulting from the dissociation of a dication XY_2^{2+}. Therefore, an alternative experimental technique is required to investigate the formation and fragmentation of doubly charged molecular ions. For this reason, coincidence experiments[7-12] are performed to detect and identify the dissociation products, pairs of fragment ions and/or electrons, produced by dissociative double ionization. From the coincidence signals, information about dicationic pathways and appearance energies can be derived. In this project, the ion-ion coincidence technique[7,9-12] has been used to investigate the dissociation of molecular dications following ionization by electron impact.

Ion-ion coincidence experiments involve the detection of a pair of singly charged ions formed from dissociative double ionization. In order for the pair of ions to give rise to 'true' coincidence signals, the two ions must be formed from the same dication dissociation event. The technique involves the collision of an electron with a neutral molecule resulting in the ejection of two electrons from the neutral to form the doubly charged ion XY_2^{2+}, which subsequently dissociates to form a fragment ion pair.

$$XY_2 + e^- \rightarrow [XY_2^{2+} + 3e^-] \rightarrow XY^+ + Y^+ + 3e^- \qquad (2.I)$$

2.3.2.2 Set-Up of the TOFMS for Coincidence Experiments

Experimental Arrangement

To record an ion-ion coincidence spectrum, the same TOFMS arrangement described above is used, with the exception that the repeller plate is no longer pulsed but maintained at a constant voltage of +400 V.

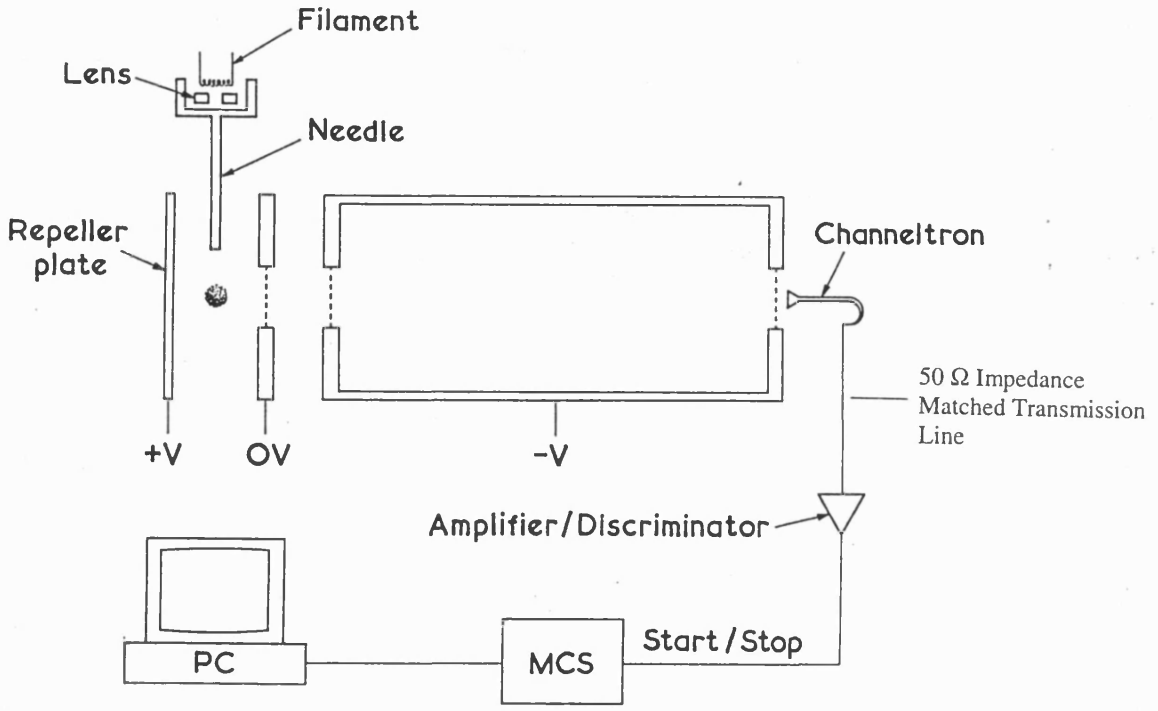

Fig. 2.5 Schematic diagram of the TOFMS set-up for the ion-ion coincidence experiments.

As indicated in Reaction (2.I), two fragment ions, *e.g.* $XY^+ + Y^+$, are created following the rapid charge-separating dissociation of the molecular dication in the source region of the TOFMS. These fragment ions are then immediately accelerated out of the source region by the constant electric field applied to the repeller plate. Since these ions are formed at the same instant their arrival times at the detector will be correlated. This correlation can be detected by measuring the time-of-flight difference between the arrival times of the pairs of ions by using the ion signal as both 'start' and 'stop' pulses to the MCS. So, to record a coincidence spectrum, the MCS starts counting input events when the lightest ion of the pair reaches the detector and stops counting when the heavier ion reaches the detector, thus measuring the time-of-flight difference between the two ions of a pair. A histogram of these time-of-flight differences, a coincidence spectrum, should show a preponderance of counts at time-of-flight differences corresponding to the pairs of ions formed by dicationic dissociation. This 'true' coincidence signal is superimposed on a background of 'false' coincidences which result from the detection of two ions which were not formed in the same ionization event, illustrated in Fig. 2.6.

The dynamics of the pair of ions in the electric fields can be modelled using a combination of Newtonian mechanics and electrostatics (Appendix 1). The time-of-flight difference Δt_{tof} between the two ions in the pair of mass m_1 and m_2 is found to be given by the following expression,

$$\Delta t_{tof} = k(\sqrt{m_1} - \sqrt{m_2}) \qquad \text{Eq. 2.6}$$

where k is a constant for a given set of electric fields and apparatus geometry. For small dications, which only have a few possible decay channels, Δt_{tof} unambiguously identifies the ions responsible for the coincidence signal.

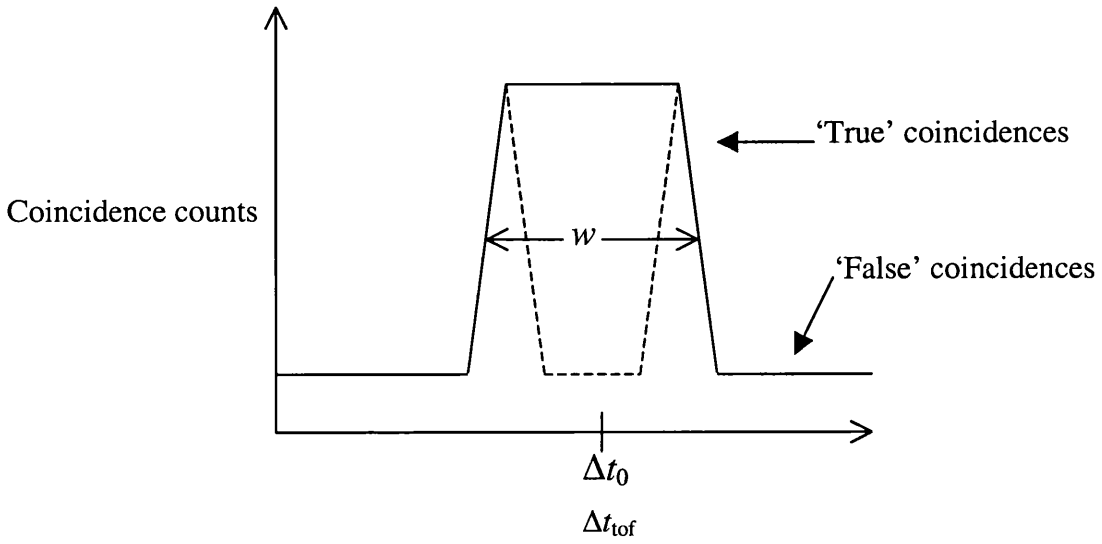

Fig. 2.6 A prototypical ion-ion coincidence peak. As discussed in the text, w can be related to the KER upon fragmentation of the dication. The peak shape expected under conditions of high angular discrimination is shown as a broken line.

The peak observed in the coincidence spectrum due to a pair of ions of mass m_1 and m_2 is centred at Δt_0, the time-of-flight difference the ions would have if they were formed with no kinetic energy.[7] The shape and width of the coincidence peak are determined by the kinetic energy release (KER) upon dissociation, the angular distribution of dissociation and apparatus parameters, such as the size of the detector and the magnitude of the source electric field.[7]

The prototypical form of a coincidence peak is shown in Fig. 2.6. It is a square peak of width w, assuming that all the ions formed from dicationic dissociation reach the detector. The coincidence peak width arises because the time-of-flight of each ion of the pair depends strongly on the direction, with respect to the axis of the TOFMS, of the initial impulse given to it by the dication dissociation event. However, as a consequence of the angular discrimination, introduced by the small entrance aperture of the channeltron detector used in these experiments, ions with a significant velocity component perpendicular to the axis of the TOFMS will miss the detector (Fig. 2.7).

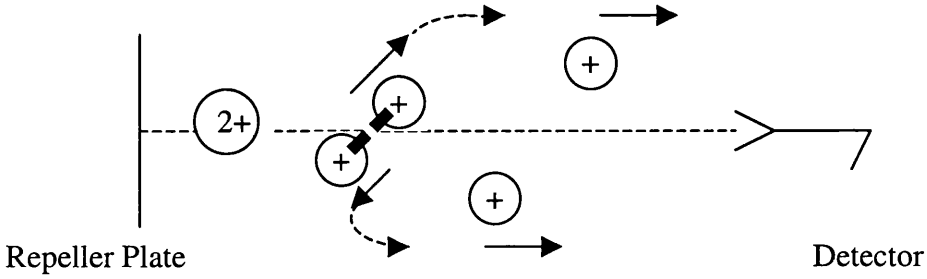

Fig. 2.7 Diagram illustrating that pairs of ions formed with significant translational energy will not be detected.

Therefore, only dissociation events where the KER is directed principally along the axis of the TOFMS will be detected. The ion pairs formed in such events have time-of-flight differences markedly greater or markedly less than Δt_0 since, as illustrated in Fig. 2.8, the time-of-flight of each ion depends on the direction of the initial impulse and, as discussed above, under the given experimental conditions the lightest ion of the pair will always arrive at the detector first.

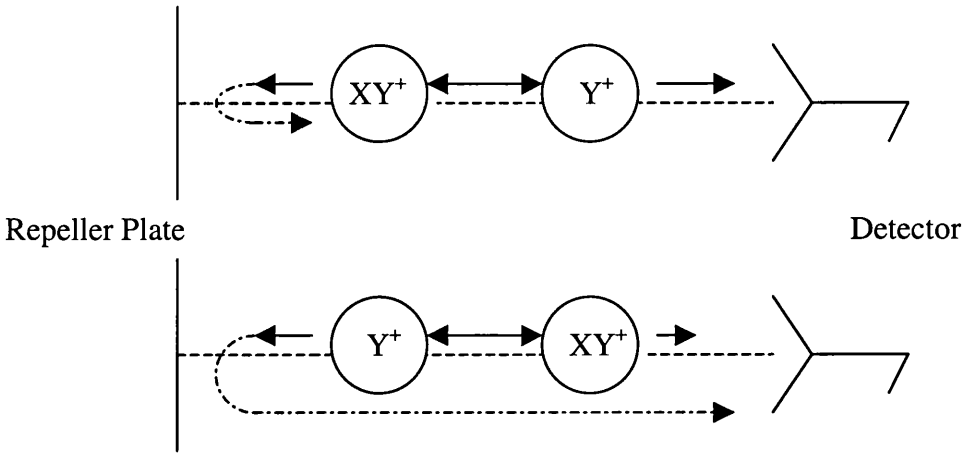

Fig. 2.8 A schematic diagram illustrating how the time-of-flight of each ion of a pair formed from dicationic dissociation depends on the direction, with respect to the TOFMS axis, of the initial impulse given to it by the dissociation event.

Thus, the coincidence signals observed in the one-dimensional coincidence experiments consist of two separate peaks, corresponding to the edges of the prototypical square coincidence peak (Fig. 2.6). This experimental angular constraint, although reducing the signal-to-noise ratio of the experiment, does have the benefit that the resulting spectra are more sensitive probes of the KER upon fragmentation.[7]

Operating Parameters

Fig. 2.9 shows a schematic diagram of a coincidence spectrum with the peak of true coincidences superimposed on a background of false coincidences. The area of the peak is measured and yields the number of coincidences N_c, both true and false, contributing to the peak. In order to determine the number of true coincidences N_t detected within Δt_c the time window for the coincidence peak, the area of the peak must be corrected for the false coincidence background N_f on which the peak is superimposed. The contribution of the false coincidences to the peak is determined by finding the area of another part of the spectrum N_b containing only false coincidence signals. Then since,

$$N_f = \frac{N_b}{\Delta t_b} \Delta t_c \qquad \text{Eq. 2.7}$$

where Δt_b is the temporal width of the time window in which the false counts were evaluated, the false coincidence contribution to the coincidence peak can be subtracted from N_c and thus N_t is obtained.

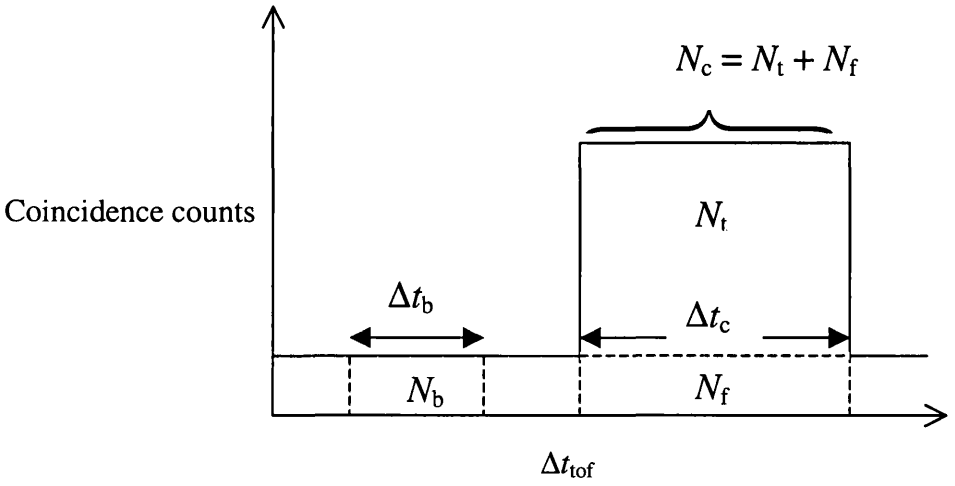

Fig. 2.9 Schematic diagram of a coincidence peak.

In time T during which the spectrum is recorded, $N_t = f_i^2 N^{2+} T$, where f_i is the ion detection efficiency and N^{2+} is the number of doubly charged ions formed in the ion source per second. In the same time, the number of background coincidence signals in the time window $N_f = C_i^2 \Delta t_c T$, where C_i is the total ion count rate given by

$$C_i = f_i N^+ + 2 f_i N^{2+} \approx f_i N^+ \qquad \text{Eq. 2.8}$$

The term containing N^{2+} in Eq. 2.8 can be neglected as the rate of formation of singly charged ions will be significantly larger than the rate of formation of doubly charged ions,[13] *i.e.* $N^+ >> N^{2+}$.

The signal-to-noise ratio in the experiment, which is the ratio of true to false coincidences, $r_{SN} = N_t/N_f$, can then be described in the following manner:

$$r_{SN} = \frac{f_i^{\,2} N^{2+} T}{f_i^{\,2} (N^+)^2 \Delta t_c T} = \frac{N^{2+}}{(N^+)^2 \Delta t_c} \qquad \text{Eq. 2.9}$$

From the Beer-Lambert Law, the number of electrons I_e that pass through a target gas of known number density n is $I_e = I_0 e^{-\sigma^{x+} nl}$, where I_0 is the number of incident electrons, σ^{x+} is the total ionization cross section and l is the pathlength. The rate of ionization N^{x+} can be expressed in the following way,

$$N^{x+} = I_0 - I_e = I_0 - I_0 e^{-\sigma^{x+} nl} \qquad \text{Eq. 2.10}$$

If $\sigma^{x+} nl$ is small then Eq. 2.10 can be simplified to give,

$$N^{x+} = I_0 \sigma^{x+} nl \qquad \text{Eq. 2.11}$$

Substituting for N^{x+} in Eq. 2.9, an expression for r_{SN} can be obtained,

$$r_{SN} = \frac{I_0 \sigma^{2+} nl}{I_0^{\,2} (\sigma^+)^2 n^2 l^2 \Delta t_c} = \frac{\sigma^{2+}}{I_0 (\sigma^+)^2 nl \Delta t_c} \qquad \text{Eq. 2.12}$$

This expression shows that to maintain a good signal-to-noise ratio, the number density of the target gas and the electron flux should be as low as possible.

To maintain a good signal-to-noise ratio in the one-dimensional coincidence experiments, typical operating pressures in the TOFMS, as recorded by an ion gauge, were of the order of 6 x 10^{-5} Pa. Low operating pressures and the selection of the optimal emission current at each electron energy were employed to give an ion count rate below 2000 s^{-1}. Typical operating parameters for the one-dimensional coincidence set-up are given in Table 2.2. The values of the parameters which remained unchanged during the modification of the TOFMS to record coincidence spectra are given in Table 2.1.

Table 2.2 Typical operating parameters for the TOFMS to record ion-ion coincidence spectra at 150 eV.

Parameter	Typical value
Lens potential	200 V
Electron needle potential	200 V
Gas needle potential	200 V
Repeller plate voltage	400 V
Channeltron potential	-2200 V
Drift tube voltage	-1550 V

2.3.2.3 Calibration of the Ion-Ion Coincidence Spectrum

Similarly to the calibration of the time-of-flight mass spectra, the ion-ion coincidence spectra are calibrated by recording a coincidence spectrum of a well-characterised target gas and using the time-of-flight differences of the known ion signals extracted from the coincidence spectrum to simultaneously solve the following equation,

$$\Delta t_{tof} = k(\sqrt{m_1} - \sqrt{m_2}) + c \qquad \text{Eq. 2.13}$$

Again, c is required because of the intrinsic delays in the electronics. Once Eq. 2.13 has been solved for k and c, the ion pair signals present in any coincidence spectrum can be identified.

Fig. 2.10 shows a typical ion-ion coincidence spectrum of CS_2, commonly used as a calibrant. In the figure, the dissociation reactions forming the $CS^+ + S^+$ and $C^+ + S^+$ ion pairs are observed.[12] Any fragmentation of CS_2^{2+} to form the pair of identical ions, $S^+ + S^+$,[12] will produce a coincidence signal centred at $\Delta t_{tof} = 0$. Due to the dead time of the channeltron and a small amount of afterpulsing ('ringing'), which generates false counts near $\Delta t_{tof} \approx 0$ (Fig. 2.10), such signals cannot be efficiently detected in the one-dimensional coincidence spectra.

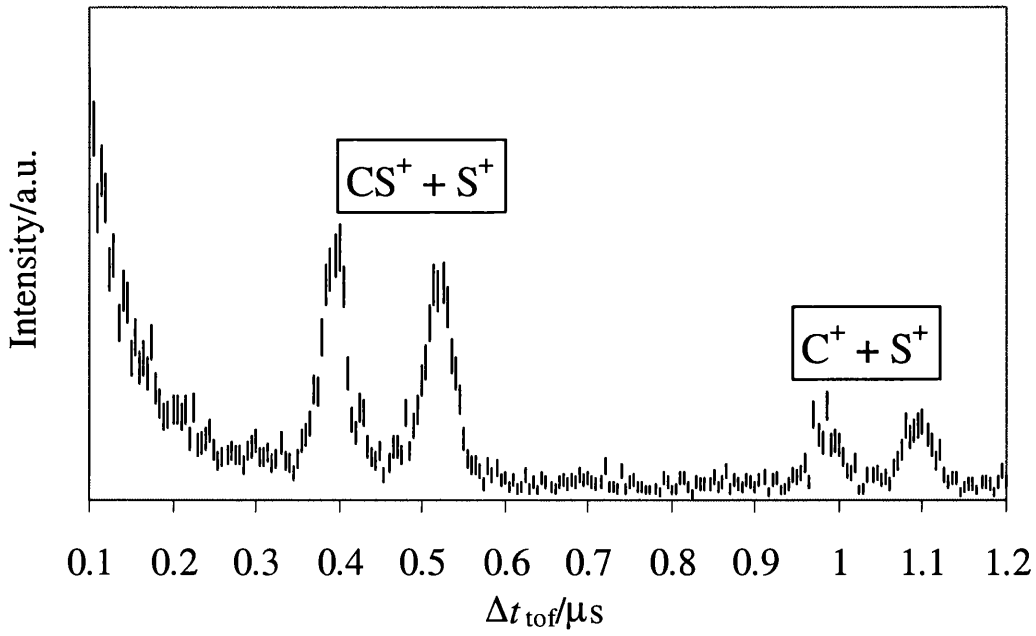

Fig. 2.10 Ion-ion coincidence spectrum of CS_2^{2+} generated by electron impact at 150 eV. The error bars shown are derived from the counting statistics and represent two standard deviations.

2.3.3 Conclusion

The first half of this chapter discusses the basis of the set of techniques used in this thesis to investigate the single and double ionization of reactive molecules, namely the experimental set-ups employed to record the one-dimensional time-of-flight mass spectra and ion-ion coincidence spectra.

As will be explained in the following chapter, from the time-of-flight mass spectra recorded, values of the relative partial single ionization cross sections of the fragment ions observed in the spectra can be obtained. Also, analysis of the ion-ion coincidence spectra can yield information concerning the formation and fragmentation of molecular dications, in particular the dicationic dissociation pathways followed and the energy of the dication states from which these dication fragmentations occur.

For small and symmetrical polyatomic dications, ion-ion coincidence experiments produce reliable data on dicationic formation and fragmentation. However, for complex molecules, it is not possible to unambiguously identify the fragmentation products observed in the ion-ion coincidence spectra. In addition, the size of the detector aperture results in the discrimination against the detection of highly energetic ions in both time-of-flight and coincidence spectra. In order to solve these two problems the apparatus arrangement needs to be modified.

The next part of this chapter discusses the experimental procedures implemented for the two-dimensional studies. The proceeding sections are concerned with the alteration of the experimental set-up required to both increase the detection efficiency of highly energetic ions and to measure the

actual flight times of the pairs of ions formed from dicationic dissociation which enables the identification of all the dication fragmentation products.

2.4 Two-Dimensional Studies

This section is entitled two-dimensional experiments since the coincidence experiments involve recording the intensity of ion pairs as a function of the individual flight times of the two ions, *i.e.* $I(t_1,t_2)$, as opposed to $I(\Delta t_{tof})$ which is recorded in the one-dimensional coincidence experiments.

2.4.1 Single Ionization

In the 2D experiments, the investigations of the single ionization of reactive molecules are again performed using time-of-flight mass spectrometry. These time-of-flight mass spectra are recorded concurrently with the 2D coincidence spectra thus enabling data concerning single and double ionization of a given molecule to be recorded at the same time. However, in order to perform these 2D experiments, substantial modifications had to be made to the experimental arrangement employed in the one-dimensional experiments. The details of these modifications to the TOFMS are discussed below.

2.4.1.1 Set-Up of the TOFMS for 2D Experiments

The basis of the experimental arrangement remains unaltered (Fig. 2.11). The TOFMS is an implementation of a two-field standard Wiley-McLaren device, with a first-order space focus.[3]

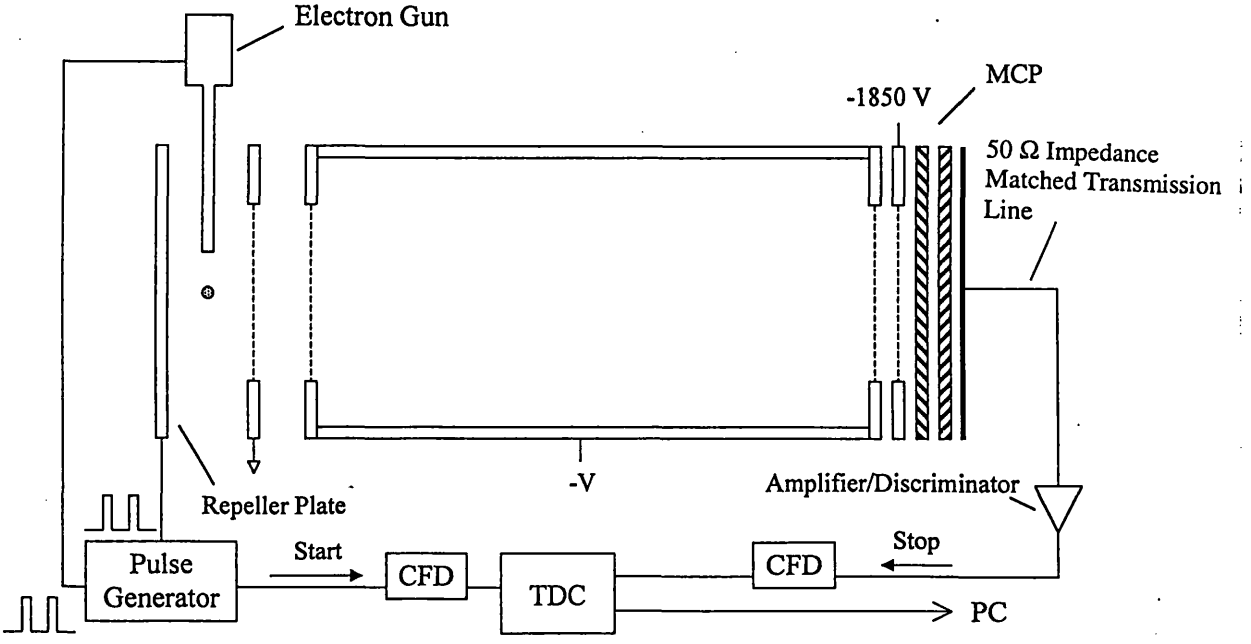

Fig. 2.11 Schematic diagram of the TOFMS set-up for the 2D experiments.

The ions are formed by electron impact, now using a pulsed electron beam (Fig. 2.11), and accelerated out of the source region by a pulsed voltage applied to the repeller plate. After being further accelerated in the second acceleration region, the ions enter the drift region and eventually impinge on a multichannel plate (MCP) detector.

Experimental Arrangement

Ionization of the target molecules occurs following the interaction of the target gas with a pulsed electron beam. The lens element of the electron gun (Fig. 2.11) is pulsed from an appropriate bias voltage (*e.g.* –150 V for 250 eV electrons) to +200 V. The bias voltage is of sufficient magnitude to stop electrons from travelling down the hypodermic needle and reaching the ionization region. Thus during the interpulse period, no ionization occurs. When the +200 V is applied to the lens, electrons pass into the ionization region and interact with the target gas. The optimal bias voltage and width of the voltage pulse applied to the lens to allow the electrons to reach the ionization region (5-40 ns) are evaluated at each electron energy in order to obtain short electron pulses and well-resolved spectra. However, at low electron energies the electron pulses are temporally broadened and therefore ionization occurs over a longer time period which results in an increase in the widths of the ion peaks observed in the mass spectra. Indeed, below 70 eV, it is not possible to produce reliable electron pulses and as a result, no spectra were recorded below 70 eV. In order to record adequate spectra at low electron energies, a new electron gun has been designed which should enable well-defined electron pulses to be produced below 70 eV. This electron gun is currently being commissioned and preliminary results indicate that reliable electron pulses are indeed being produced at low electron energies.[14]

The advantage of pulsing the electron beam is that ionization occurs immediately before the application of the ion extraction pulse. As a result, the majority of the discrimination effects discussed in Section 2.3.1.2 are eliminated, since the trapping of ions in the space-charge of the electron beam experienced in the one-dimensional experiments will no longer occur. In addition, there is no time for energetic ions to leave the focused volume and so, in principle, all the ions formed can be detected.

After a set delay (10-20 ns), ions formed following the interaction of the pulse of electrons with the target gas are accelerated into the drift region of the TOFMS by the +400 V extraction pulse applied to the repeller plate. The period between the application of the pulse to the lens element of the electron gun and the extraction pulse is also optimised for each electron energy, in order to obtain well-resolved, narrow peaks in the spectrum. As ionization occurs immediately before the application of the extraction pulse, the distribution of initial positions in the source is small and so

the distribution of flight times for a given ion will also be small, thus improving the mass resolution of the spectra.

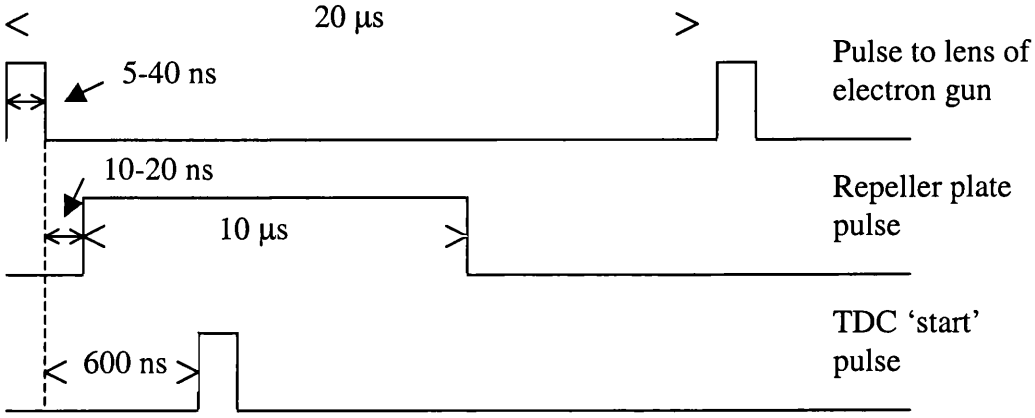

Fig. 2.12 Schematic diagram of pulse timings for the 2D experimental arrangement of the TOFMS.

At a set period (600-650 ns) after the application of the extraction pulse (Fig. 2.12), a signal is sent to the time-to-digital converter (LeCroy 3377 TDC) which acts as the 'start' pulse. The start pulse is sent after the extraction pulse is applied to the repeller plate so any RF noise resulting from the application of the +400 V will not be detected. This start pulse is sent from the pulse generator to the TDC *via* a LeCroy 3420 constant fraction discriminator (CFD) to convert the NIM pulse produced by the pulse generator to the ECL pulse required for the operation of the TDC.

Multichannel Plate Operation

The mode of operation of MCP detectors is similar to that of the single channel electron multipliers. The detector assembly used in these 2D experiments comprises a pair of plates (Fig. 2.13) with a diameter of 40 mm, constructed from special glass through which a large number of channels of 25 μm diameter pass. Each channel acts as a channeltron and the output pulse from a pair of MCPs generally contains 10^6 electrons for each input ion.[6]

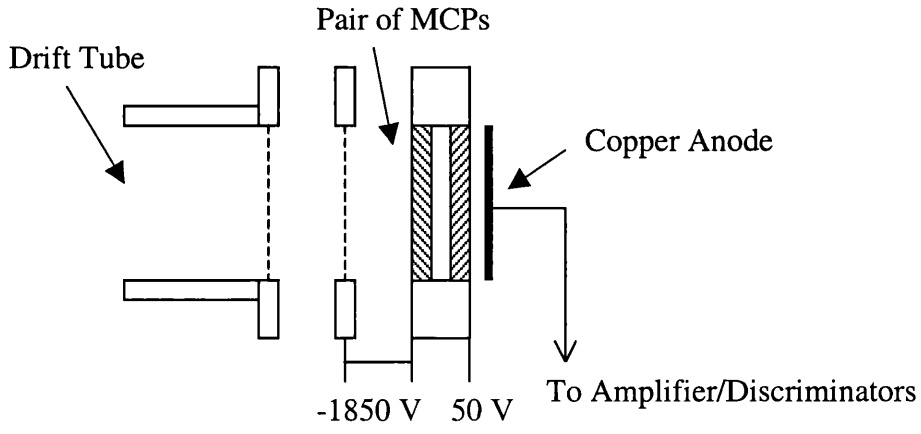

Fig. 2.13 Diagram of the MCP detector assembly used in the 2D experiments.

The pulse of electrons from the back of the MCP assembly (Fig. 2.13) are collected on a copper anode, constructed from glass/epoxy circuit board, and passed to the preamplifier (x 200) and then to a pair of discriminators. The first CFD performs the true discrimination and the second CFD is used solely to produce an ECL pulse from the NIM output of the first CFD. The second CFD also has a adjustable dead time, a time interval following the discriminator output during which the CFD cannot trigger again, which avoids multiple pulsing. For these experiments this dead time is set at 64 ns.

Recording Spectra

The ions accelerated out of the source region by the application of the extraction pulse pass into the drift region and finally impinge on the MCP detector. Thus, as in the one-dimensional experiments, t_{tof} of an ion between the source and the detector is recorded. The set-up of the TDC is such that once the start pulse has been received, there is a finite period of time during which the TDC will count up to 32 stop pulses. In the current experiments this time range is set to 10 μs. After this time period, any ion times recorded are transferred from the TDC to a memory (LeCroy 4302), using the FERA (Fast Encoding and Readout ADC) system, designed for fast conversion of analog information into a digital format. If the TDC received a single stop pulse during the 10 μs 'window', an event containing one flight time is stored in the memory. However, if the TDC received two stop pulses in the time range then a single event containing the two flight times is stored in the memory.

The acquisition procedure is repeated until the memory is full (16K of data) and the contents are then extracted by the custom-written data acquisition algorithm and transferred *via* a SCSI port to a PC. However, while the contents of the memory are being downloaded, a process which takes about 14 s, any data collected by the TDC is lost. Once the data contained in the memory has been extracted, the data acquisition continues until the cycle of filling and emptying the memory has been completed about 200 times. The data acquisition rate is estimated to be approximately 400 Hz.

The data acquisition algorithm is coded (Visual Basic) so that the events corresponding to single ions and pairs of ions can be distinguished, thus enabling time-of-flight mass spectra and coincidence spectra to be recorded concurrently. Upon extraction of the data from the memory, the algorithm works out which memory events contain either one or two ion times. If the event contains a single ion flight time then the signal is added to the histogram of the number of ions versus t_{tof}. The complete histogram, the time-of-flight mass spectrum, is displayed on a PC. To avoid confusion, these mass spectra are termed 'singles' spectra. If the algorithm determines that an event contains two ion times, then these flight times are stored. From the resulting list of pairs of ion flight times, a 2D array is constructed and this array is used to plot the histogram of number of ion pairs

versus the two flight times, t_1 and t_2. This plot of $I(t_1,t_2)$ is a 2D coincidence spectrum and, again to avoid confusion, such spectra are termed 'pairs' spectra.

There is, however, an inherent complication associated with the collection and assignment of data described above. If an ion formed from dissociative double ionization is detected within the time range but its correlated partner is not, due to the detector efficiency being <1, then this signal is plotted in the singles spectrum. So, undoubtedly there will be some contribution of fragment ions from dissociative multiple ionization in the singles spectra. It is not possible to resolve the signals of ions from double ionization plotted in the singles spectrum whilst data acquisition is in progress, but, as discussed in Chapter 3, the contribution of multiple ionization to the singles spectrum can be determined and subtracted manually.

Operating Parameters

Typical operating pressures in the TOFMS, as recorded by an ion gauge, were of the order of 1.3×10^{-4} Pa. Low operating pressures are used in conjunction with the optimal emission current to give an ion count rate of the order of 100 counts per second thus avoiding saturation of the detector. Typical operating parameters are listed in Table 2.3.

Table 2.3 Typical operating parameters for the TOFMS used in the 2D experiments to record spectra at 250 eV.

Parameter	Typical value
Electron energy	250 eV
Pulsing period	20 μs
Filament potential	-50 V
Lens potential	-150 to +200 V
Lens pulse width	5 ns
Electron needle potential	200 V
Gas needle potential	200 V
Repeller plate voltage	0 to +400 V
Onset of repeller plate pulse	10-20 ns after electron pulse
Repeller plate pulse width	10 μs
Drift tube voltage	-1550 V
Onset of TDC start pulse	600 ns after electron pulse
MCP potential	-1850 V
MCP back plate	50 V
CFD dead time	64 ns
CFD output width	32 ns
Discriminator threshold	100 mV

2.4.1.2 Calibration of the Singles Spectrum

Fig. 2.14 shows a typical singles spectrum of Ar, used to calibrate the apparatus, recorded at an ionizing electron energy of 250 eV. As in the one-dimensional experiments, from the recorded spectrum of Ar the singles spectrum can be calibrated using Eq. 2.5.

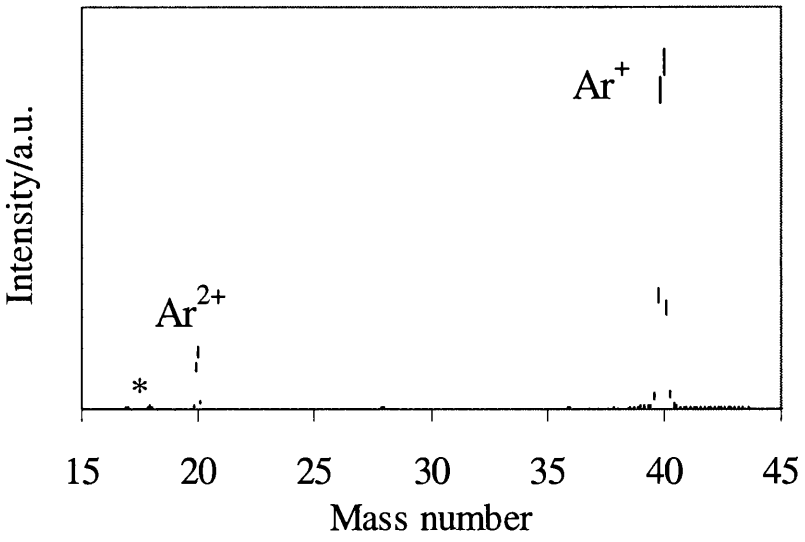

Fig. 2.14 Typical singles spectrum of Ar recorded at 250 eV. The peak marked with an asterisk corresponds to traces of water, the principal background gas in the TOFMS. To aid interpretation, the error bars shown have been scaled to represent twenty standard deviations.

Note that, in contrast to the one-dimensional time-of-flight mass spectrum (Fig. 2.4), the peak widths are narrower and the background of the singles spectrum is flat. Both these observations are a result of pulsing the electron gun. Since ionization occurs immediately before the application of the extraction pulse, the distribution of initial positions in the source is small and the smaller peak widths reflect this. In addition, as ionization no longer occurs during the extraction pulse period, the 'stepping' of the background observed in the one-dimensional mass spectrum is eliminated.

2.4.2 Double Ionization

2.4.2.1 Two-Dimensional Coincidence Techniques

For complex molecules, the ion-ion coincidence techniques used in the one-dimensional experiments do not unambiguously identify the ions responsible for the coincidence signals as there are a large number of available fragmentation channels. However, the 2D coincidence technique[15-22] involving the measurement of the actual flight times of a pair of ions, rather than time-of-flight difference, allows all the pairs of ions formed upon dicationic dissociation to be identified.

2D coincidence spectra ('pairs' spectra) are generated by plotting the flight times of a coincident pair of ions. For the dissociation of a dication m^{2+},

$$m^{2+} \rightarrow m_1^{+} + m_2^{+} \qquad \text{(2.II)}$$

the flight time of the lightest ion t_1 is plotted on the y axis and that of the second ion of the pair t_2 on the x axis. Thus a plot of t_1 versus t_2 yields a pairs spectrum where each peak in the pairs spectrum is a plot of intensity as a function of the flight times of the ion pair formed by a dicationic dissociation

event,[15-22] as illustrated in Fig. 2.15. Note that under our experimental geometry, described in Section 2.3.1.2, the lightest ion will reach the detector first.

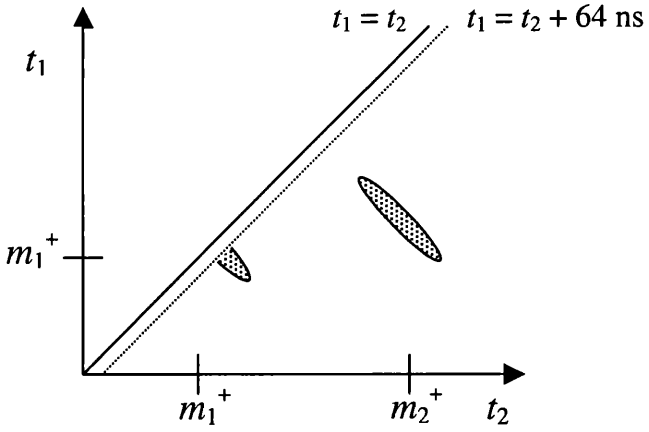

Fig. 2.15 Schematic diagram of a pairs spectrum.

Under the Wiley-McLaren focusing conditions,[3] the flight time of an ion t can be expressed in the following way,

$$t = t_0 - k\,p\cos\theta \qquad \text{Eq. 2.14}$$

where t_0 is the flight time for an ion with zero kinetic energy release (KER), k is a constant inversely proportional to the source field, p is the magnitude of the initial momentum on dissociation and θ is the angle between the initial momentum vector and the TOFMS axis (when $\theta = 0$ is parallel or anti-parallel to the axis of the TOFMS). Therefore, the peaks observed in the pairs spectra will be lozenge-shaped (Fig. 2.15) because there will be a distribution of ion flight times as a result of the KER upon dissociation and the direction of the initial impulse upon dissociation of the dication. The axial length of the peaks is the result of the deviation δt of an ion flight time from t_0,[19-21] as the ion flight time may be longer or shorter than t_0 depending on the KER and the direction of the initial impulse. The widths perpendicular to the axial lengths reflect both apparatus factors, such as temporal resolution, the random thermal motion of the parent dication before ionization and the dication dissociation mechanism followed.[19-21] As will be discussed in the following chapter, a powerful method for obtaining information concerning the dissociation mechanism involved with a given fragmentation channel is to consider the slope of the relevant peak in the pairs spectrum.[19,22]

From Fig. 2.15 it can be seen that the peak corresponding to identical ion pairs (*e.g.* $O^+ + O^+$ from O_2^{2+}) will be centred on the $t_1 = t_2$ diagonal of the pairs spectrum. However, any pairs of ions with identical or very similar flight times will not be observed in the pairs spectrum as the dead time of the CFD prevents a second stop pulses being transmitted to the TDC within 64 ns of the first pulse received. Therefore, the first ion time will be counted by the TDC but that of its correlated partner will not and so the single ion time will be plotted in the singles spectrum. As a result, there is a region in the pairs spectrum, corresponding to the dead time of the CFD, where no ion pair signals

are observed. For the majority of identical ion pairs, this dead time region does not obscure the entire peak since the ion pairs which have a large difference in flight times (*i.e.* greater than 64 ns) will still be detected and plotted in the pairs spectrum. As will be described in Chapter 3, it is possible to obtain an estimate of the area of the peak obscured by the dead time and hence the number of ion pairs which would be contained within the obscured area can be evaluated.

The use of the MCP detector, in place of the channeltron used in the one-dimensional experiments, should eliminate the angular discrimination introduced by the small aperture of the channeltron. Therefore, as indicated by the peaks in the pairs spectra, all the ions formed from dicationic dissociation reach the detector, regardless of the direction with respect to the TOFMS axis, of the initial dication dissociation impulse.[7]

2.4.2.2 Calibration of the Pairs Spectra

Fig. 2.16 shows the pairs spectrum of CS_2^{2+} and, as can be seen in the figure, the following

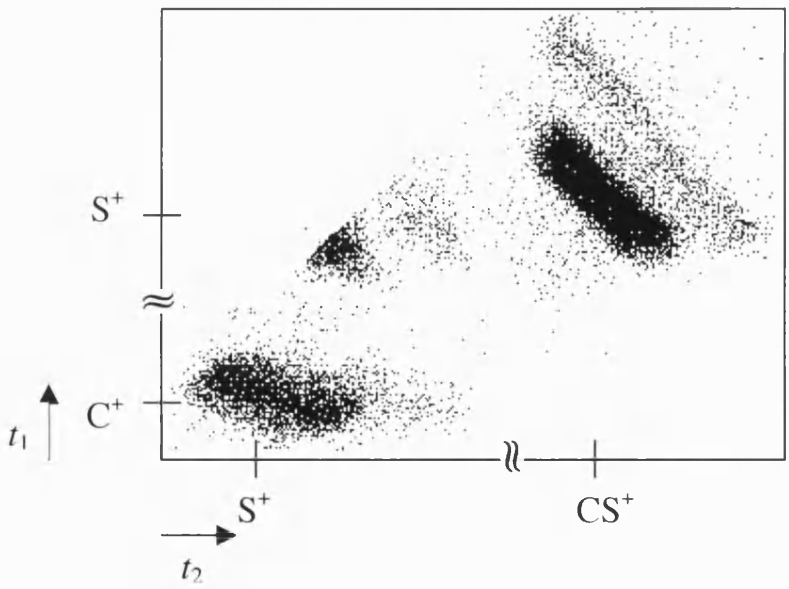

pairs of ions are formed from the dissociation of CS_2^{2+}: $CS^+ + S^+$, $C^+ + S^+$ and $S^+ + S^+$.[12]

Fig. 2.16 Pairs spectrum of CS_2^{2+} recorded at 250 eV.

As mentioned above, only a proportion of the peak corresponding to the identical ion pair $S^+ + S^+$ is observed in the spectrum as the dead time of the CFD obscures the region of the pairs spectrum where the flight times of the ions are similar.

Fig. 2.17 shows a 2D contour plot of the CS_2^{2+} pairs spectrum in the region of the $CS^+ + S^+$ ion pair to illustrate that each pairs peak is a plot of the intensity as a function of t_1 and t_2. As expected, the decreased angular discrimination induced by the MCP manifests itself in this 2D contour plot since the high intensity region is uniform along the axial length of the peak, indicating that there is no angular discrimination.

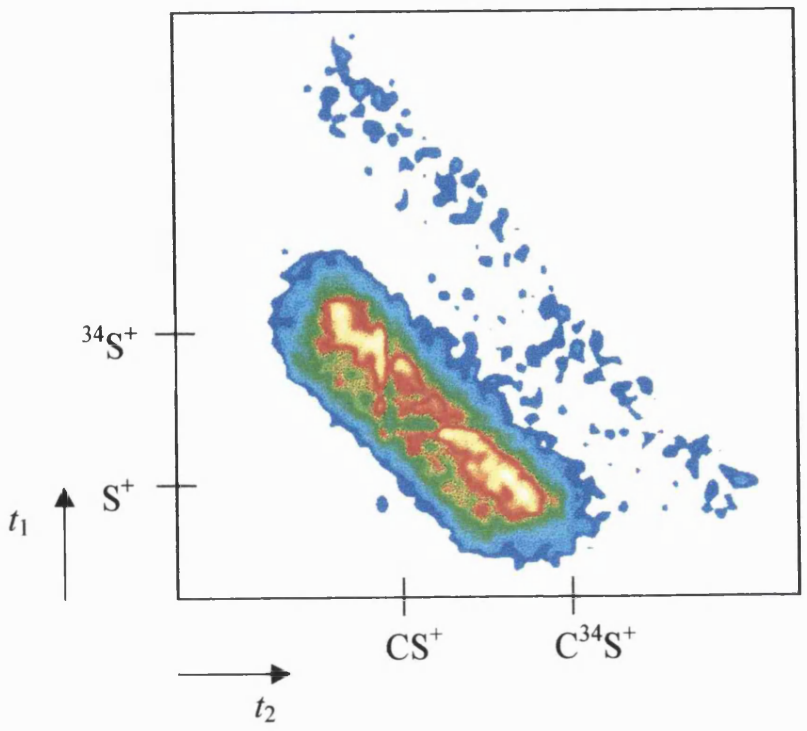

Fig. 2.17 2D contour plot of the pairs peak corresponding to the $CS^+ + S^+$ ion pair.

2.3.4 Conclusions

The second half of this chapter describes the modifications made to the TOFMS in order to allow the recording of time-of-flight mass spectra (singles spectra) and 2D coincidence spectra (pairs spectra). The basis of the 2D coincidence technique is also discussed.

As will be discussed in the following chapter, using this set of techniques, coupled with the modified apparatus set-up, relative partial single ionization cross sections for the fragment ions observed in the singles spectra can be determined. Analysis of the pairs spectra can also yield additional information concerning the dissociation dynamics of dications.

2.5 Overall Conclusions

This chapter describes the implementation and modification of a standard two-field TOFMS to perform the one and two-dimensional investigations of the single and double ionization of reactive molecules. From the single ionization studies, the cross sections for forming singly charged ions from the single ionization of the target molecule, relative partial single ionization cross sections, can be determined. From the double ionization studies, information concerning the dynamics and energetic of the dication dissociation mechanisms can be obtained.

References

1 K.A. Newson, S.M. Luc, S.D. Price and N.J. Mason, *Int. J. Mass Spectrom. Ion Proc.,* **148** (1995) 203

2 D. Price and G.J. Milnes, *Int. J. Mass Spectrom. Ion Proc.,* **99** (1990) 1

3 W.C. Wiley and I.H. McLaren, *Rev. Sci. Instrum.,* **26** (1955) 1150

4 J.H.D. Eland, *Meas. Sci. Tech.,* **4** (1993) 1522

5 M.R. Bruce and R.A. Bonham, *Z. Phys. D,* **24** (1992) 149

6 Philips, *Data Handbook: Electron Multipliers*, 1991

7 D.M. Curtis and J.H.D. Eland, *Int. J. Mass Spectrom. Ion Proc.,* **63** (1985) 241

8 K.E. McCulloh, T.E. Sharp and H.M. Rosenstock, *J. Chem. Phys.,* **42** (1965) 3501

9 K.A. Newson and S.D. Price, *Int. J. Mass Spectrom. Ion Proc.,* **153** (1996) 151

10 G. Dujardin, S. Leach, O. Dutuit, P.M. Guyon and M. Richardviard, *Chem. Phys.,* **88** (1984) 339

11 T. Masuoka, *Phys. Rev. A,* **48** (1993) 1955

12 P. Lablanquie, I. Nenner, P. Millie, P. Morin, J.H.D. Eland, M.J. Hubin-Franskin and J. Delwiche, *J. Chem. Phys.,* **82** (1985) 2951

13 T.D. Märk, in T.D. Märk, G.H. Dunn (Eds.), *Electron Impact Ionization*, Springer-Verlag, New York, 1985

14 P. Calandra and S.D. Price, *private communication,* (1999)

15 J.H.D. Eland, *Chem. Phys. Lett.,* **203** (1993) 353

16 I. Nenner and J.H.D. Eland, *Z. Phys. D,* **25** (1992) 47

17 S. Hsieh and J.H.D. Eland, *J. Chem. Phys.,* **103** (1995) 1006

18 S. Hsieh and J.H.D. Eland, *Int. J. Mass Spectrom. Ion Proc.,* **167/168** (1997) 415

19 J.H.D. Eland, *Mol. Phys.,* **61** (1987) 725

20 J.H.D. Eland, F.S. Wort and R.N. Royds, *J. Electron Spectrosc. Relat. Phenom.,* **41** (1986) 297

21 J.H.D. Eland, in C.Y. Ng (Ed.), *Vacuum Ultraviolet Photoionization and Photodissociation of Molecules and Clusters*, World Scientific, Singapore, 1991

22 M. Lange, O. Pfaff, U. Müller and R. Brenn, *Chem. Phys.,* **230** (1998) 117

3. Data Analysis

3.1 Introduction

As discussed in Chapter 2, electron-impact time-of-flight mass spectrometry is used to study the fragmentation of singly charged ions and ion-ion coincidence techniques are used to study dications. The basis of the techniques employed in this thesis to study the formation and fragmentation of singly and doubly charged molecular ions, and their implementation, has been described in detail in the preceding chapter. The analysis procedures used to derive information concerning the formation and fragmentation of monocations and dications from the recorded spectra are the subject of this chapter.

3.2 One-Dimensional Studies

The TOFMS used for the one-dimensional experiments has been described in detail in Chapter 2. In this one-dimensional experimental arrangement, the repeller plate is pulsed to record the time-of-flight mass spectra and the ions are detected using a channeltron detector.

3.2.1 Single Ionization

In the time-of-flight mass spectrometric experiments, the flight time of an ion formed by electron impact between the source region and the detector of the TOFMS is recorded. Over the data acquisition period a histogram of ion flight times is produced consisting of a series of time channels each corresponding to points on a mass scale. The number of ions in each channel is a measure of the intensity of ions of that particular mass and a complete histogram represents the mass spectrum. As mentioned in Chapter 2 and derived in Appendix 1, the flight time of an ion t_{tof} in a TOFMS is dependent on the square root of its mass m (Eq. 2.1). Following the calibration of the time-of-flight mass spectrum with a well-characterised target gas, the identity of the ions present in the time-of-flight mass spectrum can be determined using Eq. 2.5. As explained below, from this raw data, information about the branching ratios and the appearance energies of fragment ions can be deduced.

To illustrate the analysis procedure used to derive information from time-of-flight mass spectra, the single ionization of CS_2 is considered. A typical mass spectrum of CS_2 is shown in Fig. 3.1. From the figure, it can be seen that the parent ion CS_2^+ and fragment ions C^+, S^+, CS^+ and S_2^+ are detected following electron-impact ionization at 150 eV. In addition the stable parent dication CS_2^{2+} is also observed.

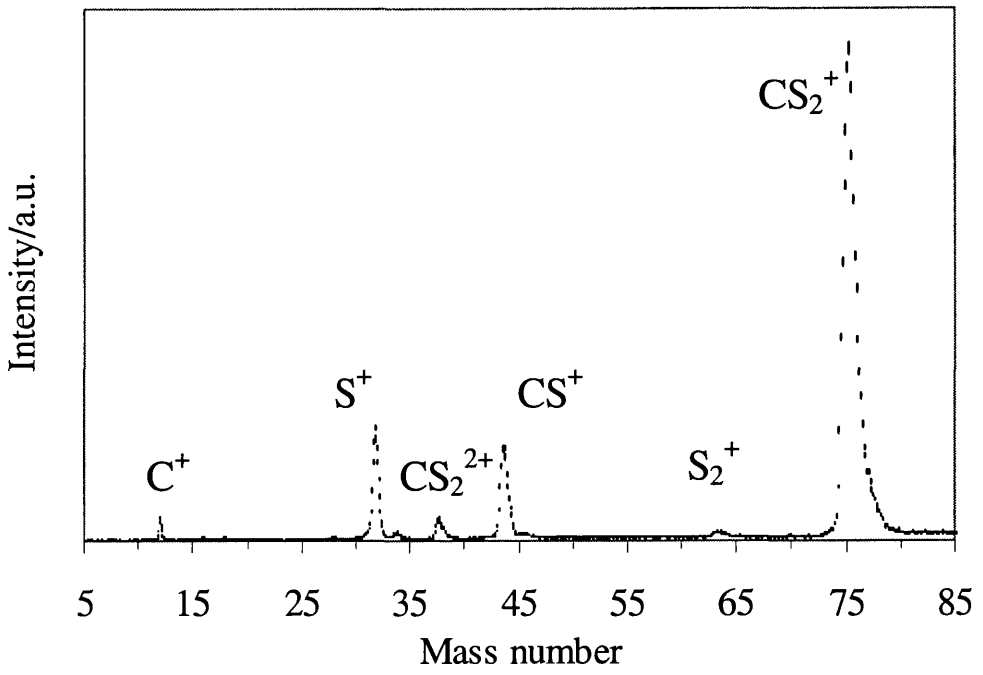

Fig. 3.1 Typical time-of-flight mass spectrum of CS_2. The error bars are derived from the counting statistics and represent two standard deviations.

3.2.1.1 Determination of the Relative Partial Single Ionization Cross Section

The raw data for the analysis of the time-of-flight mass spectra consists of the intensities of the ion signals from the recorded mass spectra, such as Fig. 3.1. The intensities of the ion signals are determined by finding the areas of the peaks and applying a suitable correction to subtract the background ion signals arising from the detection of ions formed outside the focused volume. The background correction is evaluated for each peak in turn, by determining the number of ion counts per channel in the region of the spectrum before the onset of the sharp mass peaks and thus the background contribution to the peak can be calculated and subtracted.

To derive the partial ionization cross sections of the ions from the ion intensities determined from the mass spectrum, it is necessary to consider the factors affecting their magnitudes. For a molecule XY, the intensity of a signal I_{Y+} due to Y^+ in the mass spectrum after P pulses of the repeller plate can be expressed as

$$I_{Y^+} = \alpha n_{Y^+} VP \qquad \text{Eq. 3.1}$$

where n_{Y+} is the number density of the ion Y^+ in the volume V of the source region that is focused onto the detector and α is the experimental ion collection efficiency. The constant α is assumed to be mass independent and should therefore depend only on the channeltron efficiency and electronics. If σ_{XY} is the partial ionization cross section for forming Y^+ from the neutral molecule XY, then by definition,

$$R_{Y^+} = R_e^0 n_{XY} \sigma_{XY} l \qquad \text{Eq. 3.2}$$

where R_{Y+} is the rate of formation of Y^+ in the ionization region and R_e^0 is the number of electrons per second entering the ionization region that has an electron pathlength of l.

As described in Chapter 2, any ions formed during the period between the extraction pulses are immediately accelerated towards the repeller plate due to the presence of the bias field. Hence, when the extraction pulse is applied, ions of two different masses formed with the same partial ionization cross section will have different densities in the source region, due to their differing velocities across it as a result of the presence of the bias field. Since the rate of ionization is low and the residence time of an ion in the source region is small (< 1 μs) in comparison to the inter-pulse period (30 μs), the fluxes of the two species across the source region will be the same. That is, after a period of less than 1 μs, which is the time taken for the first ions formed to leave the interaction region, the number of the two species leaving the interaction region per unit time interval will be the same, although they leave with different velocities.

If the cross sectional area of the focused volume perpendicular to the bias field is A, then the flux of Y^+, the number of species leaving the interaction region per unit time interval, across the focused volume is J_{Y+} where $J_{Y+} = R_{Y+}/A$. At any point $n_{Y+} = J_{Y+}/\upsilon_{Y+}$, where υ_{Y+} is the velocity of Y^+. Since the ions are undergoing a constant acceleration across the focused volume under the influence of the bias electric field, $\upsilon_{Y+} = b/\sqrt{m_{Y+}}$, where m_{Y+} is the mass-to-charge ratio of Y^+ and b is a constant depending on the position of Y^+ in the bias field. Combining these expressions gives,

$$I_{Y^+} = \frac{\alpha V P R_e^0 n_{XY} \sigma_{XY} l \sqrt{m_{Y^+}}}{Ab} \qquad \text{Eq. 3.3}$$

Using a Monte Carlo simulation to model the ionic motions in the source region, it is found that, under the general experimental conditions described above, ions formed at the same rate will have densities proportional to the square root of their masses, as predicted by Eq. 3.3.[1]

From the recorded time-of-flight mass spectra, one would ideally like to determine absolute partial ionization cross sections of the observed ions. However, as discussed in Chapter 1, it is very difficult to measure absolute partial ionization cross sections using a TOFMS, as an accurate determination of experimental parameters such as the electron pathlength, the number density of the target gas and the electron flux is required. The measurement of such parameters (Eq. 3.3) is difficult and complicated and so the relative partial ionization cross sections σ_r^I of the observed ions are commonly determined. Indeed, values of σ_r^I for reactive molecules are determined from the time-of-flight mass spectra recorded in these studies.

To determine σ_r^I the intensities of the ion signals in the mass spectrum are divided by the intensity of the most abundant ion to give an intensity ratio. For example, for a spectrum of CS_2

(Fig. 3.1) where the most abundant ion is the parent ion CS_2^+, the ion signals of the fragment ions C^+, S^+, S_2^+ and CS^+ are divided by the intensity of CS_2^+ to give $I(X^+)/I(CS_2^+)$ for each fragment. However, due to the ion density effects described above, a correction factor must be applied to this intensity ratio to give σ_r^I, where $\sigma_r^I = \sigma(X^+)/\sigma(CS_2^+)$. From Eq. 3.3, the values of $\sigma_r^I(X^+/CS_2^+)$ will be equal to the ratio of the intensities of the ions multiplied by the ratio of the square root of their masses (Eq. 3.4)

$$\sigma_r^{\,I} = \frac{\sigma_{X^+}}{\sigma_{CS_2^+}} = \frac{\sqrt{m_{CS_2^+}}}{\sqrt{m_{X^+}}} \frac{I_{X^+}}{I_{CS_2^+}} \qquad \text{Eq. 3.4}$$

where m is the relative molecular mass of the ion. Using the above analysis procedure, mass spectra of argon from this apparatus yield a ratio of the single-to-double ionization cross sections in good agreement with that available in the literature.[2]

Due to the small collection aperture of the channeltron detector, ions formed with a significant translational energy perpendicular to the axis of the TOFMS will miss the detector (Fig. 3.2), since their transverse trajectories along the drift tube will result in a final position at the end of the drift region beyond the channeltron aperture.

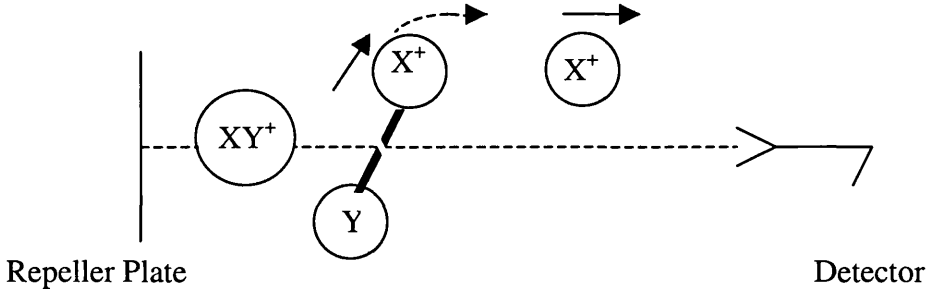

Fig. 3.2 Diagram of the trajectory of an ion formed with significant translational energy demonstrating that it will miss the detector.

Assuming a point ion source, the maximum translational energy E an ion can possess perpendicular to the axis of the TOFMS and still be detected can be calculated in the following way,

$$E = \frac{1}{2} m v_T^2 \qquad \text{Eq. 3.5}$$

where v_T is the transverse velocity of the ion, away from the axis of the TOFMS. The transverse velocity of the ion can be calculated from $v_T = r_d / t_{tof}$, where r_d is the radius of the detector. For a N_2^+ ion with a flight time in the apparatus of 2.2 μs,

$$v_T = \frac{0.3}{2.2} = 0.14 \text{ cm } \mu s^{-1} \qquad \text{Eq. 3.6}$$

and thus from Eq. 3.5, $E = 0.28$ eV. Therefore, for the one-dimensional apparatus set-up, ions with a translational energy greater than ~0.3 eV will be inefficiently detected. Hence, the above analysis procedure used to determine values of σ_r^I is only valid if an insignificant proportion of the fragment

ions are produced with kinetic energies above 0.3 eV, although the ratio of the cross section for the different fragment ions will be consistent if there are no marked differences in the high energy parts of the kinetic energy release distributions for the formation of the different fragments.[1] Studies of the fragmentation of triatomic parent ions, such as CS_2^+, N_2O^+ and O_3^+, formed by electron impact, indicate that only a small percentage of the fragment ions from these species have kinetic energies greater than 0.3 eV.[1,3] Due to the increased number of available internal modes of vibration, one would expect a similar, if not smaller, proportion of high kinetic energy fragments to result from the dissociation of polyatomic ions. Therefore, one would conclude that the analysis procedure described above should yield accurate values of the partial ionization cross sections, a conclusion supported by previous work on the ionization of O_3.[1]

It is important to realise that the small aperture detector discriminates strongly against the detection of energetic fragments produced by the dissociation of multiply charged ions, as such fragments are usually formed with kinetic energies in excess of 2 eV.[4] Hence, energetic ions are not efficiently detected in the one-dimensional experiments and as a result, the fragment ions observed in the mass spectrum are "low" energy ions arising from the dissociation of singly charged parent ions. Thus the values of σ_r^I derived using the apparatus set-up employed in the one-dimensional investigations should perhaps be correctly described as relative partial single ionization cross sections σ_r^{si}. However, if a fragment ion formed from dissociative double ionization receives an impulse from the dissociation event along the axis of the TOMFS then this ion, although highly energetic, will be detected in the time-of-flight mass spectrum since it has no translational energy perpendicular to the axis of the TOFMS. But, the double ionization cross section is generally small compared to the single ionization cross section[5]. Hence, any neglected contribution from multiple ionization to the values of the partial ionization cross sections determined in this study will for the most part be insignificant in comparison with the statistical sources of uncertainty.

3.2.2 Double Ionization

In order to investigate the formation and fragmentation of doubly charged molecular ions, ion-ion coincidence techniques[4,6-9] are used. The experimental procedure employed is described in Chapter 2. Ion-ion coincidence experiments involve measuring the time-of-flight difference Δt_{tof} between a pair of ions produced by dissociative double ionization,

$$XY_2^{2+} \rightarrow XY^+ + Y^+ \qquad (3.I)$$

and a plot of ion signal intensity as a function of Δt_{tof} is a coincidence spectrum. As discussed in Chapter 2 (Eq. 2.6), $\Delta t_{tof} \propto (\sqrt{m_1} - \sqrt{m_2})$, where m_1 and m_2 are the masses of the pair of ions. After the calibration of the coincidence spectrum with a known target gas, any ion pairs observed in the

coincidence spectrum can be identified (Eq. 2.13). The relative intensities of the peaks in the coincidence spectrum may, perhaps, be interpreted to give an indication of the structure of the dication as it may be possible to infer the connectivity within the dication from the pairs of ions produced upon dicationic dissociation.

In a TOFMS under the Wiley-McLaren focusing conditions[10], the time-of-flight of an ion t_{tof} is given by

$$t_{tof} = t_0 - \frac{v}{a} \qquad \text{Eq. 3.7}$$

where t_0 is the flight time for a thermal ion, v/a is the braking time which is the change in the flight time of the ion caused by its initial velocity , v is the initial velocity component of the ion along the axis of the TOFMS and a is its acceleration in the source region.[4]

From the temporal width of the coincidence peak, the KER associated with dicationic dissociation resulting in the formation of an ion pair can be determined. For a two-body dissociation reaction, forming the pair of product ions,

$$m^{2+} \rightarrow m_1^+ + m_2^+ \qquad \text{(3.II)}$$

conservation of linear momentum requires that $m_1v_1 + m_2v_2 = 0$ and, since the acceleration of the ions is inversely proportional to the ion mass, the braking times for the two fragments are equal in magnitude but opposite in sign. Therefore, Δt_{tof} is given by

$$\Delta t_{tof} = \Delta t_0 + \frac{2v_1}{a} \qquad \text{Eq. 3.8}$$

Since, v_1 ranges from $+v_0$ to $-v_0$, where v_0 is the initial speed of m_1^+ and $v_1 = v_0 \cos\theta$ (where θ is the angle between the axis of the TOFMS and the initial ion trajectory), the total peak width w (ns) will be $4v_0/a$. Thus, from the conservation of momentum and Newtonian mechanics, the KER upon dissociation U_0 (eV) can be obtained directly from the width of the coincidence peak using the following equation,

$$w = \frac{4v_0}{a} = \frac{5766}{E}\left[\frac{U_0 m_1 m_2}{m}\right]^{\frac{1}{2}} \qquad \text{Eq. 3.9}$$

where E (V cm^{-1}) is the source field voltage and m, m_1 and m_2 are relative molecular masses.[4]

However, for a three-body dissociation reaction, where neutral products are formed in conjunction with the pair of fragment ions, there is no unique relationship between the total KER and the width of the coincidence peak. Therefore, deductions about the overall KER can only be made with the help of assumptions about the dissociation mechanism and dynamics. For example, if the reaction mechanism is sequential, following

$$\begin{aligned} m^{2+} &\rightarrow m_1^+ + m_2m_3^+ \\ m_2m_3^+ &\rightarrow m_2^+ + m_3 \end{aligned} \qquad \text{(3.III)}$$

and it is further assumed that the KER of the monocation dissociation is negligible, the observed peak width can be related to the total energy release in the following way,[4]

$$w = \frac{2882}{E}\left[\frac{U_0(2m_3 + m_2)^2 m_1}{m(m_2 + m_3)}\right]^{\frac{1}{2}} \qquad \text{Eq. 3.10}$$

From Fig. 2.10, it can be seen that the coincidence signals observed in the one-dimensional coincidence experiments consist of two separate peaks. As described in Chapter 2, this shape arises because of the angular discrimination introduced by the small entrance aperture of the channeltron. The intensities of the coincidence signals corresponding to a given ion pair can be determined by finding the area of the coincidence signal N_c and suitably correcting for the false coincidence background N_f (Fig. 2.9). Thus, the number of true coincidence signals N_t is obtained.

$$N_t = N_c - N_f \qquad \text{Eq. 3.11}$$

3.2.2.1 Kinetic Energy Release Determination

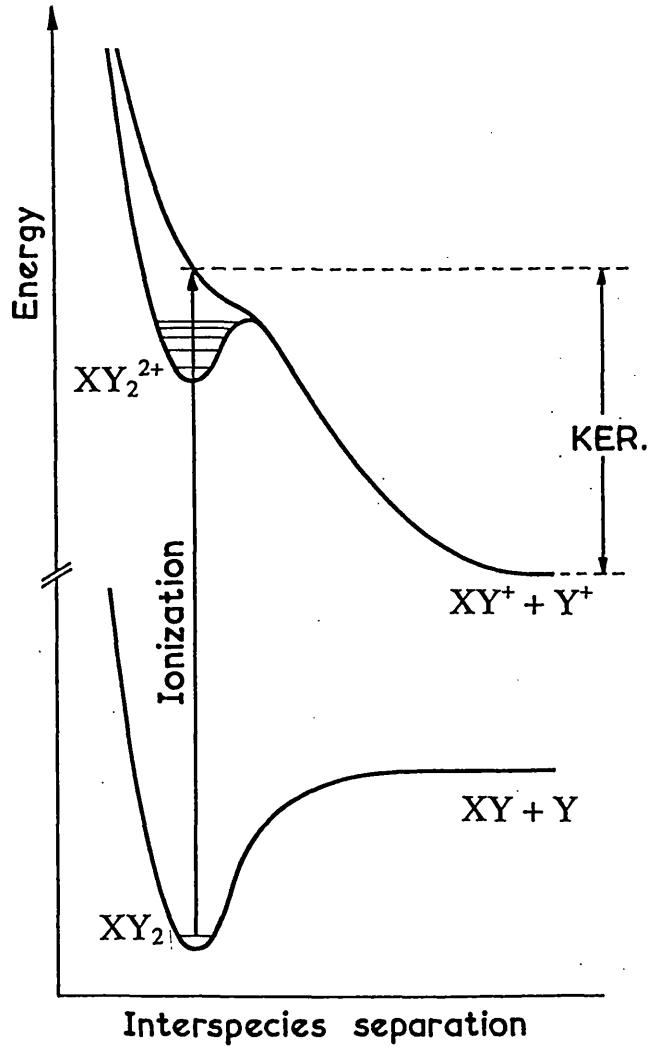

Fig. 3.3 Schematic potential energy curves for a dication illustrating the relationship of the KER to the energy of the dication state responsible for the dissociation reaction.

If the KER can be determined from the coincidence peak shape for a given dication fragmentation channel, then an estimate of the energy of the dication state $E(XY_2^{2+})$ from which the decay reaction occurred can be made by adding the KER to the energy of the products of the charge separation reaction (Eq. 3.12). Therefore, as can be seen in Fig. 3.3, the determination of the KER enables a crude form of electronic spectroscopy to be performed.

$$E(XY_2^{2+}) = E(XY^+ + Y^+) + \text{KER} \qquad \text{Eq. 3.12}$$

An estimate of the KER associated with a given dication dissociation reaction can be made by directly measuring the temporal width of the coincidence peak (Section 3.2.2). However, this procedure assumes that the KER is single-valued and makes no allowance for the effects of any apparatus parameters on the peak shape. In order to make a more sophisticated determination of the KER for a given fragmentation channel, the experimental spectrum can be modelled using a Monte Carlo simulation.[11-13] This modelling procedure allows the inclusion of all experimental parameters that affect the peak shape, such as the size of the ionization region, a distribution of KERs and an allowance for any inherent time jitter of the channeltron. The time jitter is a result of the variation in the width, height, shape and delay of the output pulse from the channeltron.[14]

Monte Carlo Simulation Procedure

The Monte Carlo simulations involve the calculation of the flight times of repeated ion trajectories under an electrostatic model of the experimental conditions. The Monte Carlo simulation models the dissociation of a dication with a Gaussian kinetic energy release distribution (KERD), a Gaussian spatial distribution of ionization events about the centre of the ionization source and an initial velocity of the neutral molecule before ionization represented by a Maxwell-Boltzmann distribution. The KERDs are modelled as a sum of Gaussian energy release distributions as the KERD of the detected fragments is expected to be a direct function of the reflection of the Gaussian ground state wavefunction on the respective repulsive potential energy curves of the dication states in the Franck-Condon region ('reflection approximation').[4,15]

The treatment of the ions in the simulation is also important, as the initial direction of motion of the parent molecules before ionization is random. Due to the spherical co-ordinates of the moving ions being projected onto the planar detector, most of the ions detected will have a significant transverse velocity away from the axis of the TOFMS, as demonstrated in Fig. 3.4.

To take account of this projection of the spherical velocity distribution onto the plane of the detector, the distribution of the initial velocities following ionization must be weighted appropriately. Analysis shows that in order to correctly simulate the distribution of ion velocities projected onto the detector, the weighting must be sinusoidal, ensuring that there a greater proportion of ions having

large angles, $\theta = \pi/2$, than ions having $\theta \approx 0$ (Fig. 3.4). This results in the satisfactory reproduction of the square prototypical coincidence peak (Fig. 2.6).[11]

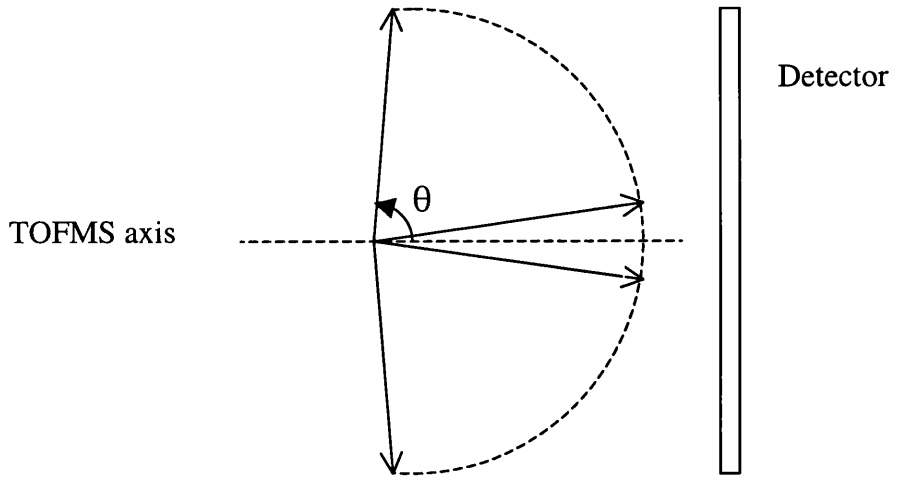

Fig. 3.4 A schematic diagram to show the angular trajectory distribution. This figure illustrates the small proportion of ions projected onto the plane of the detector with a significant velocity component along the axis of the TOFMS, $\theta \approx 0$.

The procedure followed to perform a simulation of a coincidence peak is shown in Fig. 3.5. Initially the apparatus parameters are entered into the algorithm to set up the electrostatic model of the experimental conditions. The apparatus parameters that are required are the lengths of the source, acceleration and drift regions of the TOFMS and the voltages applied to the source region, the drift region and the sandwich grid. Subsequently, the information concerning the dissociation reactions giving rise to the relevant coincidence peak are then entered. In addition to the masses of the detected ion pairs and the parent dication, the masses of the primary ions formed in the initial dicationic charge separation, *e.g.* m_1^+ and $m_2m_3^+$ in Reaction (3.III), which then dissociate to form the detected ion pair, m_1^+ and m_2^+, are also included in the program. As discussed below, the inclusion of the masses of the primary ions enables the simulation of the formation of a given ion pair *via* all the possible dication decay pathways. If more than one ion pair is contributing to the signal of the coincidence peak then the relative intensity of each ion pair signal is also incorporated in the simulation.

Once the fragmentation pathways for the dissociation reactions have been set up, the energetics of the individual dissociation reactions are entered. First it is necessary to distinguish if the KER is single-valued or if there are multiple KERs occurring. An estimate of the KER or KERs upon dissociation of the dication to form each ion pair is then entered, together with the probability of each release if the KER is multi-valued. Following the information concerning the KER, the initial gas temperatures perpendicular and parallel to the axis of the TOFMS are entered.

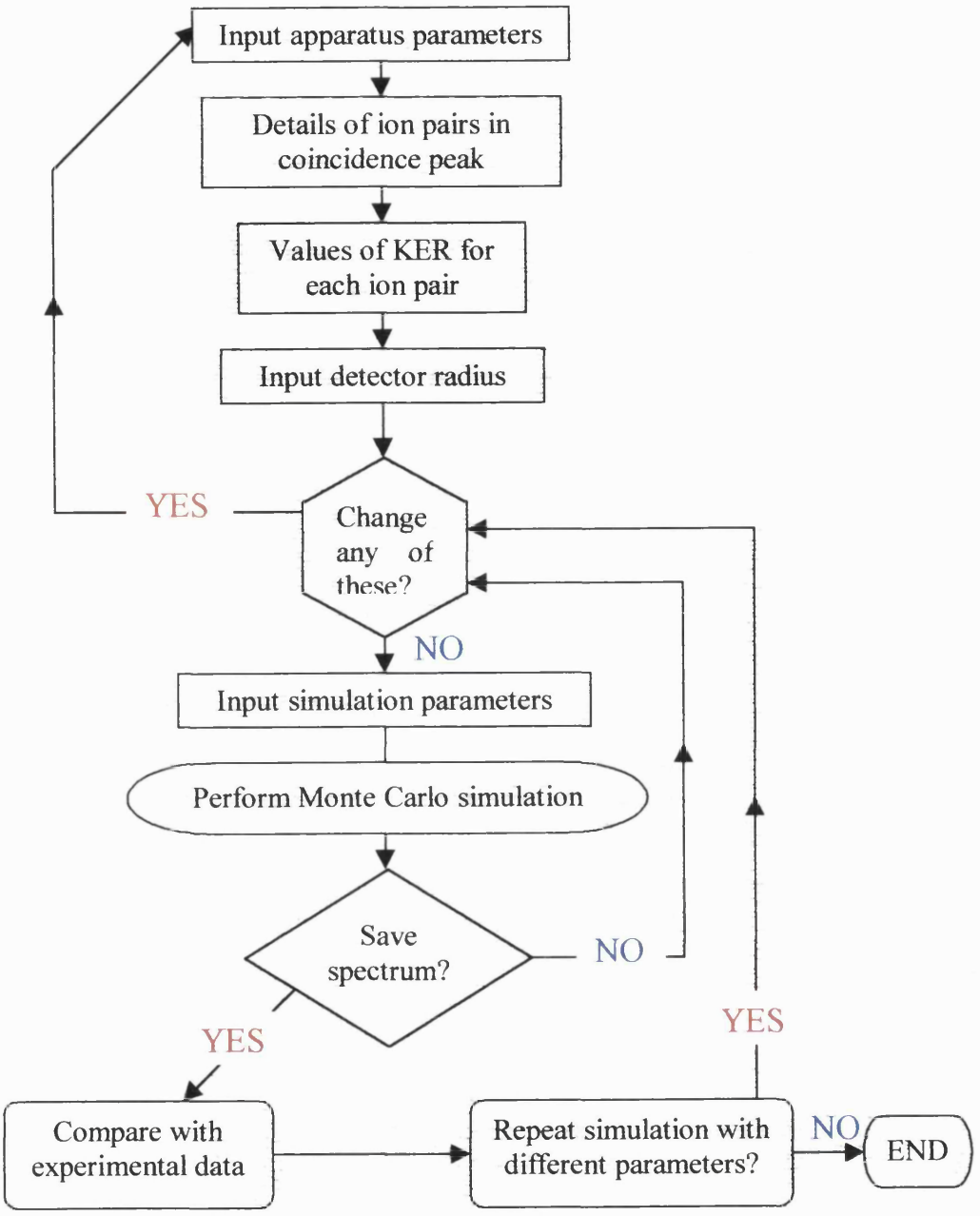

Fig. 3.5 Flow diagram showing the simulation procedure.

Once the apparatus and ion parameters have been entered into the algorithm, the simulation parameters must be entered. These parameters are the half-width of the kinetic energy release distribution F_{KERD} for each ion pair, the half-width of the Gaussian distribution of ionization events in source and half-width of the channeltron time jitter distribution.[14] Once all these values have been entered into the program, the simulation program is run and a simulated spectrum which can be compared with the experimental data is produced.

As with an experimental spectrum, the results of the Monte Carlo simulation are displayed in the form of a histogram built up as a result of repeated trajectories, with the number of ions with a particular time-of-flight plotted against Δt_{tof}. Thus, the histogram is the simulated coincidence spectrum. Repeated simulations with different energetics and simulation parameters are performed

until a satisfactory fit, judged by eye, with the experimental data is obtained. The uncertainties in the KER derived from such a fit, which are determined by the deviations necessary to significantly degrade the fit with the experimental spectrum, are of the order of ± 0.2 eV.

Table 3.1 Parameters required for the simulation of the $CS^+ + S^+$ ion pair from CS_2^{2+}.

Parameter	Value
Source length /cm	1.0
Acceleration length /cm	1.8
Drift length /cm	23.1
Source volts /V	400
Volts on drift tube /V	-1550
Volts on sandwich grid /V	3
Number of different ion pairs	1
Masses of ion pair /amu	44 32
Masses of primary ions /amu	44 32
Mass of parent ion /amu	76
Probability of this decay reaction	1
Number of KER	1
Value of KER /eV	4.2
Detector radius /mm	3
Initial gas temperature along jet axis /K	300
Initial gas temperature perpendicular to jet axis /K	300
Number of trajectories	50000
Width of display /ns	300
F_{KERD} /eV	2.2
Half-width of Gaussian distribution in source /mm	2.0
Half-width of time jitter distribution /ns	25

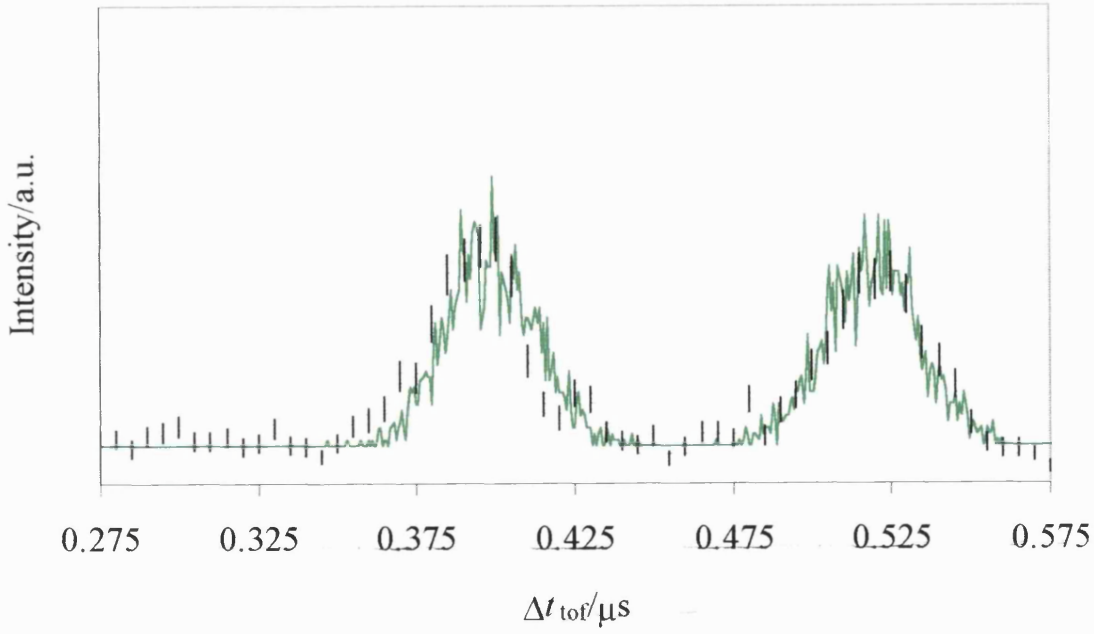

Fig. 3.6 Ion-ion coincidence spectrum of CS_2^{2+} showing the signal corresponding to the $CS^+ + S^+$ ion pair. The experimental points are indicated by error bars representing two standard deviations. The solid curve is a Monte Carlo simulation of the experimental signal.

To check the validity of the above simulation procedure, an ion-ion coincidence spectrum of CS_2^{2+} was recorded, forming the dication by electron impact at 150 eV (Fig. 2.10). The region of the spectrum containing the peak corresponding to the dissociation reaction

$$CS_2^{2+} \rightarrow CS^+ + S^+ \qquad (3.IV)$$

was simulated (Fig. 3.6) and the best fit to the experimental data was produced with a KER of 4.2 ± 0.2 eV and a distribution of initial ion positions in the source with a 2 mm half-width (Table 3.1). This value of the KER is in good agreement with the literature[4] and indicates that modelling the coincidence spectra in this way provides reliable values of the KER.

Molecular dications generally dissociate *via* two and three-body dissociation reactions to form the pairs of ions observed in the ion-ion coincidence spectra. For a two-body reaction, there is only one possible decay pathway: the direct dissociation of the molecular dication to form the pair of product ions, as illustrated in Reactions (3.II) and (3.IV).

However, for a three-body dissociation reaction, where neutral products are formed in conjunction with the pair of fragment ions, the fragmentation can occur by a variety of pathways[16] but three broad classes of mechanism can be identified. Firstly, a single-step mechanism (Coulomb explosion),

$$m^{2+} \rightarrow m_1^+ + m_2^+ + m_3 \qquad (3.V)$$

for example,[16]

$$SO_2^{2+} \rightarrow O^+ + S^+ + O \qquad (3.VI)$$

Secondly, a sequential pathway involving deferred charge separation,

$$\begin{aligned} m^{2+} &\rightarrow m_1 m_2^{2+} + m_3 \\ m_1 m_2^{2+} &\rightarrow m_1^+ + m_2^+ \end{aligned} \qquad (3.VIII)$$

for example,[16]

$$\begin{aligned} SF_6^{2+} &\rightarrow SF_4^{2+} + F_2 \\ SF_4^{2+} &\rightarrow SF_3^+ + F^+ \end{aligned} \qquad (3.VIII)$$

Finally, a sequential pathway involving an initial charge separation followed by the subsequent dissociation of one or more of the resulting singly charged ions, [Reaction (3.III)]. For example,[17]

$$\begin{aligned} C_4F_8^{2+} &\rightarrow C_2F_4^+ + C_2F_4^+ \\ C_2F_4^+ &\rightarrow CF_3^+ + CF \end{aligned} \qquad (3.IX)$$

Therefore, for a three-body reaction, the pair of ions detected may not be the same pair of ions that received the initial impulse from the dicationic dissociation event. This complicates the interpretation of the widths of the coincidence peaks in terms of the KER upon dissociation, and to make further progress it is necessary to consider by which three-body pathways the dication dissociates.

The dynamics of three-body dissociation reactions of molecular dications have been studied using triple coincidence techniques[16-22] which have revealed many subtle details of these decay pathways. These studies have shown that a true Coulomb explosion is rare and if daughter dications are not observed in the mass spectrum (*e.g.* SF_4^{2+} from SF_6^{2+})[16], the common three-body dissociation pathway for small molecular dications usually involves charge separation followed by subsequent dissociation of the monocations. Further studies[23] have shown that if the dissociation reaction involves deferred charge separation there will usually be evidence of a metastable 'tail', asymmetrical broadening, on the coincidence signals. Therefore, from the analysis of the mass spectra and coincidence spectra it is possible to get an indication of the type of dication dissociation mechanism followed.

For two-body dissociation reactions [Reaction (3.II)], the ions formed in the charge-separating reaction are the ions detected in the coincidence spectrum and so the dicationic dissociation mechanism to form these ion pairs is unambiguous. Therefore, the result of the simulation procedure for a two-body reaction is a single KER and corresponding F_{KERD}. For three-body dissociation reactions, the primary ions formed by charge separation of the dication are not necessarily the ones detected in the coincidence spectrum [Reaction (3.IX)]. Hence, to evaluate the KER for a three-body reaction, *e.g.* forming $C^+ + S^+$ from CS_2^{2+}, the simulation procedure is performed several times, modelling the formation of the detected ion pair *via* all the possible decay mechanisms, both direct and sequential [Reactions (3.X)-(3.XIII)]. For the sequential dissociation mechanism involving an initial charge separation, the formation of the ion pair is modelled *via* all the possible initial charge separations and subsequent singly charged ion dissociation pathways [Reactions (3.XII) & (3.XIII)]. In this process the KER of the monocation dissociation is assumed to be negligible in comparison to the primary KER of the dication dissociation.

Direct: $CS_2^{2+} \rightarrow C^+ + S^+ + S$ *Detected ion pair* (3.X)

Sequential:

$CS_2^{2+} \rightarrow CS^{2+} + S$ *Deferred charge separation*

$\downarrow \quad \downarrow$ (3.XI)

$C^+ + S^+ + S$ *Detected ion pair*

$CS_2^{2+} \rightarrow CS^+ + S^+$ *Initial charge separation*

$\downarrow \quad \downarrow$ (3.XII)

$C^+ + S^+ + S$ *Detected ion pair*

$CS_2^{2+} \rightarrow C^+ + S_2^+$ *Initial charge separation*

$\downarrow \quad \downarrow$ (3.XIII)

$C^+ + S^+ + S$ *Detected ion pair*

The result of the simulation procedure for a three-body reaction is a list of potential values of the KER and F_{KERD} arising from the simulation of all possible dissociation pathways. As mentioned

above, the KER derived from the coincidence peak width depends on the masses of the pair of ions formed by the initial charge-separating reaction. Since the initial ion pairs formed by the sequential and direct mechanisms are different, the values of the KER derived from the coincidence peak widths for the different pathways [Reactions (3.X)-(3.XIII)] are different. For each three-body reaction, which KER value is correct depends upon the pathway by which the dication dissociates to form the relevant ion pair.

3.2.2.2 Calculation of the Dication State Energy

In principle, a KER value, derived from the coincidence peak widths, can be used to calculate the energy of the dication state which dissociates to form the given dissociation reaction. The dication state energy $E(XY_2^{2+})$ is calculated using the following equation,

$$E(XY_2^{2+}) = E_{ASYM} + KER \qquad \text{Eq. 3.13}$$

where E_{ASYM} is the energy of the dissociation asymptote for forming the relevant products in their ground states. E_{ASYM} can be derived from thermodynamic data tables.[24] In the calculation of $E(XY_2^{2+})$, the fragment ions and any neutral products are assumed to be formed with no internal energy. Therefore, any value of $E(XY_2^{2+})$ derived in this way should be considered a lower limit.

Since there is only one possible decay pathway for a two-body dissociation reaction, the unambiguous KER, derived from the coincidence peak widths, is converted into a single value of $E(XY_2^{2+})$. For the three-body reactions, from the list of potential KER values a corresponding list of potential $E(XY_2^{2+})$ values is obtained. For a three-body reaction, the value of $E(XY_2^{2+})$ depends not only on the initial charge-separating dissociation reaction, but also on the form of the neutral products.

In order to derive some mechanistic information from these lists of potential $E(XY_2^{2+})$ values, it is necessary to determine the appearance energy of each dication fragmentation pathway and compare it with the values $E(XY_2^{2+})$ for a given ion pair. Agreement between these values can give an indication of the dicationic decay pathway followed to form the relevant ion pair.

3.2.2.3 Determination of the Appearance Energy

The appearance energy of a given dicationic dissociation reaction can be determined by monitoring the yield of a reaction, with respect to the ion count rate, as a function of electron energy. As the electron energy approaches the double ionization threshold, the yield Y of the decay reaction, determined by the area of the coincidence signal corresponding to the relevant ion pair suitably corrected for the false coincidence background, is proportional to the ionization cross section σ^{2+} for populating the lowest energy state of the dication which decays to form the relevant pair of fragment ions.

$$Y = f_i^2 \, k\sigma^{2+} \qquad \text{Eq. 3.14}$$

where f_i is the ion detection efficiency and k is a proportionality constant. Since the coincidence spectra are recorded at low count rates, the number of coincidence 'starts' S is proportional to the total number of ions arriving at the detector during the acquisition period,

$$S = f_i \, k\sigma^{+} + 2f_i \, k\sigma^{2+} \qquad \text{Eq. 3.15}$$

where σ^+ is the single ionization cross section. Since, for most molecules the single ionization cross section is significantly larger than the multiple ionization cross sections,[5] S is then approximately proportional to σ^+ and hence,

$$\frac{Y}{S} = \frac{f_i^{\,2} k\sigma^{2+}}{f_i k\sigma^{+}} \propto \frac{\sigma^{2+}}{\sigma^{+}} \qquad \text{Eq. 3.16}$$

A plot of *Y/S* against electron energy should fall to zero at the energy of the lowest energy dication state contributing to the relevant dissociation reaction, the appearance energy of the particular ion pair.

Since the calculation of $E(XY_2^{2+})$ and the determination of the appearance energy both give an estimate of the energy of the dication electronic state which dissociates to form a given ion pair (Fig. 3.3), they should be in agreement with one another. Unambiguous agreement between one of the values of $E(XY_2^{2+})$, derived assuming a particular fragmentation pathway, and the appearance energy indicates that the mechanism used to derive the KER, and hence $E(XY_2^{2+})$, is the one actually followed to form the relevant ion pair.

3.2.2.4 Estimate of the Double Ionization Energy

The double ionization energy of a closed-shell atom or molecule can be estimated by the 'rule of thumb'.[25] The empirically predicted value of the double ionization energy E^{2+} is given by,

$$E^{2+} = 2.8E^{+} \qquad \text{Eq. 3.17}$$

where E^+ is the single ionization energy. However, this estimate of the double ionization energy assumes that upon double ionization both electrons are removed from the same molecular orbital. If the two electrons are removed from different orbitals with ionization energies ε_1 and ε_2, where $\varepsilon_1 < \varepsilon_2$, a better approximation of the double ionization energy is given by

$$E^{2+} = \varepsilon_1 + 1.8 \, \varepsilon_2 \qquad \text{Eq. 3.18}$$

An estimate of the double ionization energy of a molecule derived in this way can be compared with a value of $E(XY_2^{2+})$ for a given dissociation reaction. Such a comparison can give an indication of whether or not a particular dissociation reaction occurs from the ground electronic state of the dication.

3.2.3 Conclusion

The above sections describe the data analysis procedures employed to obtain information from the time-of-flight mass spectra and ion-ion coincidence spectra recorded in the one-dimensional experiments.

The methodology for determining the relative partial single ionization cross sections of the ions observed in the time-of-flight mass spectra has been discussed. In addition, this section has indicated that from the interpretation of the coincidence peak widths, the KER upon dicationic dissociation can be obtained. Comparisons of the experimentally determined appearance energies for the dissociation reactions of a given dication with the energetics derived from the KER involved in these dication dissociation processes can give an indication of the mechanisms by which the dication dissociates and the energy of the dication electronic states which are the source of these fragments.

In the following section, the analysis procedures used to extract information from the spectra recorded in the 2D experiments are discussed.

3.3 Two-Dimensional Studies

The modifications made to the TOFMS prior to running the 2D experiments have been described in detail in Chapter 2. These modifications include the pulsing of both the repeller plate and the lens element of the electron gun and the use of a multichannel plate (MCP) detector.

3.3.1 Single Ionization

In the 2D investigations of single ionization, time-of-flight mass spectrometry is again used to investigate the fragmentation of singly charged ions. Fig. 3.7 shows a typical time-of-flight mass spectrum ('singles' spectrum) of CS_2 obtained using the modified 2D experimental arrangement.

The raw data for the analysis of the singles spectra consists of the intensities of the ion signals from the recorded singles spectra. The intensities of the ion signals are determined by finding the area of the peaks and applying a suitable background correction to subtract the contribution of stray ions.

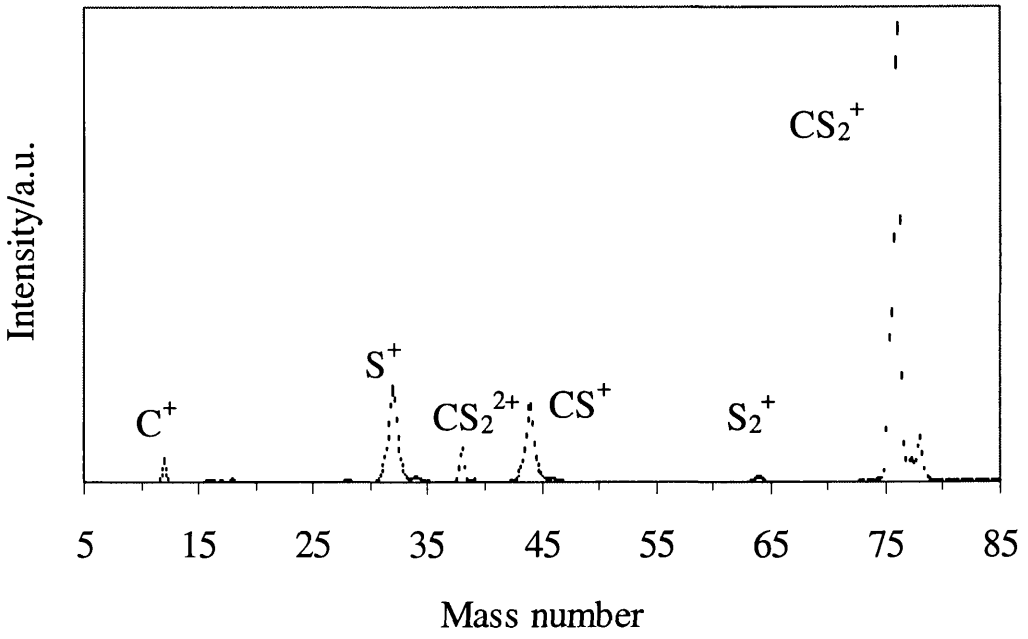

Fig. 3.7 Typical singles spectrum of CS_2 recorded at 250 eV using the 2D apparatus set-up. To aid interpretation, the error bars shown have been scaled to represent twenty standard deviations.

3.3.1.1 Determination of the Relative Partial Single Ionization Cross Section

As discussed in Section 3.2.1.1, the experimental arrangement used in the one-dimensional studies strongly discriminated against the detection of energetic fragment ions, such as those produced by dissociative double ionization. Therefore, the fragment ions observed in the one-dimensional mass spectra are low energy ions arising from the dissociation of singly charged parent ions and the analysis of these mass spectra gives values of σ_r^{si} for the observed ions. However, the modified experimental set-up used in the 2D experiments, using a MCP detector in place of a channeltron, eliminates the discrimination against energetic fragment ions. Indeed, from Eq. 3.5, ions with a translational energy of 12 eV or less perpendicular to the axis of the TOFMS will now hit the detector. The KER upon dicationic dissociation is commonly[4] less than 12 eV and so energetic fragment ions, such as those formed from dissociative double ionization, will be efficiently detected using this 2D apparatus set-up. Therefore, as well as observing the fragment ions with low kinetic energies from single ionization, now highly-energetic fragment ions from both single and double ionization are also detected. As explained in Chapter 2, due to the design of the data acquisition algorithm, and because the ion detection efficiency is not unity, *i.e.* $f_i << 1$, if a singly charged ion formed by dissociative double ionization is detected but its correlated partner is not, then the ion signal is displayed in the singles spectrum. Consequently, there is a contribution from the dissociative double ionization of the relevant molecule to the fragment ion signals in the singles spectrum. The presence of fragment ions formed by dissociative multiple ionization in the singles spectrum results in the determination of values of the relative partial total ionization cross section σ_r^I

from the singles spectra (Eq. 3.19), as opposed to values of relative partial single ionization cross section σ_r^{si} determined from the one-dimensional time-of-flight mass spectra.

In contrast to the analysis procedure used in the one-dimensional experiments, the determination of σ_r^I from the singles spectrum does not need to include a mass correction factor (Eq. 3.4). The pulsing of the electron gun negates the use of the correction factor because there are no longer any density effects in the source region of the TOFMS as there are no ions present during the interpulse period of the electron gun. In addition, the fast extraction of the ions from the source region means that the energetic ions no longer have time to leave the source region before being accelerated towards the detector and so all ions formed should be detected. Thus, the value of σ_r^I is determined from the ion to parent ion signal intensity ratio (Eq. 3.19). For example, for CS_2,

$$\sigma_r^{\ I} = \frac{\sigma_{X^+}}{\sigma_{CS_2^+}} = \frac{I_{X^+}}{I_{CS_2^+}} \qquad \text{Eq. 3.19}$$

Double Ionization Contribution Subtraction

As discussed above, the values of σ_r^I obtained in the 2D experiments cannot be compared with the values of σ_r^{si} derived from the one-dimensional study as the time-of-flight mass spectra recorded in the one-dimensional experiments may contain only a small contribution from double ionization. If the double ionization contribution can be determined and subtracted from the singles spectra, values of σ_r^{si} for the fragment ions can be determined from the 2D experiments and compared with the values of σ_r^{si} obtained in the one-dimensional experiments.

Consider an ion X^+ formed from XY^+. If N^+ is the rate of single ionization of XY to form X^+ and N^{2+} is the rate of double ionization of XY to form $X^+ + Y^+$, the number of X^+ ions observed in the singles spectrum formed from single ionization S_{SI} is

$$S_{SI} = f_i N^+ \qquad \text{Eq. 3.20}$$

and the number of singly charged X^+ ions formed from dissociative double ionization, together with an equal number of Y^+ ions, and detected in the pairs spectrum P_I is

$$P_I = f_i^2 N^{2+} \qquad \text{Eq. 3.21}$$

As discussed above, if a singly charged fragment ion, formed by dissociative double ionization, is detected but its correlated partner is not then the ion signal is recorded in the singles spectrum. Since only one ion of the non-identical pair is detected, the number of singly charged X^+ ions formed by dissociative double ionization contributing to the X^+ signal in the singles spectrum S_{DI} is

$$S_{DI} = f_i(1-f_i)N^{2+} \qquad \text{Eq. 3.22}$$

So, the total number of singly charged X^+ ions observed in the singles spectrum S is given by

$$S = S_{SI} + S_{DI} = f_i N^+ + f_i(1-f_i)N^{2+} \qquad \text{Eq. 3.23}$$

From Eq. 3.21,

$$N^{2+} = \frac{P_I}{f_i^2} \qquad \text{Eq. 3.24}$$

Substituting for N^{2+} in Eq. 3.23 and rearranging the equation,

$$S_{SI} = S - \frac{(1-f_i)}{f_i} P_I \qquad \text{Eq. 3.25}$$

So, S_{SI} can be determined from the singles spectrum. As can be seen from Eq. 3.25, in order to obtain S_{SI} from the singles spectrum it is necessary to determine the values of S, P_I and f_i. As described above, the value of S can be determined by finding the area of the X^+ peak in the singles spectrum and applying a suitable background correction. The method for obtaining P_I involves counting the number of X^+ ions in the pairs spectrum, as described in Section 3.3.2.3. The value of f_i is determined from normalisation experiments with CF_4, a well-characterised molecule. See Section 3.3.3 for further details.

Once the contribution from dissociative double ionization has been subtracted from the ion signal intensities in the singles spectrum and the values of S_{SI} have been determined for each observed ion, the values of σ_r^{si} for the fragment ions, relative to the parent ion, can be determined using Eq. 3.26.

$$\sigma_r^{si} = \frac{S_{SI}(X^+)}{S_{XY_2^+}} \qquad \text{Eq. 3.26}$$

It is not necessary to perform the above subtraction procedure for the parent ion, as there is no double ionization contribution to the parent ion signal in the singles spectrum.

In summary, the analysis of the singles spectra yields values of σ_r^{si} for the observed fragment ions that can be compared with the data derived in the one-dimensional experiments. However, in order to determine values of σ_r^{si} from the above procedure, the pairs spectrum produced from dissociative double ionization must be analysed.

3.3.2 Double Ionization

The list of ion pair flight times recorded in the 2D experiments are used to plot a 2D-coincidence spectrum ('pairs' spectrum) of the intensity of ion pairs as a function of the individual flight times of the two ions $I(t_1,t_2)$, as illustrated in Fig. 2.17.

3.3.2.1 False Coincidence Subtraction

False coincidences arise in the pairs spectrum due to the detection of pairs of ions not formed in the same dication dissociation event, *e.g.* two singly charged ions formed from the dissociation of

two ions formed in the same pulse of electrons. These fragment ion pairs should not show any momentum correlation and the peaks corresponding to these false coincidences will be "round" (Fig. 3.8).[13,15,26] Hence, the false coincidence peaks can be easily identified. However, the contribution of false coincidences to a 'real' peak in the pairs spectrum is more difficult to determine but the false coincidences must be subtracted in order to obtain realistic ion pair signal intensities.

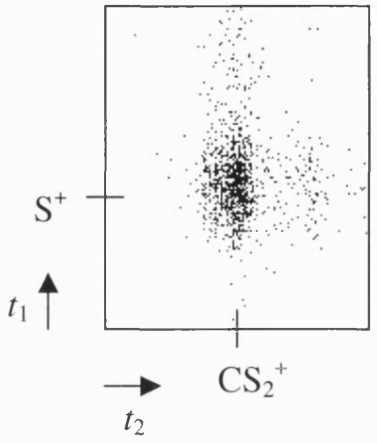

Fig. 3.8 False coincidence peak observed in the pairs spectrum of CS_2^{2+}.

Since false coincidences arise from the detection of singly charged ions not formed in the same dissociation event, the number of false coincidences F_{12} between ions with flight times t_1 and t_2 is defined as follows,

$$F_{12} = f_i^2 N_1^+ N_2^+ \qquad \text{Eq. 3.27}$$

where N_1^+ is the number of ions with a time-of-flight of t_1 and N_2^+ is the number of ions with a time-of-flight of t_2, when $N_n^{2+} << N_n^+$. From Eq. 3.27, it is obvious that one method of reducing false coincidences in the pairs spectrum would be to work at low count rates. The experiments are indeed performed at low pressures but in order to eliminate false coincidences completely, the count rates would have to be infinitely low.[13,26] This experimental constraint would, however, result in infinitely long data acquisition times! A more advanced strategy is to subtract the false coincidences in the pairs spectrum.

As can be see from Eq. 3.27, $F_{12} = \kappa\, S(1)\, S(2)$, where κ is a constant. Since, $S(i)$ is the ion intensity in the singles spectrum which is recorded concurrently with the pairs spectrum, the singles spectrum can be used to estimate and subtract the false coincidences from the pairs spectrum.[13,26] As the singles spectrum is measured concurrently with the pairs spectrum, it is simple to calculate the expected false coincidence spectrum and to normalise it to the measured pairs spectrum in a region where no real ion pair peaks occur.

To perform the false coincidence subtraction, initially a false coincidence array is constructed containing the product of $S(i)\, S(j)$ for the ion intensities in the singles spectrum. From above, the product of S needs to be scaled by κ to give the number of false coincidences present at any co-

ordinate in the pairs spectrum. To obtain this scaling factor, the number of false coincidences present in a given region of the pairs spectrum must be determined and thus the false coincidence array can be normalised to this value. A known false coincidence peak, such as coincidences between a fragment ion and the parent ion (Fig. 3.8), is identified and $S(i)$ $S(j)$ at the t_1t_2 co-ordinate in the pairs spectrum corresponding to the two falsely coincident ions is divided by the number of counts at the t_1t_2 co-ordinate in the pairs spectrum to give κ. Thus the false coincidence array can be scaled by κ and any false coincidences contributing to the real coincidence peaks can be subtracted. After this subtraction, a true pairs spectrum remains.[13]

3.3.2.2 Analysis of Peaks in Pairs Spectrum

Peak Intensity Determination

The intensity of each peak I_{pair} in the pairs spectrum is determined by summing the number of ion pair 'counts' detected within the area of the peak after the false coincidence subtraction procedure. As illustrated in Fig. 3.9, the relevant area of the pairs spectrum is selected and the number of counts contained within the specified region is evaluated.

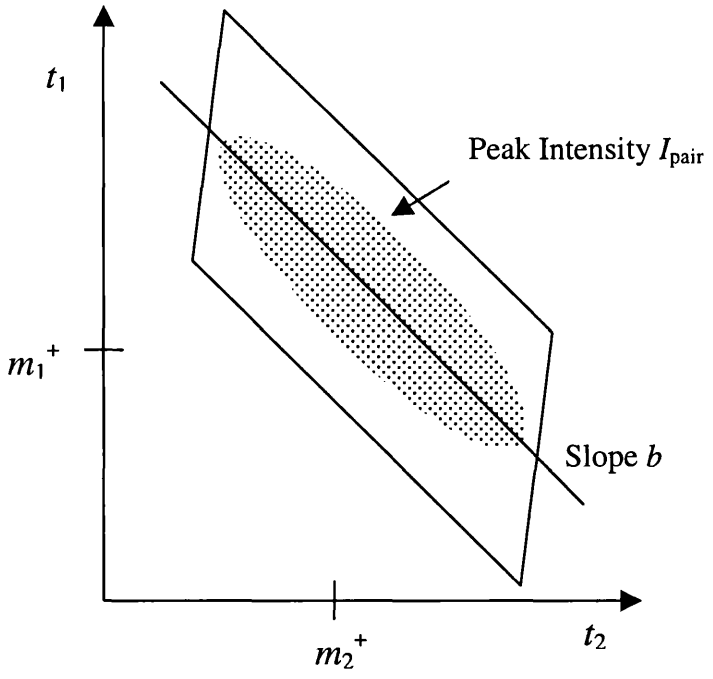

Fig. 3.9 Schematic diagram of a peak in the pairs spectrum illustrating how the intensity and slope of the peak is evaluated.

This summation is carried out by an analysis algorithm written specifically to extract relevant data from pairs spectra. The procedure is trivial for non-identical ion pairs but for identical ion pairs, where the peak is partially obscured by the dead time, the determination of the peak intensity is more complex. The complication arises because in order to evaluate the yield of the whole identical pair

peak it is necessary to determine the area of the peak obscured by the dead time and scale the intensity of the peak accordingly.

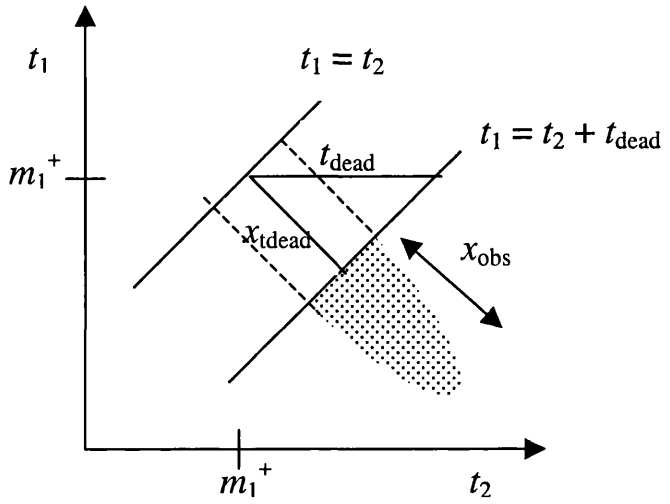

Fig. 3.10 Schematic diagram of the peak corresponding to an identical ion pair centred on the $t_1 = t_2$ diagonal illustrating how the area obscured by the dead time can be evaluated.

As can be seen in Fig. 3.10, since the dead time t_{dead} is known, the length of the portion of the peak obscured by the dead time x_{tdead} can be calculated trigonometrically. The length of the whole peak is $x_{peak} = x_{obs} + x_{tdead}$, where x_{obs} is the length of the peak observed in the pairs spectrum. If the number of counts in the observed area of the peak is I_{obs}, then the total number of counts for the whole peak I_{pair} can be worked out in the following way,

$$I_{pair} = \frac{x_{tdead}}{x_{obs}} I_{obs} + I_{obs} \qquad \text{Eq. 3.28}$$

In the one-dimensional coincidence spectra, the intensity of the coincidence signals can give an indication of the probability of a given dissociation reaction and perhaps even the structure of the dication. Similarly with the pairs spectra, a comparison of the yield of the dissociation reactions of a dication, determined from the number of counts found within the area of the peak, can give an insight into the dissociation mechanisms occurring and their probabilities. Consequently, the relative intensities I_{pair}/I_{total} of each ion pair, relative to the total number of ion pairs observed in the subtracted pairs spectrum, is calculated.

Peak Slope Determination

An informative way of extracting data concerning the fragmentation mechanism involved with a given dissociation reaction is to consider the slope b (Fig. 3.9), and perhaps shape, of the peak.[15,16,26] The slopes of the peaks observed in the pairs spectra are derived from the slope of the linear regression between t_1 and t_2 plotted within the area of a given peak (Fig. 3.9). The slope is determined by the least squares fit method,[27] giving t_1 and t_2 equal weights as they have equal uncertainties. It is essential that no stray individual isolated counts are included in the peak area

when performing the fitting procedure as this would result in a biased value of b. From the values of b obtained for the peaks in the pairs spectra, it is possible to obtain information concerning the dication dissociation mechanisms occurring.

As can be seen from the pairs spectrum of CS_2^{2+} shown in Fig. 2.16, the shapes of the peaks in the pairs spectrum are very different for the two- and three-body dissociation reactions. For the two-body dissociation of CS_2^{2+} forming $CS^+ + S^+$, the peak is orientated diagonally in the spectrum. This is due to the conservation of linear momentum upon dicationic dissociation to form only a pair of singly charged ions [Reaction (3.IV)].[16] If CS_2^{2+} dissociates to form CS^+ and S^+, both ions will have the same initial momentum p in opposite directions,

$$p_1 + p_2 = 0 \qquad \text{Eq. 3.29}$$

From the general expression for the time-of-flight t of an ion under the Wiley-McLaren focusing conditions[10] given in Eq. 2.14, it follows that the flight times of a pair of ions are given by

$$t_1 = t_0 + k\,p\cos\theta \qquad \text{Eq. 3.30}$$

$$t_2 = t_0 - k\,p\cos\theta \qquad \text{Eq. 3.31}$$

Therefore, $t_1 + t_2$ = const., and the peak corresponding to $CS^+ + S^+$ will form a straight line with a slope of –1 in the pairs spectrum.[15,16]

For a three-body dissociation reaction, *e.g.* $C^+ + S^+$ from CS_2^{2+} in Fig. 2.16, the dynamics upon dissociation may be far more complicated. As discussed above, a three-body dissociation reaction can occur *via* a variety of different mechanisms, a direct mechanism or a sequential mechanism involving either a deferred charge separation or an initial two-body charge separation followed by further dissociation to give the detected ion pair and neutrals.[16] If the three-body dissociation of the dication involves a direct mechanism then the dissociation is considered to occur *via* an instantaneous explosion [Reaction (3.VI)], breaking all the bonds simultaneously. Thus the two ions are formed with equal and opposite initial momenta while the neutral fragment receives no impulse and therefore, providing there are no collisions between any of the fragments, as with the two-body mechanism $b = -1$.[15,16] For a deferred charge separation mechanism [Reaction (3.VIII)], the dominant energy release occurs on the second dissociation step, $m_1m_2^{2+} \rightarrow m_1^+ + m_2^+$, which again is comparable to the two-body dissociation and therefore $b = -1$.[15,16]

If the dissociation mechanism is a sequential mechanism involving an initial charge separation [Reaction (3.III)], for the initial charge separation, $m^{2+} \rightarrow m_1^+ + m_2m_3^+$, from the conservation of momentum, $m_1v_1 + m_2m_3v_{23} = 0$ and therefore

$$p_1 = -p_{23} \qquad \text{Eq. 3.32}$$

For the secondary dissociation, $m_2m_3^+ \rightarrow m_2^+ + m_3$,

$$p_2 = m_2v_{23} = \frac{m_2}{(m_2 + m_3)}\,p_{23} \qquad \text{Eq. 3.33}$$

and from Eq. 3.32,

$$p_1 = -\frac{(m_2 + m_3)}{m_2} p_2 \qquad \text{Eq. 3.34}$$

Hence, b = $-(m_2+m_3)/m_2$,[15,16] when the flight time of the heavier ion is plotted on the x-axis. However, this is a limiting case where $m_2m_3^+$ has time to rotate freely and leave the Coulomb field of m_1^+ before the secondary dissociation occurs. If $m_2m_3^+$ dissociates within the Coulomb field of the other fragment ion, m_2^+ will gain increased momentum and therefore b will increase towards –1. Consequently the value of b will lie between -1 and the mass ratio $-(m_2+m_3)/m_2$. This is an indication of a fast dissociation as it occurs before the fragments formed in the initial charge separation have time to leave each other's Coulomb field (~ 1 ps).[15,16]

In PEPIPICO experiments,[16-20,26] further details concerning the dication dissociation mechanisms can be obtained from the peak shapes as for a three-body dissociation reaction the resulting peak shapes are characteristic of directional correlations between the fragments. However, the resolution in a PEPIPICO spectrum is better than in the pairs spectra presented here because the detection of the photoelectron in PEPIPICO as a time zero precisely defines the instant of dissociation. As a result, extremely well-resolved peaks are observed in the PEPIPICO spectrum from which information concerning the dissociation dynamics can be derived. However, in the 2D experiments discussed in this thesis, there is a finite time during which dications can be formed in the electron pulse and hence an inherent uncertainty (~ 10 ns) of when the dissociation event occurred. This is apparent as an increased perpendicular width of the peaks.

Kinetic Energy Release Determination

It is difficult to directly obtain data about the energetics associated with a given dissociation reaction just by looking at the peaks in the pairs spectrum.[16] In order to extract information about the KER upon dicationic dissociation to form a particular ion pair it is convenient to convert the pairs peak into an ion-ion coincidence peak.

To transform a pairs spectrum into an ion-ion coincidence spectrum, the time-of-flight difference Δt_{tof} between the two ions of a pair is determined for all the pairs recorded,

$$\Delta t_{tof} = t_2 - t_1 \qquad \text{Eq. 3.35}$$

As with the one-dimensional ion-ion coincidence spectrum, a plot of Δt_{tof} against intensity is constructed, with the number of ion pairs in each channel being a measure of the number of ion pairs with that particular Δt_{tof}.

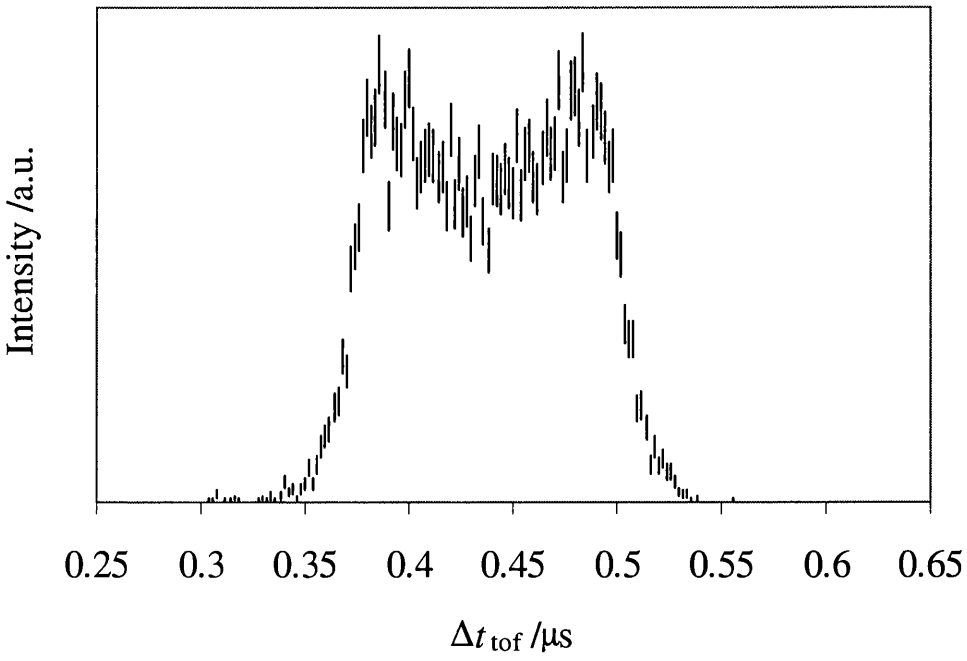

Fig. 3.11 Ion-ion coincidence peak of the $CS^+ + S^+$ ion pair from CS_2^{2+} transformed from the pairs spectrum. The error bars shown are derived from the counting statistics and represent two standard deviations.

A Monte Carlo simulation of this coincidence peak can be performed using the same procedure described in Section 3.2.2.1, in order to obtain values of the KER and F_{KERD} for the given dissociation reaction for comparison with the values of these parameters obtained from the one-dimensional coincidence spectra.

For the peak corresponding to $CS^+ + S^+$ shown in Fig. 3.11, a value of the KER as 4.4 ± 0.2 eV is determined, a value which is in good agreement both with the literature[4] and the one-dimensional study of CS_2^{2+}.

3.3.2.3 The Contribution of Double Ionization to the Singles Spectrum

As discussed in Section 3.3.1.1, there is undoubtedly a contribution from dissociative double ionization to the ion signals in the singles spectra. Therefore, this double ionization contribution must be subtracted in order to obtain values of σ_r^{si} from the singles spectra. To accomplish this, the pairs spectrum must be transformed into a conventional time-of-flight mass spectrum which will only contain signals corresponding to fragment ions formed from dissociative multiple ionization. The intensities of these double ionization ion signals P_I can then be extracted from the spectrum and used to subtract the double ionization contribution from the ion signal intensities in the singles spectrum S to give the S_{SI} (Eq. 3.25).

A mass spectrum of the fragment ions formed from dissociative double ionization is obtained by transforming the data set consisting of pairs of ion times, used to plot the pairs spectrum, and plotting all these flight times as a simple mass spectrum. Fig. 3.12 shows a double ionization mass

spectrum obtained after converting the pairs spectrum of CS_2^{2+}. Note that the widths of the peaks in this double ionization mass spectrum are larger than in the singles spectrum (Fig. 3.7). This broadening of the peaks is due to the considerable velocity of the ions that are formed from double ionization. As can be seen in Fig. 3.12, there is a small signal corresponding to the parent ion CS_2^+ observed in the double ionization mass spectrum. The presence of the parent ion signal in Fig. 3.12 is a result of the imperfect subtraction of the false coincidences from the pairs spectrum.

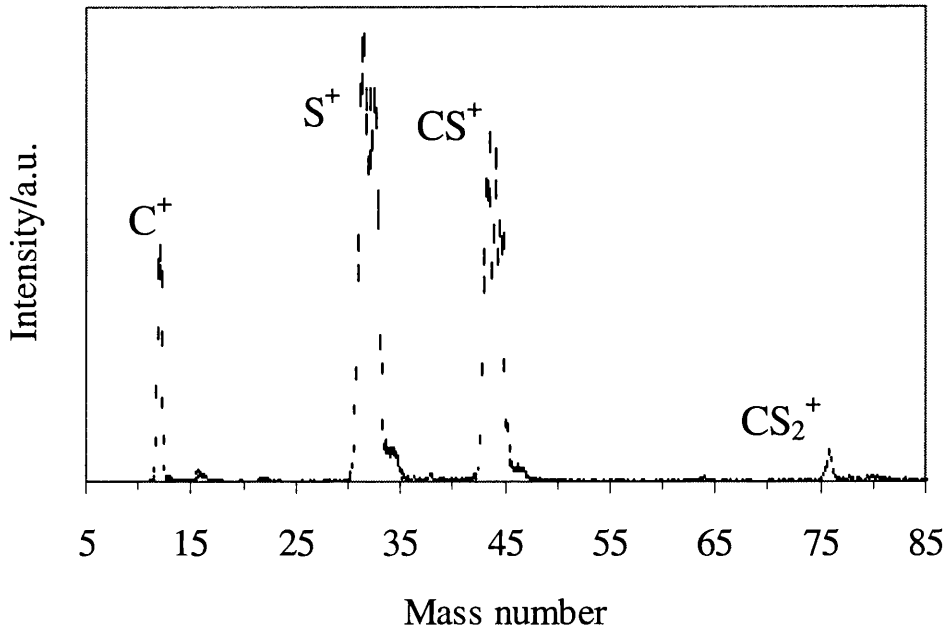

Fig. 3.12 Double ionization mass spectrum of CS_2, converted from the correlated pairs spectrum recorded at 250 eV. The error bars shown are derived from the counting statistics and represent two standard deviations.

The values of P_I are obtained from the double ionization mass spectrum by finding the areas of the peaks and applying a suitable background correction. The values of P_I can then be placed in Eq. 3.25 and the values of S_{SI} calculated for each ion observed in the singles spectrum.

3.3.2.4 Determination of the Ratio of Double-to-Single Ionization Cross Sections

From the analysis of the singles and pairs spectra of a given molecule recorded concurrently, the ion signal intensities of the singly charged ions and the intensities of the ion pairs formed from dissociative double ionization are both known. Using this data it is possible to obtain an estimate of the double-to-single ionization cross section ratio σ^{2+}/σ^+ for the respective molecule, where σ^+ is the total single ionization cross section and σ^{2+} is the total double ionization cross section.

The number of ion pairs formed from dissociative double ionization is P_P, where

$$P_P = f_i^2 \, k\sigma^{2+} \qquad \text{Eq. 3.36}$$

k is a constant of proportionality, and the value of P_P is determined from the total ion pair intensity in the pairs spectrum. The total number of singly charged ions observed in the singles spectrum is S_T, where

$$S_T = f_i\, k\sigma^+ + 2f_i(1\text{-}f_i)\, k\sigma^{2+} \qquad \text{Eq. 3.37}$$

and S_T is the sum of the ion signal intensities in the singles spectrum. The second term in Eq. 3.37 is the number of singly charged ions formed from dissociative double ionization contributing to the singles spectrum. Since the total number of singly charged ions in the singles spectrum is now being evaluated this second term contains a factor of 2 (Eq. 3.37) to take into account the possibility of detecting either ion of the pair. Combining the two expressions given in Eq. 3.36 & Eq. 3.37,

$$\frac{S_T}{P_P} = \frac{f_i k\sigma^+}{f_i^{\,2} k\sigma^{2+}} + \frac{2f_i(1-f_i)k\sigma^{2+}}{f_i^{\,2} k\sigma^{2+}} \qquad \text{Eq. 3.38}$$

Therefore,

$$\frac{\sigma^+}{\sigma^{2+}} = f_i\left(\frac{S_T}{P_P} - \frac{2(1-f_i)}{f_i}\right) \qquad \text{Eq. 3.39}$$

and taking the reciprocal of the value obtained from Eq. 3.39, the ratio of total σ^{2+}/σ^+ is determined. As mentioned above, the values of S_T and P_P are determined from the ion signal intensities in the singles and pairs spectra respectively. In addition, in order to solve Eq. 3.39, an estimate of f_i is required. The value of f_i is determined from the analysis of the singles and pairs spectra of CF_4, as discussed in the following section.

3.3.3 Determination of the Ion Detection Efficiency

As mentioned above, it is necessary to have an estimate of the ion detection efficiency f_i in order to determine S_{SI} from the singles spectrum (Eq. 3.25) and the ratio of σ^{2+}/σ^+ (Eq. 3.39). An estimate of f_i must be made since $f_i << 1$ because of the inherent dead time of the electronics and the 90 % transmission of the grids and MCP. Typical values of f_i obtained for experiments using similar apparatus set-ups are f_i ~ 10-20 %.[4] For ion-electron coincidence experiments, it is possible to directly measure the value of f_i.[26] If an atomic gas is ionized at a wavelength where only single ionization is possible the observed count rate of ion-electron coincidences C_{ie} will be

$$C_{ie} = N^+ f_e(E) f_i(m) \qquad \text{Eq. 3.40}$$

where f_e is the electron detection efficiency, N^+ is the rate of single ionization events and the ion collection efficiencies are expressed as functions of the electron energy and the ion mass respectively. The electron count rate R_e will be

$$R_e = N^+ f_e(E) \qquad \text{Eq. 3.41}$$

Thus,

$$f_i = \frac{C_{ie}}{R_e} \qquad \text{Eq. 3.42}$$

However, for ion-ion coincidence spectra, this absolute method of deriving f_i is inapplicable, as electrons are not detected. Therefore, in order to derive a value of f_i for ion-ion coincidence spectra, it is necessary to perform normalisation experiments with a well-characterised molecule. In particular, a molecule for which the ratio of σ^{2+}/σ^{+} is known.

From P_P and S_T derived in Eq. 3.36 & Eq. 3.37 above,

$$\frac{P_P}{S_T} = \frac{f_i^{\,2} k\sigma^{2+}}{f_i k\sigma^{+} + 2(1-f_i) f_i k\sigma^{2+}} \qquad \text{Eq. 3.43}$$

So, in order to solve Eq. 3.43 for f_i, the values of σ^{2+} and σ^{+} for a given target gas must be extracted from the literature and the values of P_P and S_T determined from the pairs and singles spectrum respectively.

Such normalisation experiments were performed using CF_4, as the electron impact partial single ionization cross sections and the absolute positive ion pair production cross sections for the ion pairs produced upon dissociation of CF_4^{2+} are reported in the literature.[28]

Singles and pairs spectra of CF_4 were recorded concurrently at an electron energy of 250 eV. The following ions were observed in the singles spectrum of CF_4; C^+, F^+, CF_2^{2+}, CF^+, CF_3^{2+}, CF_2^+ and CF_3^+.

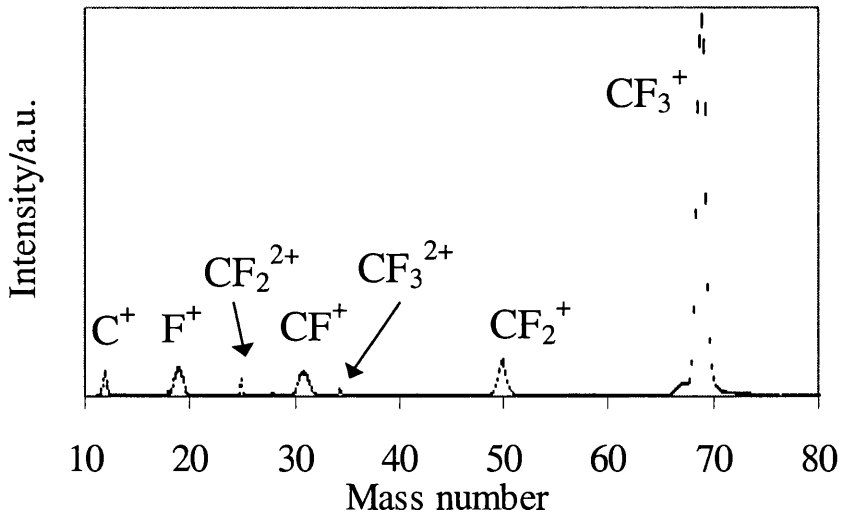

Fig. 3.13 Singles spectrum of CF_4 recorded at 250 eV. To aid interpretation, the error bars shown have been scaled to represent twenty standard deviations.

The ion signal intensities of the singly charged ions $S(X^+)$ were determined from the singles spectrum by finding the area of the relevant peak and applying a suitable background correction. The total number of singly charged ions in the singles spectrum S_T can be evaluated,

$$S_T = \sum S(X^+) \qquad \text{Eq. 3.44}$$

The pairs spectrum of CF_4 contained the signals corresponding to the following dissociation reactions of CF_4^{2+}; $C^+ + F^+$, $F^+ + F^+$, $CF^+ + F^+$, $CF_2^+ + F^+$, $CF_3^+ + F^+$, $CF^+ + F_2^+$ and $CF_2^+ + F_2^+$.

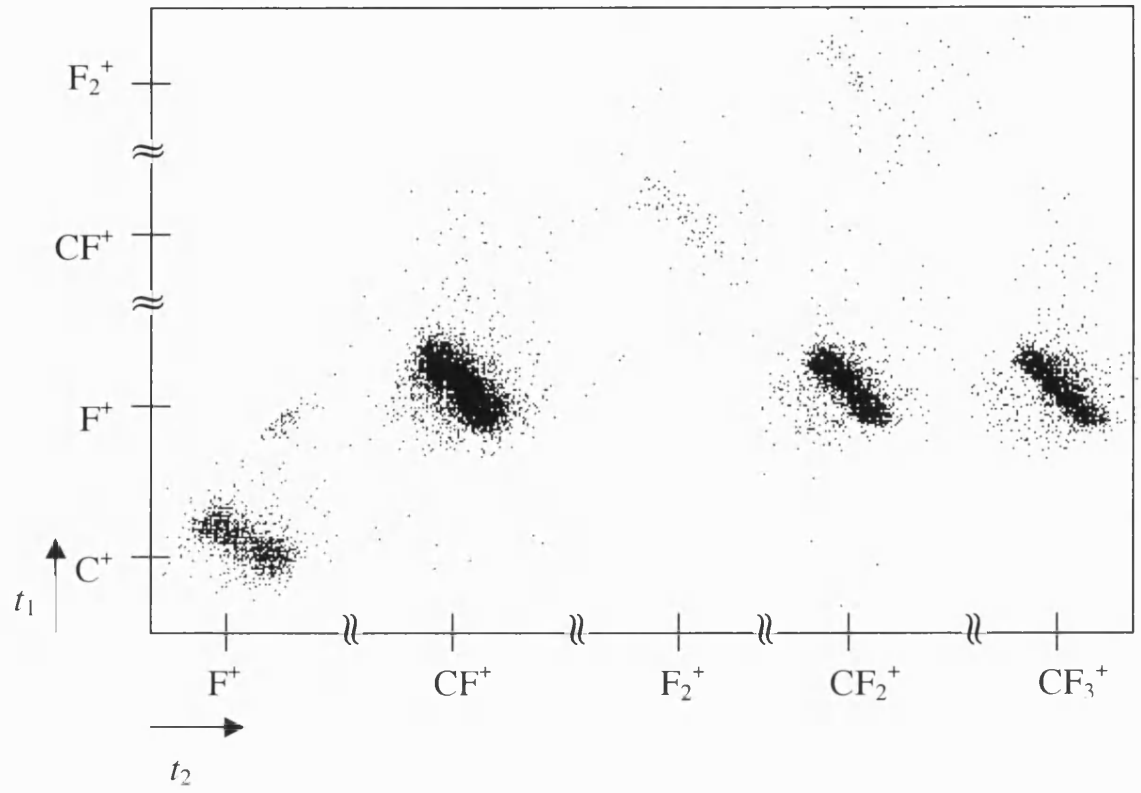

Fig. 3.14 Pairs spectrum of CF_4 recorded at 250 eV.

Similarly the ion pair signal intensities in the pairs spectrum were determined by summing the number of ion pair counts detected within the area of the peak, as described in Section 3.3.2.2. The ion pair intensities were then summed to give the total number of ion pairs observed in pairs spectrum P_P. However, only the ion pair intensities of $C^+ + F^+$, $CF^+ + F^+$, $CF_2^+ + F^+$ and $CF_3^+ + F^+$ were included in the summation as the remaining ion pairs had not been observed in the previous study of CF_4^{2+} and their absolute positive ion pair cross sections had therefore not been determined.[28] The omitted dissociation reactions of CF_4^{2+} are however significantly weaker than the pairs coincident with the F^+ ion (Fig. 3.14) and therefore the omission of these minority dissociation reactions does not have a significant impact on the calculated value of f_i.

The literature values of total σ^{2+} and σ^+ were determined by summing the absolute positive ion pair production cross sections and the corrected electron impact partial ionization cross sections for all the ion pairs and fragment ions respectively, giving $\sigma^{2+} = 0.266$ Å^2 and $\sigma^+ = 3.719$ Å^2.[28] Thus the values of σ^{2+}, σ^+, P_P and S_T can be entered into Eq. 3.43 and a value of $f_i = 0.063 \pm 0.014$ is obtained.

3.3.4 Conclusion

This section of the chapter discusses the data analysis methods used to obtain information from the singles and pairs spectra recorded in the 2D experiments. It explains how, from the singles spectra, values of σ_r^{si} for the observed fragment ions are determined and from the analysis of the pairs spectra information concerning the dication dissociation mechanisms can be gained. In addition, from the analysis of both the singles and pairs spectrum, an estimate of the ratio of total σ^{2+}/σ^{+} can be obtained.

3.4 Overall Conclusions

This chapter introduces the data analysis procedures implemented for interpretation of the time-of-flight mass spectra and coincidence spectra recorded in the one and two-dimensional experiments. In the single ionization experiments, time-of-flight mass spectrometry is used to determine the relative partial single ionization cross sections of reactive molecules over a range of electron energies from near threshold to 500 eV.

Coincidence techniques are used to investigate the formation and fragmentation of molecular dications. As has been described in this chapter, comparisons of experimentally determined appearance energies for dication dissociation reactions with the energetics derived from the kinetic energy release involved in these dication dissociation processes can give an indication of the mechanisms involved in dissociative double ionization and the energy of the dication electronic states which are the source of the fragment ions. In addition, analysis of the ion pair intensities and peak slopes in the pairs spectra can also be interpreted to yield information concerning dication dissociation dynamics. As will be demonstrated in the results chapters, the analysis procedures described in this chapter can be applied to the results obtained from the investigation into the dications of reactive molecules to reveal details of their dissociation processes.

As indicated in this chapter, the analysis procedures employed yield accurate data on the relative partial single ionization cross sections of CS_2 and the energetics and dissociation mechanisms of CS_2^{2+}.

References

1 K.A. Newson, S.M. Luc, S.D. Price and N.J. Mason, *Int. J. Mass Spectrom. Ion Proc.,* **148** (1995) 203

2 M.R. Bruce and R.A. Bonham, *Z. Phys. D,* **24** (1992) 149

3 R. Locht, G. Hagenow, K. Hottmann and H. Baumgärtel, *Chem. Phys.,* **151** (1991) 137

4 D.M. Curtis and J.H.D. Eland, *Int. J. Mass Spectrom. Ion Proc.,* **63** (1985) 241

5 T.D. Märk, in T.D. Märk, G.H. Dunn (Eds.), Electron Impact Ionization, Springer-Verlag, New York, 1985

6 G. Dujardin, S. Leach, O. Dutuit, P.M. Guyon and M. Richardviard, *Chem. Phys.,* **88** (1984) 339

7 T. Masuoka, *Phys. Rev. A,* **48** (1993) 1955

8 K.E. McCulloh, T.E. Sharp and H.M. Rosenstock, *J. Chem. Phys.,* **42** (1965) 3501

9 K.A. Newson and S.D. Price, *Int. J. Mass Spectrom. Ion Proc.,* **153** (1996) 151

10 W.C. Wiley and I.H. McLaren, *Rev. Sci. Instrum.,* **26** (1955) 1150

11 S. Leach, J.H.D. Eland and S.D. Price, *J. Phys. Chem.,* **93** (1989) 7575

12 P.G. Fournier, J.H.D. Eland, P. Millie, S. Svensson, S.D. Price, J. Fournier, G. Comtet, B. Wannberg, L. Karlsson, P. Baltzer, A. Kaddouri and U. Gelius, *J. Chem. Phys.,* **89** (1988) 3553

13 L.J. Frasinski, M. Stankiewicz, P.A. Hatherly and K. Codling, *Meas. Sci. Tech.,* **3** (1992) 1188

14 Philips, Electron Multipliers, 1991

15 M. Lange, O. Pfaff, U. Müller and R. Brenn, *Chem. Phys.,* **230** (1998) 117

16 J.H.D. Eland, *Mol. Phys.,* **61** (1987) 725

17 J.H.D. Eland, *Chem. Phys. Lett.,* **203** (1993) 353

18 S. Hsieh and J.H.D. Eland, *J. Chem. Phys.,* **103** (1995) 1006

19 I. Nenner and J.H.D. Eland, *Z. Phys. D,* **25** (1992) 47

20 S. Hsieh and J.H.D. Eland, *Int. J. Mass Spectrom. Ion Proc.,* **167/168** (1997) 415

21 M. Simon, P. Morin, P. Lablanquie, M. Lavollee, K. Ueda and N. Kosugi, *Chem. Phys. Lett.,* **238** (1995) 42

22 K. Codling, L.J. Frasinski, P.A. Hatherly, M. Stankiewicz and F.P. Larkins, *J. Phys. B,* **24** (1991) 951

23 P.J. Richardson, J.H.D. Eland and P. Lablanquie, *Org. Mass Spec.,* **21** (1986) 289

24 S.G. Lias, J.E. Bartmess, J.F. Liebman, J.L. Holmes, R.D. Levin and W.G. Mallard, *J. Phys. Chem. Ref. Data,* **17 S1** (1988) 1

25 B.P. Tsai and J.H.D. Eland, *Int. J. Mass Spectrom. Ion Proc.,* **36** (1980) 143

26 J.H.D. Eland, in C.Y. Ng (Ed.), Vacuum Ultraviolet Photoionization and Photodissociation of Molecules and Clusters, World Scientific, Singapore, 1991

27 D. York, *Can. J. Phys.*, **44** (1966) 1079

28 M.R. Bruce, C. Ma and R.A. Bonham, *Chem. Phys. Lett.*, **190** (1992) 285

4. Single and Double Ionization of N_2O_5

4.1 Introduction

Dinitrogen pentoxide, N_2O_5, plays an important role in the complex chemistry of the ozone cycle in the Earth's upper atmosphere.[1] It is a reservoir molecule for the nitrogen oxides, NO_x,

$$N_2O_5 \leftrightarrow NO_2 + NO_3 \tag{4.I}$$

which are involved in the generation and destruction of ozone,

$$\begin{aligned} NO + O_3 &\rightarrow O_2 + NO_2 \\ NO_2 + O &\rightarrow O_2 + NO \\ \hline O_3 + O &\rightarrow 2O_2 \qquad \text{Net Reaction} \end{aligned} \tag{4.II}$$

as well as other significant atmospheric effects including the formation of nitric acid

$$N_2O_5 + H_2O \rightarrow 2HNO_3 \tag{4.III}$$

and the creation of organic nitrate compounds.[1] Despite the current interest in the properties[2-7] of N_2O_5 and its role in the stratosphere, there have been only two investigations of the single ionization of N_2O_5,[8,9] and no studies of the formation and fragmentation of $N_2O_5^{2+}$.

As part of a series of investigations of the ionization of reactive species presented in this thesis, this chapter presents a one-dimensional investigation of the single and double ionization of N_2O_5.[10,11] In the single ionization studies, time-of-flight mass spectrometry is used to determine the relative partial single ionization cross sections of N_2O_5 over a range of electron energies. Coincidence techniques are used to investigate the formation and fragmentation of $N_2O_5^{2+}$. Information obtained from the coincidence spectra can give an indication of the mechanisms by which $N_2O_5^{2+}$ dissociates and the energy of the electronic states of $N_2O_5^{2+}$ which are the source of the detected pairs of ions. These investigations also provide a first estimate for the double ionization energy of N_2O_5.

4.2 Experimental Details

In contrast to the investigations of the other reactive molecules reported in this thesis, only a one-dimensional investigation of the single and double ionization of N_2O_5 has been performed. This was due to the unavailability of the loaned apparatus required to synthesise N_2O_5 after the modification of the apparatus to allow the collection of 2D coincidence spectra. However, it is hoped that a 2D investigation of N_2O_5 will be possible in the near future.

The experimental techniques employed in the one-dimensional study of the single and double ionization of N_2O_5 have been described in detail in Chapter 2.

4.2.1 Synthesis of N_2O_5

The sample of N_2O_5 used for these experiments was generated by the reaction of ozone and nitric oxide in which oxidation of the NO to NO_2 is followed by further oxidation to N_2O_5.[4] Streams of the NO and O_3 were merged in a glass manifold (Fig. 4.1) and the resulting N_2O_5, potentially contaminated with NO_2, was condensed in a cold trap (196 K). The flow rates of the gases were carefully adjusted so there was no trace of NO_2 reaching this trap.

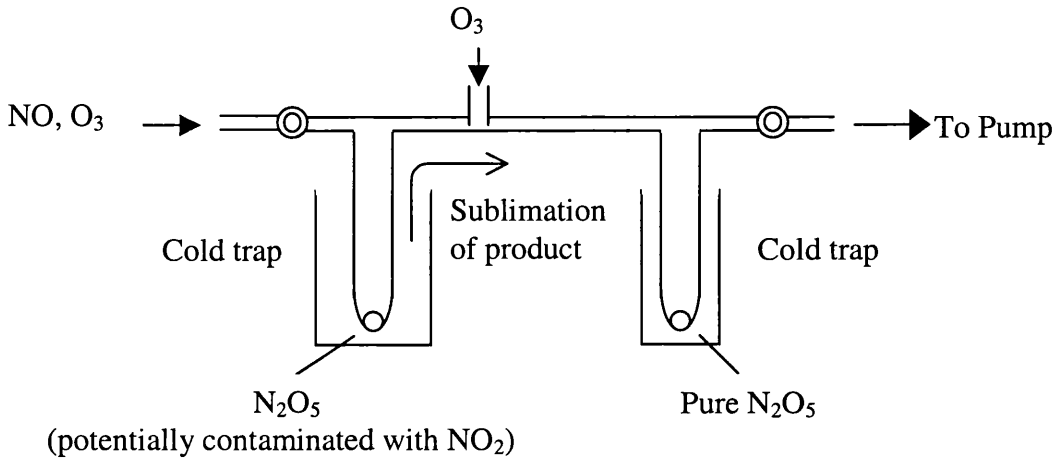

Fig. 4.1 Apparatus used for the synthesis of N_2O_5.

When sufficient solid N_2O_5 had collected in the trap, the NO stream was turned off and the condensed products were sublimed in a stream of ozone into further traps (196 K) until any condensed NO_2 is reacted away. The formation of N_2O_5 as opposed to N_2O_4 was verified by the melting temperature (303 K) and the form of the crystals obtained, as N_2O_5 forms white needle-like crystals.[12]

During the experiments the solid N_2O_5 sample was kept in an acetonitrile slush bath, at a temperature[13] of approximately 230 K and the amount of gaseous N_2O_5 flowing into the TOFMS was controlled by slight variations in the temperature of the slush bath. Due to the reactive nature of N_2O_5, both the purity and the degradation of the sample present problems. Therefore careful synthesis of N_2O_5, *via* an unbranched mechanistic pathway, is carried out and the gaseous sample is transported to the ionization region of the TOFMS *via* the glass/Teflon inlet system (Chapter 2) to avoid any sample degradation.

4.2.2 Procedures

For the study of the single ionization of N_2O_5, time-of-flight mass spectra were recorded at incident electron energies of 35-500 eV in order to determine the relative partial single ionization cross sections σ_r^{si} of the ions produced by the single ionization of N_2O_5. In order to determine the appearance energy of a previously unobserved fragmentation of $N_2O_5^+$ to form N^+, the values of σ_r^{si} for the formation of N^+ were evaluated at electron energies from 27 to 55 eV.

Coincidence spectra were recorded at an ionizing electron energy of 150 eV to investigate the formation and fragmentation of $N_2O_5^{2+}$. Coincidence spectra were also recorded at a range of lower electron energies, from 25 to 65 eV, in order to determine the appearance energies of the pairs of fragment ions produced by the dissociative double ionization of N_2O_5.

4.3 One-Dimensional Studies

4.3.1 Data Analysis

4.3.1.1 Single Ionization

A typical mass spectrum recorded for N_2O_5 is shown in Fig. 4.2. As can be seen from this figure, only the fragment ions N^+, O^+, NO^+ and NO_2^+ are detected and, as in the two previous studies of the ionization of N_2O_5,[8,9] no stable parent ions ($N_2O_5^+$) are observed.

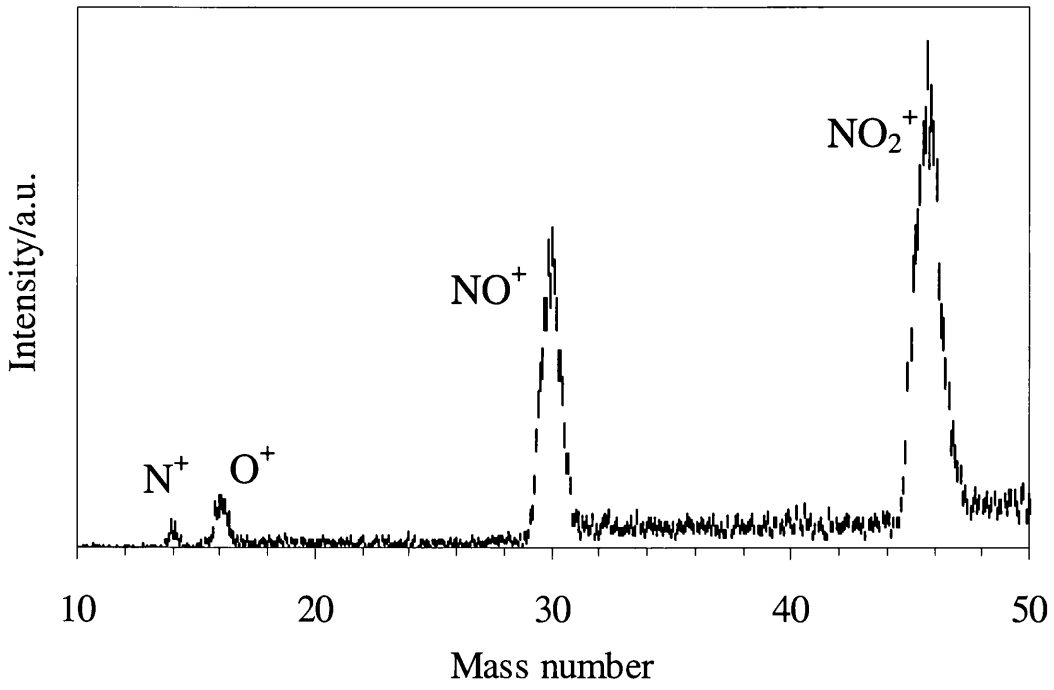

Fig. 4.2 A typical time-of-flight mass spectrum of N_2O_5. The error bars shown are derived from the counting statistics and represent two standard deviations.

The fragment ion signal intensities are obtained from the raw ion signals in the mass spectrum recorded at a range of electron energies from 30 to 500 eV. The relative partial single ionization cross sections σ_r^{si} of the ions observed in the N_2O_5 spectrum, relative to the most abundant ion NO_2^+, are determined from the ion signal intensities as described in Chapter 3, using the appropriate mass correction factor (Eq. 3.4).

Table 4.1 Values of σ_r^{si} for the formation of the indicated product ion from N_2O_5, relative to NO_2^+ (the number in parentheses gives the standard deviation in the last figure of each cross section).

Electron	σ_r^{si}		
energy/eV	N^+	O^+	NO^+
35	0.0036(8)	0.0424(37)	0.536(14)
45	0.0079(10)	0.0603(32)	0.624(15)
55	0.0120(13)	0.0793(13)	0.666(10)
65	0.0168(14)	0.0935(16)	0.702(11)
75	0.0213(15)	0.1049(23)	0.732(56)
86	0.0265(20)	0.1162(63)	0.740(16)
134	0.0394(29)	0.1375(90)	0.758(21)
187	0.0400(67)	0.134(11)	0.727(28)
239	0.0413(31)	0.1335(72)	0.741(18)
285	0.0388(26)	0.1232(54)	0.716(26)
341	0.0350(20)	0.1183(60)	0.696(12)
389	0.0339(21)	0.1139(50)	0.689(16)
444	0.0319(13)	0.1100(51)	0.684(18)

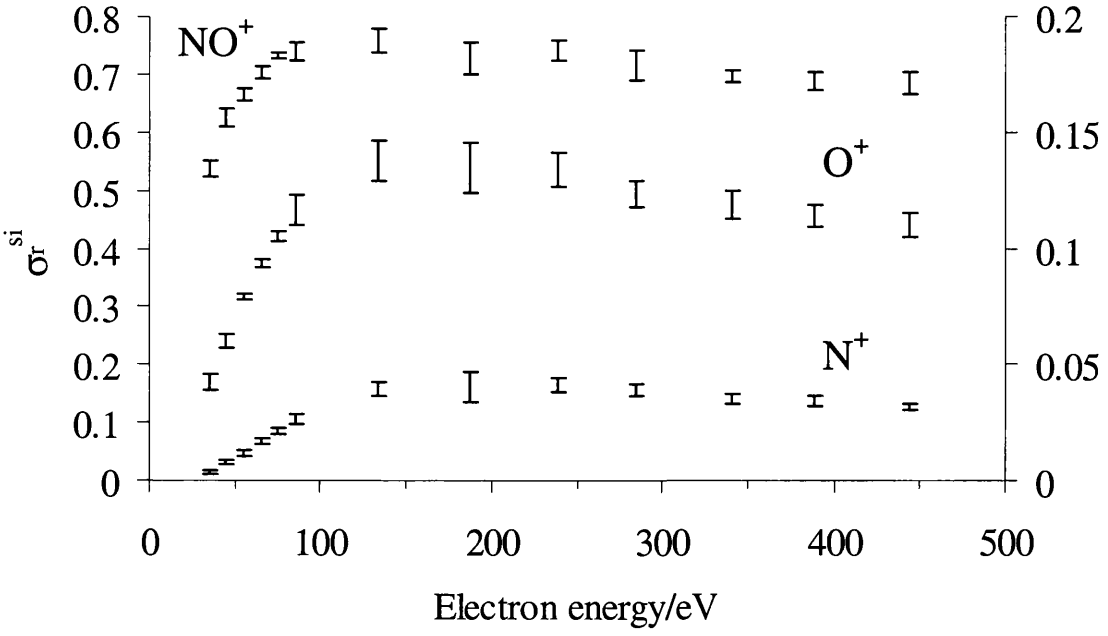

Fig. 4.3 Values of σ_r^{si} for forming NO^+, O^+ and N^+ from N_2O_5. The values for O^+ and N^+ should be read from the right hand axis. The error bars on the values represent two standard deviations.

The values of σ_r^{si} obtained for N_2O_5, shown in Fig. 4.3 and listed in Table 4.1, are the average of seven independent determinations. The standard deviations of these determinations at each electron energy are also shown in Table 4.1 and plotted as the error bars in Fig. 4.3. The standard deviations are small in accord with the statistical (counting) error in each individual determination. The standard deviations in the values of σ_r^{si} do not, however, take into account any systematic errors present in the experiment due to, for example, any unresolved mass dependent detection efficiencies. But, owing to the efforts described in Chapter 2 to resolve any such problems, *i.e.* the application of the bias voltage and the use of the correction factor in the calculation of σ_r^{si}, and the good agreement between literature values and previous values of σ_r^{si} determined using this experimental arrangement,[14] the standard deviations quoted are considered to be a good estimate of the error in the reported values of σ_r^{si} (Table 4.1).

In the two previous investigations of the ionization of N_2O_5 reported in the literature,[8,9] no N^+ fragments were detected. The observation of N^+ fragments in this study (Fig. 4.2) is undoubtedly due to the higher electron energies employed. The values of σ_r^{si} for the formation of N^+ were carefully evaluated at electron energies from 27 to 65 eV to determine the appearance energy of this fragment. Fig. 4.4 shows a weighted least squares fit[15] applied to the values of σ_r^{si}, each the average of four independent determinations, above and below the appearance energy.

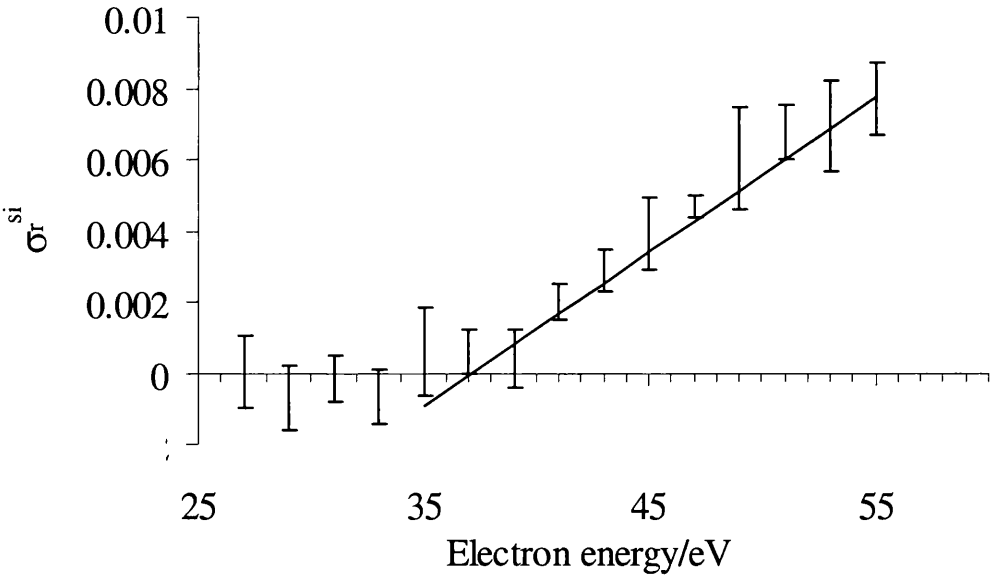

Fig. 4.4 A weighted least squares fit applied to the values of σ_r^{si} for forming N^+ from N_2O_5 at low ionizing electron energies. The error bars shown represent two standard deviations.

The variation of σ_r^{si} above the appearance energy appears to be well modelled, within the error limits, by a linear function in terms of the excess electron energy. Such an approximately linear function in terms of the excess electron energy would be predicted if the absolute cross section for forming N^+ was dominated by the Wannier Law[16] over this energy regime whilst the absolute cross

section for forming NO_2^+ remained approximately constant.[17] As discussed in Chapter 1, the threshold Wannier Law[16] gives the dependence of the electron-impact single ionization cross section on the amount of energy, above the ionization energy, possessed by the system.

As illustrated in Fig. 4.4, the appearance energy for the N^+ fragment is found to be 36 ± 2 eV. The appearance energies for the NO_2^+, NO^+ and O^+ fragments have been previously determined at better energy resolution than can be achieved using the current apparatus and were not redetermined in this study.[8]

4.3.1.2 Double Ionization

A typical ion-ion coincidence spectrum of $N_2O_5^{2+}$ recorded at 150 eV is shown in Fig. 4.5.

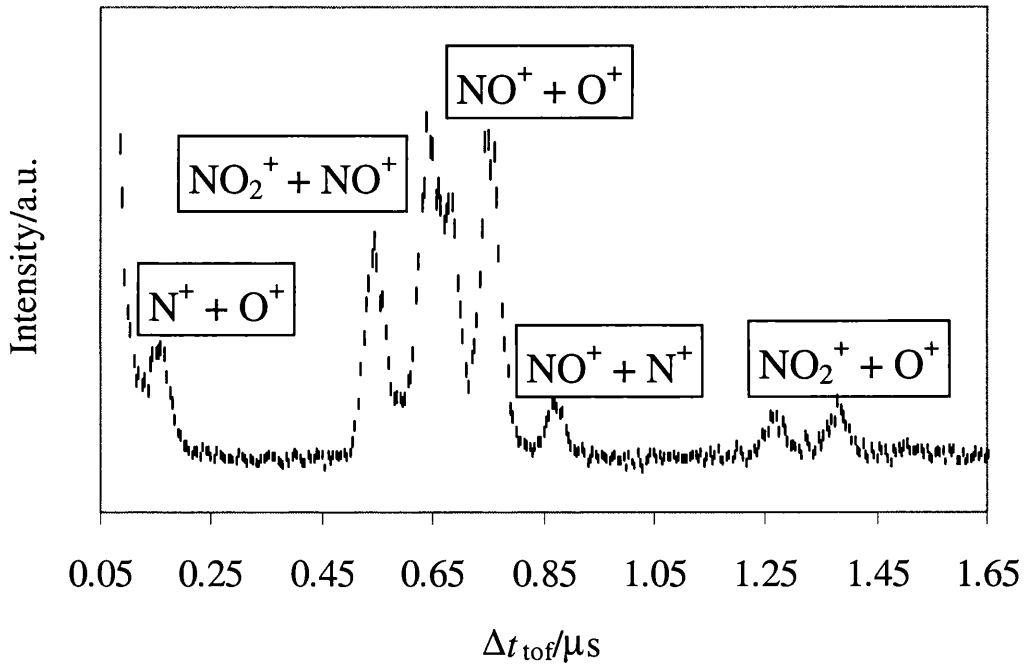

Fig. 4.5 Ion-ion coincidence spectrum of $N_2O_5^{2+}$ generated by electron impact at 150 eV. The error bars shown are derived from the counting statistics and represent two standard deviations.

The dissociation reactions observed are

$$N_2O_5^{2+} \rightarrow N^+ + O^+ [+ N + 4O] \quad (4.IV)$$

$$N_2O_5^{2+} \rightarrow NO_2^+ + NO^+ [+ 2O] \quad (4.V)$$

$$N_2O_5^{2+} \rightarrow NO^+ + O^+ [+ N + 3O] \quad (4.VI)$$

$$N_2O_5^{2+} \rightarrow NO^+ + N^+ [+ 4O] \quad (4.VII)$$

$$N_2O_5^{2+} \rightarrow NO_2^+ + O^+ [+ N + 2O] \quad (4.VIII)$$

where the neutrals are listed in parentheses as they are not detected, but, as described below, they are most likely to be completely fragmented. As can be seen in Fig. 4.5, half of the coincidence signal due to the formation of the $N^+ + O^+$ ion pair is masked by the 'ringing' present when Δt_{tof} is small

(Chapter 2). Any coincidence signals produced at $\Delta t_{tof} = 0$, corresponding to the fragmentation of $N_2O_5^{2+}$ to form identical ions, for example,

$$N_2O_5^{2+} \rightarrow NO^+ + NO^+ [+ 3O] \qquad (4.IX)$$

cannot be efficiently detected because of the 'ringing' and therefore were not investigated further.

Kinetic Energy Release Determination

The kinetic energy release (KER) and half-width of the kinetic energy release distribution (F_{KERD}) associated with the formation of the ion pairs observed in the coincidence spectrum of $N_2O_5^{2+}$ have been determined by performing a Monte Carlo simulation of the experimental data (Chapter 3).

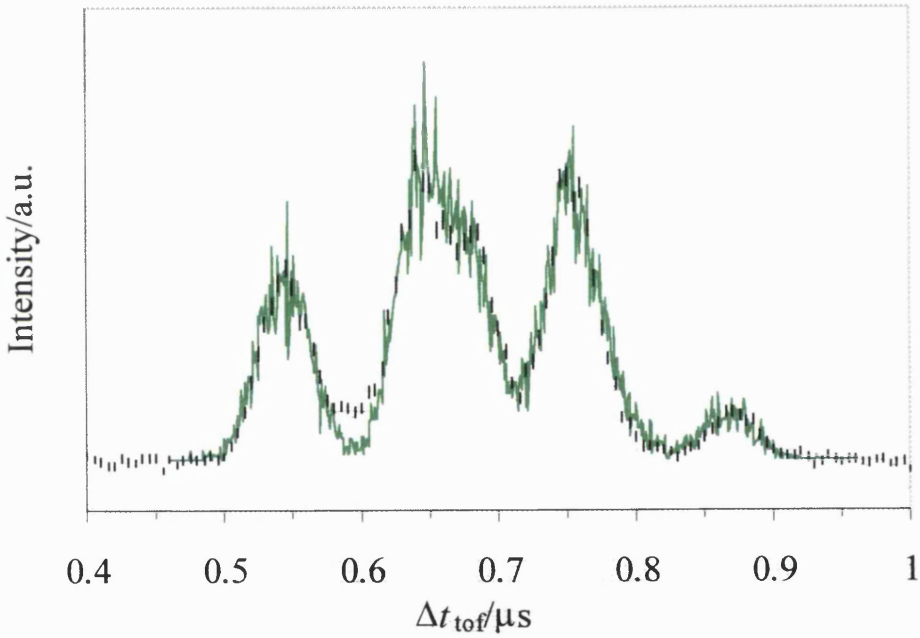

Fig. 4.6 Ion-ion coincidence spectrum of $N_2O_5^{2+}$ showing the peaks corresponding to the $NO_2^+ + NO^+$, $NO^+ + O^+$ and $NO^+ + N^+$ ion pairs. The experimental points are indicated by error bars representing two standard deviations. The solid curve is a Monte Carlo simulation of the experimental signal.

Fig. 4.6 shows the comparison of a simulated spectrum with typical experimental data to indicate the high quality of fit achieved. There is, however, a region of the coincidence spectrum, at $\Delta t_{tof} \sim 0.6$ μs, where the simulation does not perfectly fit the experimental data. Possible explanations for this poorer fit are that one of the KERs is not single valued or that the distribution of the KERs is non-Gaussian. The poorer quality of fit in this region is however not significant, as it does not affect the dominant KER derived from the coincidence peak shape.

The ion pairs observed in the coincidence spectrum following the dissociation of $N_2O_5^{2+}$ are all due to three-body dissociation reactions. The three-body dissociations of $N_2O_5^{2+}$ could involve either a direct mechanism (Coulomb explosion) or a sequential mechanism (Chapter 3). Triple

coincidence studies of molecular dications have shown that true Coulomb explosions are rare.[18-23] In addition, no daughter dications are observed in the mass spectrum (Fig. 4.2) and there are no metastable tails on the coincidence peaks (Fig. 4.5), thus implying that the dissociation mechanism is unlikely to involve a deferred charge separation.[18-24] So, further progress in analysing the coincidence peak shapes can be made if the dissociation mechanism of $N_2O_5^{2+}$ is assumed to be sequential involving an initial charge-separating reaction followed by the dissociation of the resulting singly charged ions to form the detected ion pair.

The KER derived from the coincidence peak widths depends on the masses of the pair of ions formed by the initial charge-separating reaction. But, for a three-body dissociation reaction, the ions formed in the initial charge separation are not necessarily the ones detected in the coincidence spectrum, for example,

$$\begin{array}{c} N_2O_5^{2+} \rightarrow NO_3^+ + NO_2^+ \\ \downarrow \quad\quad \downarrow \\ NO_2^+ + NO^+ \ [+ 2O] \end{array} \qquad (4.X)$$

or

$$\begin{array}{c} N_2O_5^{2+} \rightarrow NO_2^+ + NO_3^+ \\ \downarrow \\ NO_2^+ + NO^+ \ [+ 2O] \end{array} \qquad (4.XI)$$

Therefore, the simulation procedure has been performed several times modelling the formation of each detected ion pair *via* all the possible initial charge separations and subsequent singly charged ion dissociation pathways. In this process, the KER of the monocation dissociation is assumed to be negligible in comparison with the KER upon dication dissociation. The result of the simulation procedure for the dissociation of $N_2O_5^{2+}$ to form $NO_2^+ + NO^+$ and $NO^+ + O^+$, the most intense peaks in the coincidence spectrum, is a list of potential KER values given in Table 4.2 and Table 4.3 respectively.

Table 4.2 Potential values of KER, F_{KERD} and $E(N_2O_5^{2+})$ for forming $NO_2^+ + NO^+$ from $N_2O_5^{2+}$. As indicated in the table and described in the text, the $E(N_2O_5^{2+})$ values are dependent on the dissociation pathway of $N_2O_5^{2+}$ and the form of the neutral products.

Initial charge separation	KER /eV	F_{KERD} /eV	Possible $E(N_2O_5^{2+})$ /eV	
			[+ 2O]	[+ O_2]
$NO_3^+ + NO_2^+$	7.5	3.6	32.9	—
$NO_2^+ + NO_3^+$	6.5	3.3	31.9	26.7
$NO_3^+ + NO^+$	6.5	3.0	31.9	—
$NO_2^+ + NO_2^+$	6.0	3.2	31.4	—

From the potential values of the KER derived from the simulation procedure, the corresponding potential values of the energy of the dication state $E(N_2O_5^{2+})$ from which the

particular dissociation reaction occurs is obtained using Eq. 3.13. The potential values of $E(N_2O_5^{2+})$ for the $NO_2^+ + NO^+$ and $NO^+ + O^+$ ion pairs are listed in Table 4.2 and Table 4.4 respectively. From Table 4.2 and Table 4.4 it can be seen that the value of $E(N_2O_5^{2+})$ depends not only on the initial charge-separating reaction but also on the form of the neutral products. In the calculations of $E(N_2O_5^{2+})$, the fragment ions and neutral products are assumed to be formed with no internal energy. Therefore, any value of the dication state energy derived in this way should be considered a lower limit.

Table 4.3 Potential values of KER and F_{KERD} for forming $NO^+ + O^+$ from $N_2O_5^{2+}$.

Initial charge separation	KER /eV	F_{KERD} /eV
$NO_3^+ + NO_2^+$	13.0	3.0
$NO_2^+ + NO_3^+$	10.5	3.0
$NO_3^+ + NO^+$	11.2	3.0
$NO^+ + NO_3^+$	7.5	3.3
$NO_2^+ + NO^+$	9.5	2.8
$NO^+ + NO_2^+$	7.2	3.0
$NO_2^+ + NO_2^+$	10.0	3.4
$NO^+ + NO^+$	7.0	3.1
$NO_2^+ + O^+$	8.0	2.8
$NO_3^+ + O^+$	8.5	3.0
$N_2O_4^+ + O^+$	9.5	2.5

In order to progress further and derive some mechanistic information from the lists of potential values of $E(N_2O_5^{2+})$ for each ion pair, it is necessary to evaluate the appearance energy of the dication fragmentation pathways for comparison.

Table 4.4 Potential values of $E(N_2O_5^{2+})$ for forming $NO^+ + O^+$ from $N_2O_5^{2+}$. As indicated in the table and described in the text, the $E(N_2O_5^{2+})$ values are dependent on the dissociation pathway of $N_2O_5^{2+}$ and the form of the neutral products.

Initial charge separation	Possible $E(N_2O_5^{2+})$ /eV						
	[N+3O]	[N+O$_3$]	[N+O+O$_2$]	[NO+2O]	[NO+O$_2$]	[NO$_2$+O]	[NO$_3$]
$NO_3^+ + NO_2^+$	51.9	—	46.8	45.4	40.2	—	—
$NO_2^+ + NO_3^+$	49.4	—	44.3	42.9	—	39.7	—
$NO_3^+ + NO^+$	50.1	—	45.0	—	—	—	—
$NO^+ + NO_3^+$	46.4	—	41.3	39.9	—	36.7	—
$NO_2^+ + NO^+$	48.4	—	43.3	—	—	—	—
$NO^+ + NO_2^+$	46.1	—	41.0	39.6	34.4	—	—
$NO_2^+ + NO_2^+$	48.9	—	—	42.4	—	—	—
$NO^+ + NO^+$	45.9	39.7	40.8	—	—	—	—
$NO_2^+ + O^+$	46.9	—	41.8	40.4	—	37.2	—
$NO_3^+ + O^+$	47.4	—	42.3	40.9	35.7	—	—
$N_2O_4^+ + O^+$	48.4	42.2	43.4	41.9	36.7	38.7	36.6

Determination of the Appearance Energy

The appearance energies of the $NO_2^+ + NO^+$ and $NO^+ + O^+$ dissociation reactions of $N_2O_5^{2+}$ have been determined by evaluating the ratio of the yield *Y* of each dissociation reaction to the number of coincidence starts *S* at electron energies from 25 to 65 eV. As explained in Chapter 3, *Y/S* is approximately proportional to σ^{2+}/σ^+, where σ^{2+} is the double ionization cross section and σ^+ is the single ionization cross section. A plot of *Y/S* should, therefore, fall to zero at the energy of the lowest dication state contributing to the relevant dissociation reaction, thus giving the appearance energy of the relevant ion pair.

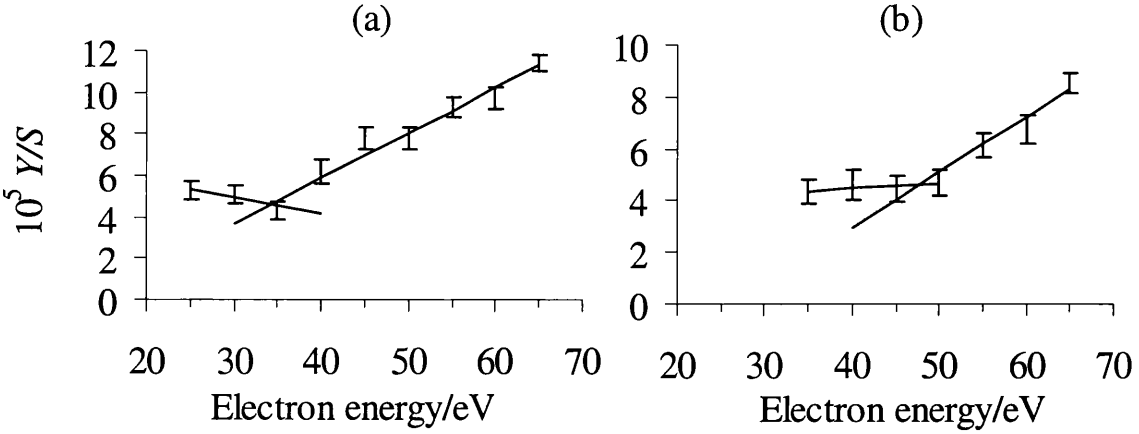

Fig. 4.7 Plots of *Y/S* as a function of electron energy for (a) $NO_2^+ + NO^+$ and (b) $NO^+ + O^+$ dissociation reactions of $N_2O_5^{2+}$. These plots can be interpreted to yield the appearance energy of the lowest energy dication state responsible for each decay reaction.

Fig. 4.7 shows a weighted least squares fit applied to the values of *Y/S* for the dissociation reactions of $N_2O_5^{2+}$ forming $NO_2^+ + NO^+$ and $NO^+ + O^+$ above and below the threshold. The variation of *Y/S* above the appearance energy appears to be well modelled, within the error limits, by a linear function in the excess electron energy. However, it can be seen from Fig. 4.7 that *Y/S* does not fall to zero even at energies below the appearance energy. This non-zero background is due to a small amount of residual double ionization which is always present in the apparatus. This residual signal, which is swamped when the electron energy is above the appearance energy, is attributed to the presence of stray electrons which are accelerated across the ionization region of the TOFMS by the source electric field. Since the rate of background double ionization does not vary significantly with electron energy (Fig. 4.7), *Y/S* can be extrapolated to the background level to obtain the appearance energies of these two dissociation reactions. From Fig. 4.7, values of 34.5 ± 2 and 48 ± 2 eV are obtained for the appearance energy of the $NO_2^+ + NO^+$ and $NO^+ + O^+$ ion pairs respectively. These values are interpreted as the energy of the lowest lying state responsible for the dissociation of $N_2O_5^{2+}$ to form the relevant ion pair. The errors associated with the appearance energy values are determined by considering the energy resolution of the ionizing electron beam. The appearance energies of the $N^+ + O^+$, $NO^+ + N^+$ and $NO_2^+ + O^+$ ion pairs were not determined as at low electron

energies the statistical uncertainties in *Y/S* for these weak signals is significantly increased making the evaluation of their appearance energies impractical.

Table 4.5 Experimentally determined appearance energies for the $NO_2^+ + NO^+$ and $NO^+ + O^+$ ion pairs formed from $N_2O_5^{2+}$.

Dissociation reaction	Appearance energy /eV
$NO_2^+ + NO^+$	34.5 ± 2
$NO^+ + O^+$	48.0 ± 2

The appearance energies determined for the $NO_2^+ + NO^+$ and $NO^+ + O^+$ ion pairs can now be compared with the potential values of $E(N_2O_5^{2+})$ derived from the coincidence peak shapes. If unambiguous agreement is found between one of the values of $E(N_2O_5^{2+})$ derived from the simulation procedure and the appearance energy, then this provides good evidence that the mechanism used to derive the KER is the one that is actually followed to form the detected ion pair.

4.3.2 Discussion

4.3.2.1 Single Ionization

Only two previous reports of the single ionization and subsequent fragmentation of N_2O_5 have been reported in the literature: one PIMS study [8] in the energy range 10-20 eV, and a second EIMS work[9] at an ionizing electron energy of 11.5 eV. In the EIMS study, only NO^+ and NO_2^+ were detected and the NO^+ fragments were observed to be three times more abundant than the NO_2^+ fragments. In the PIMS work, both NO_2^+ and NO^+ ions were again observed and in addition O^+ fragments were also detected.[8] In this case, in contrast to the EIMS study, the most abundant fragment was found to be NO_2^+ (Table 4.6). In addition, this investigation of the photoionization of N_2O_5 determined the appearance energies of the NO_2^+, NO^+ and O^+ fragment ions to be 11.91, 12.95 and 16.8 eV respectively.[8]

In the present work, at electron energies from 35 to 500 eV, NO_2^+, NO^+, O^+ and N^+ fragment ions were observed in the time-of-flight mass spectra (Fig. 4.2). The most abundant ion was found to be NO_2^+. As in the other studies, no parent ion ($N_2O_5^+$) was observed. The obvious conclusion from this observation is that any bound region of the $N_2O_5^+$ potential energy surface cannot be accessed by a vertical transition from the equilibrium of the neutral molecule. The plot of the values of σ_r^{si} of the fragment ions against electron energy (Fig. 4.3) shows, as expected, an initial increase in σ_r^{si} as the electron energy is raised, as ionic fragmentation becomes more likely with increasing electron energy and associated ionic excitation.

The intensity ratio of NO^+ to NO_2^+ determined at 35 eV in this work (Table 4.1) is significantly different from that presented in the earlier EIMS study[9] using 11.5 eV electrons, where

markedly more NO^+ than NO_2^+ was detected. A dominance of the ion yield by NO^+ at these lower electron energies runs counter to the trends displayed by the data obtained in the current study. However, the quantitative validity of these early mass spectrometric data is called into question as, although the electron energy employed lies below the appearance energy for NO^+, these ions were observed to be the most abundant fragments.[9]

In this work the intensity ratios of the fragment ions of $N_2O_5^+$ at 70 eV, the ionizing energy often considered to result in the same energy deposition[25] as the 20.7 eV photons employed in the PIMS experiments,[8] are markedly larger than those reported in the PIMS study. The smaller yields reported in the PIMS study could be a result of mass discrimination effects in the PIMS work or the different ionizing agents, photons or electrons, result in the population of distinct electronic states. However, the most likely explanation for the dramatic difference in the yields of the fragment ions is an increased efficiency in the collection of fragment ions from dissociative single ionization using the current apparatus. Therefore, given the efforts made in this work to obtain a pure sample of N_2O_5 and the efficient detection of the majority of energetic fragments from dissociative single ionization, the values of σ_r^{si} given in Table 4.1 and Fig. 4.3 are likely to be the most reliable to date.

Table 4.6 Comparison of fragment ion intensities observed in the mass spectrum of N_2O_5.

		Ionization energy /eV	Observed ions			
			N^+	O^+	NO^+	NO_2^+
Present work	EIMS	70	2.7	11.6	74	100
Jochims *et al*[8]	PIMS	20.7	—	1	30	100

As described above, the appearance energy for the formation of N^+ from N_2O_5 has been determined to be 36 ± 2 eV. With such a high appearance energy, this fragment ion could be due to the dissociation of the monocation or the dication. Considering the monocation, an attractive assignment for this dissociation pathway involves the complete fragmentation of the $N_2O_5^+$ ion,

$$N_2O_5^+ \rightarrow N^+ + N + 5O \qquad (4.XII)$$

This process has a thermodynamic asymptote of 37.1 eV,[26] assuming all the fragments are formed in their ground states, which lies within the error limits of the appearance energy determined above. Alternatively, the N^+ ions could arise from a dissociation process involving a smaller degree of fragmentation of the monocation, such as that illustrated in Reaction (4.XIII), together with the formation of neutral species in excited electronic states:

$$N_2O_5^+ \rightarrow N^+ + N + 3O + O_2 \qquad (4.XIII)$$

The experimental results cannot, however, distinguish between a large number of such possibilities.

The N^+ fragments detected could also be produced by the fragmentation of the molecular dication, $N_2O_5^{2+}$, which should be formed at an electron energy of 36 eV. One possible decay pathway that would generate N^+ is shown in Reaction (4.XIV):

$$N_2O_5^{2+} \rightarrow NO_2^+ + NO^+ + 2O$$
$$NO^+ \rightarrow N^+ + O \qquad (4.XIV)$$

The double ionization energy of N_2O_5 can be estimated as 33.3 eV by the 'rule of thumb'[27] (Chapter 3) and investigations of the double ionization of N_2O_5 described below indicate that this is a satisfactory estimate. Owing to the discrimination effects discussed in Chapter 3, any N^+ fragments formed by double ionization would be expected to be very inefficiently detected by the apparatus because of their significant kinetic energies. If the formation of N^+ from $N_2O_5^{2+}$ has a high probability and the double ionization cross section of N_2O_5 is significant, then the dication cannot be discounted as the source of the N^+ fragments. However, as discussed below, it is indicated that the decay of $N_2O_5^{2+}$ does not yield a large number of N^+ ions nor is the double ionization cross section very large. Hence, the monocation is the most likely source of the N^+ fragment ions observed in the time-of-flight mass spectrum.

4.3.2.2 Double Ionization

The coincidence spectra show that $N_2O_5^{2+}$ dissociates *via* a variety of three-body reactions [Reactions (4.IV)-(4.VIII)]. No stable parent dication ($N_2O_5^{2+}$) or daughter dications were observed in the time-of-flight mass spectrum of N_2O_5 (Fig. 4.2). The absence of an $N_2O_5^{2+}$ signal implies that any bound region of the ground state potential energy surface of the dication cannot be accessed by a vertical transition from the equilibrium geometry of the neutral molecule.

$NO_2^+ + NO^+$

For the dissociation reaction of $N_2O_5^{2+}$ forming the $NO_2^+ + NO^+$ ion pair, the experimentally determined appearance energy is 34.5 ± 2 eV (Table 4.5). From Table 4.2, it is apparent that the value of $E(N_2O_5^{2+})$ which agrees best with this appearance energy is 32.9 eV. The other values of $E(N_2O_5^{2+})$ derived assuming different initial charge separations are well outside the error limits of the appearance energy. The value of 32.9 eV is derived assuming an initial two-body fragmentation to form $NO_3^+ + NO_2^+$ followed by the dissociation of these singly charged ions to give the detected ion pair [Reaction (4.X)]. Note that in this decay mechanism NO_2^+ is produced in a dissociative electronic state by the initial charge separation but in a stable electronic state by the dissociation of NO_3^+. This behaviour, where the first step of a dicationic three-body reaction is a two-body charge separation is well documented in the literature.[18,20]

The difference between the values of the energy of the dication state responsible for forming $NO_2^+ + NO^+$ obtained from the appearance energy and from the KER can be accounted for either by the uncertainties involved in the determination of the appearance energy or by the internal excitation of the products as a result of the dissociation event. The good agreement between the two estimates

of the dication state energy obtained for this dissociation reaction and an estimate of the double ionization energy as 33.3 eV, derived using the 'rule of thumb'[27] (Chapter 3) indicates that the dissociation of $N_2O_5^{2+}$ to form $NO_2^+ + NO^+$ probably occurs from the ground electronic state of $N_2O_5^{2+}$. Given the assumption made in deriving the dication state energy of 32.9 eV from the coincidence peak shape, despite the fact that the uncertainties in the fitting procedure are only ± 0.2 eV, it is felt that the experimental determination of the appearance energy of the fragmentation channel provides the most reliable estimate from this work of the double ionization energy of N_2O_5 as 34.5 ± 2 eV.

$NO^+ + O^+$

The appearance energy of the dissociation reaction forming the $NO^+ + O^+$ ion pair is determined to be 48 ± 2 eV (Table 4.5). As the ionic products of the reaction are $NO^+ + O^+$, there are a large number of possible initial charge separations which could form these products when followed by further dissociation of the resulting singly charged ions (Table 4.3). For example, an initial charge separation to form $NO_2^+ + NO_2^+$, $NO_3^+ + NO_2^+$ or $NO_3^+ + O^+$ could all, when followed by secondary monocation dissociation, result in the formation of $NO^+ + O^+$. Using the simulation procedure described in Chapter 3, the potential values of $E(N_2O_5^{2+})$ were calculated for all the possible initial charge separation reactions. Unfortunately, as can be seen in Table 4.4, there are a large number of dissociation pathways which yield a value of $E(N_2O_5^{2+})$ within the error limits of the appearance energy. Therefore, a definitive dicationic fragmentation mechanism for the formation of $NO^+ + O^+$ cannot be assigned by this method. However, if the three-body dissociation of $N_2O_5^{2+}$ is a sequential decay involving an initial two-body charge separation, as is commonly reported in the literature,[28] then a large number of the possible initial fragmentations can be disregarded. The remaining possible fragmentation pathways are

$$\begin{array}{l} N_2O_5^{2+} \rightarrow NO_3^+ + NO_2^+ \\ \qquad\quad \downarrow \qquad \downarrow \\ \qquad\quad NO^+ + O^+ + N + 3O \end{array} \qquad (4.XV)$$

$$\begin{array}{l} N_2O_5^{2+} \rightarrow NO_3^+ + NO_2^+ \\ \qquad\quad \downarrow \qquad \downarrow \\ \qquad\quad O^+ + NO^+ + N + 3O \end{array} \qquad (4.XVI)$$

$$\begin{array}{l} N_2O_5^{2+} \rightarrow N_2O_4^+ + O^+ \\ \qquad\quad \downarrow \qquad \downarrow \\ \qquad\quad NO^+ + O^+ + N + 3O \end{array} \qquad (4.XVII)$$

For the initial charge separations given in Reactions (4.XVI) and (4.XVII), the values of $E(N_2O_5^{2+})$ derived from the coincidence peak widths (49.5 and 48.4 eV respectively) are within the

error limits of the experimentally determined appearance energy. The value of $E(N_2O_5^{2+})$ derived for the mechanism given in Reaction (4.XV) is well outside the error limits of the appearance energy and is therefore not considered a viable mechanism. In addition, as no indication of any $N_2O_4^+$ signal is seen in the coincidence or mass spectra, the most likely decay pathway is the one shown in Reaction (4.XVI). This dissociation pathway involves an initial two-body charge separation to form NO_3^+ + NO_2^+, the same fragmentation deduced to be responsible for the reaction forming NO_2^+ + NO^+, followed by the dissociation of the singly charged ions and complete fragmentation of the neutral products.

As before, the difference between the values of the energy of the state of $N_2O_5^{2+}$ dissociating to form the $NO^+ + O^+$ ion pair determined experimentally and calculated from the KER, 48 ± 2 eV and 49.4 ± 0.2 eV respectively, could either be due to the uncertainties in the appearance energy measurement or to internal excitation of the dissociation products.

$N^+ + O^+$, $NO^+ + N^+$ and $NO_2^+ + O^+$

A more detailed analysis of the decay reactions of $N_2O_5^{2+}$ forming the ion pairs $N^+ + O^+$, $NO^+ + N^+$ and $NO_2^+ + O^+$ is difficult because of the lack of experimentally determined appearance energies for comparison with any values of $E(N_2O_5^{2+})$ derived from the coincidence peak widths. If, however, the reactions are assumed to occur *via* the same initial two-body charge separation to $NO_3^+ + NO_2^+$ that is deduced to be responsible for the reactions forming the $NO_2^+ + NO^+$ and $NO^+ + O^+$ ion pairs, then the values of KER and the corresponding values of F_{KERD} determined *via* the Monte Carlo simulation are given in Table 4.7. The associated values of $E(N_2O_5^{2+})$ for the $N^+ + O^+$, $NO^+ + N^+$ and $NO_2^+ + O^+$ ion pairs are listed in Table 4.8, together with a summary of the energetic data derived for the $NO_2^+ + NO^+$ and $NO^+ + O^+$ ion pairs.

Table 4.7 Values of KER and F_{KERD} for the formation of the indicated product ion pairs from $N_2O_5^{2+}$, assuming an initial two-body charge separation to form $NO_3^+ + NO_2^+$ followed by subsequent dissociation of the singly charged ions.

Dissociation reaction	KER /eV	F_{KERD} /eV
$N^+ + O^+$	8.8	2.7
$NO^+ + N^+$	8.5	3.0
$NO_2^+ + O^+$	8.3	3.0

A comparison of the values of $E(N_2O_5^{2+})$ associated with the reactions forming $NO^+ + O^+$ and $NO^+ + N^+$ indicates that these decay processes may result from the dissociation of the same electronic state of $N_2O_5^{2+}$. The remaining reactions forming $N^+ + O^+$ and $NO_2^+ + O^+$ ion pairs appear to result from the population of distinct electronic states.

Table 4.8 Estimates of the values of $E(N_2O_5^{2+})$ and appearance energies for the dissociation reactions of $N_2O_5^{2+}$, where available.

Dissociation reaction	$E(N_2O_5^{2+})$ /eV*	Appearance energy /eV
$N^+ + O^+$ [+ N + 4O]	59.6	
$NO_2^+ + NO^+$ [+ 2O]	32.9	34.5 ± 2
$O^+ + NO^+$ [+ N + 3O]	49.4	48 ± 2
$NO^+ + N^+$ [+ 4O]	48.4	
$NO_2^+ + O^+$ [+ N + 2O]	44.6	

*These values are obtained assuming an initial dicationic fragmentation to form $NO_3^+ + NO_2^+$ followed by the dissociation of the singly charged ions accompanied by the complete fragmentation of the neutrals (given in parentheses).

4.4 Overall Conclusions

This study presents a determination of relative partial single ionization cross sections of N_2O_5 for incident electron energies from 35 to 500 eV using time-of-flight mass spectrometry. Fragment ions N^+, O^+, NO^+ and NO_2^+ are detected, the most abundant ion being NO_2^+. The appearance energy of the previously unobserved N^+ fragment was determined to be 36 ± 2 eV.

Ion-ion coincidence experiments were performed to study the formation and dissociation of $N_2O_5^{2+}$. Coincidence peaks due to the formation of $N^+ + O^+$, $NO_2^+ + NO^+$, $NO^+ + O^+$, $NO^+ + N^+$ and $NO_2^+ + O^+$ ion pairs were observed. The appearance energies of the dissociation reactions forming the $NO_2^+ + NO^+$ and $NO^+ + O^+$ ion pairs were determined to be 34.5 ± 2 eV and 48 ± 2 eV respectively. Comparisons of this experimental data with dication state energies calculated using values of the KER upon charge separation seems consistent with the conclusion that the initial charge separation is a two-body reaction forming $NO_3^+ + NO_2^+$. These ions subsequently dissociate to produce the detected ion pairs. The energy of the dication state responsible for forming the $NO_2^+ + NO^+$ ion pair indicates that this dissociation reaction probably occurs from the electronic ground state of $N_2O_5^{2+}$ and hence this study provides the first estimate of the double ionization energy of N_2O_5 as 34.5 ± 2 eV.

In order to confirm the conclusions reached concerning the dissociation mechanism for the formation of the observed ion pairs from $N_2O_5^{2+}$ it would be necessary to perform a 2D investigation of $N_2O_5^{2+}$ or triple coincidence experiments.

References

1 B.A. Thrush, *Rep. Prog. Phys.*, **51** (1988) 1341

2 C. Camy-Peyret, J.-M. Flaud, L. Lechuga-Fossat, G. Laverdet and G. Le Bras, *Chem. Phys. Lett.*, **139** (1987) 345

3 J.P. Burrows, G.S. Tyndall and G.K. Moortgat, *Chem. Phys. Lett.*, **119** (1985) 193

4 J.A. Davidson, A.A. Viggiano, C.J. Howard, I. Dotan, F.C. Fehsenfeld, D.L. Albritton and E.E. Ferguson, *J. Chem. Phys.*, **68** (1978) 2085

5 C.A. Cantrell, J.A. Davidson, R.E. Shetter, B.A. Anderson and J.G. Calvert, *J. Phys. Chem.*, **91** (1987) 6017

6 C.A. Cantrell, R.E. Shetter, J.G. Calvert, G.S. Tyndall and J.J. Orlando, *J. Phys. Chem.*, **97** (1993) 9141

7 H. Wincel, E. Mereand and A.W. Castleman, *J. Phys. Chem.*, **99** (1995) 1792

8 H.-W. Jochims, W. Denzer, H. Baumgärtel, O. Lösking and H. Willner, *Ber. Bunsenges. Phys. Chem.*, **96** (1992) 573

9 G. Liuti, S. Dondes and P. Harteck, *J. Phys. Chem.*, **72** (1968) 1081

10 C.S.S. O'Connor, N.C. Jones, K. O'Neale and S.D. Price, *Int. J. Mass Spectrom. Ion Proc.*, **154** (1996) 203

11 C.S.S. O'Connor, N.C. Jones and S.D. Price, *Chem. Phys.*, **214** (1997) 131

12 D.R. Lide (Ed.), *CRC Handbook of Chemistry and Physics*, CRC Press, London, 1992

13 A.M. Phipps and D.N. Hume, *J. Chem. Educ.*, **45** (1968) 664

14 K.A. Newson, S.M. Luc, S.D. Price and N.J. Mason, *Int. J. Mass Spectrom. Ion Proc.*, **148** (1995) 203

15 P.R. Bevington, *Data Reduction and Error Analysis for the Physical Sciences*, McGraw-Hill, New York, 1992

16 G.H. Wannier, *Phys. Rev.*, **90** (1953) 817

17 F.H. Read, in T.D. Märk, G.H. Dunn (Eds.), *Electron Impact Ionization*, Springer-Verlag, New York, 1985

18 J.H.D. Eland, *Mol. Phys.*, **61** (1987) 725

19 J.H.D. Eland, *Chem. Phys. Lett.*, **203** (1993) 353

20 S. Hsieh and J.H.D. Eland, *J. Chem. Phys.*, **103** (1995) 1006

21 I. Nenner and J.H.D. Eland, *Z. Phys. D*, **25** (1992) 47

22 M. Simon, P. Morin, P. Lablanquie, M. Lavollee, K. Ueda and N. Kosugi, *Chem. Phys. Lett.*, **238** (1995) 42

23 K. Codling, L.J. Frasinski, P.A. Hatherly, M. Stankiewicz and F.P. Larkins, *J. Phys. B*, **24** (1991) 951

24 P.J. Richardson, J.H.D. Eland and P. Lablanquie, *Org. Mass Spec.*, **21** (1986) 289

25 S. Leach, J.H.D. Eland and S.D. Price, *J. Phys. Chem.*, **93** (1989) 7575

26 S.G. Lias, J.E. Bartmess, J.F. Liebman, J.L. Holmes, R.D. Levin and W.G. Mallard, *J. Phys. Chem. Ref. Data,* **17 S1** (1988) 1

27 B.P. Tsai and J.H.D. Eland, *Int. J. Mass Spectrom. Ion Proc.*, **36** (1980) 143

28 D.M. Curtis and J.H.D. Eland, *Int. J. Mass Spectrom. Ion Proc.*, **63** (1985) 241

5. Single and Double Ionization of Cl_2O

5.1 Introduction

The first reported synthesis of dichlorine monoxide, also known as chlorine monoxide, was in 1834 by Balard.[1] Its composition was determined by both Balard[1] and Gay-Lussac[2] and the formula Cl_2O assigned to it. As a simple, non-linear triatomic molecule with C_{2v} symmetry, the spectroscopy of Cl_2O has been extensively studied.[3-8] More recently the photochemistry of Cl_2O, in particular its photodissociation dynamics, have been investigated.[9,10] The interest in the photochemistry of Cl_2O stems from the significance of halogen oxides in atmospheric chemistry, most notably the involvement of chlorine oxides in the loss of stratospheric ozone.

$$Cl + O_3 \rightarrow ClO + O_2 \qquad (5.I)$$

$$ClO + O \rightarrow Cl + O_2 \qquad (5.II)$$

The chlorine catalytic cycle, comprising of this pair of reactions, may add to or dominate the Chapman reaction[11] between O and O_3 in the stratosphere, seriously affecting the levels of ozone in the atmosphere.

Cl_2O is thought to play only a minor role in stratospheric chemistry but an understanding of the photochemistry and dissociation dynamics of this molecule can lead to an improved understanding of the more complex chlorine oxides, which may play a significant role in the ozone cycle. Cl_2O is also frequently used as a source of ClO in laboratory studies[12] of this atmospherically important radical and in the synthesis of HOCl, a significant chlorine reservoir in the atmosphere.

Despite the interest in the spectroscopy and photodissociation of Cl_2O, there have been relatively few investigations of the ionization of Cl_2O. Indeed, there have only been a handful of studies investigating the single ionization of Cl_2O[12-15] and no investigations of the formation and fragmentation of Cl_2O^{2+}.

As a continuation of investigations of the ionization of reactive species presented in this thesis, this chapter presents a one and two-dimensional study of the single and double ionization of Cl_2O.[16] In the single ionization studies of Cl_2O, time-of-flight mass spectrometry is used to determine the relative partial single ionization cross sections of Cl_2O over a range of electron energies. Coincidence techniques are used to investigate the formation and fragmentation of Cl_2O^{2+}. Information obtained from the one-dimensional and 2D coincidence spectra can give an indication of the mechanisms by which Cl_2O^{2+} dissociates and the energy of the electronic states of Cl_2O^{2+} which are the source of the pairs of ions formed by dicationic dissociation. These investigations also

provide first estimates of both the double ionization energy and the ratio of the double-to-single ionization cross sections of Cl_2O.

5.2 Experimental Details

The mass spectrometric methods used in the one-dimensional and 2D studies of the single and double ionization of Cl_2O have been described in detail in Chapter 2.

5.2.1 Synthesis of Cl_2O

The sample of dichlorine monoxide used in these experiments was prepared *in situ*, as required, by the reaction of chlorine on solid mercury oxide.[3]

$$2Cl_2 + nHgO \rightarrow HgCl_2.(n\text{-}1)HgO + Cl_2O \qquad (5.III)$$

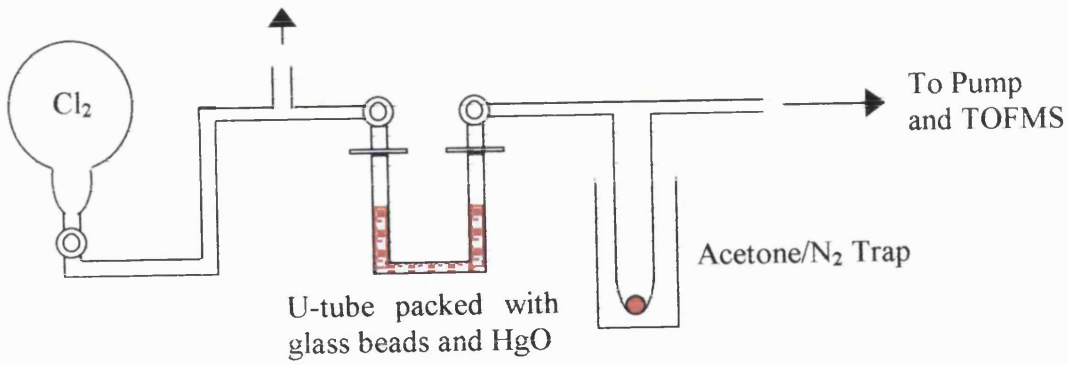

Fig. 5.1 Apparatus used for the synthesis of Cl_2O.

Chlorine gas is slowly flowed through a U-tube packed with glass beads and dried yellow mercury oxide (Fig. 5.1). The resulting Cl_2O is trapped in an acetone/N_2 slush bath at 179 K and any unreacted Cl_2, the main impurity, is pumped away. The liquefied sample is then allowed to warm up and the first fraction of gas evolved is pumped away so any remaining traces of Cl_2, being more volatile than Cl_2O, are eliminated. The pure Cl_2O sample is then warmed to room temperature and the vaporised Cl_2O molecules are drawn into the TOFMS *via* the clean, non-catalytic glass/Teflon inlet system described previously (Chapter 2). To avoid any photodissociation of the Cl_2O molecules, the inlet system was blacked out. As there appeared to be no improvement in the purity of the sample with multiple freeze/pump cycles, it is assumed that this experimental methodology provides an adequately pure sample of Cl_2O.

Due to the reactive nature of Cl_2O, the filament of the electron gun is rapidly attacked by the gaseous sample causing fluctuations in the emission current, which increase the statistical uncertainty

in the recorded mass spectra. Indeed, the filament lifetime is markedly reduced following even the briefest exposure to Cl_2O. Accordingly, spectra of Cl_2O have been recorded for a shorter time than usual, again increasing the statistical uncertainty of the results.

5.2.2 Procedures

For the one-dimensional studies, time-of-flight mass spectra were recorded at incident electron energies of 30-450 eV in order to determine the relative partial single ionization cross sections σ_r^{si} of the ions produced by the single ionization of Cl_2O. One-dimensional coincidence spectra were recorded at an ionizing electron energy of 150 eV and also at a range of lower electron energies, from 25 to 80 eV, in order to determine the appearance energies of the pairs of fragment ions produced by the dissociative double ionization of Cl_2O.

For the 2D studies, time-of-flight mass spectra were recorded at electron energies of 70, 100, 250 and 320 eV to determine the values of σ_r^{si} for the fragment ions of Cl_2O by collecting all ionic fragments, including previously undetected highly-energetic monocations, and subtracting the contribution of dissociative multiple ionization to the ion signal intensities in the mass spectrum. Coincidence spectra were recorded at the same electron energies and the intensities and slopes of the peaks corresponding to the fragment ion pairs formed from Cl_2O^{2+} were determined.

5.3 One-Dimensional Studies

5.3.1 Data Analysis

5.3.1.1 Single Ionization

A typical time-of-flight mass spectrum of Cl_2O recorded at an electron energy of 150 eV is shown in Fig. 5.2. As can be seen from the figure, the stable parent ion, Cl_2O^+, fragment ions Cl^+, ClO^+ and Cl_2^+ and their isotopes are detected. The spectrum also contains a small signal corresponding to the background gas, principally water, in the apparatus.

The parent and fragment ion signal intensities are obtained from the raw ion signals in the mass spectrum recorded at a range of electron energies from 30 to 450 eV. The values of σ_r^{si} for the ions observed in the Cl_2O spectrum, relative to the most abundant ion, ClO^+, are determined from the ion signal intensities as described in Chapter 3, using the appropriate mass correction factor (Eq. 3.4).

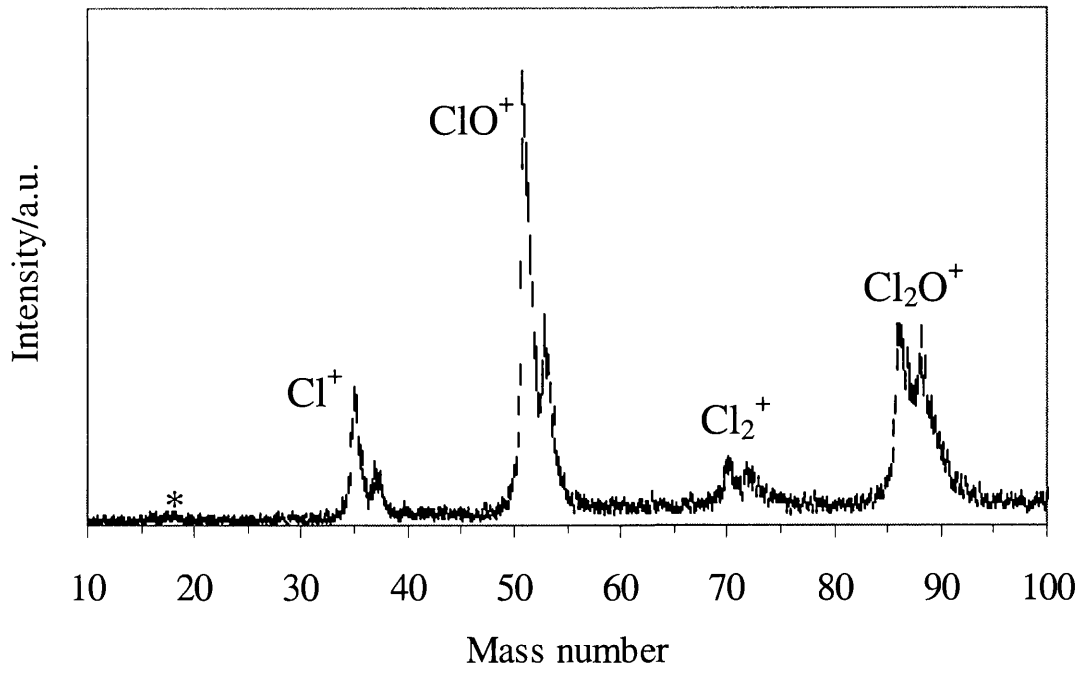

Fig. 5.2 Typical time-of-flight mass spectrum of Cl_2O recorded at 150 eV. The error bars shown, derived from the counting statistics, represent two standard deviations. The peak marked with an asterisk corresponds to signal from the residual gas.

The values of σ_r^{si} obtained, shown in Fig. 5.3 and listed in Table 5.1, are the average of five independent determinations. The standard deviations of these determinations at each electron energy are also shown in Table 5.1 and plotted as the error bars in Fig. 5.3. The standard deviations are small in accord with the statistical error in each individual determination.

Table 5.1 Values of σ_r^{si} for the formation of the indicated product ion from Cl_2O, relative to ClO^+ (the numbers in parentheses indicate the standard deviation in the last figure of each cross section).

Electron	σ_r^{si}		
energy/eV	Cl^+	Cl_2^+	Cl_2O^+
30	—	0.13(13)	0.35(17)
40	0.411(59)	0.151(59)	0.477(77)
50	0.413(31)	0.140(44)	0.482(26)
60	0.419(30)	0.136(40)	0.492(29)
70	0.455(33)	0.146(49)	0.467(35)
80	0.447(33)	0.123(32)	0.461(25)
100	0.404(27)	0.144(29)	0.510(14)
150	0.402(9)	0.120(32)	0.489(8)
200	0.401(37)	0.130(24)	0.487(14)
250	0.383(23)	0.122(29)	0.478(24)
300	0.378(15)	0.116(22)	0.492(27)
350	0.363(20)	0.123(17)	0.488(22)
400	0.345(10)	0.124(31)	0.514(12)
450	0.332(32)	0.113(17)	0.506(34)

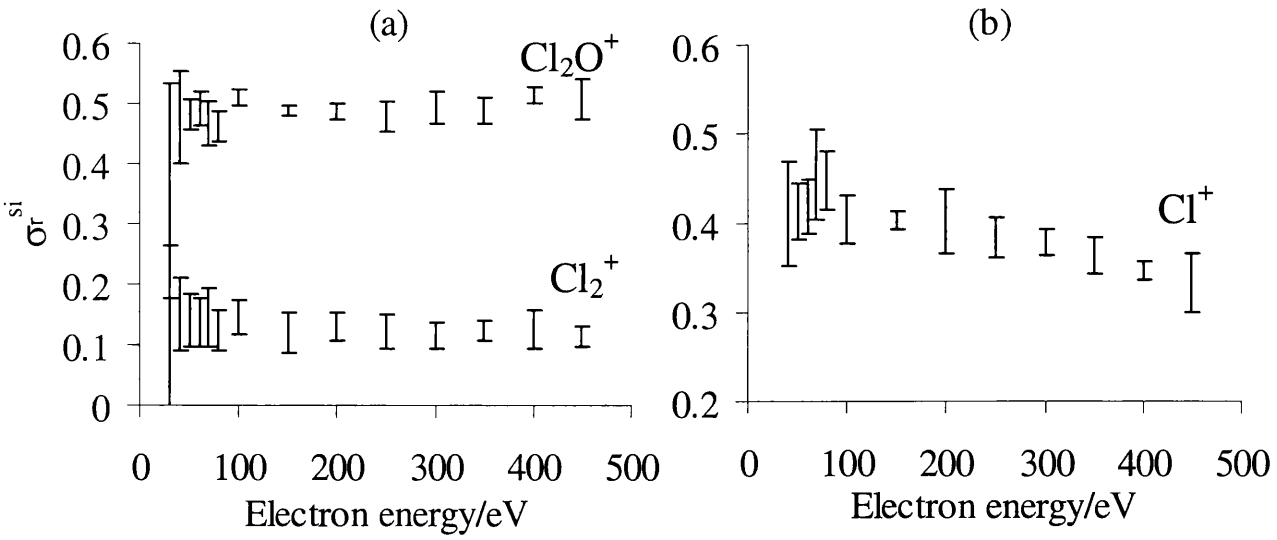

Fig. 5.3 Values of σ_r^{si} for forming (a) Cl_2O^+ and Cl_2^+ and (b) Cl^+ from Cl_2O, relative to the most abundant ion in the mass spectrum, ClO^+. The error bars represent two standard deviations.

The appearance energy of the fragment ion ClO^+ has been previously determined[12] at better energy resolution than can be achieved using the current experimental arrangement, conservatively estimated to be ± 2 eV, and was therefore not redetermined in this study. The appearance energies of the Cl^+ and Cl_2^+ fragment ions have not been reported in the literature. However, with this apparatus, at low electron energies the statistical uncertainties in the values of σ_r^{si} for the Cl^+ and Cl_2^+ fragment ions are significantly increased since, as explained above, the data gathering runs are short to limit the extent of the degradation of the filament by the Cl_2O, making an evaluation of their appearance energies impractical.

5.3.1.2 Double Ionization

A typical one-dimensional ion-ion coincidence spectrum of Cl_2O^{2+} recorded at 150 eV is shown in Fig. 5.4. The observed dissociation reactions are

$$Cl_2O^{2+} \rightarrow Cl^+ + ClO^+ \qquad (5.IV)$$

$$Cl_2O^{2+} \rightarrow O^+ + Cl^+ [+ Cl] \qquad (5.V)$$

$$Cl_2O^{2+} \rightarrow Cl^+ + Cl^+ [+ O] \qquad (5.VI)$$

where the neutral atoms are not detected. As can be seen in Fig. 5.4, the majority of the peak corresponding to the $Cl^+ + Cl^+$ dissociation reaction is not observed in the coincidence spectrum as it is masked by the 'ringing' when Δt_{tof} is small.

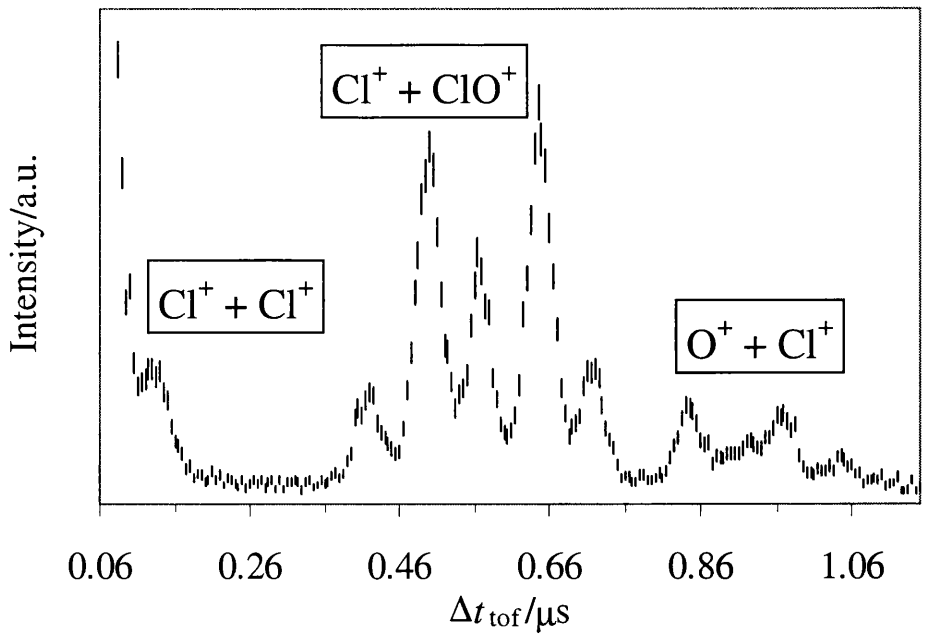

Fig. 5.4 Ion-ion coincidence spectrum of Cl_2O^{2+} generated by electron impact at 150 eV. The error bars shown are derived from the counting statistics and represent two standard deviations.

Kinetic Energy Release Determination

The first evaluation of the kinetic energy release (KER) and half-width of the kinetic energy release distribution (F_{KERD}) associated with the formation of the ion pairs observed in the coincidence spectrum of Cl_2O^{2+} have been determined by performing a Monte Carlo simulation of the experimental data, the method being described in detail in Chapter 3. The KER associated with the formation of the fragment ion pairs is assumed to be the same for both chlorine isotopes.

The formation of the $Cl^+ + ClO^+$ ion pair from Cl_2O^{2+} is a two-body dissociation reaction [Reaction (5.IV)], thus the only possible fragmentation pathway is direct dissociation of the dication to form the product ion pair. So the result of the simulation procedure for the $Cl^+ + ClO^+$ ion pair is a single value of the KER and corresponding F_{KERD} listed in Table 5.2.

Table 5.2 Values of KER and F_{KERD} for forming $Cl^+ + ClO^+$ from Cl_2O^{2+}, derived by simulation of the ion-ion coincidence spectrum at 150 eV.

Dissociation mechanism	KER/eV	F_{KERD}/eV
Direct	5.2	2.0

For the three-body dissociation reactions of Cl_2O^{2+} forming $O^+ + Cl^+$ and $Cl^+ + Cl^+$ [Reactions (5.V) and (5.VI) respectively], where neutral atoms are formed in conjunction with the pairs of singly charged ions, the fragmentation pathway is not as clear. The pathway could involve either a direct mechanism [Reactions (5.VII) and (5.VIII)] or a sequential mechanism (deferred charge separation or initial charge separation and subsequent monocation dissociation). No daughter

dications are observed in the mass spectrum (Fig. 5.2) and there are no metastable tails on the coincidence peaks (Fig. 5.4), thus implying that the sequential dissociation mechanism is unlikely to involve a deferred charge separation.[17-23] Therefore, the sequential mechanism is assumed to involve an initial charge separation followed by the subsequent dissociation of one of the resulting ions to form the detected pair of singly charged ions [Reactions (5.IX) and (5.X)].

Direct:

$$Cl_2O^{2+} \rightarrow O^+ + Cl^+ + Cl \qquad (5.VII)$$

$$Cl_2O^{2+} \rightarrow Cl^+ + Cl^+ + O \qquad (5.VIII)$$

Sequential:

$$\begin{array}{l} Cl_2O^{2+} \rightarrow ClO^+ + Cl^+ \\ \qquad\quad \downarrow \\ \qquad\quad O^+ + Cl^+ + Cl \end{array} \qquad (5.IX)$$

$$\begin{array}{l} Cl_2O^{2+} \rightarrow ClO^+ + Cl^+ \\ \qquad\quad \downarrow \\ \qquad\quad Cl^+ + Cl^+ + O \end{array} \qquad (5.X)$$

As mentioned in Chapter 3, the KER upon dicationic dissociation to form a given pair of ions is associated with the temporal width of the coincidence peak and depends on the masses of the primary ions formed in the charge separation. But, for the three-body dissociation reactions, the pairs of ions detected in the coincidence spectrum may not be the same two ions that received the initial impulse from the dicationic dissociation event [Reactions (5.IX) and (5.X)]. Therefore, when analysing the coincidence spectra of Cl_2O^{2+} it is necessary to consider the three-body fragmentation pathways by which the dication dissociates. The simulation procedure has consequently been performed for the three-body dissociation reactions of Cl_2O^{2+} modelling the formation of $O^+ + Cl^+$ and $Cl^+ + Cl^+$ *via* the two remaining possible dissociation pathways, the direct mechanism and the sequential mechanism involving initial charge separation and subsequent monocation dissociation. In the simulation procedure, the KER of the monocation dissociation is assumed to be negligible in comparison to the primary KER of the dication dissociation.

When the coincidence peak corresponding to the $O^+ + Cl^+$ reaction is modelled using a single KER a satisfactory fit with the experimental spectrum is not obtained using realistic values for the variable parameters, for example, F_{KERD} (Table 5.3, Fig. 5.5a). In general,[24] values of F_{KERD} tend to range from 1-4 eV and as can be seen in Table 5.3, the values of F_{KERD} derived assuming a single KER lie higher in value thus suggesting that they are unrealistic. The poor fit of the simulated spectrum with the experimental data (Fig. 5.5a), and the shape of the coincidence peak, suggest that more than one KER is involved in the formation of the $O^+ + Cl^+$ ion pair. Hence, this reaction has been modelled for both the sequential and direct fragmentation pathways using two KER values. Table 5.3 shows the potential multiple KER and F_{KERD} values required to fit the experimental spectrum for the two possible decay pathways that could form $O^+ + Cl^+$ from Cl_2O^{2+}. Note that the values of F_{KERD} are now reasonable and the inclusion of a multiple KER in the simulation of this

coincidence peak also markedly improves the fit of the simulated spectrum with the experimental spectrum (Fig. 5.5b).

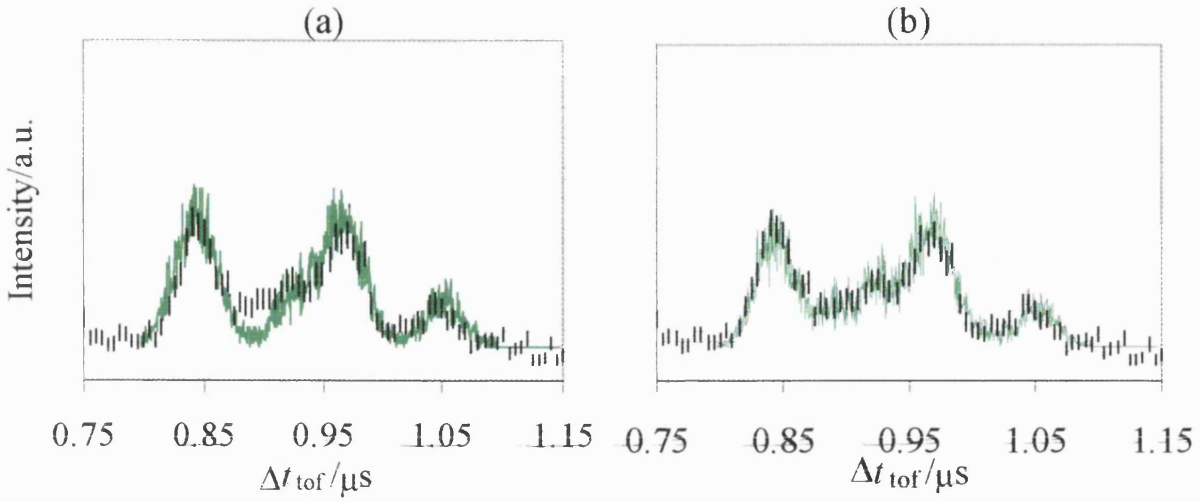

Fig. 5.5 Ion-ion coincidence spectrum of Cl_2O^{2+} showing the signal corresponding to the O^+ + Cl^+ ion pair. The solid curve is a Monte Carlo simulation of the experimental signal assuming a sequential dissociation mechanism and (a) a single KER and (b) a multiple KER, using the parameters listed in Table 5.3. Error bars representing two standard deviations indicate the experimental points.

Table 5.3 Potential values of KER and F_{KERD} for forming O^+ + Cl^+ from Cl_2O^{2+}.

	Dissociation mechanism		KER/eV	F_{KERD}/eV	Relative Importance of KER
Single KER	Direct		7.2	6.0	
	Sequential		9.2	5.5	
Multiple KER	Direct	KER 1	7.3	1.5	0.96
		KER 2	1.5	1.5	0.04
	Sequential	KER 1	9.0	1.5	0.96
		KER 2	1.5	1.5	0.04

The coincidence peak for the Cl^+ + Cl^+ reaction has also been modelled for the direct and sequential (initial charge separation) fragmentation mechanisms. Due to the majority of this peak being masked under the "pickup" peak (Fig. 5.4), it is not possible to discern whether a single or multiple KER occurs upon formation of this ion pair nor to determine an accurate value of F_{KERD}. So the result of the simulation procedure for the Cl^+ + Cl^+ ion pair is a single value of the KER obtained for the two different mechanisms (Table 5.4).

Table 5.4 Potential values of KER and F_{KERD} for forming Cl^+ + Cl^+ from Cl_2O^{2+}.

Dissociation mechanism	KER /eV
Direct	3.3
Sequential	3.5

From the potential KERs derived from the simulation procedure, the corresponding potential values of the energy of the dication state $E(Cl_2O^{2+})$ from which the particular dissociation reaction occurs is obtained using Eq. 3.13. A summary of the potential KER and F_{KERD} values for all the dissociation reactions observed for Cl_2O^{2+}, together with the corresponding $E(Cl_2O^{2+})$ values are listed in Table 5.5. In the calculations of $E(Cl_2O^{2+})$, the fragment ions and neutral atoms are assumed to be formed with no internal energy. Therefore, any value of the dication state energy derived in this way should be considered a lower limit.

Table 5.5 Summary of the potential values of KER, F_{KERD} and $E(Cl_2O^{2+})$ for the dissociation reactions of Cl_2O^{2+}.

Dissociation reaction	Dissociation mechanism	KER /eV	F_{KERD} /eV	$E(Cl_2O^{2+})$ /eV
$Cl^+ + ClO^+$	Direct	5.2	2.0	30.6
$O^+ + Cl^+$	Direct	7.3	1.5	38.2
		1.5	1.5	32.4
	Sequential	9.0	1.5	39.9
		1.5	1.5	32.4
$Cl^+ + Cl^+$	Direct	3.3	—	33.5
	Sequential	3.5	—	33.7

Determination of the Appearance Energy

The appearance energies of the $Cl^+ + ClO^+$ and $O^+ + Cl^+$ ion pairs have been determined by evaluating the ratio of the yield Y of each dissociation reaction to the number of coincidence starts S at electron energies from 25 to 80 eV. Fig. 5.6 shows plots of Y/S against electron energy for the $Cl^+ + ClO^+$ and $O^+ + Cl^+$ ion pairs.

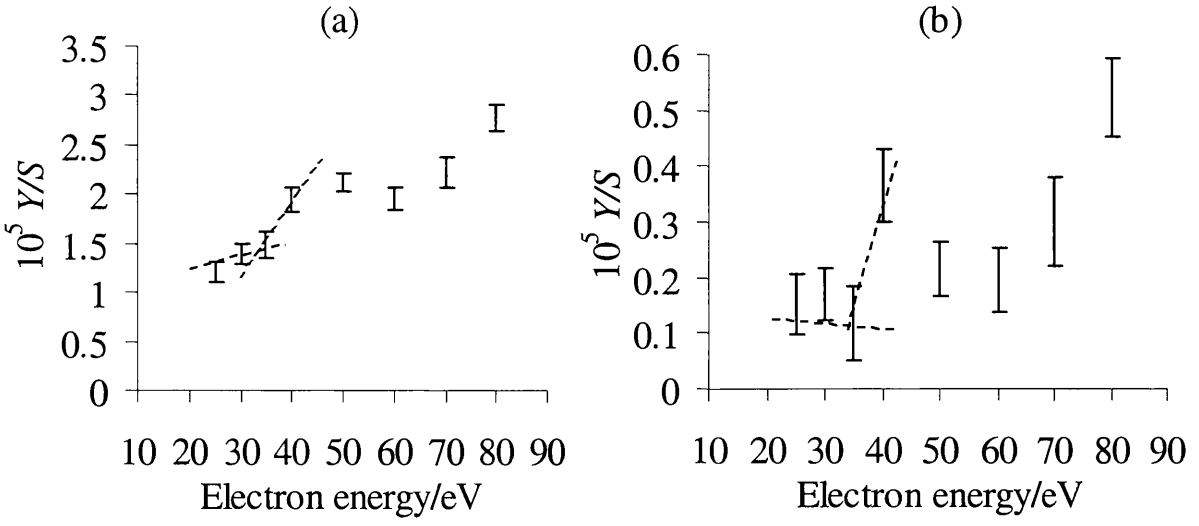

Fig. 5.6 Plot of the ratio of Y/S as a function of electron energy for (a) $Cl^+ + ClO^+$ and (b) $O^+ + Cl^+$. These plots can be interpreted to yield the appearance energy of the lowest energy dication state responsible for each decay reaction. The dashed lines in the figure are to guide the eye.

As has been explained in Chapter 4, the plots of *Y/S* can be extrapolated to the non-zero background level to obtain values of the appearance energy of the relevant ion pair, as indicated by the dashed lines in Fig. 5.6.

The appearance energy for the fragment ion pairs of Cl_2O^{2+} could not be determined to the usual accuracy due to weak signals at low electron energies and the poor counting statistics arising because the degradation of the filament necessitates short run times. However, from Fig. 5.6a, the appearance energy for the $Cl^+ + ClO^+$ ion pair is estimated to be 33 ± 2 eV whereas for the $O^+ + Cl^+$ ion pair the appearance energy is approximately 35 ± 5 eV (Fig. 5.6b). These values are listed in Table 5.6 and are interpreted as the energy of the lowest-lying states responsible for the dicationic decay reaction forming the relevant ion pair. The appearance energy for the $Cl^+ + Cl^+$ dissociation reaction was not determined as the uncertainties in *Y/S* for this minority process at low electron energies were so large as to make an evaluation of the appearance energy impractical.

Table 5.6 Experimentally derived appearance energies for the $Cl^+ + ClO^+$ and $O^+ + Cl^+$ ion pairs formed from Cl_2O^{2+}.

Dissociation reaction	Appearance energy /eV
$Cl^+ + ClO^+$	33 ± 2
$O^+ + Cl^+$	35 ± 5

As explained in Chapter 3 and illustrated in Chapter 4, it is hoped that some mechanistic information can be derived for three-body dication dissociation reactions by comparing the appearance energy of a three-body dication fragmentation channel with values of $E(Cl_2O^{2+})$ calculated using the potential KER values derived from the simulation procedure. However, as can be seen from Table 5.5, for the three-body dissociation reactions of Cl_2O^{2+}, there is no discernible difference between the KERs, and hence values of $E(Cl_2O^{2+})$, obtained for the different dissociation mechanisms. In addition, the uncertainty in the appearance energy obtained for $O^+ + Cl^+$ is large and no appearance energy can be measured for the $Cl^+ + Cl^+$ ion pair. Consequently, it is not possible to assign fragmentation mechanisms for the three-body dissociation reactions of Cl_2O^{2+}. As shown below, information concerning the energetics of the dissociative dicationic states can still be obtained.

5.3.2 Discussion

5.3.2.1 Single Ionization

There have been a number of previous reports in the literature concerning the ionization and fragmentation of Cl_2O^+, using both photoionization mass spectrometry (PIMS) and electron-impact

mass spectrometry (EIMS). A single PIMS study of Cl_2O has been reported[12] and a number of EIMS studies at differing ionizing electron energies: Fisher[13] and Freeman *et al*[14] performed their electron-impact experiments at 50 eV and Cordes *et al*[15] at 70 eV.

The PIMS investigation[12] detected Cl_2^+ and Cl_2O^+ at a photon energy of 11.8 eV and ClO^+ at 23.6 eV, the formation of the latter ion due to second-order light. They also detected $HOCl^+$, an impurity that the authors attribute to the reaction of Cl_2O with water adsorbed on the HgO. The most abundant ion signal was ClO^+ but since the ClO^+ ions were formed using a different ionizing photon energy to the Cl_2^+ and Cl_2O^+ ions, with the relative intensity of the second-order light unquantified, it is hard to make an informative comparison between the relative intensities obtained in the current work and the data they report. This PIMS study did, however, determine the appearance energy of the ClO^+ fragment ion to be 12.29 eV.

The EIMS studies[13-15] all observed Cl^+, ClO^+, Cl_2^+ and Cl_2O^+, the ClO^+ fragment being the most abundant ion and the intensities of the ion signals determined in these EIMS studies are given in Table 5.7. The investigation by Fisher detected trace amounts of impurities from air and, despite purification of the sample at reduced temperatures and pressures, he reported that contributions from the ionization of Cl_2 were present. Freeman *et al* reported the presence of impurities in the spectrum from air, water and protonated species, although in this investigation some purification of the Cl_2O sample was performed. Cordes *et al* also purified their Cl_2O sample at a reduced temperature and pressure and, in addition to Cl^+, ClO^+, Cl_2^+ and Cl_2O^+, they also reported the observation of O^+ and Cl^{2+}.

Table 5.7 Comparison of the ion yields observed in EIMS studies of Cl_2O.

	Electron energy /eV	Ions observed in EIMS spectra					
		O^+	Cl^{2+}	Cl^+	ClO^+	Cl_2^+	Cl_2O^+
Present work	50	—	—	41.3	100	14.0	48.2
Fisher[13]	50	—	—	1.04	100	5.4	57.3
Freeman *et al*[14]	50	2.12	—	58.3	100	21	54.7
Cordes *et al*[15]	70	0.88	0.51	25.0	100	11.9	52.8

In the present study, at electron energies ranging from 30 to 450 eV, the parent ion Cl_2O^+ and fragment ions, Cl_2^+, ClO^+ and Cl^+ with the expected relevant isotopic abundance, were detected (Fig. 5.2). The plots of σ_r^{si} against electron energy for the Cl_2O^+ and Cl^+ ions show an initial increase in σ_r^{si} as the electron energy is raised (Fig. 5.3), due to the increased likelihood of ionic fragmentation with increased electron energy and associated ionic excitation. For the Cl_2^+ ion, the uncertainties in the values of σ_r^{si} are so large at low electron energies that little information can be extracted from the plot of σ_r^{si} against electron energy.

In this study, the intensity of the parent ion Cl_2O^+ relative to the ClO^+ fragment ion at 50 eV, the ionizing energy used in the two earlier EIMS studies by Fisher[13] and Freeman *et al*[14], is 48.2% (Table 5.7, Fig. 5.3). This value is in reasonable agreement with the relative intensities given in the other EIMS studies. The reported intensities of the Cl_2^+ ion, relative to ClO^+, are more wide ranging. In the current work at 50 eV, the relative intensity of Cl_2^+ is 14.0% (Table 5.7, Fig. 5.3), a value lower than that measured by Freeman *et al*, but higher than those determined by Fisher and Cordes *et al*, despite Cordes *et al* performing their experiments at electron energies 20 eV higher. The higher value obtained by Freeman *et al* is perhaps due to an impure sample of Cl_2O containing some unreacted Cl_2. The discrepancy between the relative intensity of Cl_2^+ obtained here and those quoted by Fisher and Cordes *et al* is possibly due to the inefficient collection of the superthermal fragment ions from the dissociation of Cl_2O^+ in those studies. Despite highly energetic ionic fragments being inefficiently detected with the current apparatus set-up (Chapter 3), many fragments formed from dissociative single ionization are likely to have kinetic energies of less than 0.3 eV and so will still be detected. Although the relative intensity of Cl_2^+ in the current work is higher than that reported in the studies by Fisher and Cordes *et al*, despite the acknowledgement by Fisher that his sample may have contained traces of Cl_2, it is felt that this higher Cl_2^+ value obtained here is reliable because of the efforts made to purify the Cl_2O sample and the quantifiable efficiency of the apparatus for collecting the ionic fragments from single ionization.

The relative intensity of Cl^+ obtained in the current experiments is 41.3% (Table 5.7, Fig. 5.3), which again is lower than the value measured by Freeman *et al* and higher than those given by Fisher and Cordes *et al*. Similarly to the above discussion, the high relative intensity of Cl^+ quoted by Freeman *et al* is probably due to the detection of Cl^+ fragments from the dissociative ionization of any Cl_2 or HOCl present in the sample, in addition to the Cl^+ fragments from Cl_2O^+. The low relative intensities of Cl^+ obtained by Fisher and Cordes *et al* are probably a result of the especially inefficient collection of superthermal atomic fragment ions. The PIMS study[12] detected no Cl^+ fragments but the spectra were probably recorded at ionizing energies below the appearance energy of the Cl^+ ion. Cordes *et al* also noted the presence of O^+ and Cl^{2+} in the mass spectrum, fragments not observed in any other investigations. There are a number of possible explanations for the presence of the O^+ and Cl^{2+}. One possible explanation is that the formation of O^+ and Cl^{2+} occurs from dissociative multiple ionization of Cl_2O. As discussed in Section 5.3.1.2, O^+ is a major dication dissociation product and therefore the detected O^+ ions could be formed from dissociative double ionization. The double ionization energy of Cl_2O can be estimated as 30.63 eV[25] and so at the ionizing electron energy employed in this EIMS study (70 eV) double ionization of Cl_2O is undoubtedly occurring. However, as mentioned above, it seems unlikely that the apparatus used by Cordes *et al* is able to detect highly energetic ions such as those formed from dissociative double

ionization. Also, there is no evidence of the formation of a deferred charge separation of Cl_2O^{2+} forming Cl^{2+}. Perhaps the most likely explanation is that, although they observed no other impurities, the O^+ may arise from traces of O_2 and the Cl^{2+} could arise from the dissociative multiple ionization of Cl_2, both of which could be present as impurities in the Cl_2O sample. The triple ionization potential of CS_2 is 54.3 ± 0.5 eV[26] and the triple ionization energy of Cl_2 would be at a comparable energy. Recent work[27] has shown that Cl^{2+} is, indeed, formed upon dissociation of Cl_2^{3+} and therefore, the Cl^{2+} fragment ions observed in the mass spectrum of Cl_2O recorded by Cordes *et al*[15] are probably formed by the dissociation of multiply charged Cl_2.

Despite the pioneering efforts of these early EIMS[13-15] investigations of Cl_2O, the above comparison of the data obtained in those studies and that obtained in the current work (Table 5.7) highlights the problems involved in investigating the ionization of reactive molecules such as Cl_2O. These problems involve the preparation of a pure sample and the efficient detection of all the ions formed upon single ionization. Given the efforts made in this work to obtain as pure a sample of Cl_2O as possible, and the design of the apparatus for the efficient collection of the majority of the energetic fragments from dissociative single ionization, the values of σ_r^{si} for the parent and fragment ions of Cl_2O^+ given in Table 5.1 and Fig. 5.3 are likely to be the most reliable to date.

5.3.2.2 Double Ionization

In the electron-impact mass spectrum of Cl_2O (Fig. 5.2) no stable parent dication (Cl_2O^{2+}) or daughter dications are observed. This implies that no bound regions of the dication potential energy surfaces can be accessed by a vertical transition from the equilibrium geometry of the neutral molecule. The coincidence spectra (Fig. 5.4) show that the dissociative double ionization of Cl_2O proceeds *via* a two-body dissociation reaction to form $Cl^+ + ClO^+$ and three-body reactions to form $O^+ + Cl^+$ and $Cl^+ + Cl^+$.

$Cl^+ + ClO^+$

For the $Cl^+ + ClO^+$ dissociation reaction, the simulation of the coincidence peak indicates that there is a single KER associated with this dication dissociation reaction. From Table 5.5 it can be seen that the estimate of the energy of the state of Cl_2O^{2+} dissociating to form $Cl^+ + ClO^+$, derived from the KER, is 30.6 ± 0.2 eV. This evaluation of $E(Cl_2O^{2+})$ from the KER, however, assumes that the fragment ions are formed with no internal energy. If excited states of Cl^+ or ClO^+ are formed then the value of $E(Cl_2O^{2+})$ will lie higher in energy. There is no experimental information on whether Cl^+ or ClO^+ are formed in excited electronic states, but consideration of the symmetry of the dissociation may be informative.

From studies of the photoelectron spectrum of Cl_2O,[8,28] the ground state electron configuration of Cl_2O^{2+} can be assumed to be $...a_2^2a_2^1b_2^2$; that is two b_1 electrons are removed upon double ionization to give a $^1A_1$ state under C_{2v} symmetry. Following the building-up principles from unlike groups to form a non-linear molecule,[29] it is found that the dissociation of Cl_2O^{2+} from its ground electronic state to form the fragment ions Cl^+ (^3P_g) and ClO^+ ($^3\Sigma^-$) in their ground states[30,31] is a symmetry and spin-allowed transition, suggesting that the two fragment ions are likely to be formed in these electronic states. However, the dissociation of ground state Cl_2O^{2+} to form one fragment ion in its first excited state, either $Cl^+(^1D)$ or $ClO^+(^1\Delta)$, and the other in its ground state are both spin-forbidden transitions, which again supports the assumption that the product ions are formed with no excess electronic energy. Making an allowance for the possibility of vibrational excitation will perhaps increase the error associated with $E(Cl_2O^{2+})$ to ± 0.5 eV. As can be seen from Fig. 5.6, it is apparent that the appearance energy of the $Cl^+ + ClO^+$ ion pair is 33 ± 2 eV, which is consistent with the calculated value of $E(Cl_2O^{2+})$ as 30.6 ± 0.5 eV. Due to the large uncertainties associated with the determination of the appearance energy for this pair of ions, and despite the assumptions involved in the determination of $E(Cl_2O^{2+})$ from the coincidence peak widths, it is felt that the value of $E(Cl_2O^{2+})$ as 30.6 ± 0.5 eV is the more realistic estimate of the energy of the state of Cl_2O^{2+} which dissociates to form $Cl^+ + ClO^+$.

The value of the double ionization energy of Cl_2O derived using the 'rule of thumb'[25] is 30.63 eV (± 10%). This estimate of the double ionization energy of Cl_2O is in very good agreement with the value of the dication state energy for the lowest electronic state dissociating to form $Cl^+ + ClO^+$, 30.6 ± 0.5 eV, suggesting that this is the ground state of the Cl_2O dication.

$O^+ + Cl^+$

For the dissociation of Cl_2O^{2+} to form the $O^+ + Cl^+$ ion pair, a determination of the appearance energy could not be obtained to the usual accuracy (± 2 eV) as the signal is very weak at low electron energies and the degradation of the filament by Cl_2O increases the statistical uncertainties in the spectra. However, from Fig. 5.6, an estimate of the appearance energy as 35 ± 5 eV can be made.

Although the simulation of the coincidence peak for this reaction yields two sets of differing KER values for the possible dissociation mechanisms (Table 5.3), there is no discernible difference between the potential KERs, and hence values of $E(Cl_2O^{2+})$, obtained for direct and sequential mechanisms. Coupled with this is an appearance energy with a large uncertainty associated with it for comparison with the potential values of $E(Cl_2O^{2+})$ and so the mechanism by which Cl_2O^{2+} dissociates to form $O^+ + Cl^+$ cannot be definitively assigned.

The simulation of the coincidence peak indicates that two distinct electronic states of Cl_2O^{2+} dissociate to form the $O^+ + Cl^+$ fragment ion pair, the first state at an energy of 32.4 eV and the second at *ca.* 39 eV (Table 5.5). Due to a difference of 2 eV between the energy of the lowest state dissociating to form $O^+ + Cl^+$ and the ground state of Cl_2O^{2+} deduced to be responsible for the formation of $Cl^+ + ClO^+$, these two electronic states of Cl_2O^{2+} are likely to be distinct. From the relative importance attributed to the two KERs required to the fit the simulated spectrum to the experimental data, the probability of forming $O^+ + Cl^+$ from the higher-lying electronic state (39 eV) is significantly larger than from the lowest-lying state (32.4 eV). Therefore, as discussed below, it is possible that the dissociation of Cl_2O^{2+} to form $O^+ + Cl^+$ occurs predominantly from the dication state at 39 eV with a small proportion of these ion pairs being formed from the state at 32.4 eV.

$Cl^+ + Cl^+$

For the remaining three-body dissociation reaction of Cl_2O^{2+}, forming $Cl^+ + Cl^+$, no measurement of the appearance energy was possible. As with the $O^+ + Cl^+$ ion pair, it is not possible to distinguish which fragmentation pathway is actually followed to form $Cl^+ + Cl^+$ because there is no evaluation of the appearance energy of this ion pair for comparison with the potential values of $E(Cl_2O^{2+})$ derived from the KER.

The simulation of the coincidence peak for these product ions yielded an evaluation of the energy of the dication state responsible for the $Cl^+ + Cl^+$ dissociation reaction as *ca.* 33.6 eV (Table 5.5). The value of $E(Cl_2O^{2+})$ associated with the state which dissociates to form $Cl^+ + Cl^+$, 33.6 eV, is close to the lowest energy dication state that was deduced to be responsible for the formation of $O^+ + Cl^+$ (32.4 eV). However, the lack of accurate data on appearance energies for either of these three-body dissociation reactions means that it is not possible to say whether or not these two ion pairs ($O^+ + Cl^+$ and $Cl^+ + Cl^+$) are formed as the result of the dissociation of two distinct states of Cl_2O^{2+}. It is possible that an electronic state of Cl_2O^{2+} at an energy of ~33 eV dissociates predominantly to form $Cl^+ + Cl^+$ with a minor reaction channel to form $O^+ + Cl^+$.

5.3.3 Conclusion

This section of the chapter presents the results of a one-dimensional investigation of the single and double ionization of Cl_2O. Time-of-flight mass spectrometry is used to determine the values of σ_r^{si} of Cl_2O for incident electron energies from 30 to 450 eV. Stable parent ions Cl_2O^+ and Cl^+, Cl_2^+ and ClO^+ fragment ions and their isotopes were detected, the most abundant ion being the ClO^+ fragment ion.

Ion-ion coincidence experiments have been performed to study the formation and fragmentation of Cl_2O^{2+}. Coincidence peaks due to the dissociation of Cl_2O^{2+} to form $Cl^+ + ClO^+$, $O^+ + Cl^+$ and $Cl^+ + Cl^+$ fragment ion pairs (and their isotopomers) were observed in the coincidence spectrum. The comparison of simulations of the coincidence spectra with the experimental data indicates that the dissociation of the dication to form the $O^+ + Cl^+$ ion pair involves a multiple kinetic energy release, suggesting that this three-body dissociation reaction of Cl_2O^{2+} occurs from two different dication electronic states.

The values derived for the energies of the dication states responsible for forming the observed ion pairs indicate that there are two distinct dication electronic states that dissociate to form the $O^+ + Cl^+$ pair. In addition, it seems clear that the two-body dissociation of Cl_2O^{2+} to form $Cl^+ + ClO^+$ occurs from the ground electronic state of Cl_2O^{2+}, thus providing a first estimate of the double ionization energy of Cl_2O as 30.6 ± 0.5 eV.

5.4 Two-Dimensional Studies

5.4.1 Data Analysis

5.4.1.1 Single Ionization

A typical singles spectrum obtained using the modified experimental arrangement employed in the 2D studies is shown in Fig. 5.7. As can been seen in the figure, the parent ion Cl_2O^+ and fragment ions Cl_2^+, ClO^+, Cl^+ and O^+ are observed in the singles spectrum.

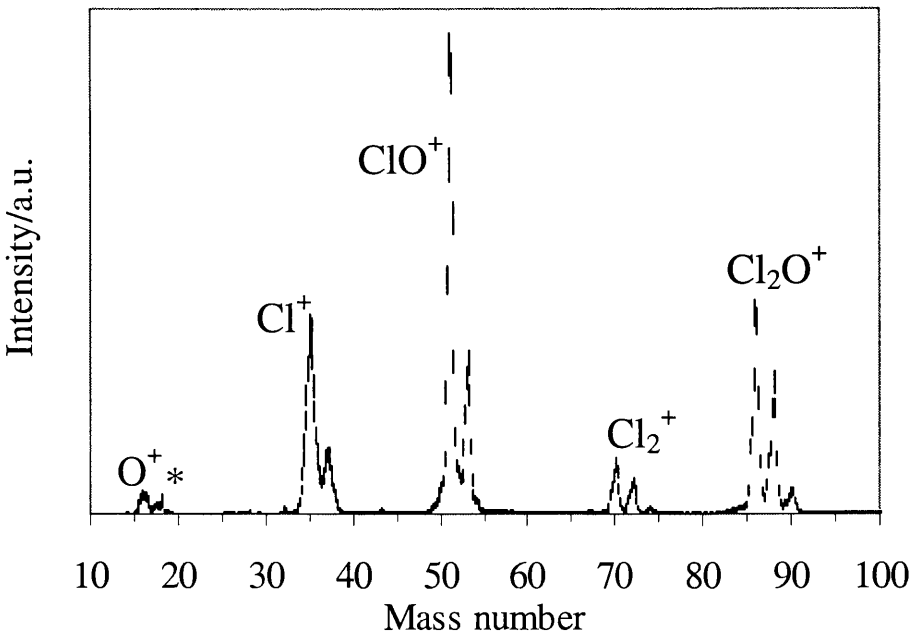

Fig. 5.7 Typical singles spectrum of Cl_2O recorded at 250 eV using the 2D apparatus set-up. The peak marked with an asterisk corresponds to signals from the residual gas. To aid interpretation, the error bars shown have been scaled to represent twenty standard deviations.

Singles mass spectra were recorded at 70, 100, 250 and 320 eV and the relative partial ionization cross section σ_r^I for the formation of the singly charged ions from Cl_2O, relative to the parent ion Cl_2O^+, have been determined using Eq. 3.19 and are given in Table 5.8. For the chlorinated ions, the ion signals of both chlorine isotopes were determined and then combined to give a single value of σ_r^I for each ion. Only one singles spectrum was recorded at each electron energy because it was necessary to run at very low count rates to avoid rapid degradation of the filament and consequently the data acquisition time had to be increased in order to obtain adequate counting statistics.

Table 5.8 Values of σ_r^I for the formation of the indicated product ion from Cl_2O (the numbers in parentheses indicate the statistical error in the last figure of each cross section).

Electron energy	σ_r^I			
/eV	O^+	Cl^+	ClO^+	Cl_2^+
70	0.169(1)	1.529(6)	2.076(8)	0.264(2)
100	0.190(1)	1.671(5)	2.167(6)	0.252(2)
250	0.149(1)	1.407(4)	1.985(6)	0.235(1)
320	0.179(1)	1.468(5)	2.069(6)	0.324(2)

As discussed in Chapter 3, using the 2D experimental arrangement, there is now certainly a significant contribution from the double ionization of Cl_2O to the fragment ion signals in the singles spectrum. Therefore, the values of σ_r^I given in Table 5.8 cannot be directly compared with the data derived from the one-dimensional investigation as values of σ_r^{si} were obtained from the one-dimensional time-of-flight mass spectra. In order to determine values of σ_r^{si} from the singles spectrum, the contribution of double ionization to the singles spectrum must be ascertained and subtracted from the fragment ion signal intensities using Eq. 3.25. In these calculations the value of f_i, derived from the normalisation experiments performed on CF_4 (Chapter 3), is 0.063 ± 0.014. The values of σ_r^{si} for the fragment ions of Cl_2O obtained from the singles spectrum are listed in Table 5.9.

Table 5.9 Values of σ_r^{si} for the formation of the indicated product ion from Cl_2O^+ (the numbers in parentheses indicate the statistical error in the last figure of each cross section).

Electron energy	σ_r^{si}			
/eV	O^+	Cl^+	ClO^+	Cl_2^+
70	0.074(22)	1.178(79)	1.951(29)	0.264(2)
100	0.027(36)	0.980(154)	1.947(50)	0.252(2)
250	0.078(16)	1.009(89)	1.823(37)	0.235(1)
320	0.061(27)	0.997(105)	1.937(30)	0.324(2)

5.4.1.2 Double Ionization

A pairs spectrum of Cl_2O^{2+} recorded at an ionizing electron energy of 250 eV is shown in Fig. 5.8.

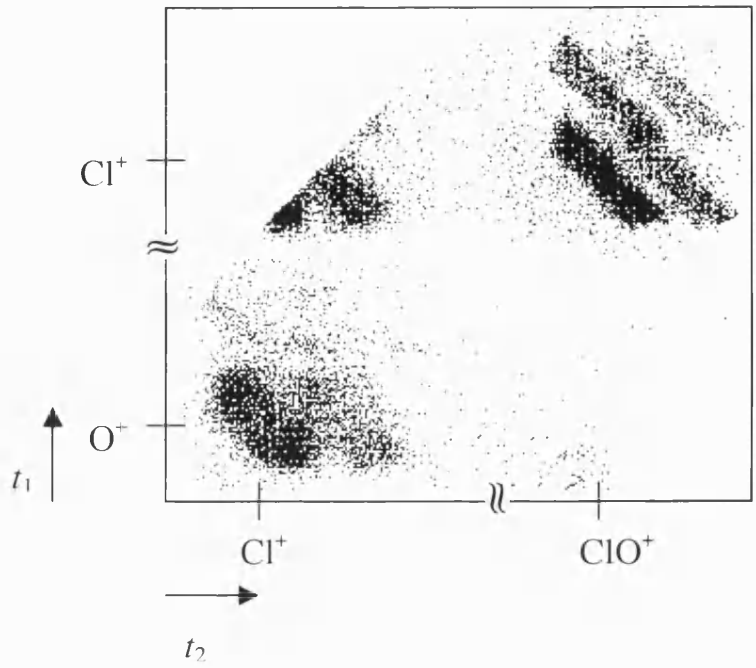

Fig. 5.8 Subtracted pairs spectrum of Cl_2O^{2+} recorded at 250 eV.

In agreement with the one-dimensional coincidence spectra of Cl_2O^{2+}, the ion pairs $Cl^+ + ClO^+$, $O^+ + Cl^+$ and $Cl^+ + Cl^+$ are observed in the pairs spectrum along with their isotopomers and the ion pair formed by the two-body dication dissociation reaction, $Cl^+ + ClO^+$, is the most abundant. Only a proportion of the peak corresponding to the identical ion pair $Cl^+ + Cl^+$ is observed in the pairs spectrum since it is partially obscured by the dead time of the CFD. The isotope pairs $^{35}Cl^+ + {}^{35}Cl^+$ and $^{35}Cl^+ + {}^{37}Cl^+$ are partially observed but, considering the relevant isotopic abundance, the intensity of the third isotope pair $^{37}Cl^+ + {}^{37}Cl^+$ is significantly weaker than the other $Cl^+ + Cl^+$ isotopic ion pairs and is indistinguishable in the pairs spectrum.

As the pairs spectra are recorded concurrently with the singles spectra, pairs spectrum of Cl_2O^{2+} have been recorded at the same ionizing electron energies, 70 100, 250 and 320 eV. Any false coincidences, pairs of ions not formed by the same dication dissociation event, present were subtracted from the pairs spectrum.

In Fig. 5.8, recorded at 250 eV, it is apparent that the mass resolution is very good at this electron energy and the isotopic peaks of the chlorinated ion pairs are clearly defined. It is therefore possible to extract information concerning the intensity and slope of the individual isotopomers in each dissociation reaction. However, at the lower electron energies it is difficult to generate as well-defined electron pulses and so the isotopic peaks become much broader, often merging together and making it difficult to extract data for each individual peak.

For each pairs spectrum recorded, the intensity of the ion pair signals was determined by summing the number of counts detected within the area of the relevant isotopomer peak (Chapter 3). But, due to the peak broadening mentioned above, at 70 eV it is not possible to determine the intensity of each individual isotopic peak and so the total intensity for the all the isotopic ion pairs in the dissociation reaction is obtained. The intensity of each ion pair formed by the dissociation of Cl_2O^{2+}, relative to the total number of ion pairs observed in the subtracted pairs spectrum, I_{pair}/I_{total} is given in Table 5.10.

Table 5.10 Values of I_{pair}/I_{total} for the dissociation reactions of Cl_2O^{2+} (the numbers in parentheses indicate the statistical error in the last figure of each value).

Electron energy	I_{pair}/I_{total}		
/eV	$Cl^+ + ClO^+$	$O^+ + Cl^+$	$Cl^+ + Cl^+$
70	0.395(18)	0.387(17)	0.218(12)
100	0.418(10)	0.283(8)	0.300(8)
250	0.453(14)	0.245(10)	0.303(11)
320	0.380(12)	0.325(11)	0.295(10)

For the pairs spectrum recorded at 250 eV the slope b of the peaks corresponding to the dissociation reactions of Cl_2O^{2+} were also determined. The values of b were only determined at 250 eV since, as mentioned above, the mass resolution of the spectrum is optimised at this electron energy and so the isotope peaks are well resolved. As discussed in Chapter 3, the slopes of the peaks in the pairs spectra can potentially provide information on dication dissociation mechanisms.

Evaluation of the Contribution of Double Ionization to the Singles Spectrum

In order to determine values of σ_r^{si} for the fragment ions of Cl_2O, the contribution of dissociative double ionization to the singles spectra must be subtracted. Thus, it is necessary to convert the pairs spectrum into a conventional mass spectrum which will contain only signals from fragment ions formed upon dicationic dissociation. Fig. 5.9 shows the double ionization mass spectrum derived by the conversion of the pairs spectrum recorded at 250 eV. Note that no Cl_2^+ or Cl_2O^+ are observed in the double ionization mass spectrum. The absence of any Cl_2^+ fragment ions indicates that there is no dissociation of Cl_2O^{2+} involving bond formation between the terminal chlorine atoms to form Cl_2^+. Such ionic dissociation involving dramatic rearrangement of the molecule to form a fragment ion can occur, *e.g.* the formation of Cl_2^+ from the terminal Cl atoms of Cl_2O^+ and S_2^+ from CS_2^+.[32] Dissociation reactions such as these can also occur from dications, *e.g.* the formation of H_3^+ from CH_3OH^{2+}.[33] However, the absence of any Cl_2^+ in the double ionization mass spectrum indicates that this type of dissociation is not occurring from Cl_2O^{2+}.

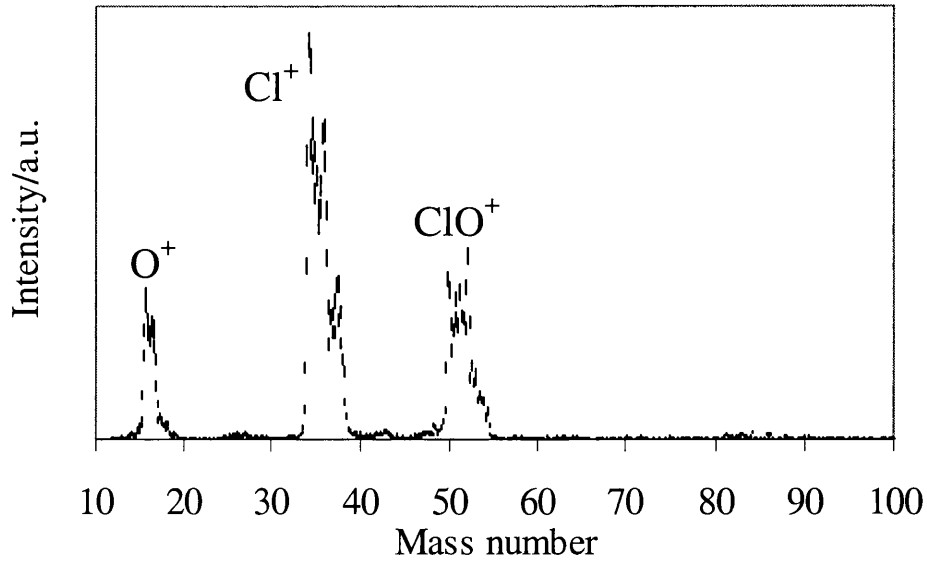

Fig. 5.9 Double ionization mass spectrum of Cl_2O, converted from pairs spectrum recorded at 250 eV. The error bars are derived from the counting statistics and represent two standard deviations.

The double ionization fragment ion signal intensities are obtained from the double ionization mass spectrum and hence, the contribution of fragment ions from the dissociation of Cl_2O^{2+} can be calculated and subtracted from the ion signal intensities in the singles spectrum using Eq. 3.25. Consequently, the values of σ_r^{si} for the fragment ions of Cl_2O can be determined (Eq. 3.26) and these values can be directly compared with the values of σ_r^{si} derived from the one-dimensional investigation.

Determination of the Ratio of Double-to-Single Ionization Cross Sections

A first estimate of the double-to-single ionization cross section ratio σ^{2+}/σ^{+} for Cl_2O can be obtained using Eq. 3.39. The ratios of the total σ^{2+}/σ^{+} for Cl_2O, at the range of electron energies employed in this part of the study, are given in Table 5.11 and plotted in Fig. 5.10.

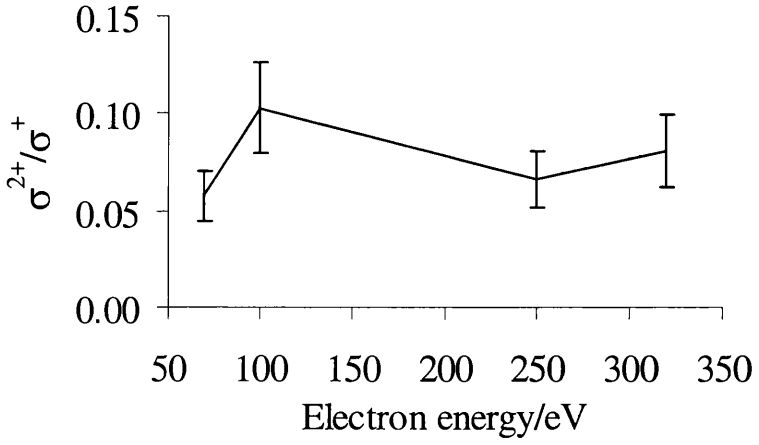

Fig. 5.10 Ratio of σ^{2+}/σ^{+} for Cl_2O. The error bars shown represent two standard deviations.

Table 5.11 Ratio of σ^{2+}/σ^{+} for Cl_2O (the numbers in parentheses indicate the statistical error in the last figure of each cross section).

Electron energy /eV	σ^{2+}/σ^{+}
70	0.057(13)
100	0.103(23)
250	0.066(15)
320	0.081(18)

5.4.2 Discussion

5.4.2.1 Single Ionization

In the 2D investigation of the single ionization of Cl_2O the stable parent ion, Cl_2O^+ and fragment ions Cl_2^+, ClO^+ and Cl^+ are observed in the singles spectrum, the ClO^+ ion being the most abundant. This is consistent with the time-of-flight mass spectrum obtained in the one-dimensional study of Cl_2O (Fig. 5.2). However, in the singles spectrum (Fig. 5.7), O^+ fragment ions are also observed, fragments which were not seen in the one-dimensional time-of-flight mass spectrum of Cl_2O.

As explained in Chapter 3, energetic fragment ions from both dissociative single and double ionization will now be detected and appear in the singles spectrum as there is no discrimination against the detection of energetic fragments in the 2D apparatus set-up. Fragment ions formed by the dissociation of Cl_2O^{2+} may be observed in the singles spectrum if the second ion of an ion pair is not detected within the specified time window of the data acquisition algorithm (Chapter 2). This increase in detection efficiency for energetic ions is apparent in Table 5.8 and Table 5.9. Indeed, most notably the value of σ_r^I of the O^+ fragment ion is 0.15 at 250 eV, whereas the value of σ_r^{si} derived by subtracting any double ionization contribution is considerably lower. From the studies of the double ionization of Cl_2O, O^+ is a major dicationic dissociation product and therefore, it appears that O^+ fragments from Cl_2O^{2+} are dominating the O^+ ion signal in the singles spectrum. In addition, no O^+ fragments were observed in the one-dimensional single ionization study of Cl_2O, again indicating that the O^+ signals in the singles spectra are due mostly to double ionization. The Cl^+ ion is the most significant dication dissociation product and therefore, it is obvious that Cl^+ fragments from Cl_2O^{2+} are contributing to the Cl^+ ion signal in the singles spectrum, in addition to the Cl^+ fragments from Cl_2O^+. Within the error limits, the values of σ_r^I and σ_r^{si} of ClO^+ given in Table 5.8 & Table 5.9 are consistent with one another, indicating that double ionization does not significantly contribute to the ClO^+ ion signal. Since Cl_2^+ fragment ions are not formed by dicationic dissociation,

as expected, the values of σ_r^I and σ_r^{si} of Cl_2^+ given in Table 5.8 & Table 5.9 are in agreement with one another.

Table 5.12 shows the comparison of the values of σ_r^{si} obtained in the one-dimensional and 2D experiments. From Table 5.12, it is apparent that the values of σ_r^{si} of the fragment ions derived from the time-of-flight mass spectra (one-dimensional work) and singles spectra (2D work) are generally in good agreement with one another. No data was recorded in the one-dimensional investigation of Cl_2O at 320 eV, but as can be seen from Table 5.1 and Fig. 5.3, there is little variation in the values of σ_r^{si} of the ions between 300 and 350 eV. So, for comparison between the one-dimensional and 2D work, the values of σ_r^{si} obtained at 300 eV in the one-dimensional study are quoted in Table 5.12.

Table 5.12 Comparison of σ_r^{si} for the fragment ions of Cl_2O in the one-dimensional (time-of-flight mass spectrum) and 2D (singles spectrum) studies (the numbers in parentheses indicate the statistical error in the last figure of each cross section).

Electron energy /eV	σ_r^{si}							
	O^+		Cl^+		ClO^+		Cl_2^+	
	1D	2D	1D	2D	1D	2D	1D	2D
70	—	0.074(22)	0.86(11)	1.178(79)	2.04(12)	1.951(29)	0.28(7)	0.264(2)
100	—	0.027(36)	0.78(6)	0.980(154)	1.96(6)	1.947(50)	0.26(10)	0.252(2)
250	—	0.078(16)	0.80(8)	1.009(89)	2.10(11)	1.823(37)	0.26(9)	0.235(1)
320*	—	0.061(27)	0.77(4)	0.997(105)	2.04(11)	1.937(30)	0.24(7)	0.324(2)

* Data recorded at 300 eV in one-dimensional study.

From the comparison of the values of σ_r^{si} derived from the mass spectrum of Cl_2O recorded in the one-dimensional and 2D work (Table 5.12), it is obvious that, as stated in Section 5.3.1.1, for the one-dimensional time-of-flight mass spectra, the analysis procedure employed does indeed yield values of σ_r^{si}. This suggests that the discrimination of the one-dimensional apparatus set-up against highly-energetic fragment ions is not a significant factor when deriving values of σ_r^{si} for Cl_2O, as the majority of these energetic ions come from dissociative multiple ionization.

5.4.2.2 Double Ionization

The pairs spectra (Fig. 5.8) show that the dissociative double ionization of Cl_2O proceeds *via* a two-body dissociation reaction to form $Cl^+ + ClO^+$ and three-body reactions to form $O^+ + Cl^+$ and $Cl^+ + Cl^+$. This is consistent with the data obtained in the ion-ion-coincidence spectra recorded in the one-dimensional investigations (Fig. 5.4). In agreement with the one-dimensional coincidence spectra, the $Cl^+ + ClO^+$ peak is the most intense in the spectrum indicating that the two-body dissociation of Cl_2O^{2+} is the most frequently occurring dissociation reaction. From the pairs spectrum recorded at 250 eV, the relative intensities I_{pair}/I_{total} of the three dissociation reactions of Cl_2O^{2+}, $Cl^+ + ClO^+$, $O^+ + Cl^+$ and $Cl^+ + Cl^+$, are 1.5:1:0.8 respectively (Table 5.10).

$Cl^+ + ClO^+$

From Fig. 5.8, it can be seen that the dissociation of Cl_2O^{2+} to form $Cl^+ + ClO^+$ gives rise to three distinct signals in the pairs spectrum corresponding to the $^{35}Cl^+ + {}^{35}ClO^+$, $^{35/37}Cl^+ + {}^{37/35}ClO^+$ and $^{37}Cl^+ + {}^{37}ClO^+$ ion pairs. The increased axial length of the central peak is due to the detection of both $^{35}Cl^+ + {}^{37}ClO^+$ and $^{37}Cl^+ + {}^{35}ClO^+$ ion pairs which overlap with one another. A 3D plot with a 2D projection of the intensities of the $Cl^+ + ClO^+$ ion pair signals is shown in Fig. 5.11.

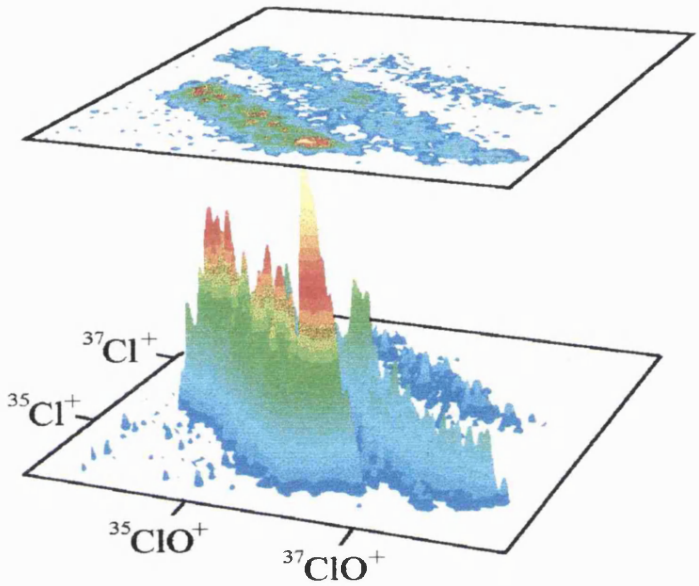

Fig. 5.11 3D plot with a 2D projection of the intensity of the dissociation reactions making up the $Cl^+ + ClO^+$ ion pair.

As shown in Fig. 5.11, the high intensity region of the peak corresponding to the $^{35}Cl^+ + {}^{35}ClO^+$ ion pair is uniform along the axial length of the peak, within the error limits of the counting statistics. This indicates that, as expected, the use of the MCP eliminates any angular discrimination and all the ion pairs formed from the dissociation of Cl_2O^{2+} are detected. The peak corresponding to the $^{35/37}Cl^+ + {}^{37/35}ClO^+$ ion pairs has a central peak, but this peak occurs at the overlap of the signals corresponding to the two ion pairs thus resulting in an area of increased signal intensity.

The dissociation of Cl_2O^{2+} to form the $Cl^+ + ClO^+$ ion pair is a two-body dissociation reaction and therefore it is expected that the peak corresponding to this ion pair in the 2D coincidence spectrum will be a narrow peak with $b = -1$,[17,34] since the two ions in the pair have equal and opposite momenta. From Table 5.13 it can be seen that the value of b for the peaks corresponding to the $^{35}Cl^+ + {}^{35}ClO^+$ dissociation reaction, within the errors in the least squares fit, is indeed unity. It was not possible to determine the value of b for the central peak corresponding to this dissociation reaction as it contains the overlapping signals from $^{35}Cl^+ + {}^{37}ClO^+$ and $^{37}Cl^+ + {}^{35}ClO^+$. For the $^{37}Cl^+ + {}^{37}ClO^+$ ion pair, the intensity of this peak is weak and therefore the error in b from the fitting procedure will be increased.

Table 5.13 Values of b for the peaks in the pairs spectrum corresponding to the ion pairs making up the $Cl^+ + ClO^+$ dissociation reaction of Cl_2O^{2+} (the number in parentheses indicates the statistical error in the last figure of each value).

Ion pair	b
$^{35}Cl^+ + {}^{35}ClO^+$	-0.98(2)
$^{37}Cl^+ + {}^{37}ClO^+$	-0.92(6)

In order to confirm that the differing apparatus set-ups in the one-dimensional and 2D investigations yield consistent data, a Monte Carlo simulation of the $Cl^+ + ClO^+$ peak was performed, in order to obtain the KER upon dissociation of Cl_2O^{2+} for forming this ion pair for comparison with the value obtained in the one-dimensional study. Table 5.14 shows the value of KER and F_{KERD} obtained from the simulation of the $Cl^+ + ClO^+$ pairs peak together with the corresponding values of $E(Cl_2O^{2+})$ derived using Eq. 3.13.

Table 5.14 Values of the KER and F_{KERD} for forming $Cl^+ + ClO^+$ from Cl_2O^{2+}, derived from the ion-ion coincidence peak widths recorded in the one and two-dimensional studies.

	KER /eV	F_{KERD} /eV	$E(Cl_2O^{2+})$ /eV
1D	5.2	2.0	30.6 ± 1
2D	5.5	1.0	30.9 ± 0.5

It is pleasing to note that the values of the KER, F_{KERD} and $E(Cl_2O^{2+})$ obtained here are in very good agreement with the values obtained from the $Cl^+ + ClO^+$ peak recorded in the one-dimensional ion-ion-coincidence spectrum (Table 5.14). The similarity of the values derived from the simulation of the coincidence peak widths again emphasises the consistency between the data obtained in the two separate investigations of the ionization of Cl_2O.

$O^+ + Cl^+$

The ion signals corresponding to the $O^+ + Cl^+$ dissociation reaction are made up of the $O^+ + {}^{35}Cl^+$ and $O^+ + {}^{37}Cl^+$ ion pairs. As can be seen from Fig. 5.8, it also appears that there are ion pair signals appearing in the spectrum above the $O^+ + Cl^+$ peak, *i.e.* at $t_1 > t_{O+}$.

Table 5.15 Values of b for the peaks in the pairs spectrum corresponding to the ion pairs making up the $O^+ + Cl^+$ dissociation reaction of Cl_2O^{2+} (the number in parentheses indicates the statistical error in the last figure of each value).

Ion pair	b
$O^+ + {}^{35}Cl^+$	-0.97(5)
$O^+ + {}^{37}Cl^+$	-1.01(7)

At 250 eV the value of b for peaks corresponding to the $O^+ + Cl^+$ dissociation reaction are *ca.* −1 (Table 5.15). Within the errors in the least squares fit, the values of b of the peaks for the two

isotopic ion pairs are the same. From the one-dimensional study of the dissociation of Cl_2O^{2+}, no definitive dissociation mechanism could be assigned to the reaction forming the $O^+ + Cl^+$ ion pair due to the similarity in the values of $E(Cl_2O^{2+})$, derived from the KER, for the possible dissociation mechanisms. If Cl_2O^{2+} dissociates directly to form $O^+ + Cl^+$ then $b = -1$ for the corresponding peaks in the pairs spectrum. If the dissociation mechanism follows a sequential pathway involving an initial charge separation to form $Cl^+ + ClO^+$ followed by the subsequent dissociation of the ClO^+ fragment ion to form O^+ then the expected slope of the $O^+ + Cl^+$ peak would be $b = -m_{O+}/m_{ClO+} = -0.31$.[17,34] From Table 5.15, the value of b for the $O^+ + Cl^+$ peaks are near unity, not -0.31 as predicted by a sequential mechanism, thus implying that the fragmentation pathway involved is perhaps a direct dissociation of Cl_2O^{2+} to form $O^+ + Cl^+$. However, the sequential decay of the dication which would give $b = -m_{O+}/m_{ClO+}$ is a limiting case since it assumes that after the initial charge separation, the ClO^+ ion has enough time to freely rotate and leave the Coulomb field of the second ion before further dissociation occurs. In fact, if the dissociation of the ClO^+ ion occurs within the Coulomb field of the Cl^+ ion then the momentum of the O^+ ion is increased, thus increasing the value of b towards -1. Although, it is still not possible to definitively assign a fragmentation mechanism to this dissociation reaction of Cl_2O^{2+}, the 2D investigation of Cl_2O^{2+} has shown that the three-body dicationic dissociation to form $O^+ + Cl^+$ is either a true Coulomb explosion (direct mechanism) or a fast sequential mechanism, with the secondary dissociation of the ClO^+ ion to form O^+ occurring within the Coulomb field of the Cl^+ fragment ion on a timescale of ~1-5 ps.

If the formation of the $O^+ + Cl^+$ ion pair is proceeding *via* a sequential dissociation of Cl_2O^{2+}, it is possible that the signals appearing in the pairs spectrum at $t_1 > t_{O+}$ may arise from the detection of pairs of slower ions which have longer flight times and therefore give rise to the secondary peak at $t_1 > t_{O+}$. The intensity of this secondary peak at $t_1 > t_{O+}$ is ~4% of the main $O^+ + Cl^+$ peak indicating that the sequential dissociation of $OClO^{2+}$ giving rise to these $O^+ + Cl^+$ ion pairs with longer flight times is a minor reaction channel. If the dissociation of Cl_2O^{2+} is proceeding *via* an initial charge separation to $Cl^+ + ClO^+$, followed by the dissociation of the ClO^+ ion [Reaction (5.XI)] over a timescale of perhaps 1 ns, then the detected ion pair, $O^+ + Cl^+$, will have longer flight times since the O^+ ion has spent some time as part of a heavier ion which would have been travelling slower.

$$\begin{array}{ccc} Cl_2O^{2+} & \rightarrow & Cl^+ + ClO^+ \\ & & \downarrow \quad \downarrow \\ & & Cl^+ + O^+ + Cl \end{array} \qquad (5.XI)$$

Therefore, some of the observed $O^+ + Cl^+$ ion pairs must be formed by a sequential dissociation of the dication. Although it is not possible to definitively assign a dication decay pathway for this dissociation reaction, triple coincidence studies[17-22] have shown that a true Coulomb explosion is

rare. So it is probable that the formation of $O^+ + Cl^+$ from Cl_2O^{2+} occurs *via* a sequential mechanism involving an initial charge separation of the dication to form $Cl^+ + ClO^+$ followed by further dissociation of the ClO^+ fragment ion to form O^+. The majority of this dissociation reaction is fast but some $O^+ + Cl^+$ ion pairs are also being formed as a result of slower dissociation of the ClO^+ ions, perhaps occurring once the ClO^+ ion has left the Coulomb field of the Cl^+ ion, which gives rise to the secondary $O^+ + Cl^+$ peak in the pairs spectrum.

$Cl^+ + Cl^+$

In the pairs spectrum of Cl_2O^{2+}, only a small portion of the $Cl^+ + Cl^+$ ion pair is observed because the signal corresponding to this identical ion pairs lies across the $t_1 = t_2$ diagonal and so a section of the $^{35}Cl^+ + {}^{35}Cl^+$ and $^{35}Cl^+ + {}^{37}Cl^+$ ion pairs are obscured by the dead time. The $^{37}Cl^+ + {}^{37}Cl^+$ ion pair was not observed in the spectrum as the yield of this ion pair is very low and indistinguishable in the pairs spectrum.

The value of b for the signals of $^{35}Cl^+ + {}^{37}Cl^+$, determined at 250 eV where the temporal resolution of the electron beam is optimised, is –0.96. The slope of the peak corresponding to the $^{35}Cl^+ + {}^{35}Cl^+$ ion pair has not been determined as the area of the peak observed in the spectrum is small and is therefore not representative of the entire peak. As with the $O^+ + Cl^+$ ion pair, in the one-dimensional study of the dissociation of Cl_2O^{2+}, no definitive mechanism was assigned for the formation of $Cl^+ + Cl^+$ due to the lack of experimental data for comparison with the derived values of $E(Cl_2O^{2+})$. The fragmentation mechanism could be a direct dissociation of the dication which would account for the -0.96 slope of the $Cl^+ + Cl^+$ peak. If a sequential pathway was followed then it would be expected that for the $Cl^+ + Cl^+$ peak b = -0.7,[17,34] but as explained for the $O^+ + Cl^+$ peak this is a limiting value and if the mechanism was sequential then the value of b could lie anywhere between –0.7 and –1.

As with the $O^+ + Cl^+$ ion pair, although it is not possible to definitively assign a fragmentation mechanism to this dissociation reaction of Cl_2O^{2+}, it is apparent that the decay pathway is either a true Coulomb explosion or a fast sequential mechanism. The dissociation mechanism is unlikely to be a Coulomb explosion[17-22] and therefore the dissociation of Cl_2O^{2+} to form $Cl^+ + Cl^+$ is probably an initial two-body charge separation followed by the fast dissociation of ClO^+ to form the detected ion pair.

Ratio of the Double-to-Single Ionization Cross Sections

The ratio of σ^{2+}/σ^+ for Cl_2O has been calculated for the dissociation reactions of Cl_2O^{2+} at electron energies of 70, 100, 250 and 320 eV using Eq. 3.39. These values are listed in Table 5.11

and plotted in Fig. 5.10. As can be seen in Fig. 5.10, there is an initial increase in σ^{2+}/σ^{+} as the electron energy is raised and there is an increased likelihood of double ionization. As the electron energy is increased further the ratio of σ^{2+}/σ^{+} gradually decreases. However, the σ^{2+}/σ^{+} ratio increases between 250 and 320 eV. Recent investigations[27] of the ionization of Cl_2 have shown that at high electron energies triple ionization of Cl_2 is occurring, resulting in the same upward trend in the σ^{2+}/σ^{+} plot at high electron energy. Therefore, it is possible that dissociative triple ionization of Cl_2O at high electron energies is resulting in an increase in the ratio of σ^{2+}/σ^{+}. Pairs of singly charged ions from dissociative multiple ionization formed at these high electron energies may contribute to the ion pair intensities in the pairs spectra thus increasing the so-called ratio of σ^{2+}/σ^{+}.

At 100 eV (Table 5.11, Fig. 5.10), the ratio of σ^{2+}/σ^{+} for Cl_2O is 10%. This value is relatively high as the cross section for multiple ionization is usually assumed to be 1-5% of the single ionization cross section.[35] So, it appears that double ionization (and perhaps higher multiple ionization) contributes a significant amount to the total ionization of Cl_2O and therefore when investigating this molecule, one must always take into account the contribution of multiple ionization to any partial ionization cross sections determined.

5.4.3 Conclusion

The second section of this chapter has discussed the 2D investigation of the single and double ionization of Cl_2O. Time-of-flight mass spectrometry is again used to determine the values of σ_r^{I} for Cl_2O for incident electron energies of 70, 100, 250 and 320 eV. Stable parent ions Cl_2O^+ and O^+, Cl^+, ClO^+ and Cl_2^+ fragment ions and their isotopes were detected, the most abundant ion being the ClO^+ ion. Due to the improved detection efficiency of energetic ions with the 2D apparatus set-up, the contribution of the dissociative double ionization to the time-of-flight mass spectrum was determined and subtracted to give values of σ_r^{si} of the fragment ions of Cl_2O. In this process, the O^+ fragment ion signals were found to be dominated by the dissociation of the Cl_2O dication.

2D coincidence experiments were also performed to investigate further the formation and fragmentation of Cl_2O^{2+}. Peaks due to the formation of $Cl^+ + ClO^+$, $O^+ + Cl^+$ and $Cl^+ + Cl^+$ ion pairs were observed in the coincidence spectrum. The two-body dissociation reaction forming $Cl^+ + ClO^+$ was the most abundant ion pair and therefore the most likely dicationic dissociation reaction channel.

From the slopes of the isotopomers of the three-body dissociation reactions forming $O^+ + Cl^+$, it was not possible to discern whether the dication fragmentation pathway was a direct mechanism or a sequential mechanism involving an initial charge separation and subsequent molecular monocation dissociation. However, it is apparent that the dissociation mechanism is either a true Coulomb explosion or a fast sequential mechanism. There is some evidence in the spectrum of a slower

sequential dissociation of Cl_2O^{2+} to form $O^+ + Cl^+$ proceeding *via* an initial two-body dissociation reaction, forming Cl^+ and a longer-lived ClO^+ intermediate ion which then dissociates to form the detected ion pair. So the dissociation of Cl_2O^{2+} to form $O^+ + Cl^+$ probably occurs *via* a fast sequential mechanism involving an initial two-body charge separation with a fraction of the ion pairs being formed by a slower sequential dication dissociation.

From the pairs spectra, the dissociation of Cl_2O^{2+} to form $Cl^+ + Cl^+$ also proceeds *via* a Coulomb explosion or fast sequential mechanism. Again, the more likely fragmentation pathway for forming the detected ion pair is the fast dissociation of the dication *via* a sequential pathway involving an initial two-body charge separation and subsequent dissociation of the molecular monocation to form $Cl^+ + Cl^+$.

The first determination of the total double-to-single ionization cross section ratio shows that multiple ionization is a significant proportion of the total ionization of Cl_2O. So when deriving partial single ionization cross sections for the formation of ions it is important to consider the possible contribution of multiple ionization to ion signal intensities in mass spectra.

5.5 Overall Conclusions

This chapter describes the investigation of the single and double ionization of dichlorine monoxide, Cl_2O. The single ionization of Cl_2O has been investigated using time-of-flight mass spectrometry in order to determine values of the relative partial single ionization cross sections. The double ionization of Cl_2O has been investigated using ion-ion coincidence techniques to derive information concerning the mechanisms and energetics of the dication dissociation reactions.

From the single ionization of Cl_2O the following ions were observed in time-of-flight mass spectra: Cl^+, ClO^+, Cl_2^+, Cl_2O^+ and from the spectra, values of the relative partial single ionization cross sections σ_r^{si} of the fragment ions, relative to the parent ion, were determined. Despite the two different methodologies of the one and two-dimensional investigations, the values of σ_r^{si} for Cl_2O determined *via* these two different approaches are in good agreement with one another. The consistency of the results obtained in the two different studies also indicates that the analysis procedure used to subtract the multiple ionization contribution from the 2D time-of-flight mass spectrum worked well. It also showed the assumption that the small detector discriminated against energetic ions from dissociative multiple ionization made in the one-dimensional study is valid.

Coincidence techniques were employed to investigate the formation and fragmentation of Cl_2O^{2+}. In the ion-ion coincidence experiments and 2D coincidence experiments the dissociation reactions of Cl_2O^{2+} corresponding to the formation of $Cl^+ + ClO^+$, $O^+ + Cl^+$ and $Cl^+ + Cl^+$ ion pairs were observed. In both the one-dimensional and 2D experiments, the two-body dissociation reaction

forming $Cl^+ + ClO^+$ was seen to be the most likely dissociation reaction occurring and investigation of the energetics of this dissociation reaction indicates that the formation of this ion pair probably occurs from the ground electronic state of the dication. Thus a first estimate of the double ionization energy of Cl_2O has been determined as 30.6 ± 0.5 eV.

For the three-body dissociation reactions of Cl_2O^{2+}, no definitive mechanisms could be assigned for the formation of the $O^+ + Cl^+$ and $Cl^+ + Cl^+$ ion pairs. However, from the data obtained in both the one-dimensional and 2D experiments, the most likely fragmentation pathways for the formation of these ion pairs from Cl_2O^{2+} is a sequential mechanism involving an initial two-body charge separation followed by subsequent dissociation of the molecular monocation to form the detected ion pair.

The first estimate of the ratio of the total double-to-single ionization cross section indicates that double ionization contributes about 10% to the total ionization cross section of Cl_2O. Therefore, multiple ionization must be considered when investigating the single ionization of molecules.

References

1 A.J. Balard, *Ann. Chim. Phys., Ser. 2,* **57** (1834) 225

2 J.L. Gay-Lussac, *Compt. Rend. Acad. Sci.,* **14** (1842) 927

3 J.J. Renard and H.I. Bolker, *Chem. Rev.,* **76** (1976) 487

4 R.P. Wayne, G. Poulet, P. Biggs, J.P. Burrows, R.A. Cox, P.J. Crutzen, G.D. Hayman, M.E. Jenkin, G. Le Bras, G.K. Moortgat, U. Platt and R.N. Schindler, *Atmos. Env. ,* **29** (1995) 2677

5 M. Sugie, M. Ayabe, H. Takeo and C. Matsumura, *J. Mol. Struct.,* **352** (1995) 259

6 Y.J. Xu, A.R.W. McKellar, J.B. Burkholder and J.J. Orlando, *J. Mol. Spectrosc.,* **175** (1996) 68

7 F. Motte-Tollet, M.-P. Ska, G.M. Marston, I.C. Walker, M.R.F. Siggel, J.M. Gingell, L. Kaminski, K. Brown and N.J. Mason, *Chem. Phys. Lett.,* **275** (1997) 298

8 F. Motte-Tollet, J. Delwiche, J. Heinesch, M.-J. Hubin-Franskin, J.M. Gingell, N.C. Jones, N.J. Mason and G. Marston, *Chem. Phys. Lett.,* **284** (1998) 452

9 T.A. Moore, M. Okumura and T.K. Minton, *J. Chem. Phys.,* **107** (1997) 3337

10 C.M. Nelson, T.A. Moore, M. Okumura and T.K. Minton, *J. Chem. Phys.,* **100** (1994) 8055

11 S. Chapman, *Mem. Roy. Meteorol. Soc.,* **3** (1930) 103

12 R.P. Thorn, L.J. Stief, S.-C. Kuo and R.B. Klemm, *J. Phys. Chem.,* **100** (1996) 14178

13 I.P. Fisher, *Trans. Faraday Soc.,* **64** (1968) 1852

14 C.G. Freeman and L.F. Phillips, *J. Phys. Chem.,* **72** (1968) 3025

15 H.F. Cordes and S.R. Smith, *J. Chem. Eng. Data,* **15** (1970) 158

16 C.S.S. O'Connor and S.D. Price, *Int. J. Mass Spectrom. Ion Proc.,* **184** (1999) 11

17 J.H.D. Eland, *Mol. Phys.,* **61** (1987) 725

18 S. Hsieh and J.H.D. Eland, *J. Chem. Phys.,* **103** (1995) 1006

19 I. Nenner and J.H.D. Eland, *Z. Phys. D,* **25** (1992) 47

20 J.H.D. Eland, *Chem. Phys. Lett.,* **203** (1993) 353

21 K. Codling, L.J. Frasinski, P.A. Hatherly, M. Stankiewicz and F.P. Larkins, *J. Phys. B,* **24** (1991) 951

22 M. Simon, P. Morin, P. Lablanquie, M. Lavollee, K. Ueda and N. Kosugi, *Chem. Phys. Lett.,* **238** (1995) 42

23 P.J. Richardson, J.H.D. Eland and P. Lablanquie, *Org. Mass Spec.,* **21** (1986) 289

24 D.M. Curtis and J.H.D. Eland, *Int. J. Mass Spectrom. Ion Proc.,* **63** (1985) 241

25 B.P. Tsai and J.H.D. Eland, *Int. J. Mass Spectrom. Ion Proc.,* **36** (1980) 143

26 N. Jeffreys, I.W. Griffiths, D.E. Parry and F.M. Harris, *Chem. Phys. Lett.,* **266** (1997) 537

27 G.S. Lidder and S.D. Price, *in preparation* (1999)

28 A.B. Cornford, D.C. Frost, F.G. Herring and C.A. McDowell, *J. Chem. Phys.*, **55** (1971) 2820

29 G. Herzberg, *Electronic Spectra and Electronic Structure of Polyatomic Molecules*, Van Nostrand, Princeton, N.J., 1966

30 C.E. Moore, *Atomic Energy Levels*, National Bureau of Standards, U.S. Government Printing Office, Washington D.C., 1949

31 D.K. Bulgin, J.M. Dyke, N. Jonathan and A. Morris, *J. Chem. Soc., Faraday Trans.* , **75** (1979) 456

32 M.V.V.S. Rao and S.K. Srivastava, *J. Geophys. Res.*, **96** (1991) 17563

33 J.H.D. Eland and B.J. Treves-Brown, *Int. J. Mass Spectrom. Ion Proc.*, **113** (1992) 167

34 M. Lange, O. Pfaff, U. Müller and R. Brenn, *Chem. Phys.*, **230** (1998) 117

35 T.D. Märk, in T.D. Märk, G.H. Dunn (Eds.), *Electron Impact Ionization*, Springer-Verlag, New York, 1985

6. Single and Double Ionization of OClO

6.1 Introduction

Chlorine dioxide, OClO, was first positively identified in 1815 by Davy[1] and is a bent molecule having C_{2v} symmetry.[2] There have been a number of investigations of the properties of OClO, several focusing, in particular, on its spectroscopic properties[3-5] and photodissociation.[6-10] The interest in OClO, as with other halogen oxides including Cl_2O (Chapter 5), stems from the possible role these molecules play in the upper atmosphere. In the Antarctic stratosphere, the photodissociation of OClO can give rise to two sets of products,

$$h\nu + OClO \rightarrow ClO + O \qquad (6.I)$$

$$h\nu + OClO \rightarrow Cl + O_2 \qquad (6.II)$$

The fragmentation pathways of OClO shown in Reactions (6.I) and (6.II) are potentially important for polar ozone depletion as they result in the formation of O and ClO, atmospherically important radicals, and atomic chlorine. Both atomic chlorine and ClO are involved in ozone-depleting reaction cycles such as the reaction pathways shown in Reactions (5.I) and (5.II). The reaction channel given in Reaction (6.II) is a secondary process[9] and proceeds either *via* isomerization of OClO into ClOO or in a concerted decay process.[6]

Despite the interest in the spectroscopy and photodissociation of OClO relatively few investigations of its ionization have been performed. There have been no studies of the double ionization of OClO and only a handful of investigations of the formation and fragmentation of $OClO^+$.[11-15]

This chapter discusses the one-dimensional and 2D investigations of the single and double ionization of OClO.[16] In the single ionization studies, time-of-flight mass spectrometry is used to determine the relative partial single ionization cross sections of OClO over a range of electron energies. Coincidence techniques are used to investigate the formation and fragmentation of $OClO^{2+}$. Information obtained from the one and two-dimensional coincidence spectra can give an indication of the mechanisms by which $OClO^{2+}$ dissociates and the energy of the electronic states of $OClO^{2+}$ which are the source of the fragment ions formed upon dissociation. Finally, estimates of the double ionization energy and the ratio of the double-to-single ionization cross sections for OClO can be made.

6.2 Experimental Details

The experimental techniques employed in both the one-dimensional and 2D studies of the single and double ionization of OClO have been described in detail in Chapter 2.

6.2.1 Synthesis of OClO

The OClO sample used in these experiments is synthesised *in situ*, as required, by the oxidation of molecular chlorine with sodium chlorite.[17]

$$2NaClO_2 + Cl_2 \rightarrow 2OClO + 2NaCl \qquad (6.III)$$

Chlorine gas is passed through a U-tube packed with glass beads and wet $NaClO_2$ and the resulting OClO is then dried over P_2O_5 (Fig. 6.1).

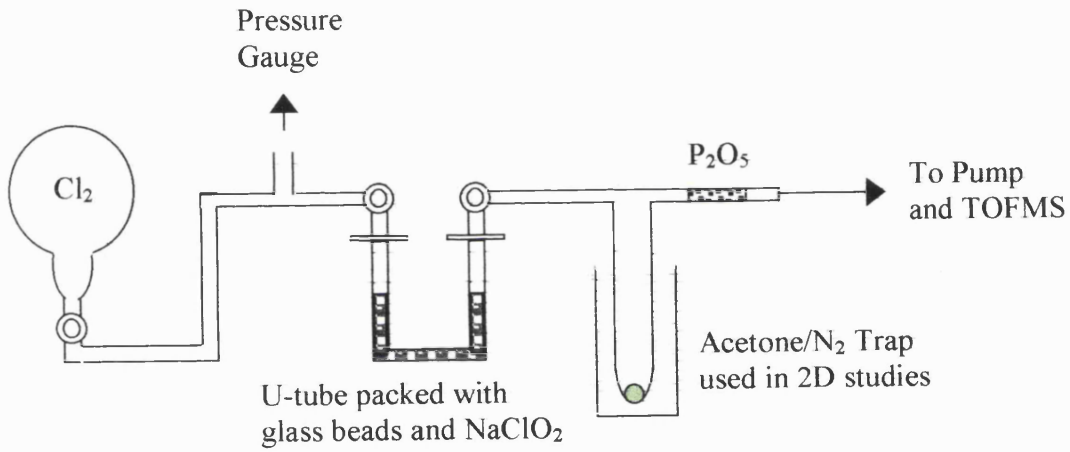

Fig. 6.1 Apparatus used for the *in situ* synthesis of OClO.

Time-of-flight mass spectra of the OClO sample synthesised using the procedure described above, showed that the first and second fractions of gaseous OClO drawn from the U-tube contained signals corresponding to unreacted molecular chlorine. These initial two fractions are therefore pumped away and the third fraction extracted from the U-tube, shown to be uncontaminated by Cl_2, is transported into the ionization region of the TOFMS. A clean glass/Teflon inlet system, which had been blackened to prevent photodissociation of the sample, was used to rapidly draw the sample into the TOFMS (Chapter 2).

In the 2D studies, to avoid rapid degradation of the filament on exposure to OClO, it was necessary to run the experiments at very low count rates and consequently the data acquisition time had be increased in order to obtain adequate counting statistics. However, using the synthetic procedure described above, insufficient volumes of OClO are produced to sustain prolonged data acquisition times. So, in order to synthesise a pure sample of OClO to use in the 2D experiments, the OClO evolved from the reaction of Cl_2 on $NaClO_2$ [Reaction (6.III)] is trapped in an acetone/N_2 slush bath (179 K)[18] and any unreacted Cl_2 is pumped away. This cycle is repeated several times

until sufficient OClO has been purified. The liquefied sample is then warmed to room temperature and the vaporised OClO molecules are transported into the TOFMS.

6.2.2 Procedures

For the one-dimensional studies, time-of-flight mass spectra were recorded at incident electron energies of 30-450 eV in order to determine the relative partial single ionization cross sections σ_r^{si} of the ions formed upon ionization of OClO. One-dimensional coincidence spectra were recorded at an ionizing electron energy of 150 eV and also at a range of lower electron energies, from 25 to 60 eV, in order to determine the appearance energies of the pairs of fragment ions produced by the dissociative double ionization of OClO.

For the 2D studies, time-of-flight mass spectra were recorded at electron energies of 70, 100, 250 and 320 eV to also determine values of σ_r^{si} of the fragment ions of OClO. Coincidence spectra were recorded at the same electron energies and the intensities and slopes of the peaks corresponding to the fragment ion pairs formed from $OClO^{2+}$ were investigated.

6.3 One-Dimensional Studies

6.3.1 Data Analysis

6.3.1.1 Single Ionization

A typical time-of-flight mass spectrum of OClO recorded at 150 eV is shown in Fig. 6.2.

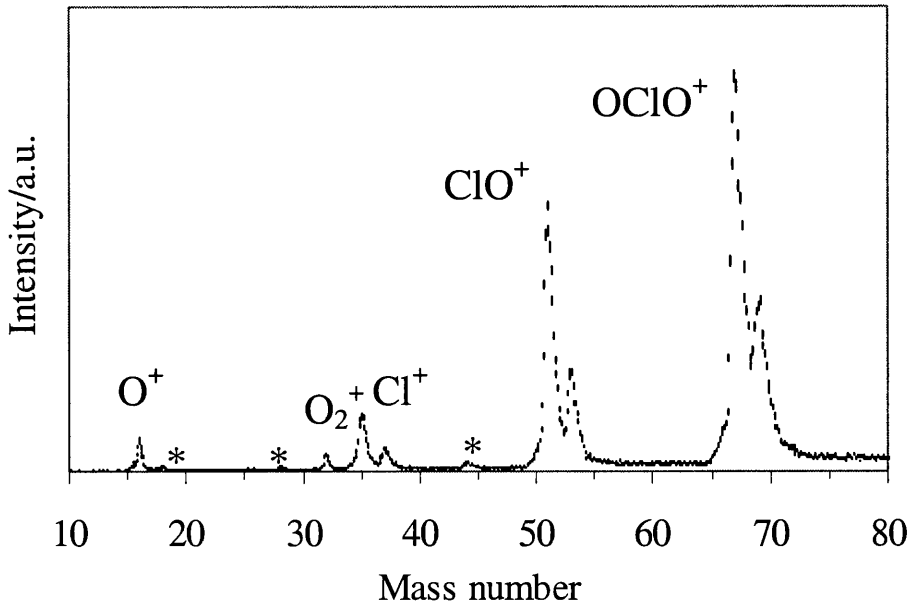

Fig. 6.2 A typical time-of-flight mass spectrum of OClO recorded at an electron energy of 150 eV. The error bars shown, derived from the counting statistics, represent two standard deviations. The peaks marked with asterisks correspond to signals from the traces of air and water (H_2O^+, N_2^+ and CO_2^+) that make up the residual gas.

As can be seen from the figure, the stable parent ion $OClO^+$ and fragment ions O^+, O_2^+, Cl^+ and ClO^+, and their relevant isotopes, are detected. The spectrum also contains small signals resulting from traces of air and water, the principal background gas in the apparatus.

The parent and fragment ion signal intensities are obtained from the raw ion signals in the mass spectrum recorded at a range of electron energies from 30 to 450 eV (Chapter 3). Any contribution from the ionization of the traces of background gas in the source region, *e.g.* O^+ from O_2, to the fragment ion signals in the OClO mass spectrum was calculated by recording the mass spectrum of air and water over the range of electron energies employed in the experiments. The relative intensities of the ions in these background gas spectra were then determined with respect to N_2^+ and H_2O^+. The contribution of the ionization of air and water to the ion signals in the OClO mass spectra can then be accurately determined, and subtracted, by scaling the relative intensities of the fragment ions from the air and water spectra using the N_2^+ and H_2O^+ signals in the OClO spectrum, as any N_2^+ and H_2O^+ signals can only arise from the background gas. Even without the background subtraction, it is clear from Fig. 6.2 that the relative intensity of the N_2^+ and H_2O^+ peaks from air and water in the OClO mass spectrum are markedly lower than the O_2^+ signal. Hence, this effectively excludes traces of air or water as a source of the O^+ and O_2^+ signals in the OClO mass spectra. For the Cl^+ and ClO^+ fragments and the parent ion $OClO^+$, the ion signals of both chlorine isotopes were determined and then combined to give a single intensity ratio.

The relative partial ionization cross sections σ_r^{si} of the ions observed in the OClO spectrum, relative to the most abundant ion, in this case the parent ion $OClO^+$, are determined from the ion signal intensities as described in Chapter 3, using the appropriate mass correction factor. The values of σ_r^{si} derived are shown in Fig. 6.3 and listed in Table 6.1.

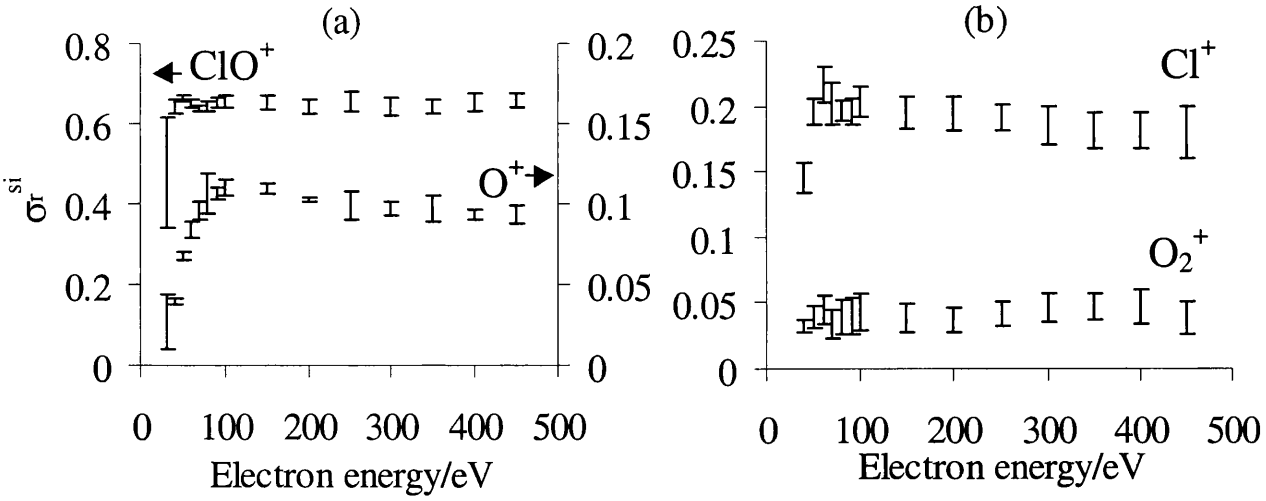

Fig. 6.3 Values of σ_r^{si} for forming (a) ClO^+ and O^+ and (b) Cl^+ and O_2^+ from OClO, relative to the most abundant ion in the mass spectrum, $OClO^+$. The values for O^+ should be read from the right hand axis. The error bars represent two standard deviations.

Table 6.1 Values of σ_r^{si} for the formation of the indicated product ion from OClO (the number in parentheses indicate the standard deviation in the last figure of each cross section).

Electron	σ_r^{si}			
energy /eV	O^+	O_2^+	Cl^+	ClO^+
30	0.027(17)	—	—	0.48(14)
40	0.0393(22)	0.032(5)	0.145(11)	0.642(16)
50	0.0671(26)	0.039(8)	0.195(10)	0.664(7)
60	0.0840(49)	0.045(11)	0.216(14)	0.649(10)
70	0.0954(53)	0.034(11)	0.202(16)	0.639(6)
80	0.107(13)	0.039(14)	0.196(8)	0.643(14)
90	0.1061(38)	0.040(14)	0.196(10)	0.652(11)
100	0.1101(49)	0.043(14)	0.203(11)	0.653(15)
150	0.1094(31)	0.039(11)	0.195(12)	0.653(17)
200	0.1204(10)	0.038(9)	0.194(13)	0.644(16)
250	0.0991(91)	0.041(9)	0.190(10)	0.653(25)
300	0.0971(42)	0.046(10)	0.185(15)	0.643(24)
350	0.0968(83)	0.047(11)	0.180(14)	0.643(18)
400	0.0931(32)	0.047(13)	0.181(13)	0.654(22)
450	0.0931(51)	0.039(12)	0.180(20)	0.656(17)

At high ionizing electron energies, the values of σ_r^{si} are the average of four independent determinations but at lower electron energies, due to the larger uncertainty, the values of σ_r^{si} are the average of seven independent determinations. The standard deviations of these determinations at each electron energy are also shown in Table 6.1 and plotted as the error bars in Fig. 6.3. The standard deviations are small in accord with the small statistical error in each individual determination.

The appearance energies of the fragment ions have been previously determined[15] at better electron energy resolution than can be achieved using the current experimental arrangement, conservatively estimated to be ± 2 eV, and were therefore not redetermined in this study.

6.3.1.2 Double Ionization

A typical ion-ion coincidence spectrum of $OClO^{2+}$ recorded at 150 eV is shown in Fig. 6.4. The observed dissociation processes are a pair of two-body reactions

$$\begin{aligned} OClO^{2+} &\rightarrow O^+ + {}^{35}ClO^+ \\ OClO^{2+} &\rightarrow O^+ + {}^{37}ClO^+ \end{aligned} \qquad (6.IV)$$

and a pair of three-body reactions:

$$\begin{aligned} OClO^{2+} &\rightarrow O^+ + {}^{35}Cl^+ [+ O] \\ OClO^{2+} &\rightarrow O^+ + {}^{37}Cl^+ [+ O] \end{aligned} \qquad (6.V)$$

where the neutral oxygen atom in the three-body dissociation reactions is not detected. Any coincidence signals produced by the dissociation reaction,

$$OClO^{2+} \rightarrow O^+ + O^+ + [Cl] \qquad (6.VI)$$

will produce a coincidence signal centred at $\Delta t_{tof} = 0$. Due to the dead time of the channeltron and a small amount of afterpulsing ("pick-up"), which generates false counts when Δt_{tof} is small (Chapter 2), such signals cannot be efficiently detected in the coincidence spectrum and were therefore not investigated further in the one-dimensional study.

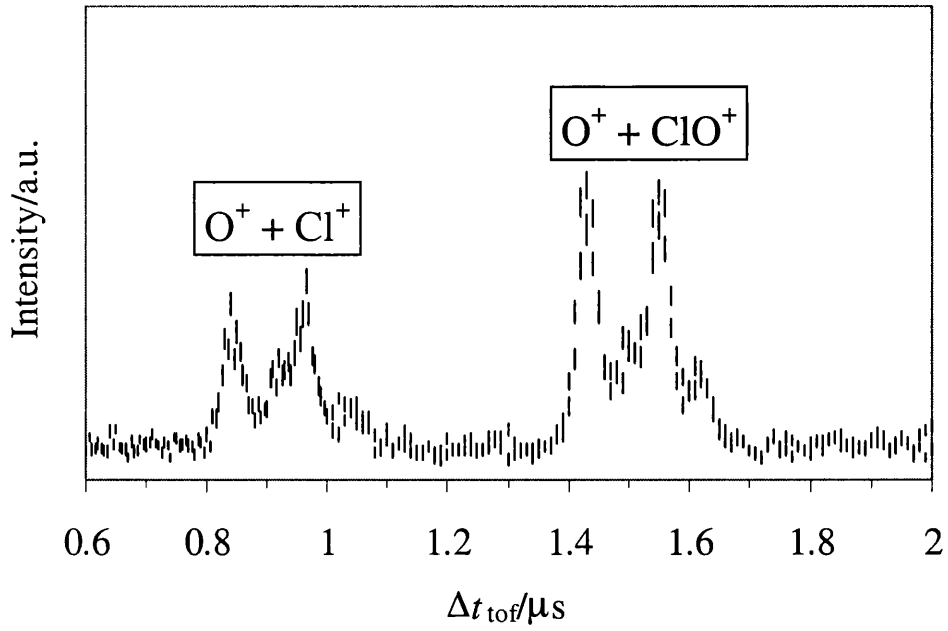

Fig. 6.4 Ion-ion coincidence spectrum of $OClO^{2+}$ generated by electron impact at 150 eV. The error bars, derived from the counting statistics, represent two standard deviations.

Kinetic Energy Release Determination

The kinetic energy release (KER) and half-width of the kinetic energy release distribution (F_{KERD}) associated with the formation of the ion pairs observed in the coincidence spectrum of $OClO^{2+}$ have been determined by performing Monte Carlo simulations of the experimental data; the method being described in detail in Chapter 3. The KER associated with the formation of the O^+ + ClO^+ and O^+ + Cl^+ fragment ion pairs is assumed to be the same for both chlorine isotopes.

The O^+ + ClO^+ ion pair observed in the coincidence spectrum following the dissociation of $OClO^{2+}$ is due to a two-body dissociation reaction [Reaction (6.IV)]. For such a dissociation reaction, the dicationic decay mechanism is unambiguous; a direct dissociation of the dication to form the pair of product ions, O^+ + ClO^+. Therefore, the result of the simulation procedure for the O^+ + ClO^+ ion pair is a single KER value and corresponding F_{KERD} listed in Table 6.2. As can be seen in Fig. 6.5, the fit of the simulated spectrum to the experimental data is of a high quality.

Table 6.2 Potential values of KER and F_{KERD} for forming O^+ + ClO^+ from $OClO^{2+}$ derived by simulation of the ion-ion coincidence spectrum at 150 eV.

Dissociation mechanism	KER/eV	F_{KERD}/eV
Direct	6.0	3.2

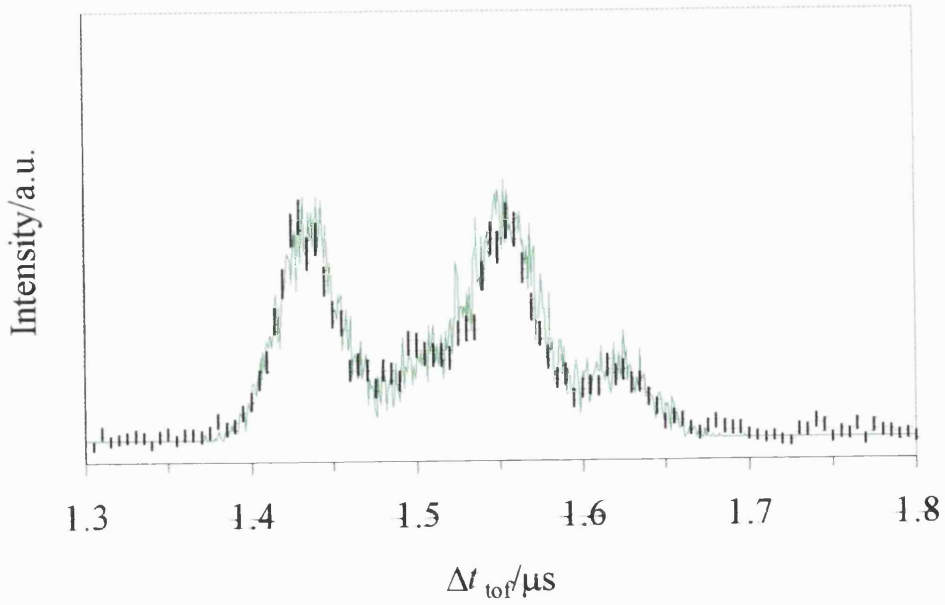

Fig. 6.5 Ion-ion coincidence spectrum of $OClO^{2+}$ showing the signal corresponding to the $O^+ + ClO^+$ ion pair. The solid curve is a Monte Carlo simulation of the experimental signal. Error bars representing two standard deviations indicate the experimental points.

For the three-body dissociation reaction of $OClO^{2+}$ forming $O^+ + Cl^+$ [Reaction (6.V)], where neutral O atoms are formed in conjunction with the pair of singly charged ions, the fragmentation pathway is not as clear. The pathway could involve either a direct mechanism [Reaction (6.VII)],

$$OClO^{2+} \rightarrow O^+ + Cl^+ + O \qquad (6.VII)$$

or a sequential mechanism. No daughter dications are observed in the mass spectrum (Fig. 6.2) and there are no metastable tails on the coincidence peaks (Fig. 6.4), thus implying that the dissociation mechanism is unlikely to involve a deferred charge separation.[19-25] So the sequential dissociation mechanism is assumed to involve an initial charge separation followed by the subsequent dissociation of one of the resulting ions to form the detected pair of singly charged ions [Reaction (6.VIII)].

$$\begin{array}{l} OClO^{2+} \rightarrow O^+ + ClO^+ \\ \qquad\qquad \downarrow \\ \qquad\qquad O^+ + Cl^+ + O \end{array} \qquad (6.VIII)$$

As mentioned in Chapter 3, the KER upon dicationic dissociation to form a given pair of ions is associated with the temporal width of the coincidence peak and depends on the masses of the primary ions formed by dicationic charge separation. The simulation procedure has consequently been performed for the three-body dissociation reaction several times, modelling the formation of $O^+ + Cl^+$ *via* the direct mechanism [Reaction (6.VII)] and the sequential mechanism involving initial charge separation and subsequent monocation dissociation [Reaction (6.VIII)]. In the simulation

process, the KER of the monocation dissociation is assumed to be negligible in comparison to the primary KER of the dication dissociation.

The coincidence peak corresponding to the $O^+ + Cl^+$ reaction has been modelled for both the sequential and direct fragmentation pathways using two KER values (Table 6.3), as indeed was the case for the $O^+ + Cl^+$ ion pair produced by the dissociative double ionization of Cl_2O (Chapter 5). The use of a multiple KER in the simulation procedure is necessary to yield realistic values[26] for the variable parameters, *e.g.* F_{KERD}, and to obtain a satisfactory fit with the experimental spectrum. Table 6.3 shows the potential KER and F_{KERD} values required to fit the experimental spectrum for the two possible decay reactions that could form $O^+ + Cl^+$ from $OClO^{2+}$.

Table 6.3 Potential values of KER and F_{KERD} for forming $O^+ + Cl^+$ from $OClO^{2+}$.

	Dissociation mechanism		KER/eV	F_{KERD}/eV	Relative Importance of KER
Single KER	Direct		7.3	5.0	
	Sequential		9.1	6.6	
Multiple KER	Direct	KER 1	8.0	0.75	0.8
		KER 2	3.4	0.75	0.2
	Sequential	KER 1	8.6	1.0	0.9
		KER 2	3.2	1.0	0.1

From the potential values of the KER derived from the simulation procedure for each ion pair, the corresponding potential values of the energy of the dication state, $E(OClO^{2+})$, from which the particular dissociation reaction occurs is obtained using Eq. 3.13. A summary of the potential KER and F_{KERD} values for the observed dissociation reactions of $OClO^{2+}$, together with the corresponding $E(OClO^{2+})$ values are listed in Table 6.4. It is important to note that the values of $E(OClO^{2+})$ should be considered a lower limit as in the calculation of these values the fragmentation products are assumed to be formed with no internal energy.

Table 6.4 Summary of the potential values of KER, F_{KERD} and $E(OClO^{2+})$ for the dissociation reactions of $OClO^{2+}$.

Dissociation reaction	Dissociation mechanism	KER/eV	F_{KERD}/eV	$E(OClO^{2+})$/eV
$O^+ + ClO^+$	Direct	6.0	3.2	33.2
$O^+ + Cl^+$	Direct	8.0	0.75	40.0
		3.4	0.75	35.4
	Sequential	8.6	1.0	40.6
		3.2	1.0	35.2

Determination of the Appearance Energy

The appearance energies of the two observed dissociation reaction of $OClO^{2+}$ have been determined by evaluating the ratio of the yield *Y* of each dissociation reaction to the number of coincidence starts *S* at electron energies from 25 to 60 eV. See Chapter 3 for details.

Fig. 6.6 shows a weighted least squares fit[27] applied to the values of *Y/S* for the dissociation reactions of $OClO^{2+}$ forming $O^+ + ClO^+$ and $O^+ + Cl^+$ above and below threshold. The variation of the ratio of *Y/S* above the appearance energy appears to be well modelled, within the error limits, by a linear function in the excess electron energy.

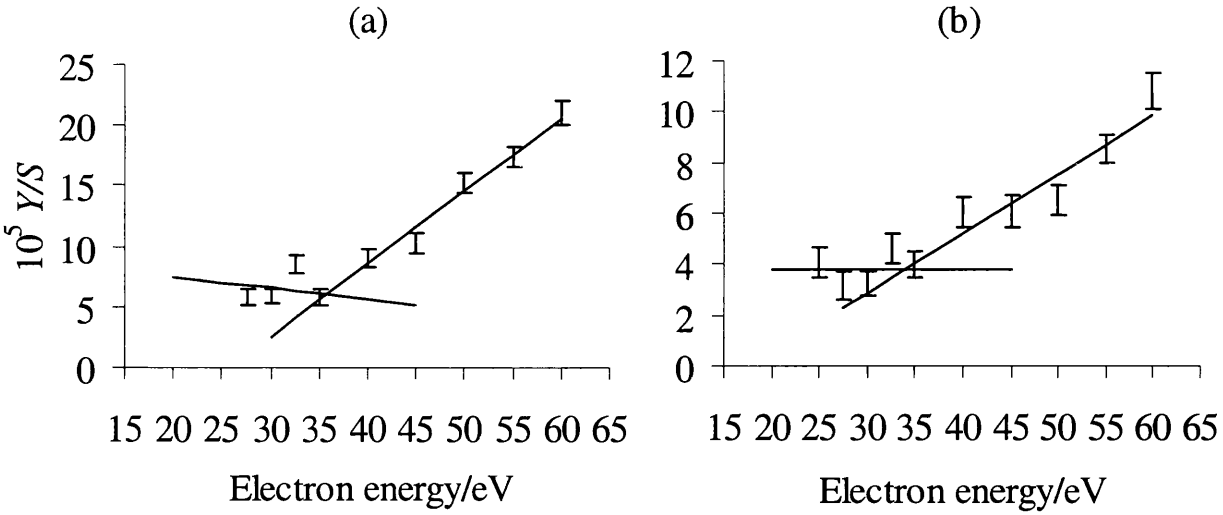

Fig. 6.6 Plots of *Y/S* as a function of electron energy for (a) $O^+ + ClO^+$ and (b) $O^+ + Cl^+$. As described in the text and illustrated in the figure, these plots can be interpreted to yield the appearance energy of the lowest energy dication state responsible for each decay reaction.

As explained in Chapter 4, the ratio of *Y/S* can be extrapolated to the non-zero background level of residual double ionization for each plot to obtain values of the appearance energy of the relevant ion pair. From Fig. 6.6, values of 35.7 ± 2 eV and 33.8 ± 2 eV are obtained for the appearance energies of $O^+ + ClO^+$ and $O^+ + Cl^+$ respectively and these values are interpreted as the energy of the lowest-lying states responsible for the dicationic decay reaction forming the relevant ion pair. The errors associated with these appearance energy determinations are derived from the energy resolution of the ionizing electron beam.

Table 6.5 Experimentally derived appearance energies for the $O^+ + ClO^+$ and $O^+ + Cl^+$ ion pairs formed from $OClO^{2+}$.

Dissociation reaction	Appearance energy /eV
$O^+ + ClO^+$	35.7 ± 2
$O^+ + Cl^+$	33.8 ± 2

As explained in Chapter 3 and illustrated in Chapter 4, it is hoped that some mechanistic information can be derived for the $O^+ + Cl^+$ dissociation reaction by comparing the appearance

energy of a three-body dication fragmentation channel with values of $E(OClO^{2+})$ calculated using the potential KER values derived from the simulation procedure. However, as can be seen from Table 6.4, for the $O^+ + Cl^+$ ion pair there is no discernible difference between the values of the KER, and hence $E(OClO^{2+})$, obtained for the different dissociation mechanisms. Therefore, even with the measured appearance energy for this ion pair, it is not possible to assign a fragmentation mechanism to this three-body dissociation reaction. However, as discussed below, information concerning the energetics of the dissociative dicationic states can still be obtained from the data derived from the simulation procedure.

6.3.2 Discussion

6.3.2.1 Single Ionization

There have been a number of previous reports in the literature concerning the ionization and fragmentation of $OClO^+$, using both PIMS and EIMS techniques. There are three separate studies of the fragmentation of $OClO^+$ employing EIMS at an ionizing electron energy of 70 eV[11-13] and two investigations using PIMS, both at a photon energy of 20.65 eV.[14,15] The three EIMS investigations[11-13] observed O_2^+, Cl^+ and ClO^+ fragment ions and the parent ion $OClO^+$, in addition to a wide range of impurity peaks, but only one study by Cordes *et al*[12] observed the O^+ fragment ion. The earlier PIMS study by Flesch *et al*[14] detected only ClO^+ and the parent monocation and, in contrast to the EIMS results, found the fragment ion to be more abundant than the parent ion. The more recent PIMS work by Rockland *et al*,[15] detected O^+, O_2^+, Cl^+, ClO^+ and $OClO^+$ and found the most abundant ion to be the parent ion. They suggested that the discrepancies between the PIMS studies might be due to the differing transmission of the different quadrupole mass spectrometers used in the two experiments. In addition, Rockland *et al*[15] determined the appearance energies of the O^+, O_2^+, Cl^+ and ClO^+ fragment ions to be 16.30, 13.20, 13.33 and 13.30 eV, respectively. A summary of the ion yields obtained in the previous studies of $OClO$[11-15] is given in Table 6.6.

In the present one-dimensional study, at electron energies ranging from 30 to 450 eV, the parent ion $OClO^+$ and fragment ions ClO^+, Cl^+, O_2^+ and O^+ and the relevant isotopes for the chlorinated ions, were detected (Fig. 6.2). The plots of σ_r^{si} of the fragment ions against electron energy all show an initial increase in σ_r^{si} as the electron energy is raised (Fig. 6.3), due to the increased likelihood of ionic fragmentation with increased electron energy and associated ionic excitation.

In the current work, the relative intensity of the O^+ fragment ion to the parent ion at 70 eV, the ionizing energy used in the previous EIMS studies[11-13] and often considered to result in the same energy deposition as the 20.65 eV photons[28] employed in the PIMS experiments,[14,15] is 9.5% (Table 6.6, Fig. 6.3). This value is higher than all the preceding studies of the dissociation of $OClO^+$, indeed

this fragment was not even detected in two of the EIMS studies.[11,13] The relative intensity of O^+ in this experiment could arise, in part, from trace amounts of air present in the source region of the TOFMS contributing to the observed O^+ signal. However, as described above, any such contribution has been carefully subtracted and the good agreement between the relative intensity of O_2^+ in this experiment, 3.4% (Table 6.6, Fig. 6.3) with that from other investigations implies the effective subtraction of any air signals. Indeed, as discussed above, the contribution of ions from the ionization of background gas to the experimental mass spectrum is very small. Therefore, a more likely explanation for the high O^+ yield observed here is an increased efficiency in the collection of superthermal O^+ fragments formed from $OClO^+$ using our experimental set-up. It is important to note that despite highly energetic ionic fragments being inefficiently detected with the current one-dimensional apparatus set-up, any fragments formed from dissociative single ionization are likely to have kinetic energies of less than 0.3 eV and so will still be detected.

Table 6.6 Comparison of ion intensities from reported mass spectra of OClO.

Ion	Present	Fisher[11]	Baluev *et al*[13]	Cordes *et al*[12]	Rockland *et al*[15]	Flesch *et al*[14]
	EIMS	EIMS	EIMS	EIMS	PIMS	PIMS
O^+	9.5	—	—	5.2	4.5	—
O_2^+	3.4	2.1	7.1	4.2	1.5	—
Cl^+	20	1.9	9.5	6.4	3.1	—
ClO^+	63	31.4	48.3	44.8	73	100
$OClO^+$	100	100	100	100	100	67

The relative intensity of Cl^+ obtained in the present work is also higher than previously determined (Table 6.6, Fig. 6.3). This increased yield in the Cl^+ signals is unlikely to be due to the dissociative ionization of molecular chlorine as no Cl_2^+ singles are observed in the mass spectrum (Fig. 6.2). Again, an increased efficiency in the collection of superthermal atomic fragments from the dissociation of $OClO^+$ or transmission effects in the quadrupole mass spectrometers used in the previous works are the probable causes of the discrepancy. The relative intensity of the ClO^+ fragment obtained here is 63% (Table 6.6, Fig. 6.3). This value is higher than EIMS determinations[11-13] but lower than the more recent PIMS determination.[15] The second PIMS study[14] found the ClO^+ fragment to be more abundant than the parent ion. These differing yields could be a result of mass discrimination effects in the previous PIMS works or the relative population of electronic states that dissociate to form fragment ions may differ when using either electrons or photons as the ionizing agent.

The above discussion illustrates the difficulties that arise when comparing ion yields obtained in PIMS and EIMS studies. The discrepancies between the ion yields obtained using photoionization and electron-impact ionization could be due to a different energy deposition from the photons and

electrons. The above comparison of data obtained in EIMS studies also highlights the problems which are involved in investigating a reactive molecule such as OClO. However, given the efforts made in this work to obtain as pure a sample of OClO as possible, and the design of the apparatus for the efficient collection of the majority of the energetic fragments from dissociative single ionization, the values of σ_r^{si} for the fragment ions of $OClO^+$ given in Table 6.1 and Fig. 6.3 are likely to be the most reliable to date.

6.3.2.2 Double Ionization

The coincidence spectrum (Fig. 6.4) shows that $OClO^{2+}$ dissociates *via* a two-body dissociation reaction to form $O^+ + ClO^+$ and a three-body reaction forming the $O^+ + Cl^+$ ion pair. In the time-of-flight mass spectrum of OClO no stable parent dication ($OClO^{2+}$) or daughter dications are observed. This implies that no bound regions of the dication potential energy surfaces can be accessed by a vertical transition from the equilibrium geometry of the molecule.

$O^+ + ClO^+$

For the two-body dissociation reaction forming $O^+ + ClO^+$, the experimentally determined appearance energy is 35.7 ± 2 eV. As mentioned above, for a two-body reaction there is only a single possible fragmentation pathway and therefore the interpretation of the width of the coincidence peak, in terms of the KER upon dissociation, is straightforward. From Table 6.4 it can be seen that the estimate of $E(OClO^{2+})$ associated with the dissociation of $OClO^{2+}$ to form the $O^+ + ClO^+$ ion pair is 33.2 ± 0.3 eV. This value of $E(OClO^{2+})$ is lower than the experimentally determined appearance energy for the formation of this ion pair (35.7 ± 2 eV). The difference between these values could be due to the uncertainties in the measurement of the appearance energy. However, the calculation of $E(OClO^{2+})$ using the method described above assumes that the fragment ions are formed with no internal energy and therefore really provides a lower limit for the energy of the dication state responsible for dissociation to form $O^+ + ClO^+$. If excited states of O^+ or ClO^+ are formed then the value of $E(OClO^{2+})$ derived from the KER will lie closer to the experimentally determined appearance energy. As with the two-body dissociation of Cl_2O^{2+} (Chapter 5), there is no experimental data on whether the fragment ions are formed in excited states, but again consideration of the symmetry of the dissociation may be informative.

From the photoelectron spectrum of OClO,[3,14] the ground state electron configuration of $OClO^+$ is $...a_1^2b_2^2a_2^2$ and so the ground state of $OClO^{2+}$ may be assumed to be $^2A_2$ under C_{2v} symmetry. Following the building-up principles from unlike groups to form a non-linear molecule,[29] the dissociation of $OClO^{2+}$ from its ground electronic state ($^2A_2$) to form the products O^+ (^4S_u) and

ClO^+ ($^3\Sigma^-$) in their ground electronic states[30,31] is found to be spin allowed but symmetry forbidden. The dissociation of the dication to form ground state O^+ and electronically excited ClO^+ ($^1\Delta$) is symmetry allowed but spin forbidden. Of course, such notional 'forbidden' dissociation reactions can, in principle, occur.[32] However, the dissociation of $OClO^{2+}$ to form electronically excited O^+ (^2D_u) and ground state ClO^+ is both symmetry and spin allowed and this dissociation limit, when coupled with our KER values, yields a dication state energy of 36.5 eV, a value in good agreement with the experimentally determined appearance energy. Hence, it is possible that the dissociation of the ground state of $OClO^{2+}$ favours the formation of an excited electronic state of O^+. Given the above discussion, the experimental determination of the appearance energy of the fragmentation channel, 35.7 ± 2 eV provides a more realistic estimate of the energy of the state of $OClO^{2+}$ which dissociates to form $O^+ + ClO^+$ than a value derived from the KER.

$O^+ + Cl^+$

For the dissociation of $OClO^{2+}$ to form the $O^+ + Cl^+$ ion pair, the experimentally determined appearance energy is 33.8 ± 2 eV. Within the error limits, this is equivalent to the appearance energy of the two-body reaction and so it is not possible to definitively state whether or not these ion pairs are formed as a result of the dissociation of two distinct states of $OClO^{2+}$. The simulation of the coincidence peak corresponding to this ion pair indicates the dissociation of two distinct electronic states of $OClO^{2+}$ to form the $O^+ + Cl^+$ fragment ion pair, the first state at approximately 35 eV and the second at approximately 40 eV. The value of $E(OClO^{2+})$ associated with the lowest energy state which dissociates to form $O^+ + Cl^+$, 35 eV, is close to the dication state energy deduced to be responsible for the two-body reaction and in good agreement with the experimentally determined appearance energy. Given this data, one possible conclusion is that both the two-body and three-body reactions proceed *via* the dissociation of an electronic state of $OClO^{2+}$ lying at approximately 35 eV.

From the relative importance attributed to the two KERs required to the fit the simulated spectrum to the experimental data, the probability of forming $O^+ + Cl^+$ from the higher-lying electronic state (40 eV) is significantly larger than from the lowest-lying state (35 eV). Therefore, it is possible that the dissociation of $OClO^{2+}$ to form $O^+ + Cl^+$ occurs predominantly from the dication electronic state at 40 eV with a small proportion of the ion pair being formed from the state at 35 eV. So the dominant dissociation pathway of the dication electronic state at 35 eV could be to form $O^+ + ClO^+$ with a minor reaction channel forming the $O^+ + Cl^+$ ion pair [Reaction (6.VIII)].

Estimate of the Double Ionization Energy

The value of the double ionization potential of OClO derived using the 'rule of thumb'[33] yields an estimate of 33.77 eV. This estimate of the double ionization potential of OClO is in fair agreement with the threshold for forming both fragment ion pairs, $O^+ + ClO^+$ and $O^+ + Cl^+$, and the value of the dication state energy for the lowest electronic state dissociating to form both these pairs, suggesting that this is the ground state of the OClO dication.

6.3.3 Conclusion

This study presents the investigation of the single and double ionization of OClO. Time-of-flight mass spectrometry is used to determine the relative partial single ionization cross sections σ_r^{si} of OClO for incident electron energies from 30 to 450 eV. Stable parent ions $OClO^+$ and O^+, O_2^+, Cl^+ and ClO^+ fragment ions and their isotopes were detected, the most abundant ion being the parent monocation.

Ion-ion coincidence experiments have been performed to study the formation and dissociation of $OClO^{2+}$. Coincidence peaks due to the dissociation of $OClO^{2+}$ to form $O^+ + ClO^+$ and $O^+ + Cl^+$ (and their isotopomers) were observed. The comparison of the simulation of the coincidence spectrum with the experimental data indicates that the dissociation of the dication to form $O^+ + Cl^+$ involves a multiple kinetic energy release.

The values derived for the energies of the dication states responsible for forming the observed ion pairs indicate that there are two distinct dication electronic states that dissociate to form the $O^+ + Cl^+$ pair. In addition, the two-body dissociation reaction to form $O^+ + ClO^+$ might well occur from the lowest of these two states although the dissociation of ground state $OClO^{2+}$ appears to favour the formation of $O^{+*} + ClO^+$. It seems clear that the lowest of these dication states is the ground electronic state of $OClO^{2+}$, giving the first estimate of the double ionization potential of OClO as 35 $\pm$ 2 eV.

6.4 Two-Dimensional Studies

6.4.1 Data Analysis

6.4.1.1 Single Ionization

A typical singles spectrum obtained using the modified experimental arrangement employed in the 2D studies is shown in Fig. 6.7. As can been seen in the figure, the parent ion $OClO^+$ and fragment ions O^+, O_2^+, Cl^+ and ClO^+ and their isotopes are observed in the spectrum. The spectrum also contains small signals resulting from traces of air and water, the principal background gas in the

apparatus and molecular chlorine. As described in the Section 6.2.1, every effort is made during the synthesis of OClO to remove any unreacted Cl_2 from the sample but it is possible that some traces of Cl_2 still remain. In addition, due to the long acquisition times required to obtain adequate counting statistics some degradation of the OClO sample is occurring, resulting in the presence of Cl_2^+ ions in the singles spectrum.

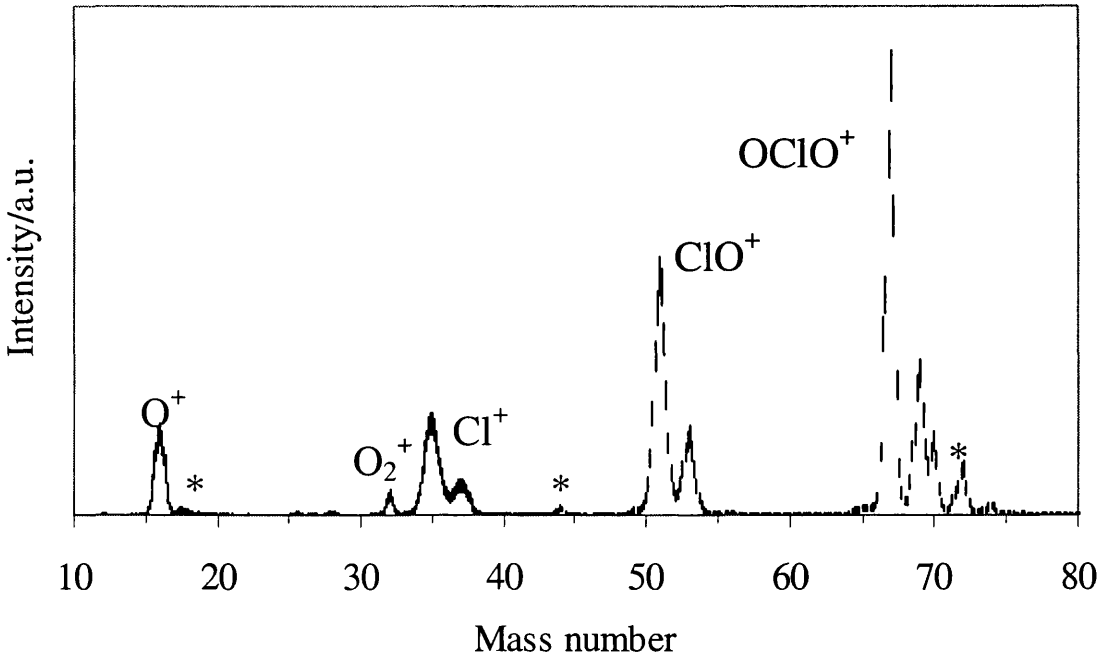

Fig. 6.7 Typical singles spectrum of OClO recorded at 250 eV. The peaks marked with an asterisk correspond to signals due to traces of CO_2^+ and Cl_2^+ from the residual gas. To aid interpretation, the error bars shown have been scaled to represent twenty standard deviations.

Singles spectra were recorded at 70, 100, 250 and 320 eV and the relative partial ionization cross sections σ_r^I for the formation of the singly charged ions from OClO, relative to the parent ion $OClO^+$, have been determined using Eq. 3.19 and are given in Table 6.7. For the chlorinated ions, the ion signals of both chlorine isotopes were determined and then combined to give a single value of σ_r^I for each ion. Only one singles spectrum was recorded at each electron energy because it was necessary to run at very low count rates to avoid degradation of the filament and consequently the data acquisition time had to be increased in order to obtain adequate counting statistics.

Table 6.7 Values of σ_r^I for the formation of the indicated product ion from OClO (the numbers in parentheses indicate the statistical error in the last figure of each cross section).

Electron energy	σ_r^I			
/eV	O^+	O_2^+	Cl^+	ClO^+
70	0.314(2)	0.0216(5)	0.270(3)	0.738(3)
100	0.390(2)	0.0324(5)	0.320(3)	0.778(3)
250	0.317(2)	0.0318(4)	0.322(3)	0.784(3)
320	0.339(2)	0.0363(5)	0.314(3)	0.785(3)

Any contribution from the ionization of Cl_2^+ to the Cl^+ fragment ion signal in the singles spectrum was calculated using the relative intensity of Cl^+ to Cl_2^+ derived from singles spectra of Cl_2 recorded over the range of electron energies employed. This subtraction process has been described in more detail in Section 6.3.1.1. Thus, the contribution of the ionization of Cl_2 to the Cl^+ ion signal in the OClO singles spectrum can be accurately determined and subtracted.

As explained in the Chapter 5, the values of $\sigma_r^{\ l}$ for the fragment ions of OClO (Table 6.7) cannot be directly compared with the data derived in the one-dimensional study, as values of $\sigma_r^{\ si}$ are determined from the one-dimensional time-of-flight mass spectra. In order to compare the data obtained in the one-dimensional and 2D studies of the single ionization of OClO, it is necessary to determine the values of $\sigma_r^{\ si}$ from the singles spectrum by subtracting the double ionization contribution. The values of $\sigma_r^{\ si}$ for the fragment ions of OClO thus derived from the singles spectra are given in Table 6.8. In these calculations the value of f_i, derived from the normalisation experiments performed on CF_4 (Chapter 3), is 0.063 ± 0.014.

Table 6.8 Values of $\sigma_r^{\ si}$ for the formation of the indicated product ion from OClO (the numbers in parentheses indicate the statistical error in the last figure of each value).

Electron energy	$\sigma_r^{\ si}$			
/eV	O^+	O_2^+	Cl^+	ClO^+
70	0.108(42)	0.0216(5)	0.108(36)	0.655(17)
100	0.078(63)	0.0324(5)	0.102(49)	0.673(21)
250	0.113(41)	0.0318(4)	0.168(35)	0.699(18)
320	0.075(53)	0.0363(5)	0.109(46)	0.700(17)

6.4.1.2 Double Ionization

A pairs spectrum of $OClO^{2+}$ recorded at an electron energy of 250 eV is shown in Fig. 6.8.

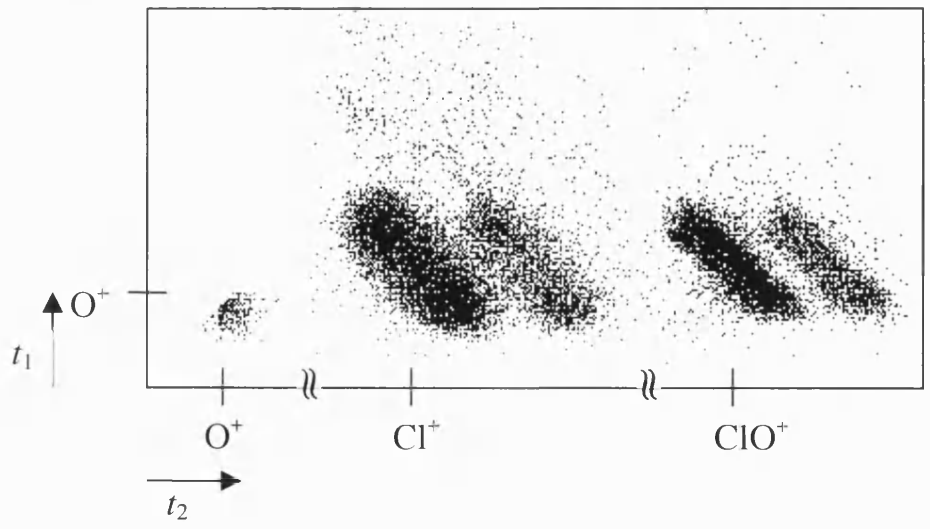

Fig. 6.8 Subtracted pairs spectrum of $OClO^{2+}$ recorded at 250 eV.

Pairs spectra of $OClO^{2+}$ were recorded concurrently with the singles spectra at 70, 100, 250 and 320 eV. Prior to analysis of the spectra, any false coincidences, pairs of ions not formed by the same dication dissociation event, are subtracted using the algorithm described in Chapter 3.

In agreement with the one-dimensional coincidence spectra of $OClO^{2+}$ (Fig. 6.4), the ion pairs $O^+ + ClO^+$ and $O^+ + Cl^+$ are observed in the pairs spectrum along with their isotopomers. In addition, the previously unobserved dissociation of the dication to form the identical ion pair $O^+ + O^+$ [Reaction (6.V)] is also detected but, due to the dead time of the TDC, only a small proportion of the $O^+ + O^+$ peak is observed in the pairs spectrum.

The $O^+ + O^+$ ion pair was not observed in the one-dimensional coincidence spectrum because the signals corresponding to this ion pair would have been obscured by the 'ringing' in the spectrum at small Δt_{tof} (Fig. 6.4). The observation of this ion pair in the pairs spectra could arise from the double ionization of background gas present in the ionization region of the TOFMS, *i.e.* O_2, CO_2. It is unlikely that the dissociation of O_2^{2+} is resulting in the reasonably intense $O^+ + O^+$ ion pair signal, as there is only a trace amount of background air present in the singles spectrum (Fig. 6.7). However, the CO_2^+ ion signal in the singles spectrum is moderately intense. In order to eliminate background CO_2 as the source of these ion pair signals, the possible contribution of CO_2^{2+} to $O^+ + O^+$ was calculated using the relative intensity of $O^+ + O^+$ to $CO^+ + O^+$ derived from pairs spectra of CO_2^{2+}. Thus, the contribution of the ionization of CO_2^{2+} to the $O^+ + O^+$ signal in the $OClO^{2+}$ spectrum can be determined and it is found to be negligible (1.4 counts). Therefore, it is clear that the $O^+ + O^+$ ion pair is indeed being produced by the dissociation of $OClO^{2+}$.

For each pairs spectrum, the intensity of the ion pairs was determined by summing the number of counts detected within the area of the relevant peak. But at low electron energies, due to the peak broadening experienced, it is difficult to determine the intensity of each individual isotopic peak. So at 70 eV the total intensity for the all the isotopic ion pairs in the dissociation reaction is obtained. The intensity of each ion pair formed by the dissociation of $OClO^{2+}$, relative to the total number of ion pairs observed in the subtracted pairs spectrum, I_{pair}/I_{total} is given in Table 6.9. Note that, in contrast to the one-dimensional coincidence study, the three-body reaction forming $O^+ + Cl^+$ is now the most intense dissociation reaction of $OClO^{2+}$.

Table 6.9 Values of I_{pair}/I_{total} for the dissociation reactions of $OClO^{2+}$ (the numbers in parentheses indicate the statistical uncertainty in the last figure of each value).

Electron energy	I_{pair}/I_{total}		
/eV	$O^+ + ClO^+$	$O^+ + Cl^+$	$O^+ + O^+$
70	0.387(19)	0.590(22)	0.022(4)
100	0.361(14)	0.586(19)	0.052(5)
250	0.402(15)	0.563(19)	0.035(4)
320	0.339(11)	0.610(17)	0.051(4)

For the pairs spectrum recorded at 250 eV the slope *b* of the peaks corresponding to the dissociation reactions was also determined. As discussed in Chapter 3, the slope of the peaks in the pairs spectrum can potentially provide information on the mechanism of the dication dissociation involved in the formation of a particular ion pair.

Evaluation of the Contribution of Double Ionization to the Singles Spectrum

Following the standard procedure described in Chapter 3, the pairs spectra are converted into double ionization mass spectra. Analysis of these spectra yields the double ionization fragment ion signal intensities which are used to determine the contribution of fragment ions from the dissociation of $OClO^{2+}$ to the singles spectrum. Thus, values of σ_r^{si} for the fragment ions of OClO can be determined from the singles spectrum (Eq. 3.26) which can be directly compared with the values of σ_r^{si} derived from the one-dimensional investigation. Fig. 6.9 shows the double ionization mass spectrum derived from the pairs spectrum of $OClO^{2+}$ recorded at 250 eV.

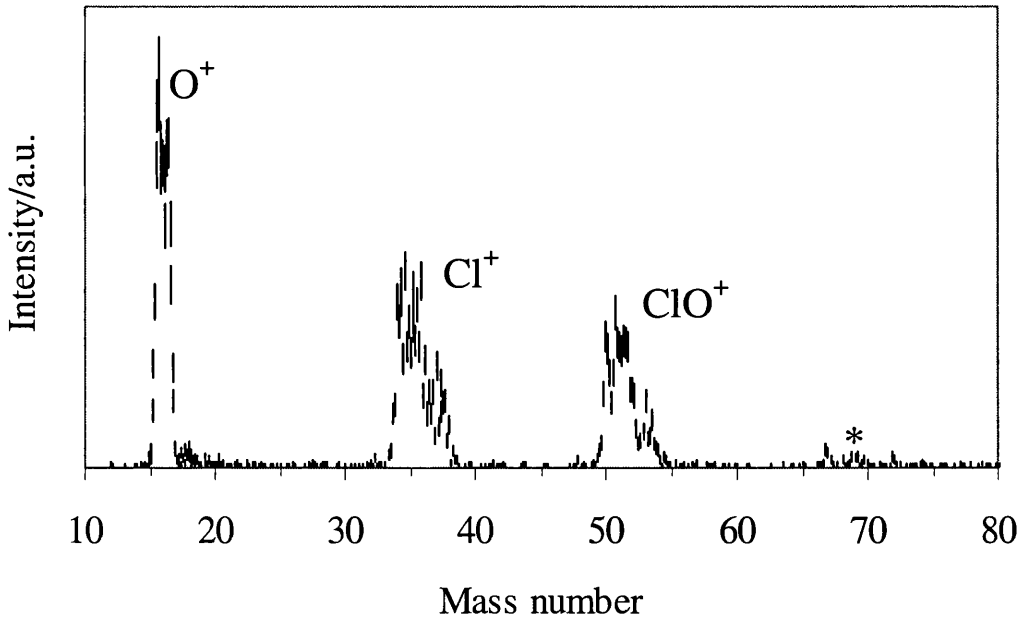

Fig. 6.9 Double ionization mass spectrum of OClO, converted from pairs spectrum recorded at 250 eV. The peak marked with an asterisk corresponds to $OClO^+$ signals arising from the statistics of the false coincidence subtraction.

Note that there is a trace signal corresponding to $OClO^+$ observed in this double ionization mass spectrum. However, due to the low $OClO^+$ ion signal intensity, it is clear that these signals arise from the statistics of the false coincidence subtraction. Indeed, the absence of any ion pairs in coincidence with $OClO^+$ in the pairs spectra confirms this assumption. The absence of any O_2^+ in this double ionization mass spectrum indicates that dissociation reactions involving the formation of

a bond between the two terminal atoms, *e.g.* the formation of O_2^+ from the terminal O atoms of $OClO^+$ and the formation of H_3^+ from CH_3OH^{2+},[34] is not occurring from $OClO^{2+}$.

Determination of the Ratio of Double-to-Single Ionization Cross Sections

From the analysis of the singles and pairs spectrum, it is now possible to obtain a first estimate of the double-to-single ionization cross sections ratio σ^{2+}/σ^+ for OClO using Eq. 3.39. The ratios of the total σ^{2+}/σ^+ for OClO, at the range of electron energies employed in this part of the study, are given in Table 6.10 and plotted in Fig. 6.10.

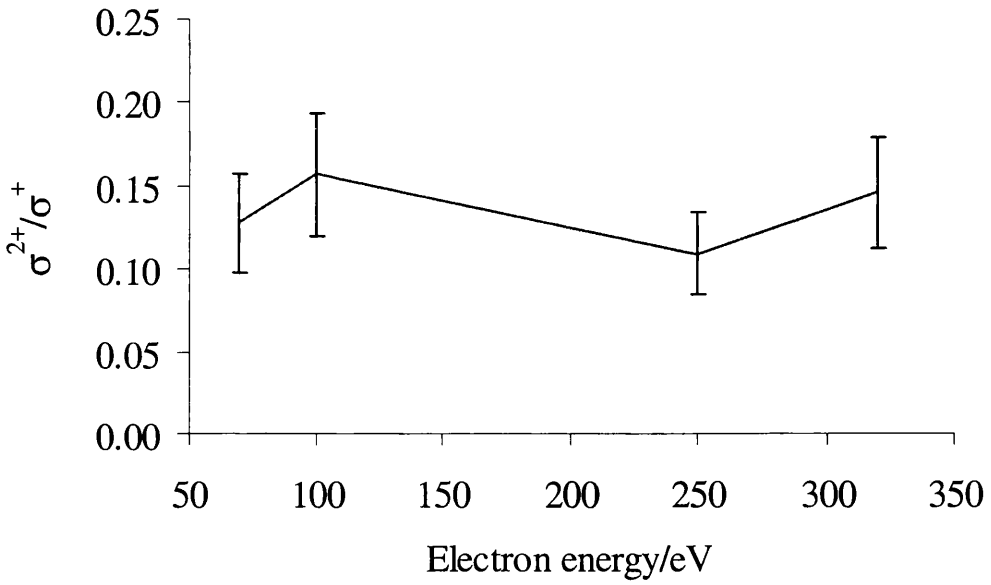

Fig. 6.10 Ratio of σ^{2+}/σ^+ for OClO. The error bars represent two standard deviations.

Table 6.10 Ratio of σ^{2+}/σ^+ for OClO (the numbers in parentheses indicate the statistical error in the last figure of each cross section).

Electron energy /eV	σ^{2+}/σ^+
70	0.127(29)
100	0.157(36)
250	0.109(25)
320	0.146(34)

6.4.2 Discussion

6.4.2.1 Single Ionization

In the 2D investigation of the single ionization of OClO the stable parent ion $OClO^+$ and fragment ions O^+, O_2^+, Cl^+ and ClO^+ are observed in the singles spectrum, the parent ion being the most abundant. This is consistent with the time-of-flight mass spectrum obtained in the one-dimensional study of OClO (Fig. 6.2).

As explained in greater detail in Chapter 5, the differing apparatus set-up employed in the 2D experiments results in the efficient detection of energetic fragments from both single and double dissociative ionization. This increase in the detection efficiency of energetic ions is apparent in Table 6.7 & Table 6.8. As expected, the values of σ_r^I (Table 6.7) for the O^+, Cl^+ and ClO^+ fragments are significantly larger than the values of σ_r^{si} (Table 6.8), both derived from the singles spectra, as a result of the contribution of energetic ions to the ion signals in the singles spectrum. From the double ionization studies of OClO, it has been seen that O^+, Cl^+ and ClO^+ fragments are all major dicationic dissociation products and therefore these dication fragmentation products are contributing to the ion signals in the singles spectrum. However, as O_2^+ is not a product of dicationic dissociation, there is no double ionization contribution to the O_2^+ ion signal in the singles spectrum and therefore, the values of σ_r^I and σ_r^{si} are the same.

Table 6.11 shows a comparison of the values of σ_r^{si} obtained in the one and two-dimensional studies of $OClO^{2+}$. No data was recorded in the one-dimensional investigation of OClO at 320 eV, but as can be seen from Table 6.1 and Fig. 6.3, there is little variation in the values of σ_r^{si} of the ions between 300 and 350 eV. So, for comparison between the one-dimensional and 2D work, the values of σ_r^{si} obtained at 300 eV in the one-dimensional study are quoted in Table 6.11.

Table 6.11 Comparison of σ_r^{si} for the fragment ions of OClO in the one-dimensional (time-of-flight mass spectrum) and 2D (singles spectrum) studies (the numbers in parentheses indicate the statistical error in the last figure of each cross section).

Fragment ion		σ_r^{si}			
		70 eV	100 eV	250 eV	320 eV*
O^+	1D	0.095(5)	0.110(5)	0.099(9)	0.097(4)
	2D	0.108(42)	0.078(63)	0.113(41)	0.075(53)
O_2^+	1D	0.033(1)	0.043(14)	0.041(9)	0.046(10)
	2D	0.0216(5)	0.0324(5)	0.0318(4)	0.0363(5)
Cl^+	1D	0.202(16)	0.203(11)	0.190(10)	0.185(15)
	2D	0.108(36)	0.102(49)	0.168(35)	0.109(46)
ClO^+	1D	0.639(6)	0.653(15)	0.653(25)	0.643(24)
	2D	0.655(17)	0.673(21)	0.699(18)	0.700(17)

* Data recorded at 300 eV in one-dimensional study.

As can be seen from Table 6.11, there is generally good agreement between the values of σ_r^{si} derived from the time-of-flight mass spectra (one-dimensional work) and singles spectra (2D work), within the error limits. However, the values of σ_r^{si} for the Cl^+ fragments derived from the singles spectra are lower than those values obtained in the one-dimensional study. It is possible that the difference between these data sets arises from a contribution of the ionization of Cl_2 to the Cl^+ ion signals in the time-of-flight mass spectrum. However, there is no evidence to suggest that any background Cl_2 is present in the sample of OClO used in the one-dimensional experiments. Therefore, a more likely explanation is that Cl^+ fragments from the dissociation of $OClO^{2+}$ were

being detected in the one-dimensional experiments. The subtraction procedure used in this 2D study will have removed any double ionization contribution from the singles spectrum thus resulting in a lower value of σ_r^{si}, indeed the true value of σ_r^{si} for Cl^+ from OClO.

From the comparison of the values of σ_r^{si} from the one and two-dimensional studies, it is clear that although the assumption that values of σ_r^{si} are derived from the one-dimensional time-of-flight mass spectra is valid for O^+, O_2^+ and ClO^+ fragments of OClO, some Cl^+ fragments from dissociative double ionization, formed along the axis of the TOFMS, are being detected. Despite the discrimination of the one-dimensional apparatus set-up against highly-energetic fragment ions, fragment ions from double ionization formed parallel to the axis of the TOFMS are detected. Therefore this double ionization contribution must be considered when deriving values of σ_r^{si} from time-of-flight mass spectra where there is a high angular discrimination.

6.4.2.2 Double Ionization

The pairs spectrum shows that the dissociation of $OClO^{2+}$ proceeds *via* a two-body dissociation reaction to form $O^+ + ClO^+$ and three-body reactions to form $O^+ + Cl^+$ and $O^+ + O^+$. In the one-dimensional coincidence experiments, only the non-identical ion pairs were observed. In contrast to the one-dimensional spectra, the $O^+ + Cl^+$ peak is the most intense with the relative intensities I_{pair}/I_{total} of $O^+ + ClO^+$, $O^+ + Cl^+$ and $O^+ + O^+$ determined at 250 eV as 1:1.4:0.09 respectively (Table 6.9). In contrast to the one-dimensional experiments, the most frequently occurring dissociation reaction of $OClO^{2+}$ is the three-body reaction forming $O^+ + Cl^+$. This suggests that the dication is more likely to fragment completely than undergo two-body fragmentation. The three-body dissociation of $OClO^{2+}$ giving rise to the $O^+ + O^+$ ion pair, is the least frequent reaction channel.

$O^+ + ClO^+$

The signals corresponding to the $O^+ + ClO^+$ dissociation reaction of $OClO^{2+}$ are made up of the $O^+ + {}^{35}ClO^+$ and $O^+ + {}^{37}ClO^+$ ion pairs. As the dissociation of $OClO^{2+}$ to form $O^+ + ClO^+$ is a two-body decay pathway, it is expected that the slope of the $O^+ + ClO^+$ peak is –1. As indicated in Table 6.12, the values of *b* for this ion pair, within the errors in the least squares fit, are unity. For the $O^+ + {}^{37}ClO^+$ ion pair, the intensity of this peak is weak and therefore the error in *b* from the fitting procedure will be increased.

Table 6.12 Values of b for the peaks in the pairs spectrum corresponding to the $O^+ + ClO^+$ ion pairs. The numbers in parentheses represent the statistical error in the value.

Ion pair	b
$O^+ + {}^{35}ClO^+$	-0.97(3)
$O^+ + {}^{37}ClO^+$	-0.95(4)

A 3D plot, with a 2D projection, of the intensities of the $O^+ + ClO^+$ ion pair signals is shown in Fig. 6.11. As can be seen in the figure, the high intensity region of the peak corresponding to the $O^+ + {}^{35}ClO^+$ ion pair is uniform along the axial length of the peak, within the error limits of the counting statistics. This indicates that, as expected, the use of the MCP detector eliminates any angular discrimination and so all the $O^+ + ClO^+$ ion pairs formed from $OClO^{2+}$ are detected.

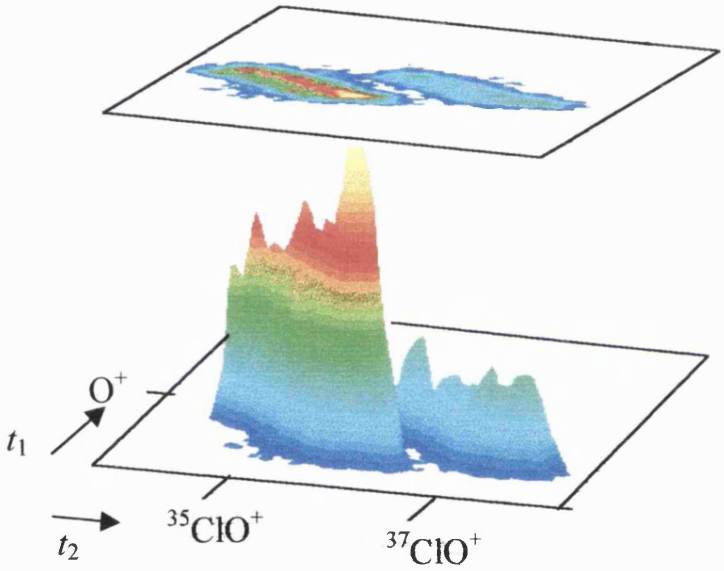

Fig. 6.11 3D plot with a 2D projection of the intensity of the dissociation reactions making up the $O^+ + ClO^+$ ion pair.

The KER upon the two-body dissociation of $OClO^{2+}$ to form $O^+ + ClO^+$ has been derived from the width of the corresponding peak in the pairs spectrum, to confirm that the differing apparatus set-ups used in the one and two-dimensional studies of $OClO^{2+}$ yield consistent results. A Monte Carlo simulation of the $O^+ + ClO^+$ peak in the pairs spectrum has been performed (Chapter 3). The values of KER and F_{KERD} for the dication dissociation reaction forming $O^+ + ClO^+$ derived from both the one and two-dimensional coincidence spectra are given in Table 6.13. Note that the values of the KER obtained from the two investigations of $OClO^{2+}$ are in good agreement with one another, again emphasising the consistency between the data obtained in the one and two-dimensional investigations of the ionization of OClO. The discrepancy between the values of F_{KERD} determined in the two studies is likely to be due to the uncertainty associated with determining the pairs peak width.

Table 6.13 Values of the KER and F_{KERD} for forming $O^+ + ClO^+$ from $OClO^{2+}$ derived from the peak widths in the one and two-dimensional coincidence spectra.

	KER /eV	F_{KERD} /eV
1D	6.0	3.2
2D	6.4	2.5

The dication state energy associated with the KER value derived from the width of the $O^+ + ClO^+$ pairs peak is 33.6 ± 0.5 eV. However, this value of $E(OClO^{2+})$ assumes that the products are formed in their ground states. As discussed in Section 6.3.2.2, this assumption is perhaps invalid and the dissociation of the ground state dication actually forms $O^{+*} + ClO^+$. The dissociation limit for this ion pair containing an excited O^+ fragment, when coupled with the KER value derived from the peak in the pairs spectrum, yields a dication state energy of 36.9 ± 0.5 eV. Within the error limits, this value of $E(OClO^{2+})$ derived from the 2D spectrum is in good agreement with the value obtained in the one-dimensional study (36.5 ± 0.2 eV).

$O^+ + Cl^+$

The signals corresponding to the $O^+ + Cl^+$ dissociation reaction of $OClO^{2+}$ are made up of the $O^+ + {}^{35}Cl^+$ and $O^+ + {}^{37}Cl^+$ ion pairs. As can be seen from Fig. 6.8, it also appears that there are ion pair signals appearing in the spectrum above the $O^+ + Cl^+$ peak, *i.e.* at $t_1 > t_{O^+}$.

The slope b of the peaks corresponding to the $O^+ + Cl^+$ dissociation reaction in the pairs spectrum recorded at 250 eV is given in Table 6.14.

Table 6.14 Values of b for the peaks corresponding to the $O^+ + Cl^+$ dissociation reaction of $OClO^{2+}$. The numbers in parentheses represent the statistical error in the value.

Ion pair	b
$O^+ + {}^{35}Cl^+$	-0.96(3)
$O^+ + {}^{37}Cl^+$	-1.05(4)

In the one-dimensional study of the dissociation of $OClO^{2+}$, no definitive fragmentation pathway could be assigned for the formation of the $O^+ + Cl^+$ ion pair due to the similarity in the values of $E(OClO^{2+})$, derived from the KER, for the possible dissociation mechanisms. If $OClO^{2+}$ dissociates directly to form $O^+ + Cl^+$ then b = -1 for the peak in the pairs spectrum. If the dissociation follows a sequential pathway involving an initial two-body charge separation to form $O^+ + ClO^+$ followed by further dissociation to form the $O^+ + Cl^+$ ion pair then the expected value of b = -0.31. From Table 6.14, it is apparent that the values of b for this ion pair are significantly nearer unity than –0.31. Thus may suggest the occurrence of a direct dissociation mechanism but, as explained in Chapter 3, the expected value of b for a sequential dissociation pathway is, in fact, a lower limit. If the secondary dissociation of the ClO^+ ion occurs within the Coulomb field of the O^+ ion then the value of b increases from the limiting value towards –1. Therefore, this three-body dissociation reaction

either involves a true Coulomb explosion or a very fast sequential mechanism, with the secondary dissociation of the ClO^+ ion to form Cl^+ occurring within the Coulomb field of the O^+ fragment ion on a timescale of ~1-5 ps.

Similarly to the formation of $O^+ + Cl^+$ from Cl_2O^{2+}, it is possible that the signals appearing in the $OClO^{2+}$ pairs spectrum at $t_1 > t_{O+}$ (Fig. 6.8) may arise from the detection of pairs of slower ions which have longer flight times and therefore give rise to the secondary peak, with an intensity of 2% of the main $O^+ + Cl^+$ peak, observed at $t_1 > t_{O+}$. Indeed, if the dissociation of $OClO^{2+}$ is proceeding *via* an initial charge separation to $O^+ + ClO^+$, followed by the dissociation of the ClO^+ ion over a timescale of perhaps 1 ns, then some of the Cl^+ ions will have longer flight times having spent some as part of a heavier, and therefore slower, ion. So, a number of the observed $O^+ + Cl^+$ ion pairs must be formed by a sequential dissociation of the dication. Although from the slope of the peak, it is not possible to definitively assign a dication decay pathway for this dissociation reaction, triple coincidence studies[19-24] have shown that a true Coulomb explosion is rare. In addition, the presence of the tail on the $O^+ + Cl^+$ peak indicates that the formation of this ion pair from $OClO^{2+}$ occurs *via* a sequential mechanism involving an initial charge separation to form $O^+ + ClO^+$ followed by secondary monocation dissociation to form $O^+ + Cl^+$. The majority (98%) of this dissociation reaction is fast but some $O^+ + Cl^+$ ion pairs are also being formed as a result of slower secondary dissociation, perhaps occurring once the ClO^+ ion has left the Coulomb field of the O^+ ion, thus giving rise to the secondary $O^+ + Cl^+$ peak in the pairs spectrum.

In contrast to the one-dimensional coincidence spectra, this three-body reaction is the most intense in the pairs spectrum. The differing relative abundances of the dissociation reactions of $OClO^{2+}$ in the 2D experiments undoubtedly arises because the improved 2D experimental arrangement, including the use of a detector with a larger cross sectional area, detects the energetic fragments produced away from the axis of the TOFMS upon sequential dissociation of $OClO^{2+}$ to form $O^+ + Cl^+$ more efficiently. In the one-dimensional study, any fragments of sequential dissociation not formed along the axis of the TOFMS would not be detected thus resulting in a biased relative intensity in favour of the linear two-body dissociation reaction. The sequential dissociation of $OClO^{2+}$ to form $O^+ + Cl^+$ suggests that, as this three-body dissociation reaction is the most frequently occurring, following the initial charge separation of the dication to form $O^+ + ClO^+$, the ClO^+ fragment is most likely to undergo secondary dissociation rather than remain stable. The dissociation of ClO^+ to dissociate to form Cl^+ requires less energy than forming O^+ and as a result, $O^+ + Cl^+$ is the most abundant three-body dissociation reaction.

$O^+ + O^+$

The slope of the peak corresponding to the $O^+ + O^+$ ion pair has not been determined as the area of the peak observed in the pairs spectrum is small and therefore the slope of this section would be biased and not representative of the entire peak. In addition, unfortunately it is not possible to determine the KER upon formation of this ion pair or to determine an accurate value of F_{KERD}, due to the majority of this peak being obscured by the dead time. Therefore, no information concerning the fragmentation mechanism for this minor dissociation reaction can be obtained from the pairs spectrum. However, as discussed above, for three-body dissociation reactions, a true Coulomb explosion is rare[19-24] and thus perhaps the dissociation mechanism involved is an initial two-body charge separation to $O^+ + ClO^+$ followed by further dissociation to form the observed $O^+ + O^+$ ion pair [Reaction (6.IX)].

$$\begin{array}{c} OClO^{2+} \rightarrow O^+ + ClO^+ \\ \downarrow \\ O^+ + O^+ + Cl \end{array} \qquad (6.VIX)$$

In order to derive some information concerning the dissociation of $OClO^{2+}$ to form $O^+ + O^+$, it is necessary to decrease the dead time of the CFD. As a result, an increased area of the $O^+ + O^+$ peak would be observed in the pairs spectrum, enabling a reasonable measurement of the peak slope and estimation of reliable KER and F_{KERD} values from the peak width to be made.

Ratio of Double-to-Single Ionization Cross Sections

The value of the ratio of σ^{2+}/σ^+ has been determined for OClO at each electron energy and are listed in Table 6.10 and plotted in Fig. 6.10. As can be seen in the figure, there is an initial increase in σ^{2+}/σ^+ as the electron energy is raised and there is an increased likelihood of double ionization, reaching a maximum at 100 eV and then decreasing as the electron energy is raised further. Between 250 and 320 eV, the ratio of σ^{2+}/σ^+ increases once more, perhaps due to the onset of triple ionization at high electron energies, resulting in an increase of σ^{2+}/σ^+. Pairs of singly charged ions from dissociative multiple ionization formed at these high electron energies may contribute to the ion pair intensities in the pairs spectra thus increasing the so-called ratio of σ^{2+}/σ^+.

At 100 eV, the ratio of σ^{2+}/σ^+ for OClO is 15 %. This value is relatively high, as multiple ionization is conventionally a minor reaction channel in comparison with single ionization.[35] Thus for OClO, multiple ionization is a significant proportion of the total ionization of OClO and the contribution of double ionization to ion signal intensities in mass spectra must be considered.

6.4.3 Conclusion

The second part of this chapter discusses the 2D investigation of the single and double ionization of OClO. Time-of-flight mass spectrometry is used to investigate the single ionization of OClO. Stable parent ions $OClO^+$ and fragment ions O^+, O_2^+, Cl^+ and ClO^+ and their relevant isotopes were observed in the mass spectra, the parent ion being the most abundant. From these mass spectra, the values of σ_r^{si} for OClO for incident electron energies of 70, 100, 250 and 320 eV, where the contribution of any fragment ions from dissociative double ionization is assessed and subtracted, have been determined.

2D coincidence experiments were performed to investigate the formation and fragmentation of $OClO^{2+}$. Peaks due to the formation of $O^+ + ClO^+$, $O^+ + Cl^+$ and the previously unobserved identical ion pair $O^+ + O^+$ were detected in the 2D coincidence spectra. Contrary to the one-dimensional investigation of $OClO^{2+}$, the three-body dication dissociation reaction forming $O^+ + Cl^+$ was the most frequently occurring reaction channel. The increased detection efficiency of the energetic fragments not formed along the axis of the TOFMS such as those from sequential dication dissociation reactions experienced using the 2D apparatus set-up accounts for the increased abundance of the $O^+ + Cl^+$ ion pair.

From the slopes of the peaks corresponding to $O^+ + Cl^+$, it is not possible to discern whether the dication fragmentation pathway forming this ion pair is a direct mechanism or a sequential mechanism involving an initial charge separation and subsequent monocation dissociation. However, it is apparent that the dissociation is either a true Coulomb explosion or a fast sequential mechanism. There is some evidence in the 2D coincidence spectrum of a slower sequential dissociation of $OClO^{2+}$ to form $O^+ + Cl^+$ proceeding *via* an initial two-body charge-separating reaction, forming O^+ and a longer-lived ClO^+ intermediate which then dissociates to form Cl^+. Therefore, the dissociation of $OClO^{2+}$ to form $O^+ + Cl^+$ probably occurs *via* a fast sequential mechanism involving an initial two-body charge separation with a fraction of the ion pairs being formed by a slower sequential dication dissociation.

The first estimate of the total double-to-single ionization cross section ratio shows that multiple ionization is a significant proportion (15%) of the total ionization of OClO. Therefore, when extracting any data from mass spectra, it is essential to consider the possible contribution of dissociative multiple ionization to fragment ion signals in the spectra.

6.5 Overall Conclusions

This chapter describes the investigation of the single and double ionization of chlorine dioxide, OClO. The single ionization of OClO has been investigated using time-of-flight mass

spectrometry in order to determine values of the relative partial single ionization cross section σ_r^{si} for the fragment ions of OClO. The double ionization of OClO has been investigated using ion-ion coincidence techniques to derive information concerning the mechanisms and energetics of the dication dissociation reactions.

From the single ionization of OClO, the parent ion $OClO^+$ and fragment ions O^+, O_2^+, Cl^+ and ClO^+ and their isotopes were observed in the time-of-flight mass spectrum. From the spectra, values of σ_r^{si}, relative to the parent ion, were derived. The two different approaches used in the one and two-dimensional investigations yielded values of σ_r^{si} for O^+, O_2^+ and ClO^+ in good agreement with one another. However, the value derived for Cl^+ from the one-dimensional mass spectrum does in fact contain a contribution from dissociative double ionization to the ion signal in the mass spectrum. Therefore, the lower value of σ_r^{si} derived from the 2D study is a more reliable indication of the value of σ_r^{si} for the Cl^+ fragment of OClO. Thus, although the assumption that energetic ions from multiple ionization are discriminated against in the one-dimensional study does generally hold true, any dicationic dissociation occurring along the axis of the TOFMS will result in a contribution of fragments from multiple ionization to the one-dimensional time-of-flight mass spectra.

Coincidence techniques were employed to investigate the formation and fragmentation of $OClO^{2+}$. In the one and two-dimensional coincidence spectra, the dissociation of $OClO^{2+}$ leads to the formation of $O^+ + ClO^+$, $O^+ + Cl^+$ and $O^+ + O^+$ ion pairs. The three-body dissociation reaction forming $O^+ + Cl^+$ is the most frequently occurring dication decay channel.

Investigations of the energetics of the dissociation reactions of $OClO^{2+}$ indicate that the formation of the two-body dissociation reaction $O^+ + ClO^+$ occurs from the ground electronic state of the dication. Thus a first estimate of the double ionization energy of OClO has been determined as 35 ± 2 eV. For the three-body dissociation reaction forming $O^+ + Cl^+$, the fragmentation pathway followed is a sequential mechanism involving an initial two-body charge separation followed by secondary dissociation of the molecular monocation to form the detected ion pair. In addition, there are two distinct dication states responsible for the formation of the $O^+ + Cl^+$ ion pair and the lowest of these dication states may be the ground state of the dication. No dication dissociation mechanism could be assigned for the formation of the $O^+ + O^+$ ion pair, although the most likely fragmentation pathway is, as for the $O^+ + Cl^+$ ion pair, a sequential mechanism involving secondary decay.

The first estimate of the ratio of the total double-to-single ionization cross sections indicates that double ionization contributes around 15% to the total ionization cross section of OClO. Therefore, multiple ionization must be considered when investigating the single ionization of molecules.

References

1 H. Davy, *Phil. Trans.*, **105** (1815) 214

2 K. Miyazaki, M. Tanoura, K. Tanaka and T. Tanaka, *J. Mol. Struct.*, **116** (1986) 435

3 A.B. Cornford, D.C. Frost, F.G. Herring and C.A. McDowell, *Chem. Phys. Lett.*, **10** (1971) 345

4 S. Hubinger and J.B. Nee, *Chem. Phys.*, **181** (1994) 247

5 V.I. Alekseev, T.S. Zyubina, A.S. Zyubin and A.V. Baluev, *Izv. Akad. Nauk SSSR, Ser. Khim.*, **10** (1989) 2278

6 E. Bishenden and D.J. Donaldson, *J. Chem. Phys.*, **101** (1994) 9565

7 R.P. Wayne, G. Poulet, P. Biggs, J.P. Burrows, R.A. Cox, P.J. Crutzen, G.D. Hayman, M.E. Jenkin, G. Le Bras, G.K. Moortgat, U. Platt and R.N. Schindler, *Atmos. Env.* , **29** (1995) 2677

8 P. Ludowise, M. Blackwell and Y. Chen, *Chem. Phys. Lett.*, **273** (1997) 211

9 M. Roth, C. Maul and K.-H. Gericke, *J. Chem. Phys.*, **107** (1997) 10582

10 E. Rühl, A. Jefferson and V. Vaida, *J. Phys. Chem.*, **94** (1990) 2990

11 I.P. Fisher, *Trans. Faraday Soc.*, **63** (1967) 684

12 H.F. Cordes and S.R. Smith, *J. Chem. Eng. Data,* **15** (1970) 158

13 A.V. Baluev, Z.K. Nikitina, L.I. Fedorova and V.Y. Rosolovskii, *Izv. Akad. Nauk SSSR, Ser. Khim.*, **9** (1980) 1963

14 R. Flesch, E. Rühl, K. Hottmann and H. Baumgärtel, *J. Phys. Chem.*, **97** (1993) 837

15 U. Rockland, H. Baumgärtel, E. Rühl, O. Lösking, H.S.P. Müller and H. Willner, *Ber. Bunsenges. Phys. Chem.*, **99** (1995) 969

16 C.S.S. O'Connor, N. Tafadar and S.D. Price, *J. Chem. Soc., Faraday Trans.* , **94** (1998) 1797

17 R.I. Derby and W.S. Hutchinson, *Inorg. Synth.*, **4** (1953) 152

18 A.M. Phipps and D.N. Hume, *J. Chem. Educ.*, **45** (1968) 664

19 J.H.D. Eland, *Mol. Phys.*, **61** (1987) 725

20 J.H.D. Eland, *Chem. Phys. Lett.*, **203** (1993) 353

21 S. Hsieh and J.H.D. Eland, *J. Chem. Phys.*, **103** (1995) 1006

22 I. Nenner and J.H.D. Eland, *Z. Phys. D,* **25** (1992) 47

23 M. Simon, P. Morin, P. Lablanquie, M. Lavollee, K. Ueda and N. Kosugi, *Chem. Phys. Lett.*, **238** (1995) 42

24 K. Codling, L.J. Frasinski, P.A. Hatherly, M. Stankiewicz and F.P. Larkins, *J. Phys. B,* **24** (1991) 951

25 P.J. Richardson, J.H.D. Eland and P. Lablanquie, *Org. Mass Spec.*, **21** (1986) 289

26 D.M. Curtis and J.H.D. Eland, *Int. J. Mass Spectrom. Ion Proc.*, **63** (1985) 241

27 P.R. Bevington, *Data Reduction and Error Analysis for the Physical Sciences*, McGraw-Hill, New York, 1992

28 S. Leach, J.H.D. Eland and S.D. Price, *J. Phys. Chem.*, **93** (1989) 7575

29 G. Herzberg, *Electronic Spectra and Electronic Structure of Polyatomic Molecules*, Van Nostrand, Princeton, N.J., 1966.

30 C.E. Moore, *Atomic Energy Levels*, National Bureau of Standards, U.S. Government Printing Office, Washington D.C., 1949.

31 D.K. Bulgin, J.M. Dyke, N. Jonathan and A. Morris, *J. Chem. Soc., Faraday Trans.* , **75** (1979) 456

32 G. Parlant, J. Senekowitsch, S.V. O'Neil and D.R. Yarkony, *J. Chem. Phys.*, **94** (1991) 7208

33 B.P. Tsai and J.H.D. Eland, *Int. J. Mass Spectrom. Ion Proc.*, **36** (1980) 143

34 J.H.D. Eland and B.J. Treves-Brown, *Int. J. Mass Spectrom. Ion Proc.*, **113** (1992) 167

35 T.D. Märk, in T.D. Märk, G.H. Dunn (Eds.), *Electron Impact Ionization*, Springer-Verlag, New York, 1985

7. Single and Double Ionization of HNO_3

7.1 Introduction

As early as the thirteenth century, nitric acid was used by alchemists to refine precious metals but its chemical composition was not established until 1816.[1] Nitric acid, HNO_3, is an important trace constituent in the Earth's upper atmosphere and plays a key role in the complex chemistry of the stratospheric ozone cycle. Nitric acid is a reservoir molecule for the nitrogen oxides, NO_x, which are involved in the generation and destruction of ozone [Reaction (4.II)] and other significant atmospheric effects (Chapter 4).[2] In the lower stratosphere NO_x radicals are generated by the photolysis of nitric acid,

$$HNO_3 + h\nu \rightarrow HO + NO_2 \qquad (7.I)$$

while the main depletion process for stratospheric NO_x involves the formation of nitric acid which is subsequently rained out of the atmosphere.[2]

$$HO + NO_2 + M \rightarrow HNO_3 + M \qquad (7.II)$$

Despite the atmospheric significance of nitric acid and the interest in its formation and photodissociation dynamics,[3-7] there have been few investigations of its ionization. In fact, the simple mass spectrum of nitric acid has not been well characterised and is not reported either in the Eight Peak Index of Mass Spectra[8] or the NIST database.[9] The two studies of the ionization of nitric acid reported in the literature are an early EIMS study[10] and a more recent PIMS study[11] but there have been no investigations of the double ionization of HNO_3. The lack of available data concerning the ionization of HNO_3 is undoubtedly due to the inherent difficulty in preparing a pure sample of this reactive molecule, which makes the recording of reproducible mass spectra problematic.

As part of the ongoing investigation of the ionization of reactive species, this chapter discusses one and two-dimensional investigations of the single and double ionization of HNO_3.[12,13] Time-of-flight mass spectrometry is used to determine relative partial single ionization cross sections of HNO_3 over a range of electron energies. One and two dimensional coincidence techniques are used to investigate the formation and fragmentation of HNO_3^{2+}. Information obtained from the coincidence spectra can give an indication of the mechanisms by which HNO_3^{2+} dissociates and the energies of the electronic states of HNO_3^{2+} which dissociate to form the observed ion pairs. Finally, estimates of the double ionization energy and the ratio of the double-to-single ionization cross sections for HNO_3 can be made.

7.2 Experimental Details

The experimental techniques employed in both the one and two-dimensional studies of the single and double ionization of HNO_3 have been described in detail in Chapter 2.

7.2.1 Preparation of HNO_3

The nitric acid sample used for these experiments was prepared by the removal of water from a commercially purchased sample of nitric acid (HNO_3 content >90%) by repeated vacuum distillation over P_2O_5. The purified sample was stored in a blackened vessel at dry ice temperature. During the experiments the anhydrous liquid acid was placed in a salted ice bath, at a temperature of approximately 255 K, and transported into the TOFMS *via* the clean and non-catalytic inlet system described in Chapter 2. The amount of gaseous HNO_3 flowing into the TOFMS was controlled by slight variations in the temperature of the ice bath.

7.2.2 Procedures

For the one-dimensional studies, time-of-flight mass spectra were recorded at incident electron energies of 45-450 eV in order to determine the relative partial single ionization cross sections σ_r^{si} of the ions produced by the single ionization of HNO_3. In order to determine the appearance energy of a previously unobserved fragmentation of HNO_3^+ to form H^+, the values of σ_r^{si} for the formation of H^+ were evaluated at electron energies from 45 to 80 eV. Coincidence spectra were recorded at an ionizing electron energy of 150 eV and also at a range of lower electron energies, from 30 to 70 eV, in order to determine the appearance energies of the pairs of fragment ions produced by the dissociative double ionization of HNO_3.

For the 2D studies, time-of-flight mass spectra were recorded at electron energies of 70, 100, 250 and 320 eV to determine values of σ_r^{si} for the fragment ions of HNO_3. Coincidence spectra were recorded at the same electron energies and the intensities and slopes of the peaks corresponding to the fragment ion pairs formed from HNO_3^{2+} were investigated.

7.3 One-Dimensional Studies

7.3.1 Data Analysis

7.3.1.1 Single Ionization

A typical one-dimensional time-of-flight mass spectrum of HNO_3 is shown in Fig. 7.1. As can be seen from this figure, the stable parent ion (HNO_3^+) and fragment ions H^+, N^+, O^+, OH^+, NO^+

and NO_2^+ are detected. The spectrum also contains small signals resulting from traces of air and water, the principal background gas in the apparatus.

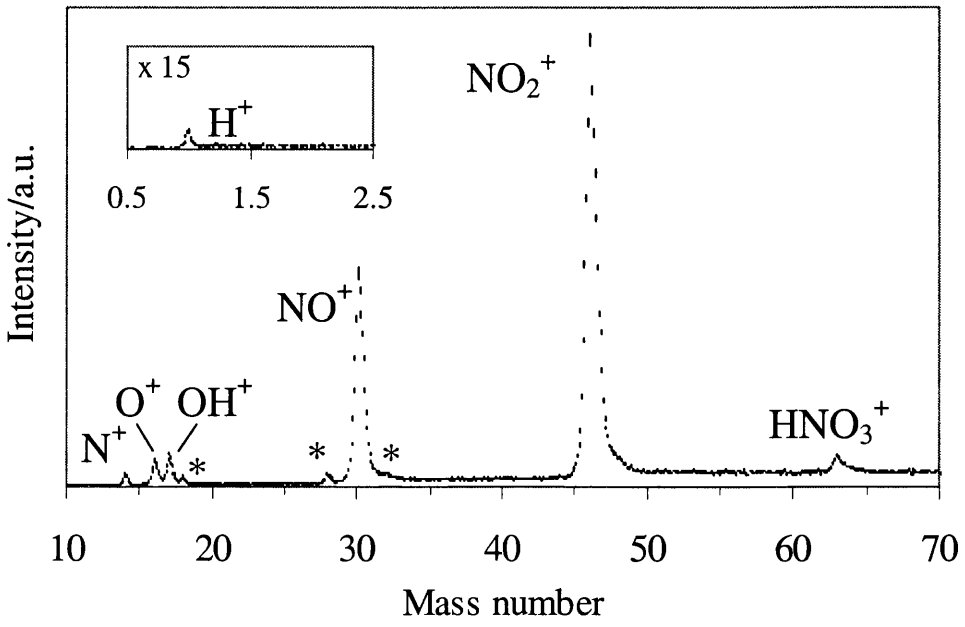

Fig. 7.1 A typical time-of-flight mass spectrum of HNO_3 recorded at an electron energy of 150 eV. The error bars shown, derived from the counting statistics, represent two standard deviations. The peaks marked with asterisks correspond to signals due to traces of air and water (H_2O^+, N_2^+ and O_2^+) from the residual gas.

The parent and fragment ion signal intensities are obtained from the raw ion signals in the mass spectrum (Chapter 3) recorded at a range of electron energies from 40 to 450 eV. To remove any contribution from the ionization of the traces of air and water in the source region to the H^+, N^+, O^+, OH^+ and O_2^+ signals in the nitric acid spectrum, mass spectra of air and water were recorded over the range of electron energies employed in these experiments. From these spectra the relative intensities of the H^+, N^+, O^+, OH^+ and O_2^+ ions were determined, relative to the N_2^+ peak for the air spectra and H_2O^+ for the water spectra. The contribution of the ionization of air or water to the H^+, N^+, O^+, OH^+ and O_2^+ signals in the HNO_3 spectrum can then be accurately determined, and subtracted, by scaling the relative intensities of the fragment ions from the air and water spectra using N_2^+ and H_2O^+ signals in the HNO_3 spectra, as the N_2^+ and H_2O^+ in the HNO_3 spectra can only arise from background gas. This background correction is found to be negligible for the H^+ and O^+ fragment ion signals but accounts for the entire O_2^+ ion signal in the nitric acid spectrum, within the experimental uncertainty. The values of σ_r^{si} for the H^+, N^+, O^+, OH^+, NO^+ and HNO_3^+ ions observed in the spectrum, relative to the most abundant ion, NO_2^+, are determined from the ion intensities as described in Chapter 3, using the appropriate mass correction factor (Eq. 3.4). The values of σ_r^{si} determined using this analysis procedure are shown in Fig. 7.2 and listed in Table 7.1.

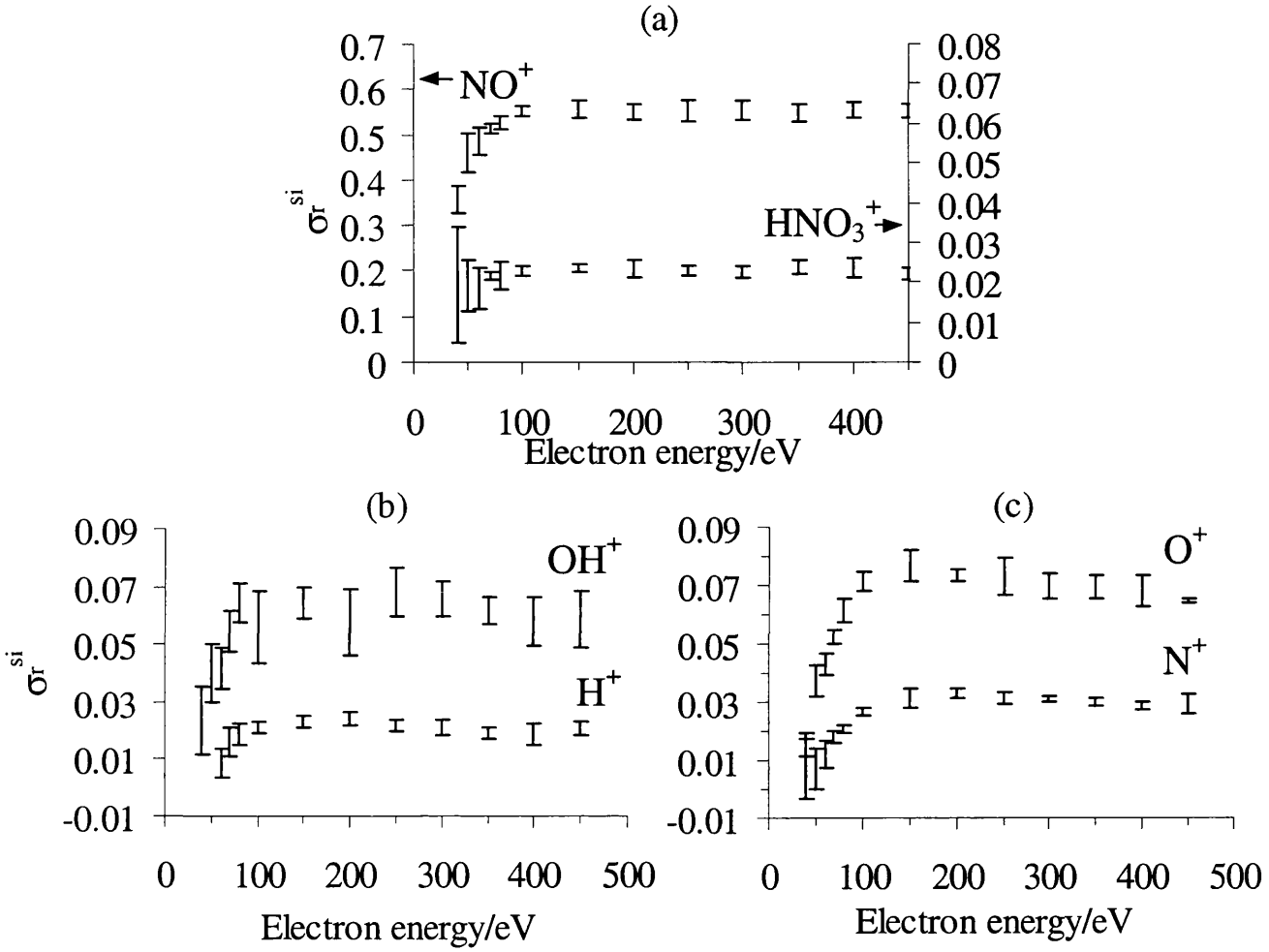

Fig. 7.2 Values of σ_r^{si} for forming (a) NO^+ and HNO_3^+, (b) OH^+ and H^+ and (c) O^+ and N^+ from HNO_3, relative to the most abundant ion in the mass spectrum, NO_2^+. The values for HNO_3^+ should be read from the right-hand axis. The error bars represent two standard deviations.

Table 7.1 Values of σ_r^{si} for the formation of the indicated product ion from HNO_3 (the numbers in parentheses indicate the standard deviation in the last figure of each cross section).

Electron	σ_r^{si}					
energy /eV	H^+	N^+	O^+	OH^+	NO^+	HNO_3^+
40	—	0.007(10)	0.0154(40)	0.024(12)	0.356(29)	0.0195(145)
50	—	0.0070(72)	0.0374(52)	0.040(10)	0.459(44)	0.0192(62)
60	0.0085(50)	0.0119(45)	0.0430(35)	0.0415(71)	0.486(29)	0.0184(50)
70	0.0159(52)	0.0181(19)	0.0523(23)	0.0546(73)	0.511(11)	0.0217(9)
80	0.0190(37)	0.0207(12)	0.0614(39)	0.0644(66)	0.527(15)	0.0215(33)
100	0.0213(21)	0.0265(13)	0.0714(35)	0.056(13)	0.552(11)	0.0228(14)
150	0.0232(19)	0.0314(31)	0.0767(53)	0.0645(54)	0.557(19)	0.0236(8)
200	0.0240(22)	0.0330(15)	0.0735(20)	0.058(12)	0.550(19)	0.0232(20)
250	0.0216(21)	0.0312(20)	0.0732(62)	0.0681(87)	0.552(23)	0.0229(12)
300	0.0212(27)	0.0307(10)	0.0698(43)	0.0659(61)	0.554(20)	0.0227(16)
350	0.0191(19)	0.0299(15)	0.0691(40)	0.0615(49)	0.549(20)	0.0239(17)
400	0.0188(37)	0.0288(13)	0.0680(55)	0.0579(87)	0.555(16)	0.0234(24)
450	0.0206(25)	0.0294(31)	0.0644(7)	0.059(10)	0.553(15)	0.0220(16)

The values of σ_r^{si} given in Table 7.1 are the average of six independent determinations and the standard deviations of these determinations at each electron energy are also shown in Table 7.1 and plotted as the error bars in Fig. 7.2. The standard deviations are small, in accord with the small statistical error in each individual determination. Note that the density correction for the light H^+ fragments involves scaling by a large factor (Eq. 3.4), therefore amplifying any errors inherent in the analysis procedure.

In the two previous investigations of the ionization and fragmentation of nitric acid reported in the literature,[10,11] no H^+ fragments were detected. The detection of H^+ fragments in the current work is undoubtedly due to the higher ionizing energies employed and the absence of any discrimination against light ions such as could have been present in the quadrupole mass spectrometer used in the PIMS study. In order to determine the appearance energy of this newly observed fragment, the values of σ_r^{si} for the formation of H^+ from HNO_3^+ were evaluated at electron energies from 45 to 80 eV and are listed in Table 7.2.

The values of $\sigma_r^{si}(H^+)$ given in Table 7.2 are the average of three independent determinations, the standard deviation at each electron energy is also given in Table 7.2. By inspection (Table 7.2), the appearance energy for the H^+ fragment is determined to lie between 55 and 60 eV. A more accurate determination of this appearance energy is very difficult, as the statistical uncertainties in the weak H^+ signal are large near threshold. The appearance energies for the fragment ions OH^+, NO^+ and NO_2^+ have been previously determined at better energy resolution than can be achieved using the current experimental arrangement[11] and were therefore not redetermined in this study.

Table 7.2 Values of σ_r^{si} for the formation of H^+ from HNO_3 at low ionizing electron energies. The standard deviation in the last figure of each cross section is given in parentheses.

Electron energy /eV	$\sigma_r^{si}(H^+)$
45	-0.30(25)
50	0.005(18)
55	-0.07(12)
60	0.0089(60)
65	0.0153(51)
70	0.0207(44)
75	0.0159(42)
80	0.0292(36)

7.3.1.2 Double Ionization

A typical ion-ion coincidence spectrum of HNO_3^{2+} recorded at 150 eV is shown in Fig. 7.3.

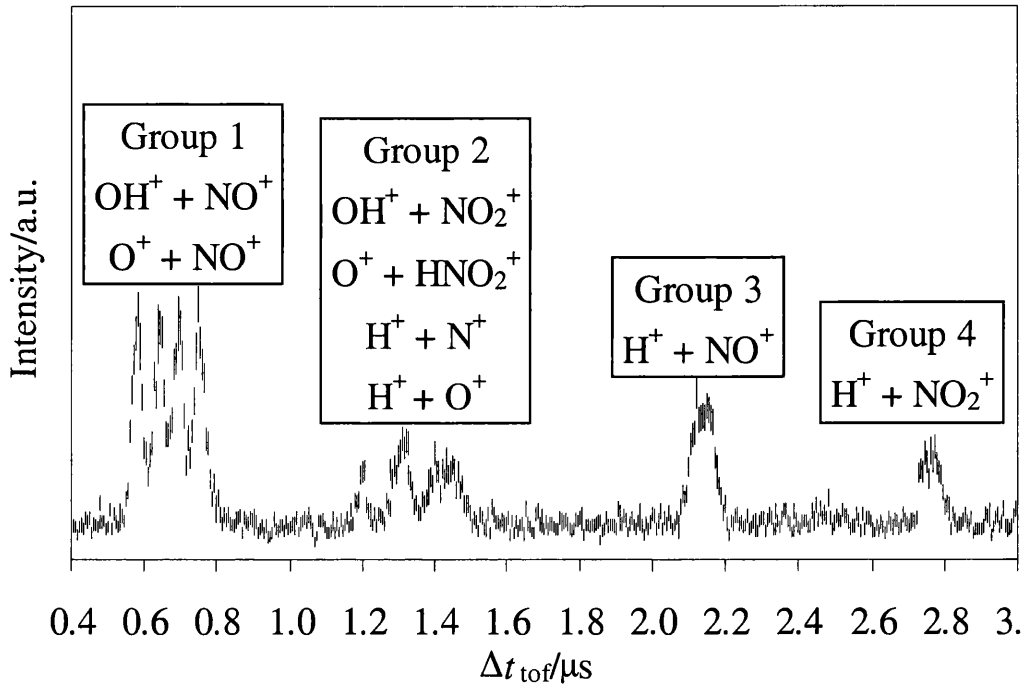

Fig. 7.3 Ion-ion coincidence spectrum of HNO_3^{2+}, generated by electron impact at 150 eV. The error bars shown, derived from the counting statistics, represent two standard deviations. As explained in the text, the coincidence peaks have been separated into four distinct groups.

The dissociation reactions observed in the ion-ion coincidence spectrum of HNO_3^{2+} are:

Group 1 $HNO_3^{2+} \rightarrow OH^+ + NO^+ [+ O]$ (7.III)

$HNO_3^{2+} \rightarrow O^+ + NO^+ [+ H + O]$ (7.IV)

Group 2 $HNO_3^{2+} \rightarrow OH^+ + NO_2^+$ (7.V)

$HNO_3^{2+} \rightarrow O^+ + HNO_2^+$ (7.VI)

$HNO_3^{2+} \rightarrow H^+ + N^+ [+ 3O]$ (7.VII)

$HNO_3^{2+} \rightarrow H^+ + O^+ [+ N + 2O]$ (7.VIII)

Group 3 $HNO_3^{2+} \rightarrow H^+ + NO^+ [+ 2O]$ (7.IX)

Group 4 $HNO_3^{2+} \rightarrow H^+ + NO_2^+ [+ O]$ (7.X)

where the neutrals are listed in parentheses as they are not detected, but, as described below, they are most likely to be completely fragmented. As can be seen from Fig. 7.3, there is a great deal of congestion in certain regions of the coincidence spectrum and upon initial inspection it is not possible to discern definitively which dissociation reactions contribute to the coincidence signals in these regions. However, as explained below, Monte Carlo simulations of the experimental data enable the identification of all the dissociation reactions present. Any coincidence signals produced by the formation of identical pairs of fragment ions

$$HNO_3^{2+} \rightarrow O^+ + O^+ [+ H + N + O] \quad (7.XI)$$

cannot be efficiently detected in the one-dimensional coincidence spectrum due to the ringing when Δt_{tof} is small (Chapter 3) and were therefore not investigated further. Pairs of similar mass ions, for example,

$$HNO_3^{2+} \rightarrow N^+ + O^+ [+ H + 2O] \qquad (7.XII)$$

can be detected using this experimental set-up, as in the coincidence spectrum of $N_2O_5^{2+}$ (Chapter 4), but no signals corresponding to this ion pair were observed in the HNO_3^{2+} spectrum. The spectrum also contains very weak signals resulting from the double ionization of water, the principal background gas in the apparatus.

As indicated in Fig. 7.3, the coincidence peaks in the spectrum have been separated into four distinct groups for ease of analysis. Group 1 contains the $OH^+ + NO^+$ and $O^+ + NO^+$ ion pairs, Group 2 contains the pairs $OH^+ + NO_2^+$, $O^+ + HNO_2^+$, $H^+ + N^+$ and $H^+ + O^+$ and Groups 3 and 4 are made up of the $H^+ + NO^+$ and $H^+ + NO_2^+$ ion pairs respectively.

Kinetic Energy Release Determination

The KER values associated with the formation of the ion pairs observed in the coincidence spectrum of HNO_3^{2+} have been determined by performing Monte Carlo simulations of the experimental data, the method being described in detail in Chapter 3. The uncertainties in the KER derived from the simulation procedure are of the order of ± 0.2 eV.

Fig. 7.4 shows the comparison of a simulated spectrum with typical experimental data in the region of the coincidence spectrum of Group 2, recorded at an ionizing electron energy of 150 eV, to indicate the high quality of fit achieved.

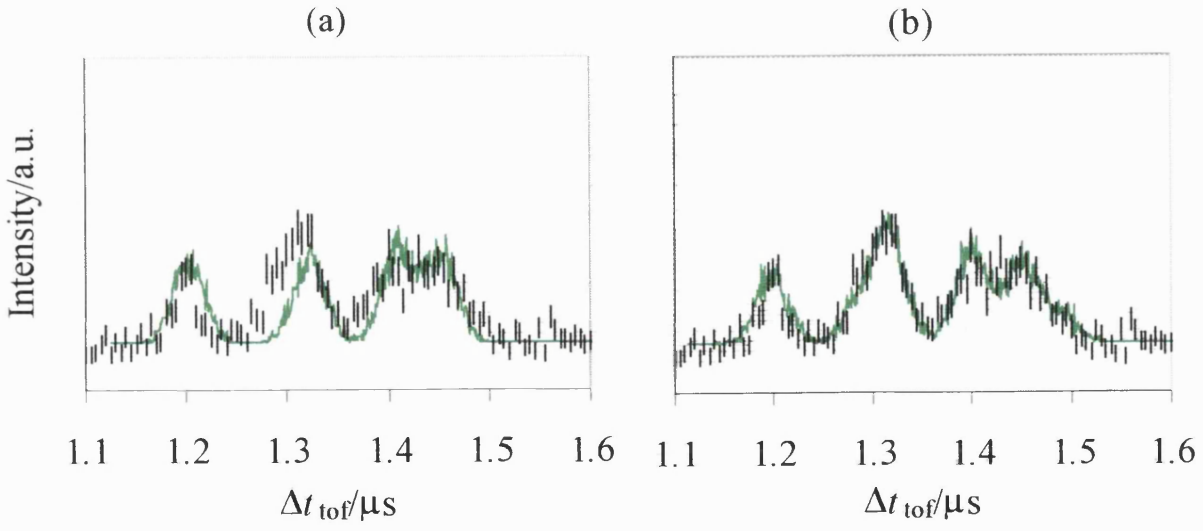

Fig. 7.4 Ion-ion coincidence spectrum of HNO_3^{2+} showing the Group 2 peak. The experimental points are indicated by error bars of length 2σ. The solid curve is a Monte Carlo simulation of the experimental signal, including signals corresponding to (a) $OH^+ + NO_2^+$ and $H^+ + O^+$ and (b) $OH^+ + NO_2^+$, $O^+ + HNO_2^+$, $H^+ + N^+$ and $H^+ + O^+$.

Due to the extensive overlapping of signals in this region of the coincidence spectrum (Fig. 7.4), it is difficult to identify by eye any weak signals that may be present. Using the simulation procedure it is possible to determine which ion pairs are contributing to the coincidence signal in a particular region of the spectrum by comparing the fit of the simulated spectrum with the experimental data. Indeed, upon inclusion of the weak signals corresponding to $H^+ + N^+$ and $O^+ + HNO_2^+$ in the simulation procedure, the fit with the experimental spectrum is markedly improved (Fig. 7.4b), providing good evidence that these dissociation reactions of HNO_3^{2+} do indeed occur. However, as the signals for the $H^+ + N^+$ and $O^+ + HNO_2^+$ ion pairs are very weak and overlapped by the more intense signals of $OH^+ + NO_2^+$ and $H^+ + O^+$, it is very difficult to derive accurately the KER associated with these dissociation reactions.

The ion pairs observed in the coincidence spectrum of HNO_3^{2+} are formed by both two and three-body dication dissociation reactions. There is only one possible decay pathway for a two-body dissociation reaction: the direct dissociation of the molecular dication to form the two product ions [Reactions (7.V) & (7.VI)]. Therefore, the result of the simulation procedure for a two-body reaction is a single value of the KER and corresponding F_{KERD}, as indicated in Table 7.3 for the $OH^+ + NO_2^+$ ion pair. As mentioned above, it is difficult to derive a value of the KER for the $O^+ + HNO_2^+$ ion pair.

Table 7.3 Values of KER, F_{KERD} and $E(HNO_3^{2+})$ for forming $OH^+ + NO_2^+$ from HNO_3^{2+}, derived by simulation of the peak corresponding to Group 2 in the ion-ion coincidence spectrum recorded at 150 eV.

	KER /eV	F_{KERD} /eV	$E(HNO_3^{2+})$ /eV
$OH^+ + NO_2^+$	5.8	2.4	30.7

As discussed in greater detail in Chapter 3, for the three-body dissociation reactions of HNO_3^{2+} [Reactions (7.III), (7.IV) & (7.VII)-(7.X)], the ions formed upon initial dissociation of the dication may not necessarily be the ones detected in the coincidence spectrum. Therefore, a consideration of the possible fragmentation pathways occurring must be made. There are no daughter dications observed in the mass spectrum, neither are there metastable tails on the coincidence signals, suggesting that the mechanism is unlikely to involve a deferred charge separation.[14-20] Since triple coincidence studies have shown Coulomb explosions to be rare for polyatomic dications,[14-19] the dissociation mechanisms followed by HNO_3^{2+} are assumed to be sequential involving an initial two-body charge separation followed by the dissociation of the resulting singly charged ions to form the detected ion pairs.

The simulation of each peak observed in the coincidence spectrum of HNO_3^{2+} has been performed several times modelling each three-body dissociation reaction *via* all the possible initial two-body charge separations and subsequent singly charged ion dissociation pathways. In this process, the KER of the monocation dissociation is negligible in comparison to the primary KER of

the dication dissociation. The result of the simulation procedure for the three-body reactions is a list of the potential KER and F_{KERD} values required to fit the simulated spectrum to the experimental data for each dissociation reaction. For example, Table 7.4 and Table 7.5 show the potential values of KER and F_{KERD} for the possible dication dissociation reactions forming the Group 1 ion pairs ($OH^+ + NO^+$ and $O^+ + NO^+$) and the Groups 3 & 4 ion pairs ($H^+ + NO^+$ and $H^+ + NO_2^+$).

Table 7.4 Potential values of the KER, F_{KERD} and $E(HNO_3^{2+})$ for forming the ion pairs making up Group 1 in the coincidence spectrum. As indicated in the table and described in the text, the values of $E(HNO_3^{2+})$ are dependent on the dissociation pathway of HNO_3^{2+} and the form of the neutral products.

Observed ion pair	Initial charge separation	KER /eV	F_{KERD} /eV	$E(HNO_3^{2+})$ /eV		
				[+ O]	[+ O + H]	[+ OH]
$OH^+ + NO^+$	$OH^+ + NO_2^+$	7.7	0.5	35.3	—	—
$O^+ + NO^+$	$OH^+ + NO_2^+$	7.0	1.1	—	39.7	35.2
	$O^+ + HNO_2^+$	7.0	0.8	—	39.7	35.2

Table 7.5 Potential values of the KER, F_{KERD} and $E(HNO_3^{2+})$ for forming the ion pairs in Groups 3 & 4 in the coincidence spectrum. See Table 7.4 caption for details.

Observed ion pair	Initial charge separation	KER /eV	F_{KERD} /eV	$E(HNO_3^{2+})$ /eV		
				[+ O]	[+ 2O]	[+ O_2]
$H^+ + NO^+$	$H^+ + NO_3^+$	10.6	7.0	—	43.2	36.1
	$OH^+ + NO_2^+$	6.5	5.0	—	39.1	—
$H^+ + NO_2^+$	$OH^+ + NO_2^+$	2.3	0.5	32.2	—	—
	$H^+ + NO_3^+$	8.0	1.0	37.9	—	—

Table 7.4 and Table 7.5 also give the potential values of $E(HNO_3^{2+})$, derived from the coincidence peak widths, from which the particular dissociation reaction occurs (Eq. 3.13). From Table 7.4 and Table 7.5 it is apparent that the value of $E(HNO_3^{2+})$ for each dissociation reaction depends not only on the form of the initial two-body charge-separating reaction but also on the form of the neutral products. As explained in Chapter 4, in the calculation of $E(HNO_3^{2+})$, the fragment ions and neutral products are assumed to be formed with no internal energy and should therefore be considered a lower limit.

Determination of the Appearance Energy

The appearance energies of the signals making up Groups 1, 3 and 4 have been determined by evaluating the ratio of the yield Y of each dissociation reaction to the number of coincidence starts S at electron energies from 30 to 70 eV. See Chapter 3 for details. In congested areas of the coincidence spectrum, *e.g.* the region of the spectrum containing the Group 1 peak (Fig. 7.3), the appearance energy of each individual dissociation reaction cannot be determined separately due to the extensive overlapping of the coincidence signals that are impossible to deconvolute near threshold, where the double ionization cross section is small. Thus, a plot of Y/S against electron energy will give the appearance energy for the formation of the particular group of ion pairs.

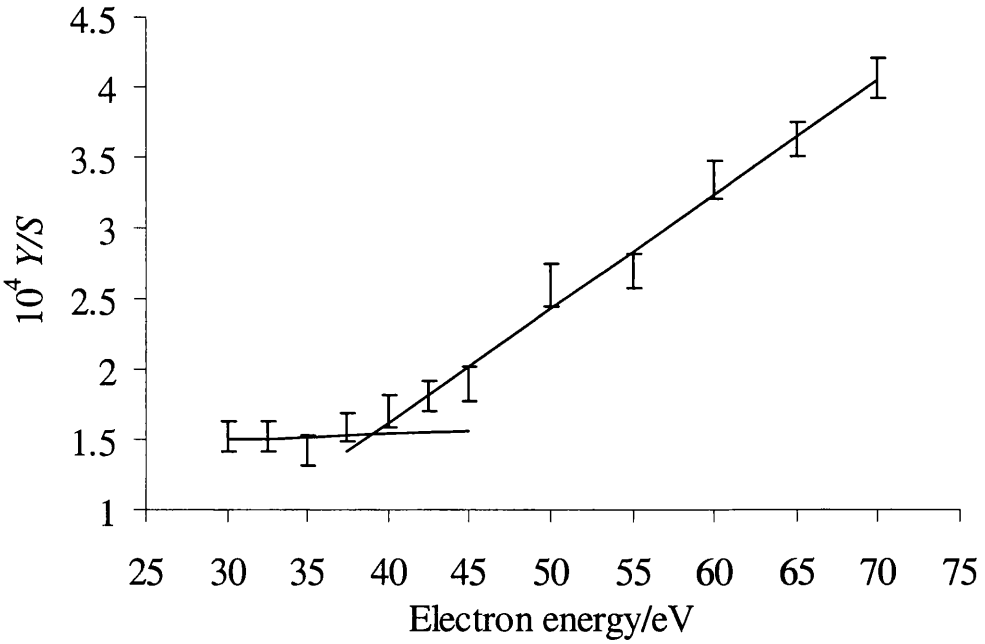

Fig. 7.5 Plot of *Y/S* against electron energy for Group 1. This plot can be interpreted to yield the appearance energy of the lowest energy dication state responsible for the decay reactions forming the $OH^+ + NO^+$ and $O^+ + NO^+$ ion pairs.

Fig. 7.5 shows a weighted least squares fit[21] applied to the values of *Y/S* for Group 1 above and below the appearance energy. Group 1 contains the ion pairs $OH^+ + NO^+$ and $O^+ + NO^+$ and the signals corresponding to both ion pairs are observed at electron energies close to the appearance energy. The ratio *Y/S* can be extrapolated to the non-zero background level of residual double ionization (Chapter 4) and a value of 39.0 ± 2 eV is obtained for the appearance energy of Group 1. The errors associated with this determination are evaluated by considering the energy resolution of the ionizing electron beam.

Table 7.6 Values of the ratio of *Y/S* against electron energy for the dissociation reactions making up Groups 3 & 4. As described in the text, these values can be interpreted to yield an appearance energy associated with each group. The numbers in parentheses indicate the standard deviation in the last figure of each *Y/S* value.

Electron	$10^4 Y/S$	
Energy /eV	Group 3	Group 4
30.0	0.150(71)	0.142(61)
32.5	0.237(70)	0.053(59)
35.0	0.226(65)	0.115(55)
37.5	0.160(66)	0.192(57)
40.0	0.130(74)	0.040(63)
42.5	0.139(67)	0.053(57)
45.0	0.270(77)	0.289(66)
50.0	0.454(92)	0.368(64)
55.0	0.486(74)	0.368(64)
60.0	0.593(87)	0.316(74)
65.0	0.558(75)	0.425(64)
70.0	0.801(87)	0.440(74)

The values of *Y/S* as a function of electron energy evaluated for Groups 3 and 4 are listed in Table 7.6 and are estimated to be 40 ± 5 eV for both $H^+ + NO^+$ and $H^+ + NO_2^+$ ion pairs. At low electron energies the statistical uncertainties in the values of *Y/S* are significantly increased for these weaker signals and the evaluation of their appearance energies is subject to a greater uncertainty. The appearance energy for Group 2 was not determined, as the uncertainties in *Y/S* were so large as to make an evaluation of the threshold impractical.

These experimentally determined appearance energies can then be compared with the potential values of $E(HNO_3^{2+})$, derived from the KER. If, for a given three-body dissociation reaction of HNO_3^{2+}, unambiguous agreement is found between one value of $E(HNO_3^{2+})$ and the appearance energy, then this provides good evidence that the mechanism used to derived the KER is the one that is actually followed to form the detected ion pair.

7.3.2 Discussion

7.3.2.1 Single Ionization

There have only been two previous reports in the literature concerning the single ionization and fragmentation of HNO_3, one PIMS study[11] in the energy range 10-20 eV and a second early EIMS study[10] at an unspecified ionizing energy. In the EIMS study[10] NO_2^+, NO^+, O_2^+, OH^+, O^+ and N^+ fragment ions were observed, in addition to the parent ion HNO_3^+ and significant impurity peaks. The NO_2^+ signal was observed to be the most abundant ion. In the PIMS work,[11] NO_2^+, NO^+, O_2^+, OH^+, O^+ and N^+ fragment ions were again observed but no parent ions were detected and, in contrast to the EIMS work, NO^+ ions were found to be more abundant than NO_2^+. In addition, the PIMS study determined the appearance energies of the NO_2^+, NO^+ and OH^+ fragment ions to be 11.90, 13.07 and 16.60 eV respectively.[11] A summary of the data reported in the two previous studies of the ionization of HNO_3 is given in Table 7.7.

Table 7.7 Intensities of fragment ions observed in the mass spectrum of HNO_3.

		Ionization energy /eV	Observed ion yields							
			H^+	N^+	O^+	OH^+	NO^+	O_2^+	NO_2^+	HNO_3^+
Present	EIMS	70	2	2	5	5	51	—	100	2
Jochims *et al*[11]	PIMS	20.7	—	1	2	9	100	1	95	—
Friedel *et al*[10]	EIMS	—	—	10	21	25	85	4	100	2

In the present one-dimensional study, at electron energies from 40 to 450 eV, the parent ion HNO_3^+ and fragment ions NO_2^+, NO^+, OH^+, O^+, N^+ and H^+ were detected. The most abundant fragment was found to be NO_2^+ (Fig. 7.1). The plots of σ_r^{si} of the ions against electron energy (Fig. 7.2) all show an initial increase in σ_r^{si} as the electron energy is raised. This increase is due to the increased likelihood of ionic fragmentation with increased energy deposition and associated ionic

excitation. In both the previous EIMS and PIMS experiments,[10,11] O_2^+ ions were detected, but at very low relative intensities (Table 7.7). However, in the current study, once the contribution from the small amount of residual gas has been subtracted, the value of σ_r^{si} for the formation of O_2^+ from HNO_3^+, within the error limit, is zero.

In the current one-dimensional work, the intensity ratio of NO_2^+ to NO^+ at 70 eV, the ionizing electron energy often considered to result in the same energy deposition as 20.7 eV photons,[22] is approximately 2:1 (Fig. 7.2, Table 7.1). The EIMS study also found the NO_2^+ ion to be more abundant than NO^+, although the ratio was found to be only 6:5. However, the electron energy used in the EIMS work is unspecified and no valid comparisons can really be made. The intensity ratio of NO_2^+ to NO^+ in the present work is, however, significantly different to that presented in the PIMS study using 20.7 eV photons, where the NO^+ signal was observed to be larger than the NO_2^+ signal. The presence of the hot filament in our electron-impact TOFMS could stimulate thermal decomposition to form NO_2 resulting in an increased NO_2^+ signal. However, an earlier study of the dissociation and fragmentation of $N_2O_5^+$ using the current experimental arrangement (Chapter 4), where any apparatus-induced thermal decomposition should have been apparent, yielded an NO_2^+ to NO^+ ratio in good accord with previous PIMS work by the same authors.[11] Therefore, the larger yield of NO_2^+ is unlikely to be due to thermal effects in the current experiments.

In the EIMS study,[10] the parent ion HNO_3^+ was observed in the mass spectrum and parent ion signals were also observed in the current work. These observations are contrary to the results of the PIMS study where no parent ions were detected.[11] There a number of possible explanations for this fundamental difference between the mass spectra obtained using electron-impact ionization and those obtained using photoionization. One such explanation is that there is a bound state of HNO_3^+ lying above the energy of the ionizing photons used in the PIMS work (20.7 eV). This is however unlikely, as such a state would lie above the majority of the dissociation asymptotes of HNO_3^+ and would thus be expected to predissociate rapidly. Alternatively, in the electron-impact experiments there could be a resonant attachment process occurring, with rapid subsequent autodetachment to form the parent monocation [Reaction (7.XIII)],

$$e^- + HNO_3 \rightarrow HNO_3^{*-} \rightarrow HNO_3^+ + 2e^- \qquad (7.XIII)$$

The autodetachment process could populate bound regions of the HNO_3 potential energy surface which are not accessible in direct ionization. This attachment process is, however, unlikely to occur at the high electron energies used in the current experiments.

A further possible explanation for the HNO_3^+ signal is due to the differing experimental arrangements used in the EIMS and PIMS studies. Unusual ions can be observed in EIMS experiments due to dissociation processes occurring at the hot filament and subsequent chemical reactions.[23] It is easy to imagine how this process could result in unusual 'fragment' molecules

which are subsequently ionized, but more difficult to see how it could lead to HNO_3 molecules in states not populated in the nascent HNO_3 sample, which could then be ionized to a bound region of the HNO_3^+ potential energy surface.

Perhaps the most probable explanation for the discrepancy between the parent ion signals observed when employing the different forms of ionization is that, following electron impact, the HNO_3 molecule is promoted into an excited state which subsequently autoionizes to form the parent monocation [Reaction (7.XIV)],

$$HNO_3 + e^- \rightarrow HNO_3^* + e^- \rightarrow HNO_3^+ + 2e^- \qquad (7.XIV)$$

The excited state of the neutral molecule, which subsequently autoionizes to form the stable HNO_3^+ ion, could either lie above the energy of the photons used in the PIMS work, or is formed as a result of a transition which cannot be accessed by photoionization.

As described above, the appearance energy for the formation of H^+ from HNO_3^+ has been determined to lie between 55 and 60 eV (Table 7.2). The thermodynamic asymptotes of the various monocation fragmentation reactions to form H^+, together with other neutral species, lie well below the determined appearance energy for this fragment. For example, the most energetically demanding dissociation pathway, involving the complete fragmentation of the HNO_3^+ ion [Reaction (7.XV)], has a thermodynamic asymptote of 29.9 eV,[24] assuming all the fragments are formed in their ground states,

$$HNO_3^+ \rightarrow H^+ + N + 3O \qquad (7.XV)$$

This thermodynamic asymptote is significantly lower than the determination of the H^+ appearance energy, which suggests that the formation of H^+ ions is most probably due to dissociative double ionization. The double ionization energy of HNO_3 can be estimated as 33.5 eV by the 'rule of thumb'[25] (Chapter 3) and it is satisfying to note that the determined appearance energy for the H^+ fragment lies above this double ionization energy. As discussed in Section 7.3.1.2, studies of the formation and fragmentation of the HNO_3 dication indicate that a large number of H^+ ions are produced upon dissociation of HNO_3^{2+}. For example, the dissociation of HNO_3^{2+} to form $H^+ + NO_2^+$ [Reaction (7.X)]. Due to the geometric discrimination effects discussed in Chapter 3, it would be expected that any fragments formed by double ionization are detected very inefficiently by the one-dimensional apparatus, due to their significant kinetic energies. However, if the formation of H^+ from HNO_3^{2+} has a significant probability, then the small number of H^+ ions which receive impulses along the axis of the TOFMS will still be detected in the time-of-flight mass spectrum. If dicationic charge separation is indeed the principal source of H^+ ions, then the values given in Table 7.1 & Table 7.2 should correctly be termed relative partial ionization cross sections σ_r^I. The markedly lower detection efficiency for these energetic species will mean that the measured values of σ_r^I (Table 7.1 & Table 7.2) should be considered a lower limit.

The results presented above show that there are major discrepancies between the ion yields obtained upon ionization and fragmentation of HNO_3 using PIMS and EIMS techniques. These differences include the observation of stable parent HNO_3^+ ions in the EIMS studies, but not using PIMS techniques, and markedly differing abundances of NO^+ and NO_2^+ fragment ions. The ionization of nitric acid obviously requires further investigation to determine whether these discrepancies are a result of fundamental differences between photons and electrons as ionizing agents, or more subtle experimental factors.

7.3.2.2 Double Ionization

The coincidence spectrum (Fig. 7.3) shows that the molecular dication HNO_3^{2+} dissociates *via* a variety of two and three-body dissociation reactions. In the electron-impact mass spectrum of HNO_3 (Fig. 7.1) no stable parent dication (HNO_3^{2+}) or daughter dications are observed. This implies that any bound regions of the dication potential energy surfaces cannot be accessed by a vertical transition from the equilibrium geometry of the neutral molecule. As explained above, the coincidence signals in the spectrum have been separated into four distinct groups for ease of analysis.

Group 1: $OH^+ + NO^+$ and $O^+ + NO^+$

The coincidence signals making up Group 1 lie in the coincidence spectrum from Δt_{tof} = 0.5-0.8 μs (Fig. 7.3). From Fig. 7.5 it can be seen that the experimentally determined appearance energy for Group 1 is 39.0 ± 2 eV. This value could be interpreted as the energy of the lowest-lying dication state responsible for forming either the $OH^+ + NO^+$ or $O^+ + NO^+$ ion pair. However, the appearance energy appears to be the same for both ion pairs, as signals corresponding to both ion pairs are observed right down to the appearance energy. Therefore, these dissociation reactions probably occur from the same electronic state of HNO_3^{2+} that lies at 39.0 ± 2 eV.

Interpretation of the $OH^+ + NO^+$ coincidence signals, assuming the obvious initial two-body charge separation to $OH^+ + NO_2^+$, yields a value of $E(HNO_3^{2+})$ of 35.3 eV (Table 7.4), a value which is considerably lower than the experimentally determined appearance energy.

For the three-body dissociation reaction forming the $O^+ + NO^+$ pair, the possible decay pathways involve initial two-body fragmentations to form $OH^+ + NO_2^+$ and $O^+ + HNO_2^+$ which both yield a value of $E(HNO_3^{2+})$ as 39.7 eV (Table 7.4), when accompanied by complete fragmentation of the neutral products. Note that both these initial two-body reactions are also observed in the coincidence spectrum, the intensity of the $OH^+ + NO_2^+$ signal being far greater than that of the $O^+ + HNO_2^+$ signal.

As the appearance energy appears to be the same for both $OH^+ + NO^+$ and $O^+ + NO^+$, it is possible that the dissociation of HNO_3^{2+} to form these ion pairs occurs from the same dicationic

electronic state. If this is indeed the case, then the formation of both ion pairs might arise from the same initial two-body charge-separating reaction: $OH^+ + NO_2^+$. The alternative pathway involving an initial fragmentation to $O^+ + HNO_2^+$ is considered less likely as the ion pair $OH^+ + NO^+$ could not be formed from this initial charge separation. Therefore, the most consistent interpretation of the experimental data is that the initial two-body dissociation for both reactions is a charge-separating reaction to $OH^+ + NO_2^+$. In this interpretation these primary monocations must have the opportunity to be formed with some internal excitation and can therefore undergo subsequent dissociation reactions to form the two ion pairs observed in this group, first $OH^+ + NO^+$ and after further dissociation $O^+ + NO^+$.

$$\begin{array}{l} HNO_3^{2+} \rightarrow OH^{+*} + NO_2^{+*} \\ \qquad\qquad\quad \downarrow \\ \qquad\quad OH^{+*} + NO^+ + O \\ \qquad\quad \downarrow \\ \qquad\quad O^+ + NO^+ [+ H + O] \end{array} \qquad (7.XVI)$$

Assuming that the mechanism shown in Reaction (7.XVI) is the pathway by which HNO_3^{2+} dissociates to form $OH^+ + NO^+$ and $O^+ + NO^+$, the relevant values of $E(HNO_3^{2+})$ for these two dissociation reactions are 35.3 and 39.6 eV respectively (Table 7.4). The value of 39.6 eV derived for the $O^+ + NO^+$ reaction is in excellent agreement with the experimentally determined appearance energy. However, the value of $E(HNO_3^{2+})$ derived for the $OH^+ + NO^+$ reaction (35.3 eV) is markedly lower than the appearance energy. But this value is expected to be too low as it does not allow for the internal excitation in the OH^+ ion that is considered to be present [Reaction (7.XVI)]. Indeed, if some of the OH^+ ions fragment to O^+ they must possess at least 5.1 eV of internal energy.[24] Hence, if this mechanism is followed, it is reasonable that the OH^+ ions detected together with NO^+ possess several electron volts of internal excitation. Therefore, given these considerations the two values of $E(HNO_3^{2+})$ derived from the coincidence spectra, 35.3 and 39.6 eV, are consistent.

Group 2: $OH^+ + NO_2^+$, $H^+ + N^+$, $O^+ + HNO_2^+$ and $H^+ + O^+$

The coincidence peaks making up Group 2 are in the region of the coincidence spectrum from Δt_{tof} = 1.1-1.6 μs (Fig. 7.3). An accurate evaluation of the appearance energy for this group is difficult to obtain as the signal is very weak at low electron energies and there are a large number of contributing dissociation reactions that cannot be accurately resolved given the low double ionization cross section at low electron energies. By using the simulation procedure described previously (Chapter 3), the values of the KER and associated $E(HNO_3^{2+})$ derived for a sequential decay pathway involving an initial two-body charge separation were determined for the reactions in this group.

As mentioned above, there are no mechanistic complications associated with the two-body dissociation reactions, as there is only a single possible decay pathway. The energy of the dication state responsible for the two-body decay reaction forming $OH^+ + NO_2^+$ was found to be 30.7 ± 0.2 eV (Table 7.3). The signal corresponding to the second two-body reaction forming $O^+ + HNO_2^+$ is very weak indeed and occurs in a region of the coincidence spectrum where there is extensive overlapping of the coincidence signals. Therefore, it is impossible to derive a reliable value of the KER associated with this decay reaction. Given the lack of information for the $O^+ + HNO_2^+$ dissociation reaction, it is not possible to discern if the pair of two-body dissociation reactions occur as a result of the population of two distinct electronic states of the dication or the population of the same electronic state. The fair agreement between the value of $E(HNO_3^{2+})$ obtained for $OH^+ + NO_2^+$ (30.7 eV) and an estimate of the double ionization energy 33.5 ± 10% eV, obtained by using the 'rule of thumb'[25] (Chapter 3) indicates that this two-body dissociation reaction probably occurs from the ground electronic state of HNO_3^{2+}. Therefore, from the coincidence spectrum of HNO_3, a lower limit can be placed on the double ionization energy of nitric acid as 30.7 ± 0.2 eV.

The signal corresponding to the $H^+ + N^+$ ion pair is also very weak indeed and occurs in a congested region of the coincidence spectrum. As a result, it is impossible to derive precise values of the KER and $E(HNO_3^{2+})$ associated with this decay reaction. More detailed analysis of the energetics and associated mechanism to form the $H^+ + O^+$ ion pair is also difficult as there are a large number of possible dissociation pathways, but the lack of an experimentally determined appearance energy for comparison with any calculated values of $E(HNO_3^{2+})$ means that no definitive mechanism can be assigned.

Group 3: $H^+ + NO^+$

The coincidence signals corresponding to $H^+ + NO^+$ lie from Δt_{tof} = 2.05-2.25 μs in the coincidence spectrum (Fig. 7.3). The appearance energy of this dissociation reaction could not be determined to the usual accuracy (± 2 eV) due to the weak signal at low electron energies but from Table 7.6 the appearance energy is found to be 40 ± 5 eV. As can be seen from Table 7.5, there are two possible initial two-body fragmentations that, after further dissociation, could result in the formation of the $H^+ + NO^+$ ion pair. As shown in Table 7.5, the values of the KER and F_{KERD}, derived assuming the formation of the $H^+ + NO^+$ ion pair *via* initial charge separation to $H^+ + NO_3^+$, are unrealistically large for the dissociation of a polyatomic dication.[26] Therefore, this decay pathway is considered unlikely to be responsible for forming $H^+ + NO^+$. The remaining fragmentation pathway involves an initial two-body fragmentation of HNO_3^{2+} to form $OH^+ + NO_2^+$, followed by further dissociation of these singly charged ions to form $H^+ + NO^+$ accompanied by complete fragmentation of the neutral oxygen atoms [Reaction (7.XVII)]:

$$\begin{array}{c} HNO_3^{2+} \rightarrow OH^{+*} + NO_2^{+*} \\ \downarrow \quad \downarrow \\ H^+ + NO^+ + 2O \end{array} \qquad (7.XVII)$$

The value of $E(HNO_3^{2+})$ associated with this fragmentation pathway is 39.1 eV, a value close to the energy of the dication state deduced to be responsible for the reactions in Group 1. Indeed, the dissociation reactions forming $OH^+ + NO^+$, $O^+ + NO^+$ and $H^+ + NO^+$ are deduced to proceed *via* the initial fragmentation of HNO_3^{2+} to $OH^+ + NO_2^+$. Therefore, it is possible that the formation of the $OH^+ + NO^+$, $O^+ + NO^+$ and $H^+ + NO^+$ ion pairs is a result of the dissociation of the same dicationic electronic state.

Group 4: $H^+ + NO_2^+$

The coincidence signals corresponding to $H^+ + NO_2^+$ lie from Δt_{tof} = 2.7-2.85 μs in the coincidence spectrum (Fig. 7.3). The experimentally determined appearance energy (Table 7.6) for this dissociation reaction is determined to be 40 ± 5 eV, a value with a larger uncertainty than can usually be achieved (± 2 eV) because of the extremely weak coincidence signals at low electron energies. Table 7.5 shows the values of $E(HNO_3^{2+})$ derived assuming the dissociation of HNO_3^{2+} *via* an initial two-body charge separation and subsequent dissociation of the singly charged ions to form the observed ion pair. From Table 7.5, the value of $E(HNO_3^{2+})$ derived assuming an initial fragmentation to form $OH^+ + NO_2^+$, 32.2 eV, is clearly outside the error limits of the appearance energy. This dissociation mechanism is therefore not likely to be followed. The remaining pathway involves an initial charge-separating reaction to form $H^+ + NO_3^+$, the latter ion subsequently dissociating to form the pair observed in the coincidence spectrum [Reaction (7.XIII)]:

$$\begin{array}{c} HNO_3^{2+} \rightarrow H^+ + NO_3^+ \\ \downarrow \\ H^+ + NO_2^+ + O \end{array} \qquad (7.XIII)$$

Interpretation of the coincidence peak widths assuming the decay of the dication *via* this pathway yields a value of $E(HNO_3^{2+})$ of 37.9 eV, an estimate lying within the error limits of the experimentally determined appearance energy.

General Discussion

The above conclusions are summarised in Table 7.8, which lists the dissociation reactions observed, the appearance energies and the derived energetic data given the most probable dissociation pathway.

Table 7.8 Proposed decay pathways and estimates of the KER, $E(HNO_3^{2+})$ and appearance energies of the observed dissociation reactions of HNO_3^{2+}, where available. The values for the three-body dissociation reactions are obtained assuming the indicated initial two-body charge separation and subsequent dissociation of the monocations accompanied by complete fragmentation of the neutral products.

Dissociation reaction	Initial charge separation	KER /eV	$E(HNO_3^{2+})$ /eV	Appearance energy /eV
$OH^+ + NO^+ [+ O]$	$OH^+ + NO_2^+$	7.7	35.3	39.0 ± 2
$O^+ + NO^+ [+ H + O]$	$OH^+ + NO_2^+$	7.0	39.6	39.0 ± 2
$OH^+ + NO_2^+$	$OH^+ + NO_2^+$	5.8	30.7	—
$O^+ + HNO_2^+$	$O^+ + HNO_2^+$	—	—	—
$H^+ + N^+ [+ 3O]$	—	—	—	—
$H^+ + O^+ [+ N + 2O]$	—	—	—	—
$H^+ + NO^+ [+ 2O]$	$OH^+ + NO_2^+$	6.5	39.1	40 ± 5
$H^+ + NO_2^+ [+ O]$	$H^+ + NO_3^+$	8.0	37.9	40 ± 5

The above comparisons of the values of $E(HNO_3^{2+})$ for each dissociation reaction, derived from the coincidence peak widths in the ion-ion coincidence spectrum of HNO_3^{2+}, with the experimentally determined appearance energy for the four groups of peaks suggests that the fragmentation of the nitric acid dication involves three initial two-body charge separations. These initial charge separations involve the cleavage of the three different bonds in the dication. The three distinct bond cleavages (Fig. 7.6) are the breaking of the H-O bond in the molecular dication, which eventually leads to the formation of $H^+ + NO_2^+$, the breaking of one of the O-N bonds, resulting in the formation of $O^+ + HNO_2^+$, and the breaking of the HO-N bond forming $OH^+ + NO^+$, $O^+ + NO^+$ and $H^+ + NO^+$.

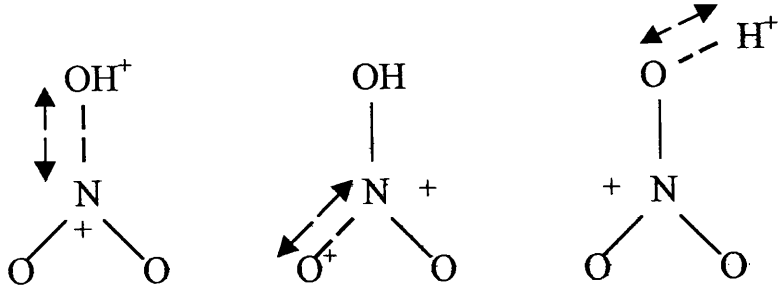

Fig. 7.6 Schematic diagrams of the three possible initial two-body charge separations of HNO_3^{2+} which result in the formation of the ion pairs observed in the ion-ion coincidence spectrum.

As described above, it is not possible to determine the fragmentation pathway that leads to the formation of $H^+ + N^+$ and $H^+ + O^+$ because of the lack of information concerning energetics and appearance energies for these ion pairs.

7.3.3 Conclusion

The first section of this chapter presents the results of a one-dimensional investigation of the single and double ionization of nitric acid. Stable parent ions HNO_3^+ and H^+, N^+, O^+, OH^+, NO^+ and NO_2^+ fragment ions were detected, the most abundant ion being NO_2^+. This study presents a

determination of the values of σ_r^{si} for the fragment ions formed from nitric acid, for incident electron energies from 40 to 450 eV using time-of-flight mass spectrometry. The appearance energy for the previously unobserved H^+ fragments was determined to lie between 55 and 60 eV and its formation is considered to be due to the dissociation of the nitric acid dication HNO_3^{2+}.

Ion-ion coincidence experiments have been performed to study the formation and dissociation of HNO_3^{2+}. Coincidence peaks due to the dissociation of HNO_3^{2+} to yield $OH^+ + NO^+$, $O^+ + NO^+$, $OH^+ + NO_2^+$, $O^+ + HNO_2^+$, $H^+ + N^+$, $H^+ + O^+$, $H^+ + NO^+$ and $H^+ + NO_2^+$ ion pairs were observed, showing HNO_3^{2+} dissociates *via* a variety of two and three-body reactions. Comparisons of experimentally determined appearance energies for the four distinct groups of peaks with values of $E(HNO_3^{2+})$ derived from coincidence peak widths for each dissociation reaction are consistent with the model of initial charge separation as a two-body reaction involving either an O—H, O—N or HO—N initial dication bond cleavage. The three-body reactions involve subsequent dissociation of one or more of the primary monocations to produce the detected ion pairs accompanied by complete fragmentation of the neutral products.

The values derived for the energies of the dication states responsible for forming the $OH^+ + NO^+$, $O^+ + NO^+$ and $H^+ + NO^+$ indicate that these dissociation reactions may all occur from the same electronic state of the dication. In addition, the energy of the dication state responsible for the two-body dissociation reaction forming $OH^+ + NO_2^+$ indicates that this dissociation reaction occurs from the ground electronic state of HNO_3^{2+}, thus providing a first estimate of the double ionization energy of HNO_3^{2+} as 30.7 ± 0.2 eV.

7.4 Two-Dimensional Studies

7.4.1 Data Analysis

7.4.1.1 Single Ionization

A typical singles spectrum of HNO_3 recorded at 250 eV using the 2D experimental arrangement is shown in Fig. 7.7. As can be seen in the figure, the parent ion HNO_3^+ and fragment ions H^+, N^+, O^+, OH^+, NO^+ and NO_2^+ are observed in the singles spectrum. The spectrum also contains signals resulting from traces of background gas in the apparatus, principally air and water.

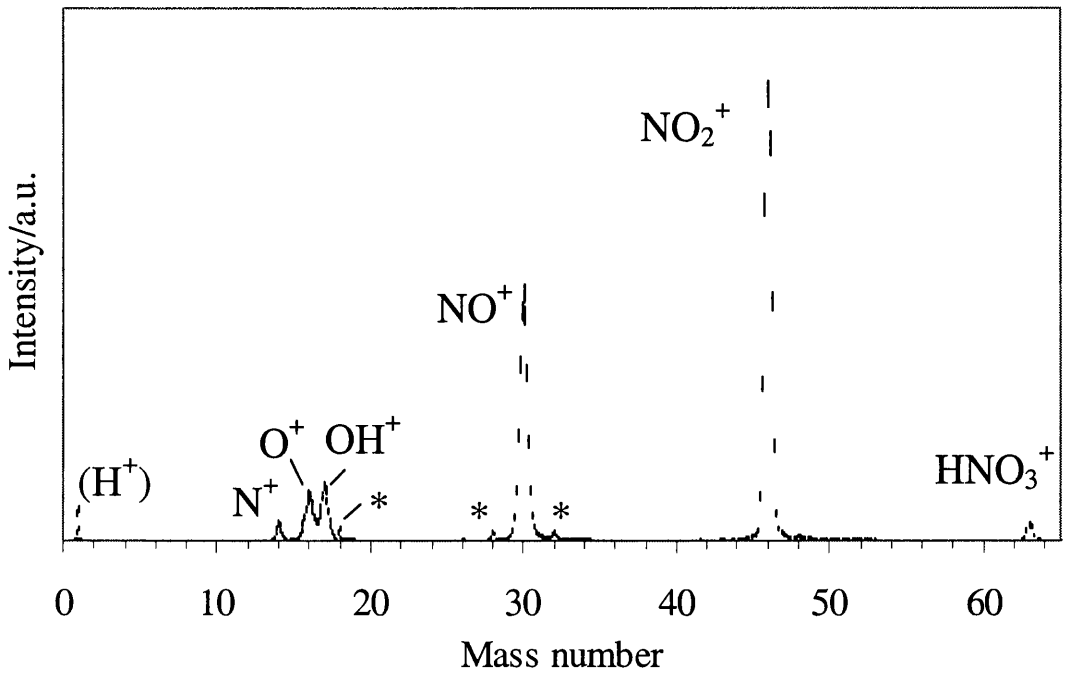

Fig. 7.7 Typical singles spectrum of HNO_3 recorded at 250 eV. The peaks marked with asterisks correspond to signals (H_2O^+, N_2^+ and O_2^+) due to traces of air and water from the residual gas. To aid interpretation, the error bars shown have been scaled to represent forty standard deviations. As described in the text, the "H^+" ion signal contains a significant contribution from background signals.

Singles spectra of HNO_3 were recorded at 70, 100, 250 and 320 eV and the values of σ_r^I of the fragment ions of HNO_3, relative to the parent ion HNO_3^+, have been determined using Eq. 3.19 and are listed in Table 7.9. Unfortunately, the HNO_3 spectrum also contains some background signals arising from electrons hitting the repeller plate and producing predominantly H^+ ions. As a result, this background signal is masking the 'true' H^+ fragment ion signals from HNO_3. Therefore, it was not possible to extract any data concerning the H^+ ion signal intensities from the singles spectra of HNO_3.

Table 7.9 Values of σ_r^I for the formation of the indicated product ion from HNO_3 (the numbers in parentheses indicate the statistical error in the last figure of each value).

Electron energy	σ_r^I				
/eV	N^+	O^+	OH^+	NO^+	NO_2^+
70	1.494(20)	6.788(77)	7.422(84)	29.73(33)	40.65(44)
100	1.927(24)	8.314(89)	8.627(92)	31.71(33)	38.08(39)
250	1.458(9)	7.605(36)	6.571(31)	29.85(14)	37.18(17)
320	2.450(37)	11.32(15)	6.473(87)	32.52(41)	37.72(48)

Prior to the determination of σ_r^I, any contribution of the ionization of the background gas to the N^+, O^+ and OH^+ fragment ion signals in the HNO_3 singles spectrum was calculated using the relative intensities of the N^+, O^+ and OH^+ ions to N_2^+ and H_2O^+ derived from singles spectra of air recorded over the same range of electron energies. As described in Section 7.3.1.1, the contribution of the ionization of air and water to the fragment ion signals in the HNO_3 singles spectrum can

therefore be accurately determined and subtracted. Only one singles spectrum was recorded at each electron energy because the experiments had to be run at low count rates in order to obtain adequate counting statistics, thus increasing the data acquisition time.

In order to compare the data derived in the one and two-dimensional studies, the values of σ_r^{si} must be determined from the singles spectrum by subtracting the contribution of double ionization from the ion signals in the singles spectrum. The analysis procedure used to derive the values of σ_r^{si} from the singles spectra has been described in greater detail in Chapter 3. The values of σ_r^{si} for the fragment ions of HNO_3 derived from the singles spectra are listed in Table 7.10. In the determination of σ_r^{si}, the value of f_i, derived from the normalisation experiments using CF_4 (Chapter 3), is 0.063 ± 0.014.

Table 7.10 Values of σ_r^{si} for the formation of the indicated product ion from HNO_3 (the numbers in parentheses indicate the statistical error in the last figure of each value).

Electron energy	σ_r^{si}				
/eV	N^+	O^+	OH^+	NO^+	NO_2^+
70	1.202(70)	4.56(60)	5.99(33)	26.86(71)	40.57(44)
100	1.474(106)	5.34(76)	5.96(60)	27.16(105)	37.41(42)
250	1.274(42)	5.28(59)	4.84(39)	26.65(72)	36.77(19)
320	1.713(170)	6.76(113)	4.42(47)	27.66(114)	37.02(50)

7.4.1.2 Double Ionization

As indicated in Section 7.3, the one-dimensional ion-ion coincidence technique does not unambiguously identify the fragmentation channels for HNO_3^{2+}. But, using 2D coincidence techniques, it is possible to identify all the pairs of ions formed upon dicationic dissociation. A pairs spectrum of HNO_3^{2+} recorded at 250 eV is shown in Fig. 7.8.

In agreement with the one-dimensional coincidence spectra, the following ion pairs are detected $OH^+ + NO^+$, $O^+ + NO^+$, $OH^+ + NO_2^+$, $H^+ + N^+$, $H^+ + O^+$, $H^+ + NO^+$ and $H^+ + NO_2^+$. However, the previously unobserved identical ion pair $O^+ + O^+$ and the similar mass ion pairs $N^+ + O^+$ and $N^+ + OH^+$ are now also detected, although most of the $O^+ + O^+$ signals are obscured by the dead time of the CFD. There is also a trace amount of $O^+ + NO_2^+$, although these signals are extremely weak. The $O^+ + O^+$ ion pair was not observed in the one-dimensional coincidence spectrum as it was obscured by the ringing when Δt_{tof} is small. Signals corresponding to ion pairs of similar mass can be detected in the one-dimensional coincidence spectra, *e.g.* $N^+ + O^+$ from $N_2O_5^{2+}$ (Chapter 4), but as the $N^+ + O^+$ and $N^+ + OH^+$ signals from HNO_3^{2+} are only moderately intense (Fig. 7.8), they were probably also obscured by the tail of the ringing in the one-dimensional coincidence spectrum.

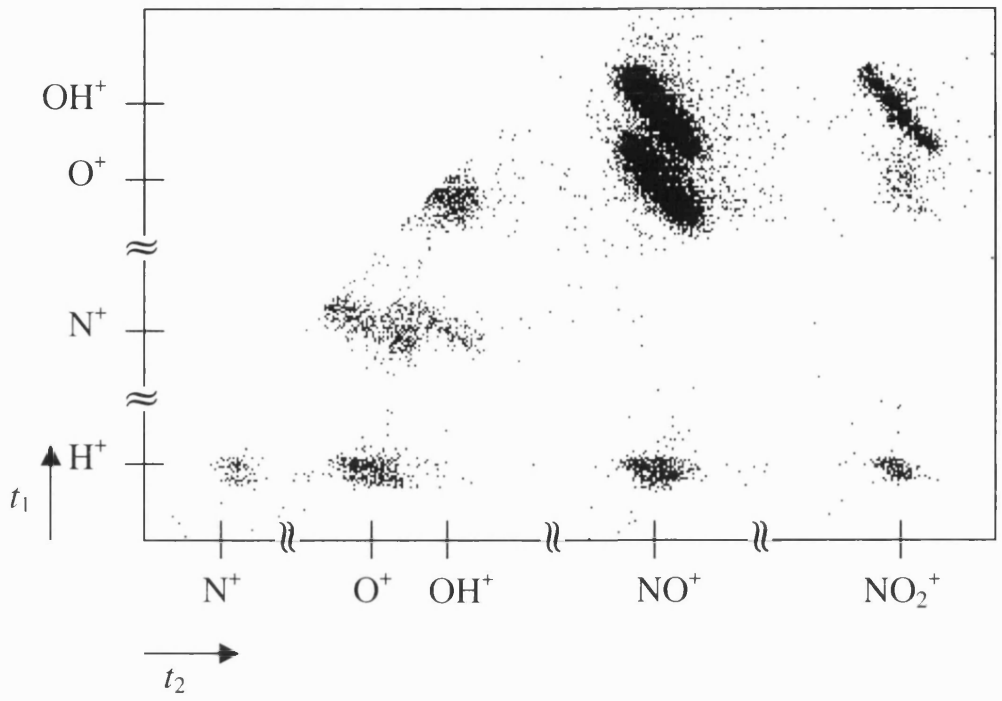

Fig. 7.8 Subtracted pairs spectrum of HNO_3^{2+} recorded at 250 eV.

Pairs spectra of HNO_3^{2+} were recorded concurrently with the singles spectra at 70, 100, 250 and 320 eV. False coincidences were subtracted from the pairs spectra and using the standard procedure, the values of I_{pair}/I_{total} were determined for each ion pair. These values are listed in Table 7.11. At 70 and 100 eV, due to the peak broadening experienced at low electron energies (Chapter 4), it is hard to distinguish between the $OH^+ + NO_2^+$ peak and the very weak $O^+ + NO_2^+$ signals. Therefore at these low electron energies, the combined intensity of these two ion pairs was determined.

Table 7.11 I_{pair}/I_{total} for the dissociation reactions of HNO_3^{2+} (the numbers in parentheses indicate the statistical error in the last figure of each value).

	I_{pair}/I_{total}			
Ion pair	70 eV	100 eV	250 eV	320 eV
$H^+ + N^+$	—	—	0.005(1)	0.021(2)
$H^+ + O^+$	—	—	0.024(1)	0.072(5)
$H^+ + NO^+$	—	—	0.037(2)	0.061(4)
$H^+ + NO_2^+$	—	—	0.013(1)	0.013(2)
$N^+ + O^+$	0.070(5)	0.054(4)	0.028(1)	0.070(5)
$N^+ + OH^+$	0.012(2)	0.012(2)	0.014(1)	0.021(2)
$O^+ + O^+$	0.102(6)	0.079(5)	0.031(2)	0.029(4)
$O^+ + NO^+$	0.415(14)	0.408(12)	0.351(6)	0.347(11)
$OH^+ + NO^+$	0.370(13)	0.367(11)	0.386(6)	0.280(10)
$O^+ + NO_2^+$	0.031(3)	0.080(5)	0.008(1)	0.014(2)
$OH^+ + NO_2^+$			0.074(2)	0.050(4)

At 70 and 100 eV, the increased period between the electron pulse and the TDC start pulse, required to eliminate any RF background noise, means that ions with small flight times, *e.g.* H^+, will reach the detector before the start pulse reaches the TDC. As a result, any ion pair signals corresponding to coincidences with H^+ ions will not appear in the pairs spectra at these low electron energies. Although the ion pairs in coincidence with H^+ are minor channels, the value of I_{total} at 70 and 100 eV is a lower limit as it does not include the intensities of these ion pairs.

For the pairs spectrum recorded at 250 eV, the slope *b* of the peaks corresponding to the dissociation reactions of HNO_3^{2+} were also determined. As discussed in Chapter 3, the value of *b* can potentially provide information on the dication dissociation mechanism involved in the formation of a particular ion pair.

Kinetic Energy Release Determination

Since using 2D coincidence techniques all the fragment ion pairs from the dissociation of HNO_3^{2+} are detected, the values of the KER for those ion pairs which were either not observed in the one-dimensional coincidence spectrum ($N^+ + O^+$ and $N^+ + OH^+$) or lay in congested regions of the spectrum ($H^+ + N^+$ and $H^+ + O^+$) can now be determined. Monte Carlo simulations of the relevant peaks can be performed (Chapter 3), simulating the formation of these ion pairs *via* all the possible sequential dissociation mechanisms involving an initial charge separation followed by subsequent monocation dissociation. Dissociation mechanisms involving deferred and initial three-body charge separation have not been considered since, as discussed in Section 7.3.1.2, the dissociation of polyatomic dications is most likely to occur *via* an initial two-body charge-separating reaction followed by further monocation fragmentation.[14-20] The results of the simulation of the $H^+ + N^+$, $H^+ + O^+$, $N^+ + O^+$ and $N^+ + OH^+$ peaks are given in Table 7.12, together with the corresponding values of $E(HNO_3^{2+})$ obtained using Eq. 3.13.

Table 7.12 Potential values of the KER, F_{KERD} and $E(HNO_3^{2+})$ for the indicated dissociation reactions of HNO_3^{2+}. These values are obtained assuming the indicated initial two-body charge separation and subsequent dissociation of the monocations accompanied by complete fragmentation of the neutral products.

Ion pair	Initial charge separation	KER /eV	F_{KERD} /eV	$E(HNO_3^{2+})$ /eV
$H^+ + N^+$ [+3O]	$H^+ + NO_3^+$	2.5	1.0	46.9
	$OH^+ + NO_2^+$	2.8	1.0	47.2
$H^+ + O^+$ [+N+2O]	$H^+ + NO_3^+$	14.0	—*	57.5
	$OH^+ + NO_2^+$	14.0	—*	57.5
	$O^+ + HNO_2^+$	4.0	3.0	47.5
$N^+ + O^+$ [+H+2O]	$OH^+ + NO_2^+$	10.5	2.0	55.0
	$O^+ + HNO_2^+$	10.5	2.0	55.0
$N^+ + OH^+$ [+2O]	$OH^+ + NO_2^+$	7.2	2.0	46.6

*For $H^+ + O^+$, no F_{KERD} values were determined for the indicated initial charge separations. See text for details.

As can be seen in Table 7.12 for the $H^+ + O^+$ ion pair, no value of F_{KERD} is given for the $H^+ + NO_3^+$ and $OH^+ + NO_2^+$ initial charge separations. The absence of F_{KERD} values for these dissociation reactions arises because the simulated spectrum did not fit the experimental data for any value of F_{KERD}. As will be discussed in Section 7.4.2.2, this implies that these fragmentation pathways are unlikely to be the ones followed to form $H^+ + O^+$. The uncertainties in the KER derived from the simulation procedure are of the order of ± 0.5 eV. The $O^+ + O^+$ and $O^+ + NO_2^+$ ion pairs were not simulated as only a portion of the $O^+ + O^+$ peak is observed and the $O^+ + NO_2^+$ peak is too weak for reliable data to be obtained.

Evaluation of the Contribution of Double Ionization to the Singles Spectrum

Following the procedure described in Chapter 3, the pairs spectra are converted into double ionization mass spectra (Fig. 7.9). Analysis of these spectra yields the double ionization fragment ion signal intensities which are used to determine the contribution of fragment ions from the dissociation of HNO_3^{2+} to the singles spectrum. Thus, values of σ_r^{si} for the fragment ions of HNO_3 can be determined from the singles spectrum (Eq. 3.26) which can be directly compared with the values of σ_r^{si} derived from the one-dimensional investigation.

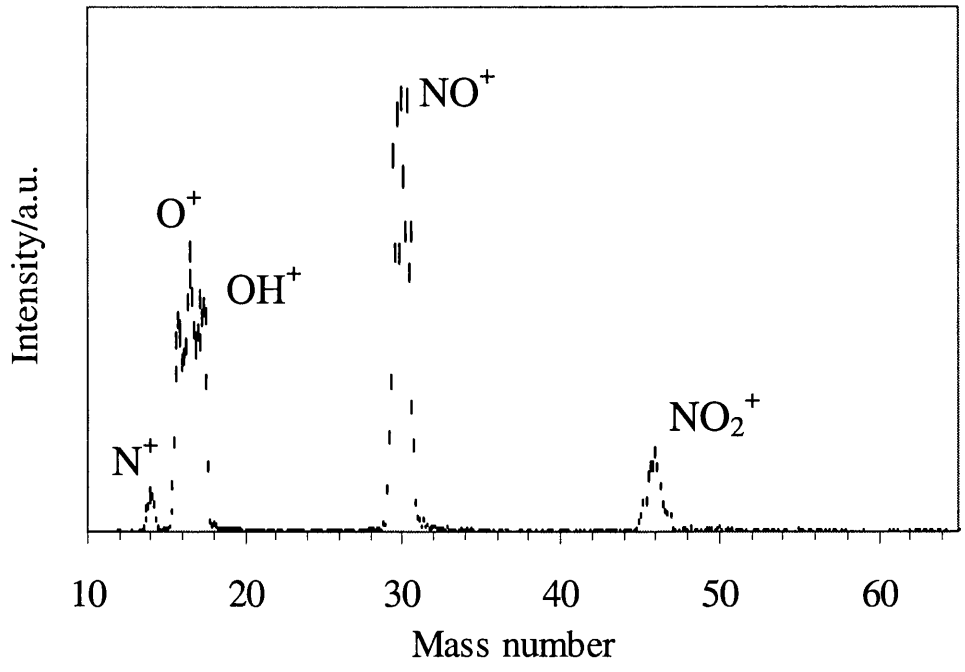

Fig. 7.9 Double ionization mass spectrum of HNO_3, converted from pairs spectrum recorded at 250 eV. The error bars, derived from the counting statistics, represent two standard deviations.

Determination of the Ratio of Double-to-Single Ionization Cross Sections

Following the analysis of the singles and pairs spectra of HNO_3^{2+}, it is now possible to obtain a first estimate of the ratio of total double-to-single ionization cross sections σ^{2+}/σ^+ for HNO_3 using

Eq. 3.39. The omission of both the H^+ ion signal intensities in the singles spectra and the intensities of the ion pairs in coincidence with H^+ in the pairs spectra from the values of S_T and P_P respectively used to calculate σ^{2+}/σ^+ (Eq. 3.39) results in an approximate value of σ^{2+}/σ^+ derived for HNO_3. The ratio of σ^{2+}/σ^+ for HNO_3, at the range of electron energies employed in this part of the study, are given in Table 7.13 and plotted in Fig. 7.10.

Table 7.13 Ratio of σ^{2+}/σ^+ for HNO_3. The standard deviation in the last figure of each ratio is given in parentheses.

Electron energy /eV	σ^{2+}/σ^+
70	0.045(10)
100	0.064(14)
250	0.055(12)
320	0.087(19)

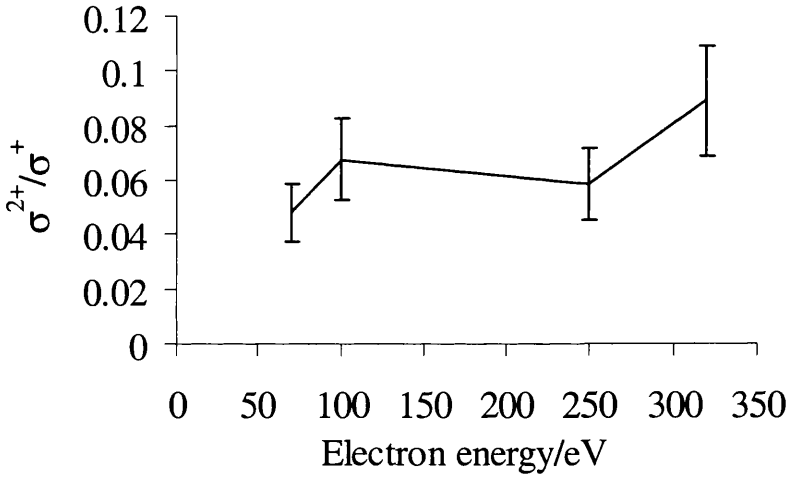

Fig. 7.10 Ratio of σ^{2+}/σ^+ for HNO_3. The error bars shown represent two standard deviations.

7.4.2 Discussion

7.4.2.1 Single Ionization

In the 2D investigation of the single ionization of HNO_3, the stable parent ion HNO_3^+ and fragment ions H^+, N^+, O^+, OH^+, NO^+ and NO_2^+ are observed in the singles spectrum, the NO_2^+ ion being the most abundant. This is consistent with the one-dimensional time-of-flight mass spectra (Fig. 7.1). However, due to the overlap of background signals with the H^+ peak in the singles spectrum, no data concerning these fragment ions could be extracted from the singles spectra.

As discussed at length in Chapters 3 & 4, the apparatus set-up employed in the 2D studies eliminates the discrimination against the detection of highly energetic ions, such as fragment ions formed from dissociative double ionization. This increased detection efficiency results in the contribution of ions formed from double ionization to the ion signal intensities obtained from the singles spectrum. This is apparent from a comparison of the data given in Table 7.9 (σ_r^I) & Table

7.10 (σ_r^{si}). From the studies of the double ionization of HNO_3, it is found that all the fragment ions observed in the singles spectra are formed upon dissociative double ionization. Therefore, upon subtraction of the double ionization contribution, any ion signals in the singles spectrum arising from the detection of fragments from the dissociation of HNO_3^{2+} will be removed. Thus, the values of σ_r^{si} will be lower than the values of σ_r^{I} derived from the singles spectrum and as can be seen from Table 7.9 & Table 7.10, this is indeed the case.

Table 7.14 Comparison of σ_r^{si} for the fragment ions of HNO_3 in the one-dimensional (time-of-flight mass spectrum) and 2D (singles spectrum) studies (the numbers in parentheses indicate the statistical error in the last figure of each cross section).

Fragment ion		σ_r^{si}			
		70 eV	100 eV	250 eV	320 eV*
N^+	1D	0.83(8)	1.17(11)	1.36(13)	1.36(13)
	2D	1.20(7)	1.47(11)	1.27(4)	1.71(17)
O^+	1D	2.41(8)	3.15(30)	3.20(39)	3.09(32)
	2D	4.56(60)	5.34(76)	5.28(59)	6.76(113)
OH^+	1D	2.53(39)	2.45(53)	2.97(40)	2.92(35)
	2D	5.99(33)	5.96(60)	4.84(39)	4.42(47)
NO^+	1D	23.62(95)	24.33(163)	24.15(205)	24.58(237)
	2D	26.86(71)	27.16(106)	26.65(72)	27.66(114)
NO_2^+	1D	46.19(184)	44.05(274)	43.69(241)	44.30(318)
	2D	40.57(44)	37.42(42)	36.78(19)	37.02(50)

* Data recorded at 300 eV in one-dimensional study.

Table 7.14 shows the comparison of the values of σ_r^{si} obtained in the one and two-dimensional experiments. No data was recorded at 320 eV in the one-dimensional experiments, but as can be seen from Table 7.1 and Fig. 7.2, there is little variation in the values of σ_r^{si} of the ions between 300 and 350 eV. So, for comparison between the one and two-dimensional work, the values of σ_r^{si} obtained at 300 eV in the one-dimensional experiments are quoted in Table 7.14.

In contrast to the studies of Cl_2O and OClO, there is no general trend apparent when comparing the values of σ_r^{si} for the fragment ions of HNO_3 derived from the two different studies. From Table 7.14, it can be seen that, within the error limits, there is no difference between the values of σ_r^{si} for N^+ and NO^+ obtained in the one and two-dimensional studies. Therefore, as assumed in the one-dimensional study, there is no double ionization contribution to the N^+ or NO^+ ion signals in the one-dimensional mass spectrum neither are any 'superthermal' ions from dissociative single ionization missing the detector. This is in contrast to the O^+ and OH^+ fragments where the values of σ_r^{si} derived from the singles spectra are higher than those derived from the one-dimensional mass spectrum. This increased value for O^+ and OH^+ could arise from the imperfect subtraction of background gas contribution. However, this is unlikely as the values obtained for N^+ in the one and two-dimensional studies are in good agreement. A more probable explanation is that the apparatus set-up used in the one-dimensional experiments is discriminating against superthermal O^+ and OH^+

ions formed from dissociative single ionization. The 2D apparatus does not have this discrimination against energetic ions and therefore they will be detected.

Finally, the values of σ_r^{si} for NO_2^+ derived from the singles spectra are lower than those derived in the one-dimensional experiments. This suggests that some NO_2^+ fragments formed from dissociative double ionization are being observed in the one-dimensional time-of-flight mass spectrum. Although energetic ions are discriminated against in the one-dimensional experiments by using a small detector, any dication dissociation events occurring along the axis of the TOFMS will be detected and therefore contribute to the time-of-flight mass spectra. Any such contribution would be subtracted when determining values of σ_r^{si} from the singles spectra.

From the comparison of the data derived from the one and two-dimensional studies of the single ionization of HNO_3, it is apparent that the assumptions made concerning the discrimination against energetic ions in the one-dimensional experiments are less good for HNO_3. Despite the small detector used in the one-dimensional experiments discriminating against energetic ions from double ionization, any dication dissociation products formed along the axis of the TOFMS will be detected. In addition, it appears that superthermal O^+ and OH^+ fragment ions formed from dissociative single ionization are missing the detector in the one-dimensional experiments and are only detected when the angular discrimination is removed by using the larger MCP detector, as in the 2D experiments.

7.4.2.2 Double Ionization

The pairs spectrum shows that HNO_3^{2+} dissociates *via* a two-body reaction to form $OH^+ + NO_2^+$ and three-body reactions to form $H^+ + N^+$, $H^+ + O^+$, $H^+ + NO^+$, $H^+ + NO_2^+$, $N^+ + O^+$, $N^+ + OH^+$, $O^+ + O^+$, $O^+ + NO^+$, $OH^+ + NO^+$ and $O^+ + NO_2^+$. With the exception of the identical and similar mass ion pairs and $O^+ + NO_2^+$, this is consistent with the one-dimensional coincidence spectrum. In the one-dimensional coincidence spectrum, the two-body dissociation reaction $O^+ + HNO_2^+$ was thought to be present, but there is no evidence of a peak corresponding to this ion pair in the pairs spectrum. As the $O^+ + NO_2^+$ peak is extremely weak and has a similar time-of-flight difference to $O^+ + HNO_2^+$, it is probable that an error was made when assigning the minority signals in the one-dimensional coincidence spectrum. Despite this misidentification, the observation of the $H^+ + N^+$ and $O^+ + NO_2^+$ ion pairs in the pairs spectrum demonstrates that the simulation procedure used in the one-dimensional study to distinguish all the coincidence signals contributing to a congested region of the spectrum is still a satisfactory way of identifying minority dissociation reactions.

In agreement with the one-dimensional coincidence spectrum, the $OH^+ + NO^+$ and $O^+ + NO^+$ ion pairs are the most abundant ion pairs in the pairs spectrum (Table 7.11). From the one-dimensional investigation, these ion pairs are thought to be formed by secondary decay following an initial charge separation reaction to form $OH^+ + NO_2^+$. The abundance of these three-body reactions

suggests that the dominant dication reaction channel involves the breaking of a single bond. However, the dissociation reactions involving maximum disintegration of HNO_3^{2+}, even though they are minor channels, are not negligible.

The analysis of each observed ion pair will be discussed in turn below. However, as the majority of the $O^+ + O^+$ ion pair is not observed in the pairs spectrum, this dissociation reaction was not investigated further. In addition, no statistical significant information could be derived from the analysis of the weak $O^+ + NO_2^+$ ion pair.

Two-Body Reaction: $OH^+ + NO_2^+$

The two-body dissociation of HNO_3^{2+} to form $OH^+ + NO_2^+$ should give rise to a narrow peak in the pairs spectrum with a slope of –1. As can be seen in Fig. 7.8, the peak corresponding to the $OH^+ + NO_2^+$ ion pair is indeed narrow and the observed value of b for the $OH^+ + NO_2^+$ ion pair is -1.03 ± 0.01.

In order to confirm that the data obtained from the one and two-dimensional coincidence spectra are consistent, an estimation of the KER upon dissociation of HNO_3^{2+} to form the $OH^+ + NO_2^+$ ion pair is made by simulating the peak in the pairs spectrum corresponding to this ion pair (Chapter 3). The values of KER, F_{KERD} and $E(HNO_3^{2+})$ derived from the width of the $OH^+ + NO_2^+$ pairs peak are given in Table 7.15, together with the values obtained from the one-dimensional coincidence peak widths.

Table 7.15 Values of KER, F_{KERD} and $E(HNO_3^{2+})$ for forming $OH^+ + NO_2^+$ from HNO_3^{2+} derived from the one and two-dimensional coincidence peak widths.

	KER /eV	F_{KERD} /eV	$E(HNO_3^{2+})$ /eV
1D	5.8	0.5	30.7 ± 0.2
2D	5.8	2.0	30.7 ± 0.5

As can be seen in Table 7.15, the values of KER and $E(HNO_3^{2+})$ derived from the two studies of the double ionization of HNO_3 agree with one another, indicating the consistency between the one and two-dimensional studies of the ionization of HNO_3. However, there is a difference in the values of F_{KERD} given in Table 7.15. The difference between the F_{KERD} values derived from the two coincidence spectra could arise from either the increased detection of high-energy fragments in the 2D spectra or the large uncertainty in determining the width of the $OH^+ + NO_2^+$ peak in the congested region of the one-dimensional coincidence spectrum.

Three-Body Reactions: $H^+ + N^+$

No information concerning the formation of $H^+ + N^+$ from HNO_3^{2+} was determined in the one-dimensional study due to the lack of information concerning energetics and appearance energies

for this ion pair. However, it is hoped that some mechanistic information for this ion pair can be derived from the pairs spectrum.

The slope of the $H^+ + N^+$ peak in the pairs spectrum is –0.39 (Table 7.16). This value of *b* indicates that the formation of $H^+ + N^+$ follows a sequential pathway involving an initial charge separation followed by further dissociation of the singly charged ions to form the observed ion pair. Table 7.16 also lists the expected values of *b* for $H^+ + N^+$ derived assuming the indicated initial two-body charge separation and subsequent singly charged ion dissociation. It is important to note that the expected values of *b* listed in Table 7.16 are limiting values (Chapter 3) and it is also assumed that there is no molecular rearrangement prior to the formation of the ion pair. For a three-body dissociation reaction involving an initial charge separation, the observed value of *b* will lie between the expected *b*, derived assuming the limiting dissociation conditions, and –1. However, one has to be careful when making comparisons between the observed and expected values of *b* for ion pairs coincident with H^+, since the slopes of the peaks of these ion pairs are very susceptible to factors such as field inhomogenities present in the apparatus[27] and any background noise present. Nevertheless, a comparison between the observed and expected *b* values can give an indication of the dication dissociation mechanism. From Table 7.16, it seems likely that the formation of $H^+ + N^+$ from HNO_3^{2+} occurs *via* an initial charge separation to form $OH^+ + NO_2^+$ as the expected *b* value for the $H^+ + NO_3^+$ initial charge separation is more negative than -1. In addition, the lack of a secondary peak for $H^+ + N^+$ at longer flight times implies that this a fast dissociation (~1-5 ps). Although it appears that the formation of $H^+ + N^+$ is occurring *via* the mechanism involving an initial charge-separating reaction to form $OH^+ + NO_2^+$, the potential influence of apparatus factors means that the assignment of this mechanism to the $H^+ + N^+$ dissociation reaction is not definitive.

Table 7.16 Values of *b* for the peaks in the pairs spectrum corresponding to the $H^+ + N^+$, $H^+ + O^+$, $H^+ + NO^+$ and $H^+ + NO_2^+$ ion pairs. The numbers in parentheses indicate the statistical error in the last figure of the value.

Ion pair	Initial charge separation	Expected *b*	Observed *b*
$H^+ + N^+$	$H^+ + NO_3^+$	-4.4	-0.39(15)
	$OH^+ + NO_2^+$	-0.19	
$H^+ + O^+$	$H^+ + NO_3^+$	-3.88	
	$OH^+ + NO_2^+$	-0.17	-0.17(3)
	$O^+ + HNO_2^+$	-0.02	
$H^+ + NO^+$	$H^+ + NO_3^+$	-2.06	-0.12(3)
	$OH^+ + NO_2^+$	-0.09	
$H^+ + NO_2^+$	$H^+ + NO_3^+$	-1.34	-0.37(5)
	$OH^+ + NO_2^+$	-0.06	

The potential values of the KER, derived from the width of the $H^+ + N^+$ peak in the pairs spectrum, for the two possible initial charge-separating reactions are similar to one another (Table 7.12). Therefore, from the analysis of the KER upon dissociation, no distinction between the possible fragmentation pathways for forming $H^+ + N^+$ can be made.

Thus, although a definitive dissociation mechanism cannot be assigned for the $H^+ + N^+$ ion pair, it is possible that the decay pathway involves an initial charge separation to form $OH^+ + NO_2^+$ followed by further dissociation to form $H^+ + N^+$ and completely fragmented neutral products. From the simulation of the pairs peak width, the value of $E(HNO_3^{2+})$ responsible for the formation of $H^+ + N^+$ is ~47 eV (Table 7.12). This value is significantly higher than any dication state energies derived previously (Table 7.8), suggesting that the dissociation of HNO_3^{2+} to form $H^+ + N^+$ occurs from a high-lying distinct dication electronic state.

$H^+ + O^+$

No information concerning the dissociation mechanism followed to form the $H^+ + O^+$ ion pair was obtained from the one-dimensional investigation due to a lack of information concerning energetics and appearance energy for this ion pair. However, it is hoped that the analysis of the pairs spectra will provide some mechanistic information for this ion pair.

From the pairs spectrum, the slope of the $H^+ + O^+$ peak is –0.17 (Table 7.16). This value of *b* indicates that $H^+ + O^+$ is formed by a sequential pathway involving an initial charge separation and from the comparison of the observed and expected values of *b* given in Table 7.16, it is probable that the formation of $H^+ + O^+$ occurs *via* an initial charge separation to form either $OH^+ + NO_2^+$ or $O^+ + HNO_2^+$. Once again, due to the possible influence of apparatus factors, it is not possible to distinguish between these two possible initial charge-separating reactions using the values of *b*.

From the simulation of the pairs peak corresponding to the $H^+ + O^+$ ion pair, the values of the KER derived assuming the formation of $H^+ + O^+$ *via* initial charge separation to $H^+ + NO_3^+$ or $OH^+ + NO_2^+$ (Table 7.12), are unrealistically large for the dissociation of a polyatomic dication.[26] In addition, the fit of the simulated spectrum with the experimental data is very poor for these decay pathways and therefore, they are considered unlikely to be responsible for forming this ion pair. The remaining fragmentation pathway involves an initial charge separation to form $O^+ + HNO_2^+$ followed by further dissociation to form $H^+ + O^+$, accompanied by the complete fragmentation of the neutral products [Reaction (7.XIX)].

$$\begin{array}{c} HNO_3^{2+} \rightarrow O^+ + HNO_2^+ \\ \downarrow \\ O^+ + H^+ [+ N + 2O] \end{array} \qquad (7.XIX)$$

The value of $E(HNO_3^{2+})$ associated with this dissociation mechanism is 47.5 eV, a value close to the energy of the dication state deduced to be responsible for the $H^+ + N^+$ dissociation reaction. However, the initial charge separations deduced to be responsible for the $H^+ + N^+$ and $H^+ + O^+$ ion pairs are different. Hence, perhaps the dissociation of HNO_3^{2+} to form these ion pairs occurs from distinct but close-lying electronic states.

$H^+ + NO^+$

In the one-dimensional study, the formation of $H^+ + NO^+$ was thought to follow an initial charge separation to form $OH^+ + NO_2^+$ and subsequent monocation dissociation to form the ion pair [Reaction (7.XVII)].

From the pairs spectrum, the slope of the $H^+ + NO^+$ peak is -0.12. From the comparison of the observed and expected values of *b* (Table 7.16), it seems apparent that the observed value of *b* agrees very well with the expected value of the slope assuming an initial charge separation to form $OH^+ + NO_2^+$. This is consistent with the information derived from the one-dimensional investigation. Indeed, the good agreement between the observed value of *b* and the expected limiting case suggests that the sequential dissociation is occurring once the singly charged ions have left each other's Coulomb field on a timescale of >5 ps.

$H^+ + NO_2^+$

In the one-dimensional study, the formation of $H^+ + NO_2^+$ was assumed to follow an initial charge separation to form $H^+ + NO_3^+$ and subsequent monocation dissociation to form the ion pair [Reaction (7.XVIII)].

From the pairs spectrum, the slope of the $H^+ + NO_2^+$ peak is –0.37. From Table 7.16, the comparison of the observed and expected values of *b*, derived assuming the indicated initial charge separation, suggests that $H^+ + NO_2^+$ is likely to be formed *via* charge separation to $OH^+ + NO_2^+$. This is contradictory to the dissociation mechanism derived for the $H^+ + NO_2^+$ ion pair in the one-dimensional investigation. However, the discrepancy between the two investigations may be due to apparatus factors influencing the shape of the H^+ ion pairs. Therefore, in order to confirm the conclusions reached in the one-dimensional coincidence experiments, the ion pairs formed in coincidence with H^+ ions need to be investigated further.

$N^+ + O^+$

As the $N^+ + O^+$ ion pair was not observed in the one-dimensional coincidence spectrum, there is no previous information concerning this dissociation reaction. However, some mechanistic information for this ion pair may be derived from the pairs spectrum.

The value of *b* for the peak in the pairs spectrum corresponding to $N^+ + O^+$ is –0.48 and the expected values of *b* derived by considering the possible initial two-body dissociation of HNO_3^{2+}, assuming there is no rearrangement of the dication prior to forming $N^+ + O^+$, are given in Table 7.17.

Table 7.17 Values of *b* for the peaks in the pairs spectrum corresponding to the $N^+ + O^+$ and $N^+ + OH^+$ ion pairs. The numbers in parentheses indicate the statistical error in the last figure of the value.

Ion pair	Initial charge separation	Expected *b*	Observed *b*
$N^+ + O^+$	$OH^+ + NO_2^+$	-0.32	-0.48(3)
	$O^+ + HNO_2^+$	-0.3	
$N^+ + OH^+$	$OH^+ + NO_2^+$	-0.3	-0.59(4)

As can be seen from Table 7.17, the observed value of *b* for the $N^+ + O^+$ ion pair is lower than the expected values of *b* derived assuming the indicated initial charge separation. The $N^+ + O^+$ and $N^+ + OH^+$ peaks are moderately weak and lie very close to one another in the spectrum (Fig. 7.8). Therefore, there is undoubtedly a larger uncertainty (± 0.1) associated with the observed value of *b* for these ion pairs than the quoted value derived from the error in the least squares fitting. But, even with an increased error in *b*, the experimental value does not agree with the limiting values derived by considering the conservation of momentum. This suggests that the dicationic dissociation mechanism followed to form this ion pair is a fast sequential reaction with secondary dissociation occurring within the Coulomb fields of the monocations. However, it is not possible to distinguish between the possible dissociation mechanisms, as both initial charge separations yield similar expected values of *b*.

The simulation of the $N^+ + O^+$ peak yields values of the KER upon dissociation for the two possible fragmentation pathways which are also very similar in value (Table 7.12). Therefore, although from the analysis of the peak slope and KER upon dissociation, the fragmentation pathway followed to form $N^+ + O^+$ from HNO_3^{2+} cannot be definitively assigned, the value of *b* suggests that the dicationic dissociation is fast and follows a sequential pathway. In addition, the simulation of the pairs peak yields an evaluation of the energy of dication state responsible for the $N^+ + O^+$ dissociation reaction as *ca.* 55 eV. This value of $E(HNO_3^{2+})$ is higher than any value of $E(HNO_3^{2+})$ determined for the dissociation reactions of HNO_3^{2+} (Table 7.8 & Table 7.12). Therefore the dissociation of HNO_3^{2+} to form $N^+ + O^+$ occurs from a high-lying distinct electronic state of the dication.

$N^+ + OH^+$

Similarly to the $N^+ + O^+$ pair, the $N^+ + OH^+$ ion pair was not observed in the one-dimensional coincidence spectrum and therefore is no previous information concerning this dissociation reaction.

The slope of the $N^+ + OH^+$ peak in the pairs spectrum is –0.59. For the $N^+ + OH^+$ ion pair, there is only one possible dicationic dissociation reaction that can form this ion pair, an initial charge-separating reaction to form $OH^+ + NO_2^+$ followed by dissociation of these monocations to form the detected ion pair [Reaction (7.XX)].

$$HNO_3^{2+} \rightarrow OH^+ + NO_2^+$$
$$\downarrow \qquad (7.XX)$$
$$OH^+ + N^+ [+ 2O]$$

Similarly to the $N^+ + O^+$ ion pair, the variation in the observed and expected value of *b* suggests that a fast sequential dissociation reaction is occurring to form the $N^+ + OH^+$ ion pair.

The simulation of pairs peak corresponding to this ion pair indicates that the formation of the $N^+ + OH^+$ ion pair occurs from the dissociation of a dication electronic state of 46.6 eV. This estimate of the energy of the dication state responsible for forming the $N^+ + OH^+$ ion pair lies close to the values of $E(HNO_3^{2+})$ derived for the $H^+ + N^+$ and $H^+ + O^+$ ion pairs. Indeed, the $H^+ + N^+$ and $N^+ + OH^+$ dissociation reactions are both deduced to proceed *via* the initial fragmentation of HNO_3^{2+} to $OH^+ + NO_2^+$. Therefore, it is possible that the formation of the $H^+ + N^+$ and $N^+ + OH^+$ ion pairs is a result of the dissociation of the same dicationic electronic state.

$O^+ + NO^+$

In the one-dimensional coincidence study, the $O^+ + NO^+$ ion pair was deduced to be formed *via* an initial charge separation to form $OH^+ + NO_2^+$ which then undergoes secondary decay to form first $OH^+ + NO^+$ and after subsequent dissociation forming $O^+ + NO^+$ [Reaction (7.XVI)].

The slope of the peak corresponding to the $O^+ + NO^+$ ion pair has been determined from the pairs spectrum (Table 7.18) and this observed value of b = -1.11 indicates that the dissociation of HNO_3^{2+} to form $O^+ + NO^+$ follows a sequential mechanism. The expected values of *b* derived from the indicated two-body dissociation reactions which, following further monocation dissociation, could form this ion pair are also listed in Table 7.18.

Table 7.18 Values of *b* for the peaks in the pairs spectrum corresponding to the $O^+ + NO^+$ and $OH^+ + NO^+$ ion pairs. The numbers in parentheses indicate the statistical error in the last figure of the value.

Ion pair	Initial charge separation	Expected *b*	Observed *b*
$O^+ + NO^+$	$OH^+ + NO_2^+$	-1.4	-1.11(1)
	$O^+ + HNO_2^+$	-1.6	
$OH^+ + NO^+$	$OH^+ + NO_2^+$	-1.5	-1.18(1)

There are two possible dication dissociation pathways by which the $O^+ + NO^+$ ion pair could be formed: the initial dissociation of HNO_3^{2+} to form either $OH^+ + NO_2^+$ or $O^+ + HNO_2^+$ followed by subsequent monocation dissociation. From the data given in Table 7.18, it is not possible to distinguish between the possible mechanisms, since the difference between the observed and expected values of *b* only indicates that the mechanism by which $O^+ + NO^+$ is formed is a fast sequential dissociation of the dication. Therefore, although it is not possible to confirm that the dissociation reaction forming $O^+ + NO^+$ involves an initial charge separation to $OH^+ + NO_2^+$, the

dissociation mechanism followed is fast and sequential, which is consistent with the one-dimensional study.

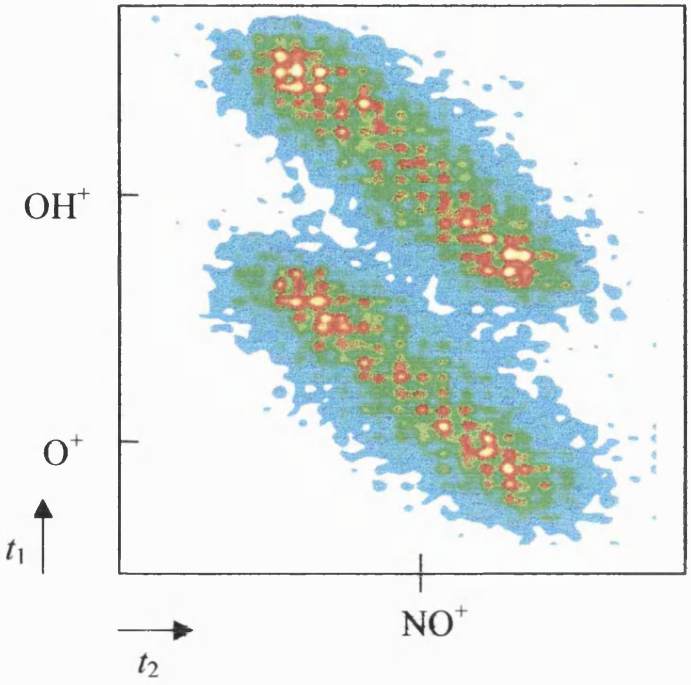

Fig. 7.11 2D contour plot of the peaks in the pairs spectrum of HNO_3^{2+} corresponding to $O^+ + NO^+$ and $OH^+ + NO^+$. The regular structure observed in the peaks arises from the smoothing of the data in the graphics programme.

$OH^+ + NO^+$

The slope of the $OH^+ + NO^+$ peak in the pairs spectrum is –1.18. If the dissociation of HNO_3^{2+} is assumed to follow an initial two-body charge-separating reaction, there is only one possible pathway by which the $OH^+ + NO^+$ ion pair could be formed; the dissociation of HNO_3^{2+} to form $OH^+ + NO_2^+$ followed by further dissociation to form the detected ion pair. Indeed, this is the dissociation mechanism derived from the one-dimensional coincidence spectrum to be responsible for the formation of the $OH^+ + NO^+$ ion pair. The difference between the observed and expected values of *b* is consistent with a fast sequential mechanism, with the secondary dissociation of the NO_2^+ ion to form NO^+ occurring within the Coulomb field of the OH^+ fragment ion.

Fig. 7.11 shows a 2D plot of the $O^+ + NO^+$ and $OH^+ + NO^+$ peaks in the pairs spectrum. This plot of the most intense ion pairs in the spectrum shows the elimination of any angular discrimination by using the MCP detector in the 2D apparatus set-up, as the high intensity region is uniform along the axial lengths of the peaks.

General Discussion

The above conclusions are summarised in Table 7.19, which lists the observed dissociation reactions of HNO_3^{2+} and the derived energetic data given the most probable dissociation mechanism. In addition, the data derived in the one-dimensional study is also listed in the table.

Table 7.19 Proposed decay pathways and estimates of $E(HNO_3^{2+})$ and appearance energies, where available, of the dissociation reactions of HNO_3^{2+}. The values of the three-body reactions are obtained assuming the indicated initial charge separation and subsequent monocation dissociation accompanied by complete fragmentation of the neutral products.

Ion pair	Initial charge separation	$E(HNO_3^{2+})$ /eV	Appearance energy /eV
$H^+ + N^+$ [+3O]	$OH^+ + NO_2^+$	47.0	—
$H^+ + O^+$ [+N+2O]	$O^+ + HNO_2^+$	47.5	—
$H^+ + NO^+$ [+2O]	$OH^+ + NO_2^+$	39.1	40 ± 5
$H^+ + NO_2^+$ [+O]	$H^+ + NO_3^+$	37.9	40 ± 5
$N^+ + O^+$ [+H+2O]	—	55.0	—
$N^+ + OH^+$[+2O]	$OH^+ + NO_2^+$	46.6	—
$O^+ + O^+$ [+H+N+O]	—	—	—
$O^+ + NO^+$ [+H+O]	$OH^+ + NO_2^+$	39.6	39.0 ± 2
$OH^+ + NO^+$ [+O]	$OH^+ + NO_2^+$	35.3	39.0 ± 2
$O^+ + NO_2^+$ [+H]	—	—	—
$OH^+ + NO_2^+$	$OH^+ + NO_2^+$	30.7	—

From Table 7.19, it is apparent that the dissociation of HNO_3^{2+} can occur *via* three possible initial two-body charge separations, where the most dominant of these charge-separating reactions is the formation of $OH^+ + NO_2^+$. Indeed, all the fragment ion pairs of HNO_3^{2+}, apart from $H^+ + NO_2^+$, $H^+ + O^+$ and the unclassified reactions, are formed following this initial charge separation. In addition, the $OH^+ + NO_2^+$ ion pair is the only two-body dissociation reaction observed in the pairs spectra. Thus, the breaking of the OH-N bond in the dication is most common bond cleavage. As described above, it is not possible to determine the fragmentation pathway that leads to the formation of $N^+ + O^+$, $O^+ + O^+$ and $O^+ + NO_2^+$ because of the lack of information concerning peak slopes and energetics for these ion pairs.

In order to derive more information concerning the dissociation reactions of HNO_3, a more detailed investigation of the pairs spectra must be performed. A reduction in the dead time of the CFD would result in an increased area of the $O^+ + O^+$ peak observed in the pairs spectra, thus enabling a reasonable measurement of the peak slope and estimation of reliable values of the KER from the peak width to be made. In order to derive more information concerning minority dissociation reactions of HNO_3^{2+}, such as $H^+ + N^+$, $H^+ + O$, $N^+ + O^+$, $N^+ + OH^+$, it is necessary to increase the data acquisition time and improve the counting statistics to yield sharp, temporally resolved peaks in the pairs spectrum. As a result, improved estimates of the energetics of dissociation can be made by simulation of the peaks. In addition, it would be useful to work at low electron energies to obtain estimates of the appearance energies of these ion pairs for comparison with values of $E(HNO_3^{2+})$ derived from the coincidence peak widths.

Ratio of Double-to-Single Ionization Cross Sections

The values of the ratio of σ^{2+}/σ^{+} for HNO_3 have been determined at each electron energy and are listed in Table 7.13 and plotted in Fig. 7.10. As can be seen in the figure, there is an initial increase in σ^{2+}/σ^{+} as the electron energy is raised and there is an increased likelihood of double ionization. As the ionizing electron energy is raised above 100 eV, there is a decrease in the ratio of σ^{2+}/σ^{+}, but between 250 and 320 eV the value of σ^{2+}/σ^{+} increases significantly once more to reach a maximum of almost 0.09. The larger value of σ^{2+}/σ^{+} at 320 eV may be due to the onset of multiple ionization at high electron energies accounting for the increase in the ratio of σ^{2+}/σ^{+}. Pairs of singly charged ions from dissociative multiple ionization formed at these high electron energies may contribute to the ion pair intensities in the pairs spectra thus increasing the so-called ratio of σ^{2+}/σ^{+}.

At its maximum at 320 eV, the "double" ionization cross section is 9% of the single ionization cross section but, as mentioned above, this value may be biased due to the contribution of multiple ionization at high electron energies. However, at 100 eV the value of σ^{2+}/σ^{+} is 6.4%, suggesting that double ionization is a relatively minor reaction channel for HNO_3. But, although the single ionization of HNO_3 may predominate, the double ionization cannot be disregarded since, as has been shown in this chapter, there is a contribution of fragments from dicationic dissociation to the ion signals in the time-of-flight mass spectra.

7.4.3 Conclusion

The second section of this chapter has discussed the 2D investigation of the single and double ionization of HNO_3. Time-of-flight mass spectrometry is used to determine the values of σ_r^{si} for HNO_3 for incident electron energies of 70, 100, 250 and 320 eV. Stable parent ions HNO_3^+ and fragment ions H^+, N^+, O^+, OH^+, NO^+ and NO_2^+ ions were detected, NO_2^+ being the most abundant ion. In order to obtain the values of σ_r^{si} for the ions observed in the 2D time-of-flight mass spectrum, the contribution of fragment ions from double ionization first had to be assessed and subtracted from the ion signals in the mass spectrum.

2D coincidence experiments were performed to investigate the formation and fragmentation of HNO_3^{2+}. Peaks due to the formation of $H^+ + N^+$, $H^+ + O^+$, $H^+ + NO^+$, $H^+ + NO_2^+$, $N^+ + O^+$, $N^+ + OH^+$, $O^+ + O^+$, $O^+ + NO^+$, $OH^+ + NO^+$, $O^+ + NO_2^+$ and $OH^+ + NO_2^+$ were observed in the spectrum.

The dissociation reactions of HNO_3^{2+} are assumed to proceed *via* initial two-body charge separations and subsequent dissociation of these precursor ion pairs. The dissociation of HNO_3^{2+} to form the $O^+ + NO^+$ and $OH^+ + NO^+$ ion pairs proceeds *via* fast sequential dissociation mechanisms. For the ion pairs not previously observed in the one-dimensional coincidence spectrum, $N^+ + O^+$ and $N^+ + OH^+$, the observed peak slopes indicate that dication dissociation to form these ion pairs also

proceeds *via* fast sequential mechanisms. From the simulation of the peaks corresponding to these ion pairs, it is not possible to assign a fragmentation pathway for the $N^+ + O^+$ ion pair, assuming an initial two-body charge separation. However, from the values of the dication state energy derived from the simulation procedure, it is apparent that the formation of $N^+ + O^+$ occurs from a distinct high-lying electronic state. In addition, the $H^+ + N^+$ and $N^+ + OH^+$ ion pairs may be formed from the dissociation of the same dicationic state, lying in close proximity to the one responsible for $H^+ + O^+$ ion pair. From the slopes and simulation of the peaks in the pairs spectrum, $H^+ + N^+$ is formed *via* an initial charge separation to $OH^+ + NO_2^+$ whereas the $H^+ + O^+$ dissociation reaction proceeds *via* $O^+ + HNO_2^+$.

The first estimate of the total double-to-single ionization cross sections ratio for HNO_3 shows that double ionization of nitric acid is a relatively minor reaction channel. However, despite being an insignificant proportion of the total ionization cross section, the possible contribution of dissociative double ionization to ion signals in the mass spectra must be considered when determining values of σ_r^{si} for the ions formed upon single ionization of HNO_3.

7.5 Overall Conclusions

This chapter describes the investigation of the single and double ionization of nitric acid. The single ionization of HNO_3 has been studied using time-of-flight mass spectrometry in order to determine values of the relative partial single ionization cross section σ_r^{si} for the fragment ions of HNO_3. Double ionization of HNO_3 has been investigated using ion-ion coincidence techniques to derive information concerning the mechanisms and energetics of the dication dissociation reactions.

From the single ionization of HNO_3, parent ion HNO_3^+ and fragment ions N^+, O^+, OH^+, NO^+ and NO_2^+ were observed in the time-of-flight mass spectrum. From the spectra recorded using the two different methodologies of the one and two-dimensional investigations, values of σ_r^{si} were derived. The two sets of values of σ_r^{si} were not generally in good agreement with one another and there was no obvious trend to the differences between the values of σ_r^{si} derived in the one and two-dimensional studies. This suggests that for HNO_3 the assumptions made in the one-dimensional study, that the small detector discriminated against energetic ions solely from dissociative double ionization, do not necessarily hold true.

Coincidence techniques were employed to investigate the formation and fragmentation of HNO_3^{2+}. The following ion pairs were observed following the dissociation of HNO_3^{2+}: $H^+ + N^+$, $H^+ + O^+$, $H^+ + NO^+$, $H^+ + NO_2^+$, $N^+ + O^+$, $N^+ + OH^+$, $O^+ + O^+$, $O^+ + NO^+$, $OH^+ + NO^+$, $O^+ + NO_2^+$ and $OH^+ + NO_2^+$. Investigations of the dissociation reactions of HNO_3^{2+} showed that the dication can dissociate *via* one of the following three possible initial charge separations involving the cleavage of

a single dication bond: $OH^+ + NO_2^+$, $O^+ + HNO_2^+$ or $H^+ + NO_3^+$. These precursor ion pairs subsequently dissociate to form the observed ion pairs. The most frequently occurring initial charge separation forms $OH^+ + NO_2^+$ and the majority of the fragment ion pairs arise from the sequential dissociation of HNO_3^{2+} *via* this precursor ion pair. The investigation of the energetics of HNO_3^{2+} suggests that the dissociation to form $OH^+ + NO_2^+$ occurs from the ground electronic state of the dication, thus giving a first estimate of the double ionization energy of HNO_3 as 30.7 ± 0.2 eV. In addition, it is possible that the $H^+ + NO^+$, $O^+ + NO^+$ and $OH^+ + NO^+$ dissociation reactions all occur from the same electronic state of the dication and also the dissociation of a distinct dication electronic state results in the formation of $H^+ + N^+$ and $OH^+ + N^+$.

The first estimate of the ratio of the double-to-single ionization cross sections indicates that double ionization contributes around 6% to the total ionization cross section of HNO_3. Therefore, although double ionization is minor, the design of the apparatus is such that it can never be completely disregarded when investigating the single ionization of molecules.

References

1 F.D. Miles, *Nitric Acid Manufacture and Uses*, Oxford University Press, London, 1961

2 B.A. Thrush, *Rep. Prog. Phys.*, **51** (1988) 1341

3 A.C. Aikin, *J. Geophys. Res.*, **102** (1997) 12921

4 S.J. Baek, C.R. Park and H.L. Kim, *J. Photochem. Photobiol. A*, **104** (1997) 13

5 D. Bingemann, M.P. Gorman, A.M. King and F.F. Crim, *J. Chem. Phys.*, **107** (1997) 661

6 A.A. Turnipseed, G.L. Vaghjiani, J.E. Thompson and A.R. Ravishankara, *J. Chem. Phys.*, **96** (1992) 5887

7 P.S. Yeh, G.H. Leu, Y.P. Lee and I.C. Chen, *J. Chem. Phys.*, **103** (1995) 4879

8 Eight Peak Index of Mass Spectra, Mass Spectra Data Centre, 1970, Vol. 1

9 NIST (1998), Vol 69

10 R.A. Friedel, J.L. Shultz and A.G. Sharkey, *Anal. Chem.*, **31** (1959) 1128

11 H.-W. Jochims, W. Denzer, H. Baumgärtel, O. Lösking and H. Willner, *Ber. Bunsenges. Phys. Chem.*, **96** (1992) 573

12 C.S.S. O'Connor and S.D. Price, *Int. J. Mass Spectrom. Ion Proc.*, **177** (1998) 119

13 C.S.S. O'Connor, N.C. Jones and S.D. Price, *Int. J. Mass Spectrom. Ion Proc.*, **163** (1997) 131

14 J.H.D. Eland, *Mol. Phys.*, **61** (1987) 725

15 S. Hsieh and J.H.D. Eland, *J. Chem. Phys.*, **103** (1995) 1006

16 I. Nenner and J.H.D. Eland, *Z. Phys. D*, **25** (1992) 47

17 J.H.D. Eland, *Chem. Phys. Lett.*, **203** (1993) 353

18 K. Codling, L.J. Frasinski, P.A. Hatherly, M. Stankiewicz and F.P. Larkins, *J. Phys. B*, **24** (1991) 951

19 M. Simon, P. Morin, P. Lablanquie, M. Lavollee, K. Ueda and N. Kosugi, *Chem. Phys. Lett.*, **238** (1995) 42

20 P.J. Richardson, J.H.D. Eland and P. Lablanquie, *Org. Mass Spec.*, **21** (1986) 289

21 P.R. Bevington, *Data Reduction and Error Analysis for the Physical Sciences*, McGraw-Hill, New York, 1992

22 S. Leach, J.H.D. Eland and S.D. Price, *J. Phys. Chem.*, **93** (1989) 7575

23 J. Marriott and J.D. Craggs, *J. Electron. Control*, **3** (1957) 194

24 S.G. Lias, J.E. Bartmess, J.F. Liebman, J.L. Holmes, R.D. Levin and W.G. Mallard, *J. Phys. Chem. Ref. Data*, **17 S1** (1988) 1

25 B.P. Tsai and J.H.D. Eland, *Int. J. Mass Spectrom. Ion Proc.*, **36** (1980) 143

26 D.M. Curtis and J.H.D. Eland, *Int. J. Mass Spectrom. Ion Proc.*, **63** (1985) 241

27 J.H.D. Eland, *Meas. Sci. Tech.*, **4** (1993) 1522

8. Further Work

As has been illustrated in the previous chapters, a great deal of information concerning the formation and fragmentation of both singly and doubly charged molecular ions can be obtained from a relatively simple piece of apparatus. However, as is also apparent in these chapters, there is scope for improvement of the two-dimensional apparatus set-up to obtain, for example, low electron energy spectra and improved counting statistics. Indeed, work is currently underway on the TOFMS commissioning a new electron gun design which it is hoped will improve the quality of the electron pulses at low electron energies, thus enabling reproducible spectra to be recorded down to electron energies comparable to typical double ionization energies. The recording of such low energy spectra will make it possible to investigate the appearance energies of dication dissociation reactions using 2D coincidence techniques. These appearance energies can then be compared with the dication state energies derived previously in order to obtain further information on the fragmentation pathways of dications. In particular, such information may provide more detail on the weak dication dissociation reactions for which no definitive dissociation mechanisms could be assigned in this thesis.

There are a number of other improvements currently being made to the 2D apparatus set-up in order to produce well-resolved and reliably reproducible singles and pairs spectra, which will hopefully reduce the uncertainties associated with data derived from the spectra. Modifications to the data acquisition algorithm have dramatically increased the rate of data acquisition from ~400 Hz up to 50 kHz. Therefore, the length of time taken to record spectra can be shortened which reduces the possibility of sample degradation in the inlet system, such as was observed in the 2D study of OClO. Also, the reduced data acquisition time means that spectra can be recorded at a number of electron energies in the time it would previously have taken to record spectra at a single ionizing energy. Therefore, the range of ionizing electron energies can be expanded and hopefully spectra can be recorded from threshold to 500 eV, as in the one-dimensional studies. In addition, the improved acquisition rate means that it is easier to record spectra with better counting statistics thus reducing experimental uncertainties.

As discussed in Chapter 7, background signals arising from the interaction of electrons with the surface of the repeller plate were obscuring the H^+ fragment ion signals from the dissociation of HNO_3^+. It is hoped that a new design for the repeller plate, involving the replacement of the solid plate with a 90% transmissive grid, will solve this problem as any electrons accelerated towards the repeller plate will pass through the grid, thereby eliminating the source of the interference. Thus, it will be possible to extend the HNO_3 experiments and re-estimate the ratio of the double-to-single ionization cross section, with all the fragment ion and ion pair signals included in the calculation.

As discussed in Chapter 4, no 2D spectra were recorded for N_2O_5, due to the unavailability of the loaned apparatus required to synthesis N_2O_5. It is hoped that in the near future, this apparatus will be made available once more, allowing the continuation of the investigation of N_2O_5.

An obvious extension to the single ionization studies is the calculation of the mass spectra using the statistical theories of unimolecular reactions, *i.e.* RRKM/QET,[1-3] for comparison with the experimental data. The next step in the double ionization studies could perhaps be the addition of a position-sensitive detector to the apparatus to enable the intensities of fragment ion pairs to be measured at a given scattering angle. Recent PEPIPICO experiments performed using a position-sensitive detector (PSD-PEPIPICO)[4,5] have shown that experiments such as these reveal finer details of the major reaction pathways confirming their sequential nature and identify minor pathways previously unobserved. Thus using this technique it is possible to determine the full kinematics of each dication dissociation event, as in molecular beam dynamics. Finally, it is hoped that investigations of the single and double ionization of other atmospheric molecules, such as molecular chlorine[6] and bromine oxides, can be performed using the TOFMS discussed in this thesis.

References

1 A. Maccoll, *Org. Mass Spec.,* **26** (1991) 235

2 T. Baer and W.L. Hase, *Unimolecular Reaction Dynamics: Theory and Experiments*, Oxford University Press, New York, 1996

3 T. Baer and P.M. Mayer, *J. Am. Soc., Mass Spectrom.,* **8** (1997) 103

4 S. Hsieh and J.H.D. Eland, *J. Phys. B,* **30** (1997) 4515

5 S. Hsieh and J.H.D. Eland, *Int. J. Mass Spectrom. Ion Proc.,* **167/168** (1997) 415

6 S.D. Price and G.S. Lidder, *in preparation,* (1999)

Appendix 1

As mentioned in Chapter 2, the flight time of an ion in a time-of-flight mass spectrometer (TOFMS) can be derived using a combination of Newtonian mechanics and electrostatics. From such a derivation, it is found that the time it takes an ion to travel a certain distance in a given set of electric fields t_{tof} is proportional to the square root of its mass m (Eq. 2.1). The derivation of the expression given in Eq. 2.1 is given below.

The TOFMS used in the experiments discussed in this thesis is a two-field device and a schematic diagram of this type of TOFMS is shown in Fig. 2.1. The TOFMS contains a source region of length $2S$, an acceleration region of length d and a field-free drift region of length D. The flight time t_{tof} of an ion of mass m in the TOFMS, from the centre of the source region where the ion is formed to the detector at the end of the drift region, is the sum of the ion's flight time in the three regions of the TOFMS,

$$t_{tof} = t_S + t_d + t_D \qquad \text{Eq. A1.1}$$

where t_S, t_d and t_D are the flight times in the source, acceleration and drift regions respectively.

The time-of-flight of an ion in the source region t_S can be derived from Newtonian mechanics (Eq. A1.1), note that as the ion is not necessarily at rest in the source region, it will possess an initial velocity u.

$$t_S = \left[\frac{\left(u^2 + 2a_S S\right)^{\frac{1}{2}} - u}{a_S}\right] = \left[\frac{\left(u^2 + 2E_S qS\right)^{\frac{1}{2}} m^{\frac{1}{2}} - u}{E_S q}\right] \qquad \text{Eq. A1.2}$$

where a_S is the acceleration of the ion in the source field,

$$a_n = \frac{E_n q}{m} \qquad \text{Eq. A1.3}$$

and the electric field strength is given by

$$E_n = \frac{V_S}{S} \qquad \text{Eq. A1.4}$$

The time-of-flight of the ion in the second acceleration region t_d is derived in the same manner and substituting for Eq. A1.3 gives

$$t_d = \left[\frac{\left(u^2 + 2E_S qS\right)^{\frac{1}{2}} m^{\frac{1}{2}} + \left(2E_d qd\right)^{\frac{1}{2}} m^{\frac{1}{2}} - \left(u^2 + 2E_S qS\right)^{\frac{1}{2}} m^{\frac{1}{2}}}{E_d q}\right] \qquad \text{Eq. A1.5}$$

Finally, the time taken for the ion to pass through the field-free drift region t_D is

$$t_D = \frac{Dm^{\frac{1}{2}}}{\left[\left(u^2 + 2E_S qS\right)^{\frac{1}{2}} + \left(2E_d qd\right)^{\frac{1}{2}}\right]} \qquad \text{Eq. A1.6}$$

Therefore, the flight time of an ion in the TOFMS can be determined from Eq. A1.1 using Eq. A1.2, Eq. A1.5 & Eq. A1.6. From the summation of the ion flight times in the individual regions in the TOMFS, t_S, t_d and t_D, it is found that

$$t_{tof} = k\sqrt{m} \qquad \text{Eq. A1.7}$$

This expression shows that the time of flight of an ion in a given set of electric fields represented by a constant k is proportional to the square root of its mass m.